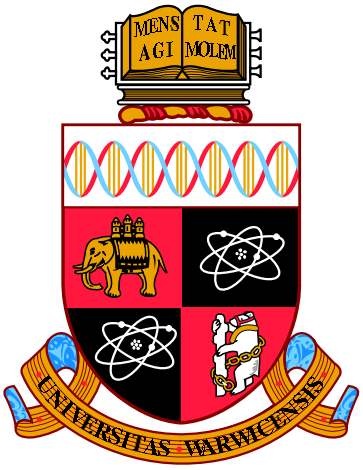

Micro-hotplate based CMOS sensor for smart gas and odour detection

by

Yuxin Xing

Thesis submitted to the University of Warwick

for the degree of

Doctor of Philosophy

School of Engineering

December 2019

Contents

Declarations

This thesis is submitted to the University of Warwick in support of my application for the degree of Doctor of Philosophy. It has been composed by myself and has not been submitted in any previous application for any degree. All work presented was carried out by the author, except where otherwise indicated. Parts of this thesis have been published in peer-review journals and international conferences. The list is provided in the List of Publications.

List of Tables

List of Figures

Abbreviations

ANN	Artificial Neural Network.
CMOS	Complementary Metal Oxide Semiconductor.
CMP	Chemical Mechanical Polishing.
CNN	Convolutional Neural Network.
CNT	Carbon Nanotube.
CVD	Chemical Vapour Deposition.
CWT	Continuous Wavelet Transform.
DAQ	Data Acquisition.
DNN	Deep Neural Network.
DRIE	Deep Reactive-Ion Etching.
DWT	Discrete Wavelet Transform.
FEM	Finite Element Method.
FFT	Fast Fourier Transform.
FIR	Far Infra-red.
FTIR	Fourier Transform Infra-red.
GPM	Gap Plasmon Mode.
IOT	Internet of Things.
IR	Infra-red.
KNN	k-Nearest Neighbour.
LPCVD	Low Pressure Chemical Vapour Deposition.

MEMS	Microelectromechanical Systems.
MHR	Membrane-to-Heater Ratio.
MIR	Mid Infra-red.
MOX	Metal Oxide.
NDIR	Non-dispersive Infra-red.
NIRS	Near-infrared Spectroscopy.
PCA	Principal Component Analysis.
PECVD	Plasmon-enhanced Chemical Vapour Deposition.
PEM	Polymer Electrolyte Membrane.
PLS	Partial Least Squares.
PML	Perfectly Matched Layers.
PPB	Parts per billion.
PPM	Parts per million.
PVD	Physical Vapour Deposition.
PWM	Pulse Width Modulation.
RMSE	Root Mean Sqaure Error.
RNN	Recurrent Neural Network.
SEM	Scanning Electron Microscope.
SLR	Surface Lattice Resonance.
SOI	Silicon on Insulator.
SOM	Self-organising Maps.
SPI	Serial Peripheral Interface.
SPP	Surface Plasmon Polaritons.
SSE	Sum Square Error.
SVM	Support Vector Machine.
TE	Transverse Electric.
TM	Transverse Magnetic.
VOC	Volatile Organic Compound.

Nomenclature

α	Absorption coefficient
α_λ	Absorptivity at wavelength λ
λ	Wavelength
$\mathbf{B}$	Magnetic Field
$\mathbf{D}$	Electric Displacement
$\mathbf{E}$	Electric Field
$\mathbf{H}$	Polarised Magnetic Field
$\mathbf{J}$	Current Density
$\mathrm{J_f}$	Free Current
Q	Total Electric Charge
μm	Micrometer
μ	Permeability
μ_o	Permeability of Free Space
ω	Angular Frequency
ω_p	Plasma Frequency
ρ	Charge Density
ρ_f	Free Charge
σ	Electrical Conductivity

ε	Permittivity
ε_o	Permittivity of Free Space
ε_λ	Emissivity at wavelength λ
A	Absolute Humidity
c	Speed of Light
d	Diameter of the plasmonic dot
h	Depth of the plasmonic dot
h	Planck Constant
I	Intensity
k_B	Boltzmann Constant
k_F	Floquet Periodicity k-vector
k_o	Free space wave number
l	Optical path length
p	Pitch of the plasmonic structure
P_w	Vapour Pressure
P_{ws}	Saturated Vapour Pressure
r	Radius of the plasmonic dot
s	Natural Number
T	Temperature

Acknowledgments

I would first like to express my gratitude to my supervisors Prof. Julian Gardner and Dr. Marina Cole for the continuous support, patience and motivation during my time at the University. This thesis would not have been possible without their guidance and invaluable expertise.

I would like to acknowledge the financial support from the School of Engineering at the University of Warwick, EU H2020 SmokeBot project (Project No. 645101) and the COMET program within the K2 Center "Integrated Computational Material, Process and Product Engineering (IC-MPPE)" (Austria, Project No 859480).

I would like to thank the High Voltage Microelectronics and Sensors Group (HVMS) at Cambridge University for providing the plasmonic model and devices. I would like to thank Dr. Timothy Vincent for his advices and knowledge on NDIR sensors, as well as his assistance and collaboration on the EU SmokeBot project. I would also like to thank Dr. Barbara Urasinska-Wojcik for the development of MOX sensors used in this work, and her insights on the EPSRC Supergen project. I am also grateful to the staff in the School of Engineering, in particular, Mr. Frank Courtney for his technical support.

I would like to offer my appreciation to all my colleagues at the Microsensors and Bioelectronic Laboratory (MBL), Dr. Farah Villa Lopez, Dr. Guangfen Wei, Dr Siavash Esfahani, Geraint Rhys Jones and Jan Peter Specht.

Last but definitely not least, I am very grateful to my friends for bringing me joy and happy distractions. I want to extend my profound gratitude to my family, especially my mother, my father and my grandma. The past four years were not easy for them, but their support and unconditional love never stop. My remembrance to my dear late father, you have been an inspiration for me throughout my entire life. And my mother for her loving encouragement and support, I can never thank her enough.

List of Publications

Journals

- **Y. Xing**, T. A. Vincent, Han Fan, E. Schaffernicht, Vector Hernandez Bennetts, A. J. Lilienthal, M. Cole, and J. W. Gardner "FireNose on mobile robot in harsh environments", *IEEE Sensors Journal*, vol. 19, no. 24, pp. 12418–12431, 2019.
- **Y. Xing**, T. A. Vincent, M. Cole, and J. W. Gardner, "Real-time thermal modulation of high handwidth MOX gas sensors for mobile robot applications", *Sensors*, vol. 19, no. 5, pp. 1180–1190, 2019.
- T. A. Vincent, **Y. Xing**, M. Cole, J. W. Gardner, "Investigation of response of high-bandwidth MOX sensors to gas plumes for application on a mobile robot in hazardous environments", *Sensors and Actuators B: Chemical*, vol. 279, no. 1, pp. 351–360, 2018.

Conferences

- **Y. Xing**, M. Cole and J. W. Gardner, "Identification of urine odour using CMOS-based metal oxide resistive gas sensors", *20th International Conference on Solid-State Sensors, Actuators and Microsystems & Eurosensors XXXIII (TRANSDUCERS & EUROSENSORS XXXIII)*, Berlin, Germany, Sept. 2019.

- J. W. Gardner, **Y. Xing**, "Classification of urine smell from CMOS based odour sensor array and artificial neural network", *7th International Work-Conference on Bioinformatics and Biomedical Engineering (IWBBIO)*, Granada, Spain, May. 2019.

- T. A. Vincent, **Y. Xing**, M. Cole, and J. W. Gardner, "Thermal modulation of a high-bandwidth gas sensor array in real-time for application on a mobile robot", *MDPI Proceedings (Eurosensors 2018, Graz, Austria)*, vol. 2, no. 13, p. 858, Nov. 2018.

- **Y. Xing**, B. Urasinska-Wojcik and J. W. Gardner, "Plasmonic enhanced CMOS non-dispersive infrared gas sensor for acetone and ammonia detection", *2018 IEEE International Instrumentation and Measurement Technology Conference (I2MTC)*, Houston, TX, May. 2018, pp. 1-5.

- B. Urasinska-Wojcik, **Y. Xing**, J. W. Gardner, "Plasmonic enhanced CMOS non-dispersive infrared gas detector", *Advanced Materials World Congress 2018*, Singapore, Feb. 2018.

- **Y. Xing**, T. A. Vincent, M. Cole, J. W. Gardner, H. Fan, V. Hernandez Bennetts, E. Schaffernicht, A. J. Lilienthal, "Multi-sensor unit on mobile robot for unsupervised gas discrimination in harsh environments", *2017 IEEE SENSORS*, Glasgow, UK, Oct. 2017.

- T. A. Vincent, **Y. Xing**, M. Cole, and J. W. Gardner, "High bandwidth sensor module for mobile robot applications-wind tunnel characterization", *MDPI Proceedings (Eurosensors 2017, Paris, France)*, vol. 1, no. 4, p. 421, Aug. 2017.

- G. Wei, J. W. Gardner, M. Cole and **Y. Xing**, "Multi-sensor module for a mobile robot operating in harsh environments", *2016 IEEE SENSORS*, Orlando, FL, Oct. 2016, pp. 1-3.

- J. W. Gardner, **Y. Xing**, B. Urasinska-Wojcik, A. de Luca, and F. Udrea,

"Design of plasmonic structures in CMOS technology for low-cost, enhanced infra-red gas sensors", *META 2016*, Malaga, Spain, June. 2016.

Abstract

Low cost, highly sensitive, miniature CMOS micro-hotplate based gas sensors have received great attention recently. The global sensor market is expanding rapidly with an expected increase of $5 \sim 8\%$ growth in the next five years. The application areas for a gas sensor include but are not limited to, air quality monitoring, industrial and laboratory conditions, military, and biomedical sectors. It is the key hardware component of an electronic nose, as well as the signal processing on the software side. In this thesis, both aspects of such a system were studied with new sensor technologies and improved signal processing algorithms. In addition, this thesis also described different applications and research projects using these sensor technologies and algorithms.

A novel plasmonic structure was employed as an infrared source for a non-dispersive infrared gas sensor. This structure was based on a CMOS micro hotplate with three metal layers and periodic cylindrical dots to induce plasmon resonance, that allowed a tunable narrowband infrared radiation with high sensitivity and selectivity. Five gases were studied as target gases, namely, carbon monoxide, carbon dioxide, acetone, ammonia and hydrogen sulfide. These emitter sources were fabricated and characterised with a gas cell, optical filters and commercial detectors under different gas concentrations and humidity levels. The results were promising with the lowest detection limit for ammonia at 10 ppm with 5 ppm resolution.

On the data processing side, various signal processing methods were explored both on-board and off-board. Temperature modulation was the on-board method by switching the operating temperatures of a micro hotplate. This technique was proven to overcome and reduce some typical sensor issues, such as drift, slow response/recovery speed (from tens of seconds to a few seconds) and even cross sensitivities. Off-board post processing methods were also studied, including principal component analysis, k-nearest neighbours, self-organising maps and shallow/deep neural networks. The results from these algorithms were compared and overall an 85% or higher classification accuracy could be achieved. This work showed the potential to discriminate gases/odours, which could lead to the development of a real-time discrimination algorithm for low cost wearable devices.

Chapter 1

Introduction and Motivations

1.1 Olfactory System and Gas Sensors

Vision, audition, somatosensation, gustation and olfaction are the five human senses Aristotle described as 'the windows of the soul'. These vital mechanisms are the ways we interact and experience the surrounding environments. Not just human, all creatures have sensory systems that help them to perceive and interpret information. Scientists have been studying them for decades trying to understand and mimic these intricate systems. With the increasing interest in robotics and artificial intelligence, sensors have became the centre of attention. Different sensors are developed to perform the tasks of the sensory systems, such as camera/image sensors (vision), microphones (audition), tactile sensors (somatosensation), electronic tongues (gustation) and electronic noses (olfaction).

Gustatory and olfactory systems are parts of our chemosensory system, and together they measure flavours. But unlike gustation, which only response to five tastes (sweet, salty, sour, bitter and umami or savoury), the mammalian olfactory system has been proven to detect at least 1 trillion odours [1]. These odours are the results of a simple or complex mixture of molecules components. Each odour molecule has its own distinct smell, but the mixture, depending on the concentration levels, will have an entirely different scent. The human nose is an extraordinary organ with more than 400 olfactory receptors [2] that are used to detection these smells, it even has the possibilities to rival canines or rodents [3]. When an odour molecule triggers different receptor(s), an electrical signal is generated that process

and pass through neurons to the olfactory bulb [4]. The physiological arrangement is shown in Figure. 1.1. The odorants stimulate various parts of the olfactory centre in the brain which associate with cognition, discrimination, emotions, memory, behaviours etc. [5, 6, 7, 8]. That is the reason why the smell of fresh flowers bring us back to a tranquil summer afternoon, and the stink of roadside garbage ruin your morning!

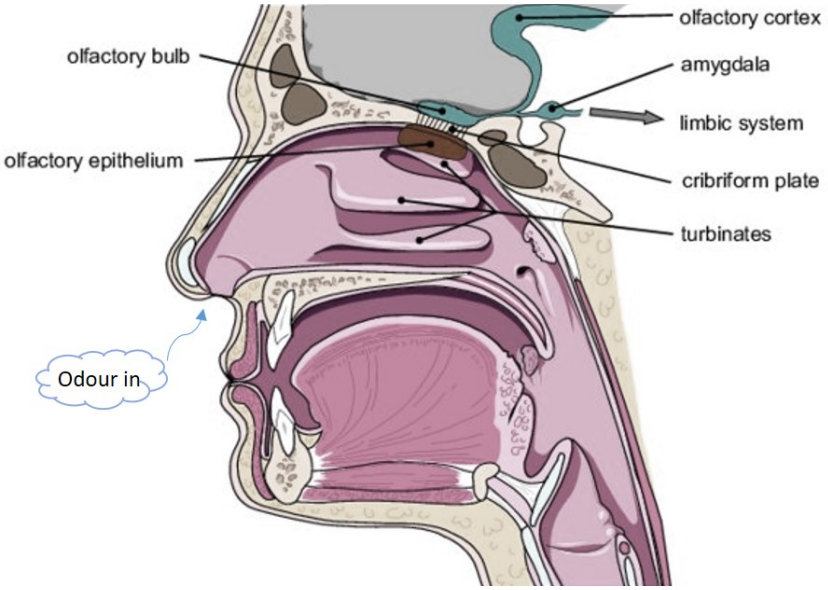

Figure 1.1: Physiology of human olfactory system(adapted from [9]).

In order to mimic the mammalian olfactory system, the concept of the electronic nose was first defined in the late 1980s [10]. It is defined by Gardner and Bartlett as 'an instrument which comprises an array of electronic chemical sensors with partial specificity and an appropriate pattern recognition system, capable of recognizing simple or complex smell' [11]. It is essentially a multi-sensor system for odour and gas detections. This system has applications such as health and safety, air quality monitoring and home appliances, where detections and qualifications are required. Figure. 1.2 shows a typical concept of such system in comparison with the human olfactory system. The main hardware component in an e-nose is the gas sensor, which can detect the presence of one or multiple gas components in the surrounding area similar to the olfactory receptors. There are several ways to do that, such as chemical sensors, mass sensors, optical sensors etc., which will be introduced in section 1.3. The other part of an e-nose is the data acquisition and recognition, which like the human brain, processes the data and classifies the signals.

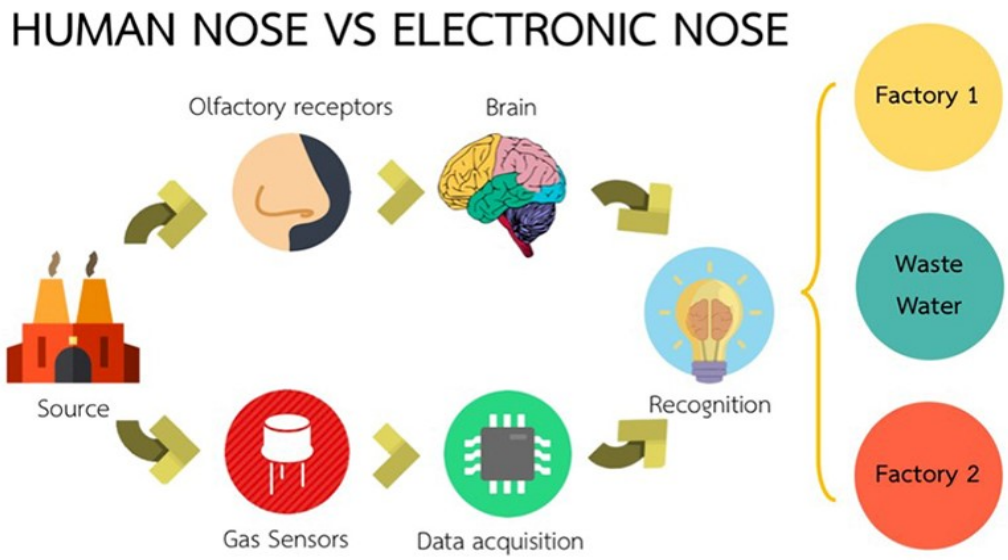

Figure 1.2: Simplified representation of the human olfactory system versus an e-nose system (reproduced from [12]).

1.2 Market and Applications for Gas Sensors

There is a growing need for gas sensors. The global sensor market was valued at USD 2.05 billion in 2018, and is expected to increase by 5 $\sim$ 8 % from 2019 to 2025 [14]. One of the main applications is air pollution and environmental monitoring. On top of that, the demand for other applications such as industrial,

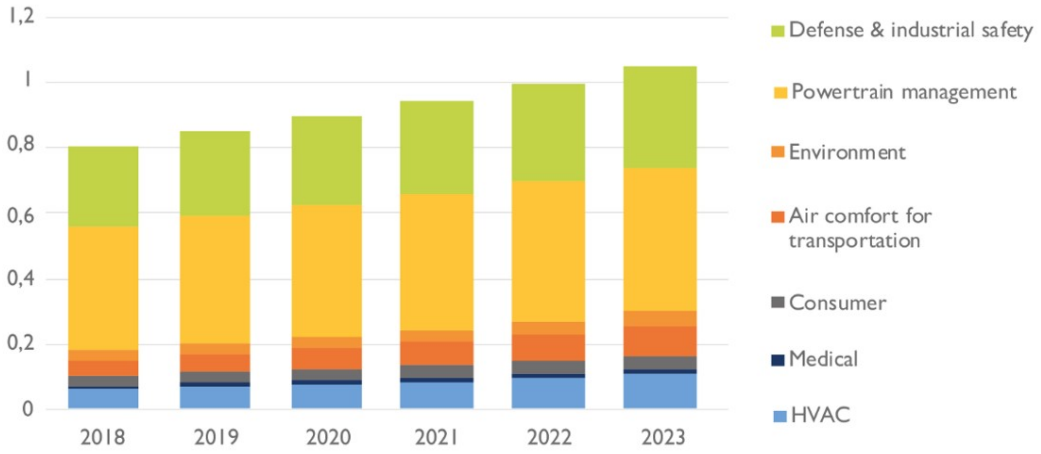

Figure 1.3: Gas sensor market in value ($B) from 2018 to 2023 (reproduced from ([13]).

military, transportation and medical, are also increasing rapidly. Figure. 1.3 shows a histogram of different gas sensing applications.

Environmental monitoring includes indoor and outdoor air quality detections. Outdoor gases, such as carbon dioxide, methane and nitrogen oxide are of interest due to their greenhouse effect. Carbon dioxide sensors are accounted for approximately 25% of the global gas sensor market [14] and this number is increasing every year. In addition, an oxygen sensor is another popular sensor not only for air quality monitoring, but also for combustion system and fuel consumptions. Indoor gases, such as carbon monoxide, carbon dioxide, methane, are closely related to the ventilation system and home appliances. For medical applications, odours and gases as biomarkers are often studied, such as acetone [16], ethyl alcohol [17], ammonia [18] and volatile organic compounds (VOCs). Other gases, for instance hydrogen sulfide, propane and butane are of interest in the combustion systems, chlorine for water quality detections, and sulfide oxide as a natural gas that is related to volcanic

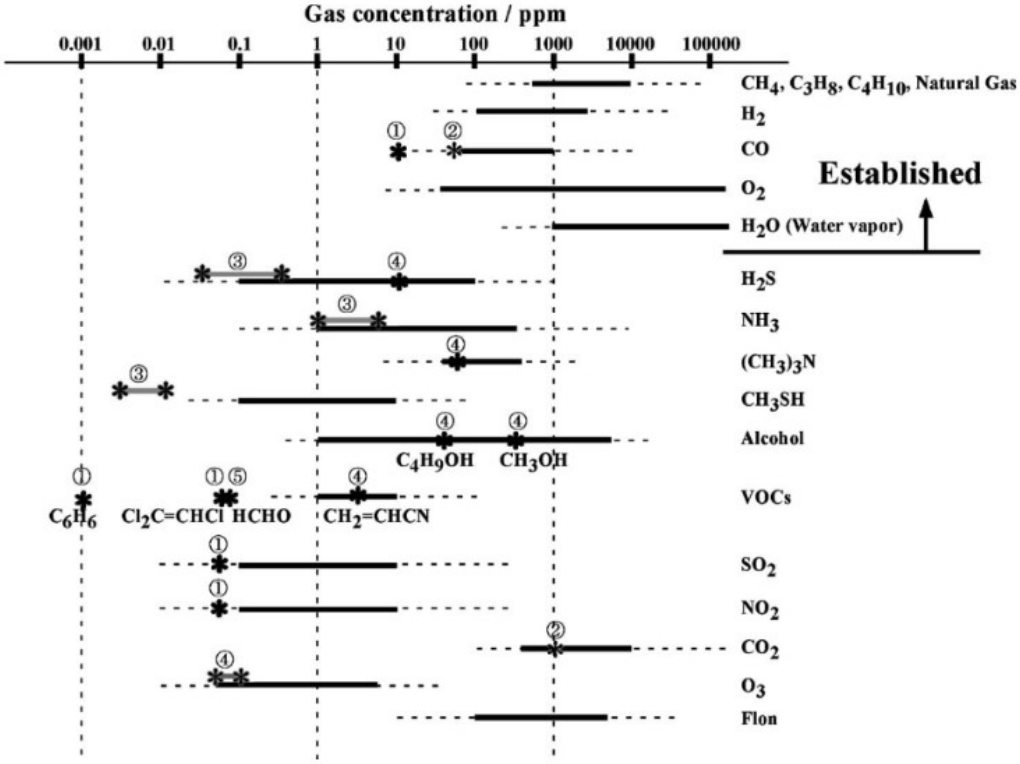

Figure 1.4: Typical concentration levels for gases of interest (①②③④⑤ indicate different legislation limits, note: not all these gases are odours. Figure reproduced from [15]).

activities. Yamazoe [15] conducted a review on the gas sensor technologies, and he summarised the typical gas concentrations for the gases mentioned above, as shown in Figure. 1.4.

1.3 Gas sensing Technologies

Various sensor technologies are available nowadays that can be found both in laboratory researches and commercial products. The technology can be based either on physical or chemical effects. For low-cost gas sensing applications, chemical sensors are more popular. Common chemical sensor technologies include electrochemical sensors, thermal sensors, mass sensors and optical sensors [19].

Electrochemical sensors are the largest group of chemical sensors. It is the most common approach and the target gas produces an electrical signal that is proportional to the concentration [20]. The electrochemical reaction happens at the working electrode, and the signal changes are then measured. Due to its operation principle, it is suitable for a variety of redox gases. It can be divided into three types, potentiometric, conductometric and amperometric/voltammetric [21], which corresponds to different signal information. This type of sensors are commercially used as oxygen sensors and toxic gas sensors, such as carbon monoxide and hydrogen sulfide, but they are bulky in size. Figure. 1.5 shows an SGX oxygen sensor and Figaro CO sensor.

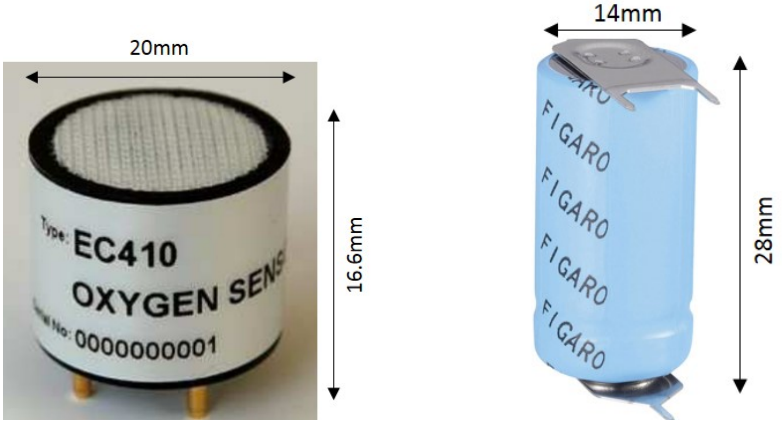

(a) SGX Sensortech oxygen sensor. (b) Figaro carbon monoxide sensor.

Figure 1.5: Two commercial electrochemical sensors.

Thermal sensors use the law of thermodynamics in which the internal energy

(a) SGX Sensortech VQ series.

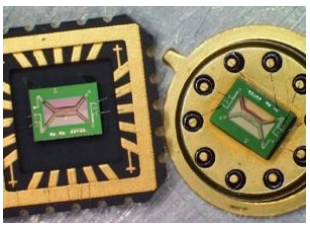

(b) Xensor Integration TCG series.

(c) Figaro TGS series.

Figure 1.6: Commercial thermal sensors.

of the system changes with heat. Since different gases have different thermal conductivities, so a thermal sensor applies the thermal energy and the thermal conductivity changes based on the gas. It has a reference channel to measure the thermal changes to the carrier gas, i.e. air, and a sensing channel to measure the target gas. It is often used to measure gas with a larger difference in thermal conductivity as compared to the carrier gas. It is also possible to measure multiple gases as long as their thermal conductivities are significantly different and not present in mixtures. The thermal sensor can be calorimetric, thermal resistive, thermal electronics and thermal electric. Figure. 1.6 shows some commercial thermal gas sensors.

Mass sensors are another type of chemical sensors. These detect the change of surface mass through the change of oscillator frequencies, such as bulk acoustic waves (BAWs) and surface acoustic waves (SAWs). These sensors are based on the piezoelectric oscillators that generate different types of acoustic waves which propagate through piezoelectric materials, such as quartz, zinc oxide, aluminium nitride and lithium niobate. These sensor has been of great interest for researchers for their high sensitivity, small size and fast response time. Figure. 1.7(a) shows a

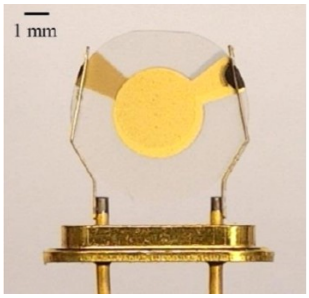

(a) Quartz crystal microbalance [22].

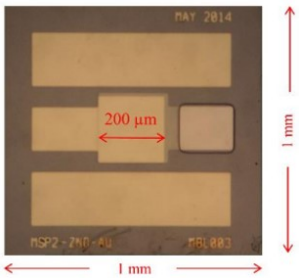

(b) Solidly mounted resonator [23].

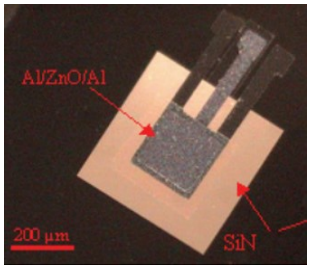

(c) Thin-film bulk acoustic resonator [24]

Figure 1.7: Some commercial mass sensors.

commercial quartz crystal microbalance (QCM) device with a round metal pattern in the centre and electrodes on the size. A QCM is a bulk acoustic device and also the most widely used one [25]. Surface acoustic waves devices, such as solidly mounted resonators (SMRs) and thin-film bulk acoustic resonators (FBARs), are also shown in Figure. 1.7 (b) and (c).

The fourth type is the optical sensor. These sensors monitor the optical absorption/emission of the target gas species in a specific wavelength region. Each gas has its own absorption/emission wavelength, and the response magnitudes depend on the concentration levels and gas types. One type of the optical sensor is infra-red, such as the non-dispersive infra-red (NDIR) sensors. NDIR sensors are often found for carbon dioxide detection as CO_2 has a strong absorption on the infra-red spectrum at 4.26 μm. Commercial sensors, such as Alphasense Ltd (UK), can produce miniaturised sensors with an integrated infra-red emitter and detector as shown in Figure. 1.8. In addition to CO_2 sensing, methane is another greenhouse gas that can be detected using NDIR. These two gases are often studied together.

Integrated (i.e. multi-gas) measurement systems are also available on the

Figure 1.8: Alphasense Ltd commercial NDIR sensors.

(a) Owlstone FAIMS system.

(b) GMI PS500 portable gas monitor system.

Figure 1.9: Commercial multi-gas detection systems.

market for a more comprehensive gas monitoring. These systems can be stationary, portable or handheld. For example, one of the most accurate gas measurement methods is mass spectroscopy, but its bulky and expensive. More portable setups, such as commercial e-noses like Owlstone FAIMS (UK) or Alpha-mos (France) FOX systems, are also sensitive and selective but they response slowly. Handheld devices can provide a more convenient way to detect and monitor gases, and they can often be found in laboratories, industries and domestic applications. Some example gas detection systems are presented in Figure. 1.9.

1.4 Motivation and Objectives

There is an increasing demand for high sensitive, high selective and low cost miniature gas sensors for applications such as handheld devices in environmental monitoring and biomedical appliances. Furthermore, with the emergence of the internet of things (IoT) and smart homes/buildings, small and integrable gas sensors are needed to monitor gases such as oxygen, carbon dioxide, carbon monoxide, methane, etc. The current generation of gas sensors can have issues, for instance, response drift, cross sensitives, slow response/recovery, and prone to poisoning. This thesis aims to develop new sensor technologies to reduce and overcome these issues.

Two sensor technologies are selected as the focus of this study, metal oxide semiconductors and non-dispersive infra-red gas sensors. Both types are highly sensitive, and with the miniaturised sizing (1 – 2 mm), low cost ($\sim$ £2 for a limited wafer run) and low power ($<$ 100 mW) consumption. The end purpose is to use such sensors for air quality monitoring and personal health care devices. The objectives of this research are listed as follows:

- Enhance the NDIR sensor performance by implementing a plasmonic nanostructure.

  Design and simulate the plasmonic model using an analytical model in COMSOL Multiphysics v5.1 software. The structure is used as the infra-red source, and should have a distinctive emission peak at the target wavelengths corresponding to the gases of interest. This is validated with a frequency spectrum simulation and the structure should meet the manufacturing standard and tolerance. The final model is then designed using Tanner EDA v2016 for mask layout, which will then be sent to a foundry for fabrication.

- Calibrate and assemble the device for gas measurements under the laboratory conditions.

  The fabricated devices are assembled into the NDIR sensor system with a gas chamber and a commercial detector. The setup is tested and calibrated under the laboratory condition with controlled gas flow and concentration levels. After the sensors have been fully characterised, it can then be integrated for real-world applications, such as gas detection or odour under harsh environment.

- Develop signal processing methods and algorithms to improve sensor response and compensate issues such as drift and slow response/recovery.

  Different signal processing methods are investigated with custom-made metal oxide semiconductors. To compensate drift and slow response/recovery of a typical MOX sensor, temperature modulation technique is applied to extract the dynamic sensor information instead of the static response. This technique can greatly shorten the response time and minimise the effect of drift. Both off-board post processing and on-board methods are studied. This technique also has the possibility to discriminate and predict gas concentrations. A regression analysis can be applied for this purpose.

- Apply algorithms to the sensor data collected by a multi-sensor unit to discriminate and classify different gases or odours.

  Various algorithms can be explored to find the most suitable one for the given set of data. The algorithm needs to be high efficient, high accuracy, and possible to implement to a microcontroller for a wearable/handheld device. Such algorithms can be principle component analysis, k-nearest neighbours, shallow artificial neural networks and deep neural networks.

1.5 Thesis Outline

This thesis addresses the objectives in the following order:

- **Chapter 1 Introduction and Motivations:** This chapter introduces the olfactory system and gas sensors with current sensor technologies and market and applications. Various sensor technologies are described and discussed

with two types selected to study in this thesis. This chapter also presents the research motivation and objectives.

- **Chapter 2 Literature Review:** A literature review is provided in this chapter as the background study of this work. The first half of the review is on plasmonic technology, such as the working principle of surface plasmon and plasmonic metamaterial. The application in gas sensing is also included here with different plasmonic structures and designs. The second half of this chapter is dedicated to different signal processing methods, including thermal modulation, regression analysis and classification techniques. These models in literature for gas sensing applications are described in this chapter.

- **Chapter 3 Design and Fabrication of Micro-hotplate Based CMOS Devices:** Micro-hotplate devices are discussed here as one of the key components for both the MOX sensors and NDIR sensors. There are two types of membrane designs, closed type and suspended type. Both types are described with different structures, patterns and materials. Furthermore, the fabrication process for such devices is illustrated, mainly the steps used in CMOS process. Finally, the applications of micro-hotplate in MOX and NDIR sensors are also included.

- **Chapter 4 Modelling and Simulation of Plasmonic IR Emitter:** A plasmon enhanced CMOS infra-red emitter source is demonstrated in this chapter. The emitter has a tunable patterned structure that can emit infra-red radiation at the target wavelength, which corresponds to the target gas. The model is simulated with COMSOL Multiphysics software and the results are presented with frequency spectra. Five structures for five target gases are presented in this chapter, and the final designs are generated for tape-out.

- **Chapter 5 Sensor Integration, Calibration and Application:** This chapter covers the characterisation of the designed plasmonic infra-red emitters. All devices are measured and tested with an automatic gas testing bench with controlled gas flow and concentration levels. The setup includes a commercial detector device and a gas chamber. This setup is also implemented into two projects, namely SmokeBot and SuperGen, to detect gases in harsh conditions and impurities in hydrogen fuel cells, respectively.

- **Chapter 6 Signal Processing Technique with Thermal Modulation for Toxic Gas Sensing:** This chapter presents the thermal modulation technique on MOX sensors. Instead of the constant operating temperature, the

sensor is pulsed between two temperatures. The sensor operating in this dynamic mode can provide gas information within a shorter period of time, which are then revealed with post-processing algorithms. This technique is trialled both off-board and on-board in real time, both are demonstrated in this chapter. In addition, the post-process data can be used in regression analysis for gas concentration predictions.

- **Chapter 7 Signal Processing with Machine Learning Algorithms for Odour Detection:** In this chapter, more signal processing methods are explored, especially various machine learning algorithms for gas classification. These algorithms are trialled on a dataset collected with four different odours using an integrated gas sensing system. The comparison among these algorithms is provided with model accuracies and performances (errors). The results prove the feasibility of using classification algorithms for odour detections which can lead to the development of an on-board classification algorithm.

- **Chapter 8 Conclusion and Further Work:** This chapter concludes the entire thesis with overall results and discussions. The objectives are reviewed here against final results, and additional work is proposed for future study.

References

[1] C. Bushdid, M. O. Magnasco, L. B. Vosshall, and A. Keller, "Humans can discriminate more than 1 trillion olfactory stimuli," *Science*, vol. 343, no. 6177, pp. 1370 – 1372, 2014.

[2] J. Morrison, "Human nose can detect 1 trillion odours," 2014. [Online]. Available: https://www.nature.com/news/human-nose-can-detect-1-trillion-odours-1.14904

[3] J. P. McGann, "Poor human olfaction is a 19th-century myth," *Science*, vol. 356, no. 6338, pp. 1–6, 2017.

[4] G. M. Shepherd, "Outline of a theory of olfactory processing and its relevance to humans," *Chemical Senses*, vol. 30, no. suppl.1, pp. 3–5, 2005.

[5] B. Winter, "Taste and smell words form an affectively loaded and emotionally flexible part of the English lexicon," *Language, Cognition and Neuroscience*, vol. 31, no. 8, pp. 975–988, 2016.

[6] K. A. Cerulo, "Scents and sensibility: olfaction, sense-making, and meaning attribution," *American Sociological Review*, vol. 83, no. 2, pp. 361–389, 2018.

[7] C. Verbeek and C. van Campen, "Inhaling memories," *The Senses and Society*, vol. 8, no. 2, pp. 133–148, 2013.

[8] E. Koster, "Does olfactory memory depend on remembering odors?" *Chemical Senses*, vol. 30, no. Supplement 1, pp. i236–i237, 2005.

[9] B. Naidoo, "Biologically inspired signal transformations and neural classification of odours in an electronic nose," 2003. [Online]. Available: https://www.researchgate.net/publication/238746672

[10] J. W. Gardner, "Pattern recognition in the Warwick electronic nose," in *8th International Congress of the European Chemoreception Research Organisation*, Coventry, UK, 1988, p. 9.

[11] J. W. Gardner and P. N. Bartlett, *Electronic noses : principles and applications*. Oxford: Oxford University Press, 1999.

[12] Electronic Nose, "E-nose can digitize and visualise the smell." [Online]. Available: http://e-nose.asia/index.php?lang=en

[13] Yole Développement, "Gas sensor market." [Online]. Available: http://www.yole.fr/2014-galery-MEMS.aspx#I00049659

[14] Grand View Research, "Gas sensor market size, share & trends analysis report," 2019. [Online]. Available: https://www.grandviewresearch.com/industry-analysis/gas-sensors-market

[15] N. Yamazoe, "Toward innovations of gas sensor technology," *Sensors and Actuators B: Chemical*, vol. 108, no. 1, pp. 2–14, 2005.

[16] S. Park, "Acetone gas detection using tio_2 nanoparticles functionalized in_2o_3 nanowires for diagnosis of diabetes," *Journal of Alloys and Compounds*, vol. 696, no. 1, pp. 655–662, 2017.

[17] P. Pandey, J. K. Srivastava, V. N. Mishra, and R. Dwivedi, "Pd-gate MOS sensor for detection of methanol and propanol," *Journal of Natural Gas Chemistry*, vol. 20, no. 2, pp. 123–127, 2011.

[18] P. T. Arasu, A. L. Khalaf, S. H. A. Aziz, M. H. Yaacob, and A. S. M. Noor, "Optical fiber based ammonia gas sensor with carbon nanotubes sensing enhancement," in *2017 IEEE Region 10 Symposium (TENSYMP)*, Cochin, India, Jul 2017, pp. 1–4.

[19] J. Janata, *Principles of Chemical Sensors*. Boston, MA: Springer US, 2009.

[20] A. C. Peixoto and A. F. Silva, "Smart devices: micro- and nanosensors," in *Bioinspired Materials for Medical Applications*. Duxford: Woodhead Publishing, 2017, pp. 297–329.

[21] N. P. Shetti, D. S. Nayak, K. R. Reddy, and T. M. Aminabhvi, "Graphene–clay-based hybrid nanostructures for electrochemical sensors and biosensors," in *Micro and Nano Technologies*. Amsterdam: Elsevier, 2019, pp. 235 – 274.

[22] F. Villa-Lopez, "CMOS compatible colidly mounted resonator for air quality monitoring," PhD Thesis, University of Warwick, Coventry, UK, 2017.

[23] F. H. Villa-López, G. Rughoobur, S. Thomas, A. J. Flewitt, M. Cole, and J. W. Gardner, "Design and modelling of solidly mounted resonators for low-cost particle sensing," *Measurement Science and Technology*, vol. 27, no. 2, pp. 1–13, 2015.

[24] H. Zhang, M. S. Marma, Eun Sok Kim, C. E. McKenna, and M. E. Thompson, "Mercury ion sensing by film-bulk-acoustic-resonator mass sensor," in *SENSORS, 2005 IEEE*, Irvine, CA, USA, 2005, pp. 1–4.

[25] B. Drafts, "Acoustic wave technology sensors," *IEEE Transactions on Microwave Theory and Techniques*, vol. 49, no. 4, pp. 795–802, 2001.

Chapter 2

Literature Review

2.1 Introduction

An electronic nose system comprises an array of chemical sensors (hardware) and a signal processing method (software). Therefore, to improve an e-nose system, two approaches can be taken. On the hardware side, the sensors can be enhanced with better materials and/or transducers; on the software side, supervisor algorithms for signal processing and pattern recognition can be developed. This thesis aims to study the e-nose system from both sides. From all the sensing technologies described in the previous chapter, two types of sensors are selected as the research focus, namely, the non-dispersive infrared sensor (NDIR) and the metal oxide semiconductor (MOX) resistive gas sensor. A plasmonic metamaterial is employed in the infrared emitter for the NDIR sensor to enhance the radiation emissivity and selectivity, thus improving the overall sensor performance. Alongside this sensor development, different signal processing algorithms are explored with MOX sensors both on-board in real time and off-board for post-processing.

In this chapter, a background study on the hardware and software aspects of the e-nose is conducted. It provides an overview of state-of-the-art research and devices. On top of that, the working principle of the plasmonic technology is explained here, as well as its applications as a metamaterial in the optical sensing area. Various design structures are explained with their performances and advantages. Furthermore, different signal processing methods are introduced: thermal modulation techniques and machine learning algorithms. Both have been of great

interests in the sensor community to compensate for noise and drift, and extract more information.

2.2 Plasmonic Technology for IR spectroscopy

Infrared technology plays a vital role in applications such as imaging and gas sensing. Gas sensors like the non-dispersive infrared (NDIR) require an infrared emitter source, a filter and an infrared detector. As a replacement of the conventional infrared bulb, several approaches using microelectromechanical system based devices are proposed in literature. In addition, metamaterials, as an emerging area, have attracted attentions due to its ability in manipulating electrical properties. By combining the MEMS devices with metamaterials, a novel infrared source can be achieved perhaps without an expensive filter. Plasmonic, in particular, is the chosen metamaterial that can tailor the electromagnetic wave, hence the wavelength of the infrared radiation.

2.2.1 Electromagnetic Waves

In the early 1860s, James Clerk Maxwell published his book, *A Treatise on Electricity and Magnetism*. In this, he presented the mathematical theory for electromagnetism and proposed an explanation for the electromagnetic phenomenon [1]. He combined various disconnected equations, such as Gauss's Law, Faraday's Law and Ampere's Law, and showed their relations [2]. These equations are:

$$\text{Gauss's Law: } \vec{\nabla} \cdot \vec{\mathrm{E}} = \frac{\rho}{\varepsilon_o} \tag{2.1}$$

$$\text{Gauss's Law for Magnetism: } \vec{\nabla} \cdot \vec{\mathrm{B}} = 0 \tag{2.2}$$

$$\text{Faraday's Law: } \vec{\nabla} \times \vec{\mathrm{E}} = -\frac{\partial \vec{\mathrm{B}}}{\partial t} \tag{2.3}$$

$$\text{Ampere's Law: } \vec{\nabla} \times \vec{\mathrm{B}} = \mu_o \vec{\mathrm{J}} + \mu_o \varepsilon_o \frac{\partial \vec{\mathrm{E}}}{\partial t} \tag{2.4}$$

where $\vec{\mathrm{E}}$ is the electric field, $\vec{\mathrm{B}}$ is the magnetic field, $\vec{\mathrm{J}}$ is the current density, ρ is the charge density, ε_o is the permittivity of free space, μ_o is the permeability of free space and t is time. All the above equations are represented with gradient operators in vector fields, they can also be written as integrals. By combining these equations

and putting them in a general format, following conclusions on the electromagnetic interactions can be made:

- the electric flux through a closed surface is proportional ($\frac{1}{\varepsilon_o}$) and to the total electric charge Q in the volume enclosed by the surface;
- the overall magnetic flux of a closed lines of loops is zero so that magnetic monopoles do not exist;
- a change in the magnetic flux can induce electromagnetic induction (electromotive force, a.k.a. EMF);
- electromagnetic waves are the changing electric and magnetic field that travels through space; and
- the speed of the electromagnetic wave is equal to the speed of light in the vacuum ($c \approx 2.99 \times 10^8\ ms^{-1}$), which is also related to the permittivity and permeability.

Unlike the equations above which are the electromagnetic waves in free space, the electromagnetic waves in dielectric and metal surfaces are slightly different. Matters are formed by neutrons, protons and electrons, but only electrons are considered here as they can be affected when an electric or magnetic field is applied, which can lead to polarisation (positive and negative). This polarisation effect can vary among materials, and for dielectric material, the electric polarisation is linearly proportional to the applied electric field [2]. Because of this polarisation, the Maxwell's equations are now written as:

$$\vec{\nabla} \cdot \vec{\mathrm{D}} = \rho_f \tag{2.5}$$

$$\vec{\nabla} \cdot \vec{\mathrm{B}} = 0 \tag{2.6}$$

$$\vec{\nabla} \times \vec{\mathrm{E}} = -\frac{\partial \vec{\mathrm{B}}}{\partial t} \tag{2.7}$$

$$\vec{\nabla} \times \vec{\mathrm{H}} = \vec{\mathrm{J}_f} + \frac{\partial \vec{\mathrm{D}}}{\partial t} \tag{2.8}$$

where $\vec{\mathrm{D}}$ is the electric displacement vector ($\varepsilon\vec{\mathrm{E}}$) and $\vec{\mathrm{H}}$ is the magnetic field ($\frac{\vec{\mathrm{B}}}{\mu}$) when the polarisation vector is considered. ρ_f and J_f are the free charge and free current density, respectively. These equations are similar to the free space equations with different symbol expressions. In addition, the local current density $\vec{\mathrm{J}}$ can be

calculated through the electric field and conductivity σ in a conductive material, as stated by the Ohm's Law:

$$\vec{\mathrm{J}} = \sigma\vec{\mathrm{E}} \tag{2.9}$$

The electromagnetic wave in metals, or conductors, is different due to the presence of free electrons. Therefore, the wave function is solved by using the curl operation of Eq. 2.7 and zero free charge density, hence:

$$\vec{\nabla}^2\vec{\mathrm{E}} = \frac{\partial}{\partial t}\left(\vec{\nabla}\times\vec{\mathrm{B}}\right) = \mu_o\varepsilon_r\varepsilon_o\frac{\partial^2\vec{\mathrm{E}}}{\partial t^2} + \mu_o\sigma\frac{\partial\vec{\mathrm{E}}}{\partial t} \tag{2.10}$$

where ε_r is relative permittivity. Because the free electrons lead to a non-zero conductivity which becomes the imaginary part of the permittivity. Therefore, the modified wave equation in a plane is written as:

$$(-i\beta-\alpha)^2\mathrm{E_o} = \mu_o\varepsilon_r\varepsilon_o(i\omega)^2\mathrm{E_o} + \mu_o\sigma(i\omega)\mathrm{E_o} \tag{2.11}$$

with the real part as:

$$-\beta^2+\alpha^2 = -\mu_o\varepsilon_r\varepsilon_o \tag{2.12}$$

and the imaginary part as:

$$2\beta\alpha = \mu_o\sigma\omega \tag{2.13}$$

where w is the angular frequency. The conductivity σ has the below relationship as:

$$\alpha = \beta = \sqrt{\frac{\mu_o\sigma\omega}{2}},\ \text{when}\ \sigma \gg \varepsilon_r\varepsilon_o\omega \tag{2.14}$$

and in an ideal situation when $\sigma\to\infty$ (perfect conductor), there are no waves and E=0 [3].

Table 2.1: Plasma frequency ($\mathrm{f_p}$) of some common metals.

Metal	**Plasma Frequency ($\mathbf{f_p = \omega_p/2\pi}$, unit=PHz)**	**Ref.**
Aluminium	3.70	[4]
Tungsten	1.45	[5]
Silver	2.32	[4]
Gold	2.18	[5]
Platinum	1.25	[5]

Permittivity of the metal is also depended on the frequency as:

$$\varepsilon_r = 1 - \frac{\omega_p^2}{\omega^2} \tag{2.15}$$

where ω_p is the plasma frequency of the metal electrons, which is a constant for different metals. Table. 2.1 below provides some common metals that will be mentioned later in this thesis and their plasma frequencies. This is also a parameter in the Drude model.

2.2.2 Surface Plasmon

Plasmonic occurs in the area where the surface electromagnetic is excited at a dielectric-metal interface [6]. The electromagnetic wave travelling through this interface is known as a surface plasmon polariton (SPP). It is a propagating wave that has two different polarisation properties, the transverse magnetic (TM) mode and the transverse electric (TE) mode. The wave equations for these two modes are shown as:

$$\frac{\partial^2 \mathrm{H_y}}{\partial z^2} + (k_o^2 \varepsilon - \beta^2)\mathrm{H_y} = 0 \tag{2.16}$$

for the TM mode and

$$\frac{\partial^2 \mathrm{E_y}}{\partial z^2} + (k_o^2 \varepsilon - \beta^2)\mathrm{E_y} = 0 \tag{2.17}$$

for the TE mode, where k_o is the wave vector of the propagating wave in vacuum, which is

$$k_o = \frac{\omega}{c} \tag{2.18}$$

and x, y, z are directions. But the surface plasmon polaritons only exist in the TM mode [7]. For the SPPs travelling between the metal-dielectric interface, the wave vector k_z along the z-axis is represented as:

$$k_z = \frac{\omega}{c}\sqrt{\frac{\varepsilon_m \varepsilon_d}{\varepsilon_m + \varepsilon_d}} \tag{2.19}$$

where ε_m and ε_d are the constants for the metal and dielectric layer, respectively.

SPPs can be excited either by electrons or photons. The electron excitation is caused by electron scattering that transfers the energy to plasma, hence the SPPs. For a photon to excite SPPs, the surface plasmons (free electrons) are affected by an incident light, resulting in a coupled state which is the polariton. For instance,

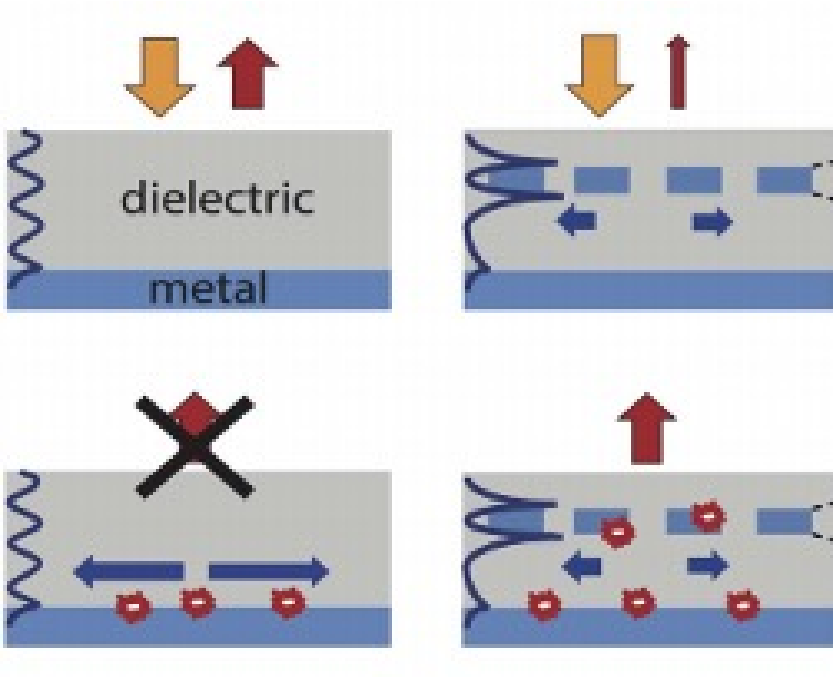

Figure 2.1: Absorption (top): an incoming light is absorbed in a bare device (left) but will trapped by the plasmonic crystals (right) in a plasmonic mode. Emission (bottom): plasmons are induced in a heated surface only happens with plasmonic crystals(reproduced from [8]).

an absorption plasmonic based device traps the incident light in a plasmonic mode, while an emission device can spontaneously excite surface plasmon with a heated surface, which is then coupled to the external light-field [8]. This process is shown in Figure. 2.1 with $\vec{q}$ as the plasmon wave vector and $\vec{k}$ as the electron wave vector.

The coupling mediums such as gratings are used to match the photon wave

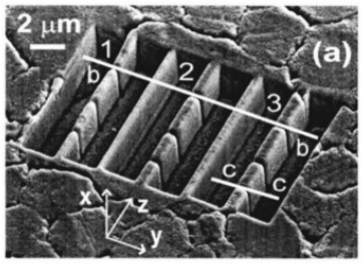

(a) Gap gratings for gap surface plasmon polaritons [9].

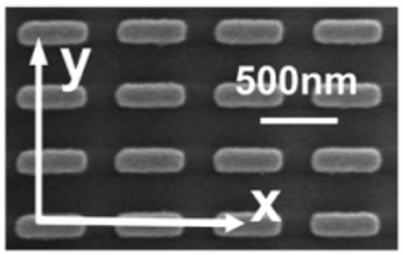

(b) Nano-antennas for lattice surface plasmon polaritons [10].

Figure 2.2: Two surface plasmon coupling modes (reproduced from [9] and [10]).

vector and the surface plasmon wave vector. They also act as waveguides that can overcome the diffraction limitation of lights and tune the surface plasmon resonance. The grating can be slots, holes, dots, etc. They help with the coherent scattering of the SPPs, and the grating vector $k_g = 2\pi/\lambda_g$, where k_g is the wavevector of the grating and λ_g is the period of the grating structure [11]. The coupling state can happen in two ways, one is the gap surface plasmon polariton and the other one is the surface lattice resonance between individual nanostructures. In the gap surface plasmon polaritons, the wave propagates in the plane of the structure and shows a strong localisation and significant propagation distance with increased width and height of the grating/gap structure [9]. The lattice surface mode is the coupling in the periodic arrays of plasmonic crystals or nanostructures (nano-antennas). This can support the collective resonances of the localised surface plasmons and significantly enhance the emission (tenfold) in a particular wave range [10]. Figure. 2.2 shows two grating structures corresponding to the two coupling modes.

2.2.3 Plasmonic Metamaterial

Metamaterials are metal-dielectric composites structured on a microscale or nanoscale that can enhance the electrical properties from the structure instead of the materials [12, 13]. A plasmonic metamaterial is a metamaterial that uses a surface plasmon to manipulate electromagnetic radiation. The resonance frequency is determined by the material property, especially the plasma frequency as presented in Table. 2.1. However, in a plasmonic metamaterial, it is controlled by carefully designed periodically or randomly distributed artificial structures, which usually have the size and spacing much smaller than the wavelength of interest [14].

Plasmonic materials generally are metallic components with free electrons that provide negative real permittivity [15]. The real and imaginary parts of the permittivities of some common metal are presented in Figure. 2.3. These materials also exhibit negative refractive indexes that refract or bend the light differently over certain frequency ranges. To utilise the material properties as a plasmonic metamaterial, various structures and layouts are investigated in literature, for instance, a bulk sandwich structure with metal and insulation layers, graphene based devices, and lattice structures. A sandwich structure can be silver glass bulk stacks for ultraviolet lights [17] or silver thin film with a gold underlay and silicon nitride [18]. Graphene has found to be able to generate surface plasmons from terahertz to infrared regions [19, 20, 21]. It has electromagnetic conductivity in both the TM and

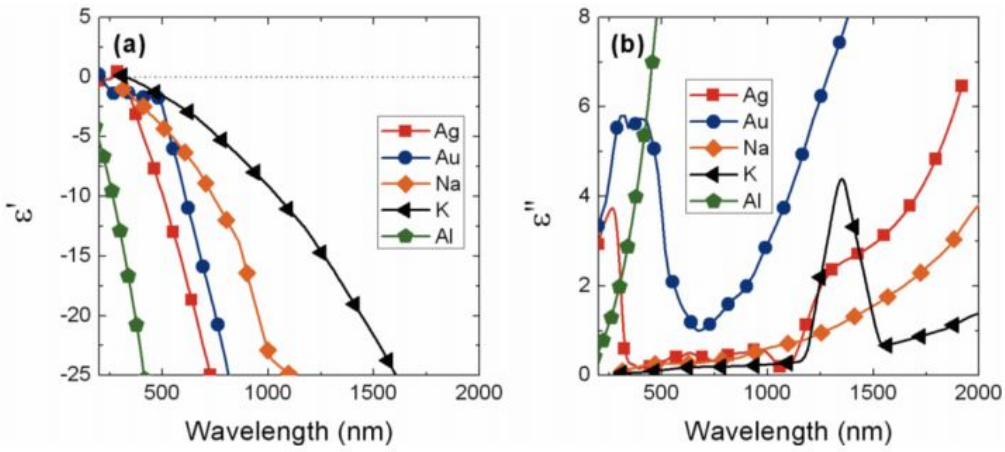

Figure 2.3: Real and imaginary parts of the permittivities for silver, gold, sodium, potassium and aluminium (reproduced from [15, 16]).

TE modes [22], and allows high propagation distances [23]. The lattice structures have been most studied because they can tailor the resonance frequency. They can incorporate both bulk metal-dielectric stacks and graphene to maximise the wavelength calibration for various applications. Depending on the frequency ranges, the applications include antennae [24], solar cells (absorbers) [25], emitters [26, 27], and sensors [28, 29, 30]. This thesis focus on the sensing applications. In the next section, recent researches on plasmonic in gas sensing will be presented, particularly with tunable lattice structures.

2.2.4 Plasmonic in Gas Sensing

The study of plasmonics has been an area of interest for the past two decades. In the sensing applications, it can be used in bio-sensing [31, 32], particle sensing [33, 34], and chemical sensing [35]. In addition, optical gas sensing is a major application that can benefit from the enhanced optical materials, such as infrared emitters and detectors. There have been several reports on applying the plasmonic technology into the emitter designs. Daly *et al.* [36] published a design using a plasmonic patterned structure to demonstrate the effect of the periodic patterns on the emission rate. The pattern Daly used was cross-shaped cavities. He concluded that the enhancement of the emission peak and the peak wavelength could be tuned by altering the cavity size and depth. Therefore, this periodically patterned structure has been used in the literature for a tunable, selectable infra-red emitter.

A typical emitter design is a sandwich structure with a dielectric layer between two metal layers where the top metal layer perforated periodically. The plasmonic metal layer sits on top of a heater that on heating, induces plasmon resonances. Silver is commonly reported in the literature as the metal layer, and silicon oxide or silicon [37] used as the dielectric layer. Titanium layer could be used between the substrate and the bottom metal layer [38], or chromium and gold layer below substrate as the heating source [39]. There are also other novel materials used in realizing the plasmonic structure, such as graphene [40, 41], superconductors [23], or doped semiconductors [42]. For instance, Tay *et al.* [43] reported using titanium nitride doped nano-amorphous carbon as the metal layer to increase the electrical conductivity and IR reflectivity of the device. The patterned structure on the plasmonic layer can be perforated in square [39, 44], round [38, 37], or quantum dots [45, 46], and it can either be in square or hexagonal arrays. For a more complex design, the pattern can be placed on multiple layers. Design reported by Li *et al.* [47] was an Al/SiO_2/Si structure with all three layers perforated with hexagonal holes array. Similarly, Ji *et al.* [48] designed a perforated membrane structure with patterned platinum layers. They were both based on a silicon substrate and back etched to form the membrane. They had thermal insulation and wavelength selectable characteristics, but the multi-perforated membrane layer could weaken the device structural integrity. A membrane is used to isolate thermally the structure as well as to reduce the power consumption. Other membrane materials, such as a polymer, were proposed by Araci *et al.* [49, 50]. A detailed study on the micro hotplate and its membrane will be provided in the next chapter.

As the Kirchhoff's law of thermal radiation stated, only a good absorber makes a good emitter, designs for absorbers are also investigated. The difference between a emitter and a detector with plasmonic structure is the micro-heater and the thermopile/pyroelectric. In the detector design, thermopiles are used [51] and the change in the temperature by excited plasmons will reflect as voltage changes to the external circuit. Because the physics principles behind the plasmonic design is identical between emitters and detectors, the patterned emitter design can also be implemented into absorbers. The absorber structure is a thermopile on a dielectric membrane supported by a silicon substrate [52]. The top metal layer in the membrane is patterned cavities [53, 54], thin metal films [55], square gratings [56], extruded square design [57, 58, 59], extruded cross design [60] or dual cross design [61, 62], quantum dots [63, 64], and nano pillars [65]. Figure. 2.4 shows some examples of the plasmonic patterns.

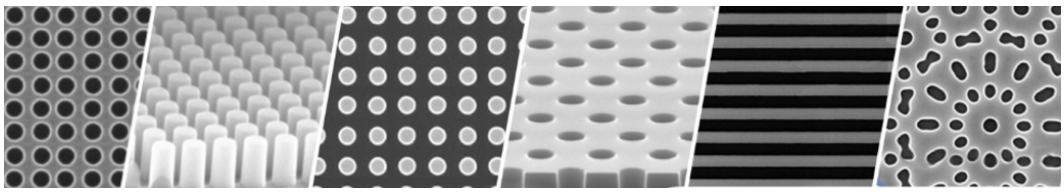

Figure 2.4: Examples of the plasmonic patterns, from left to right: holes, pillars, dots, perforated holes, gratings and irregular designs.

The plasmonic structures mentioned above are mostly micromachined. However, for mass production at a lower cost, CMOS process is preferred. Ali *et al.* [66] designed a plasmonic structure that was compatible with CMOS fabrication. It was a dielectric membrane on top of a silicon substrate, and the metal layers are embedded within the dielectric layer. Either the top or multiple metal layers can be patterned. The plasmonic material used in this design is CMOS metal such as aluminium, tungsten or molybdenum. Tungsten has a high melting point and is the first choice in this work. The bottom metal layer works as the heating source (a micro hotplate). The pattern can be either square lattices, or hexagonal lattices, or a mixed structure for multiple emission peaks. This design will have low power consumption, low cost from CMOS fabrication, and high stability and sensitivity from the plasmonic structure. Table. 2.2 summarised various plasmonic designs used in some recent studies.

Table 2.2: Plasmonic designs in recent literature.

Ref.	**Year**	**Emitter/ Absorber**	**Plasmonic Structure**	**Plasmonic Materials**	**Structure Dimensions**	**Wavelength Range**	**Broadband/ Peaks**	**CMOS Fabrication**
[67]	2019	Absorber	Nano-antennae: fan pad-rod and rectangular pad-rod	Au	2.1 μm size, 60 nm thickness	2–6 μm	dual/triple peaks resonator	No
[68]	2019	Absorber	Colloidal Crystals	Silicon, Au	$\sim$ 1 μm diameter	0–2.4 μm (near IR)	Dualband	No
[69]	2019	Absorber	nanorods/nanoparticles	Au, MoS_2	Few nm width	0.4-1.4 μm	Single peak	No
[70]	2014	Absorber	Square cavity with gratings	Au	$>$ 1 μm cavity and 7 μm period	2–30 μm	Single peak	No
[71]	2014	Absorber	Periodic gratings	Ti/Au	750 nm width, 100 nm gap, 5 $\sim$ 30 nm thickness	8–14 μm	Single peak $\sim$ 10 μm	No
[72]	2012	Absorber	Square periodic pattern	ZnS, Au	few μm size	6–12 μm	Four distinctive peaks	No
[73]	2016	Absorber	Square periodic gratings	Silicon	3–4 μm width, 1.2 μm thickness	5–20 μm	Broadband	Yes
[74]	2016	Absorber	Periodic square nanostructure	W	800 nm length, 700 nm gap	1–7 μm	Single peak	Yes
[75]	2016	Absorber	Dots	CMOS metal	Few μm	5–15 μm	Broadband	Yes
[76]	2017	Emitter	Rectangular cavities	Doped Si	Few hundreds nm	4-10 μm	Narrow peak	Yes
[77]	2016	Emitter	Dots	TiN	100–500 nm diameter	500–1200 nm	Broadband	Yes
[78]	2017	Emitter	Discs	ITO	1–2 μm diameter	5–10 μm	Broadband	Yes
[79]	2011	Emitter	Square gratings	Au	3 μm width	8–14 μm	Single peak	No
[80]	2012	Emitter	Rectangular blocks	Ag	1 μm width and 1–3 μm length	2–24 μm	Three peaks	No
[43]	2009	Emitter	Hexagonal lattice of holes	Nanoamorphous carbon, TiN	4–6 μm diameter	3–15 μm	Broadband	No
[81]	2015	Emitter	Periodic gratings	TiN	1.5 μm width, 3 μm thickness	2–4 μm	Single peak at 3 μm	No

2.3 Signal processing methods

2.3.1 General Overview

The metal oxide semiconductor (MOX) sensor is one of the most studied sensors due to its commercial availability. It is easy to use and respond to a wide range of redox gases. As a result, it is also a much studied material for signal processing methods. The signal processing section of an e-nose is roughly similar to the human brain function, which extracts only the useful information and obtains the underlying relationships between the received data and the known information. For a sensor array commonly applied in an e-nose [82], a response pattern from the sensors are depending on factors such as gas types, concentration levels and operating conditions. Therefore, based on the response patterns, the known information can be deduced through algorithms, such as pattern recognition. Through finding the relationship between the known information and the response patterns, the prediction of the unknown information will be more accurate. Like a human brain, this information will become a 'memory' that is used to discriminate and classify unknown gases and odours. In this section, two types of problems are discussed for gas prediction, regression problems and classification problems.

Furthermore, a gas sensor can be influenced by various operating conditions, such as ambient temperature, pressure, humidity, and flow. All of them can contribute to the drift in the sensor response. The drift can be reduced when these factors are compensated or avoided. Many researchers have studied various methods to improve the sensor response in terms of stability, sensitivity and selectivity, for the purpose of drift compensation and gas discrimination [83, 84, 85]. These approaches can be roughly separated into two categories, on-board and off-board. On-board methods include sensing materials, improved circuitries [86], and signal process techniques before the data collection step. These technique, for instance, a reference channel [87] can be used with a mixer in the circuitry to add/subtract two signals. Another method, which will be studied later in this section, is the temperature modulation technique. A MOX sensor is operated with a micro hotplate and it is sensitive to the change of the operating temperature. Therefore, studies show that this technique can greatly increase the stability and selectivity of MOX sensors. The off-board signal processing happens after the data have been collected. It can be filters to remove drifts and noises, or advance algorithms for discriminations and predictions.

2.3.2 Thermal modulation

Thermal modulation is a dynamic signal processing method that can find the sensor characteristics both in the time domain and the frequency domains. A MOX sensor operates with a micro hotplate that can heat up from 100 °C to 500 °C. By adjusting the operating temperature of the micro hotplate, the sensor response can be improved. In addition, it can reduce the power consumption [88] and increase the selectivity of the MOX sensors. In a research conducted by Lee *et al.* [89], he showed the conductance versus temperature profile of different analytes, such as carbon monoxide and propane, that could be used in the sensor selectivity study.

There are multiple ways to modulate a micro hotplate. One way is to pulse it between the operating temperature and off phase. For instance, Burgués *et al.* [90] proposed a discontinuous powering method that only warmed-up the micro hotplate within a short amount of time. This helped with power reduction up to 60%, and at the same time, increased the prediction error and detection limits. The modulation cycle period was not specified in this study, but there have been other researches on different duty cycles. Oletic *et al.* [91, 92] trialled four pulse periods and duty cycles, and came to the conclusion that a better sensor sensitivity could be achieved with reduced power consumption at a higher pulse period and a lower duty cycle. The pulse period is usually in tens of seconds. With the lower duty cycle, the power consumption of such sensor operation can drop from tens of mW to just a few mW [93]. The period can also be shorter, for example in ms as presented in [94].

Another method is to operate the micro hotplate between two operating temperatures. This operation mode will increase the power consumption as there is no off time, but it allows a higher operating temperature without reducing the sensor lifetime. Shaposhnik *et al.* [95] studied a SnO_2 MOX sensor that operated between 100 °C and 450 °C instead of the constant 300 °C, and a duty cycle of 13%. By using this method, the sensor response towards the same gas at the same concentration increased by two-four of magnitude. A possible explanation of the increase in the sensor sensitivity and response is the lower temperature deactivate the adsorption process which then protects the surface materials.

The third modulation method that has been mentioned in literature is to operate the sensor at a higher temperature from time to time, instead of the regular pulse mode. This is to act as a cleaning mechanism to desorb certain adsorbates and restore the initial metal oxide material properties, such as 150–300 °C for sulfur

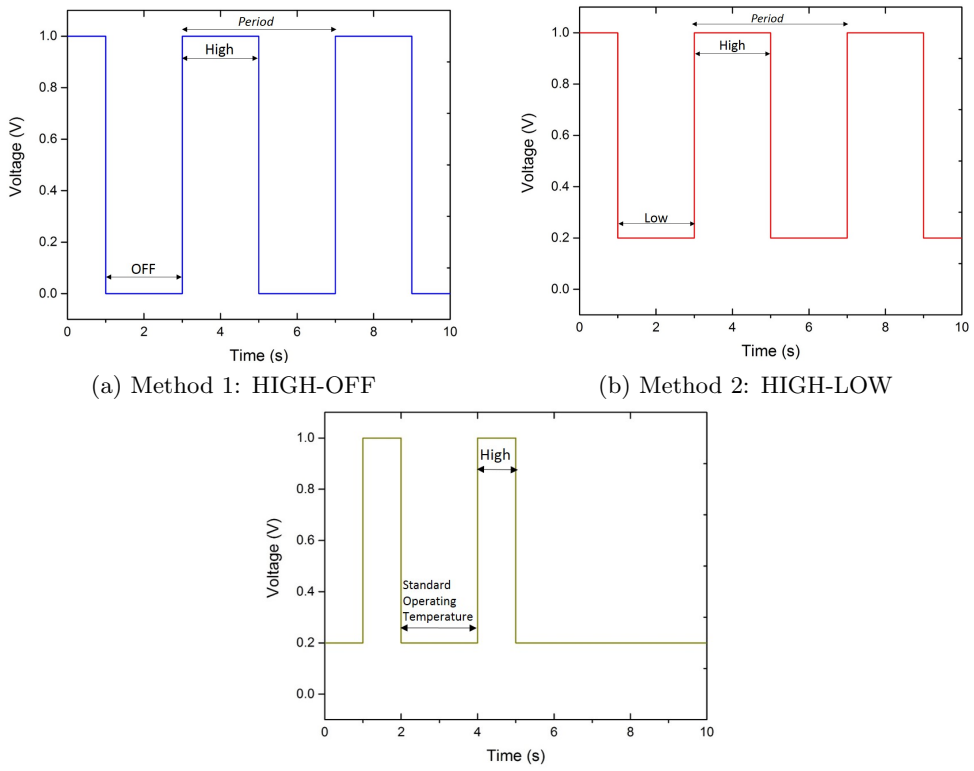

(a) Method 1: HIGH-OFF

(b) Method 2: HIGH-LOW

(c) Method 3: Occasional higher temperature (low pulse-width modulation)

Figure 2.5: Three operating methods of the temperature modulation technique.

and 250–500 °C for carbon [96, 97, 98].

Figure. 2.5 shows the three above modulation methods. They share the same basic principle of a modulated heater voltage. Based on this voltage, the sensor response is measured overtime towards various gas components. The collected data are then processed to extract features and perform quantitative analysis, such as Fourier transform [99, 100], discrete wavelet transform (DWT) [101], principal component analysis [102, 103], partially least square [104], artificial neural networks [105, 106] or a combination of multiple steps. Fast Fourier transform can extract data based on the operating frequency of the temperature modulation [107], and the harmonic peaks on the frequency spectrum can be used as the gas information. The higher harmonic of the FFT shows the non-linear characteristics of the response at the sensor surface, and its amplitude changes depending on the kinetics of the gas species, i.e. vary gas by gas [108]. Apart from FFT, wavelet transform, either discrete or continuous, can be used to perform feature extractions. It was discussed that the transitory sensor characteristics, such as drift, might affect the FFT results which

the wavelet transform could overcome [109]. The DWT is a windowing technique that varies with frequencies and provides a sparse representation of the signal, while continuous wavelet transform (CWT) scales the windows more finely and provides a better overall signal representation. Huang *et al.* [110] performed a study that compared the FFT with CWT. It was found that the wavelet transform function was more suited for frequency-time problems with a clearer variation between gases for discrimination. After the feature extraction step, additional analysis can be performed, such as regression analysis or classification technique. These two techniques will be discussed in the following sections.

2.3.3 Regression Techniques

Regression analysis can provide a relationship/model between a set of independent variables and dependent variables. It can be either linear or non-linear problems. For an e-nose, the classification problems can be treated in a similar manner as the regression problems. Gutierrez-Osuna [111] categorised the regression problems in the machine olfaction system into three types: multicomponent analysis, process monitoring and sensory analysis. In multicomponent analysis, the dependent variable is the concentration of the gas; in the process monitoring, the dependent variable is the process variable such as quality level; and in the sensory analysis, the dependent variable is the score of a human sensory panel. Here, multicomponent analysis will be focused mainly to estimate the gas concentration levels.

There are three commonly used methods for regression analysis on a gas sensing system, namely, neural network (ANN), support vector machine (SVM) and partial least squares regressions (PLS). Spinelle *et al.* [112] reported a study of three sensor calibration methods, simple linear regression, multivariate linear regression (least squares) and artificial neural network. By comparing these three methods, it was found that the ANN with raw or scaled sensor inputs was more suited to solve the sensor interference problem. ANN is widely used both as a non-linearclassification method and as a prediction method. Eklöv *et al.* [113] reported a feed-forward ANN with one hidden layer using the Levenberg-Marquardt optimization algorithm. The root mean square error (RMSE) was used to evaluate the model and the ANN model gave a better prediction result with the RMSE of 1.6 ppm. Different variations of the neural network can also be applied. For instance, Huang *et al.* [114] used a generalised regression neural network to model the

methane concentrations for coal mine shafts. This model was also compared with a back-propagation based neural network, and the regression network was more precise and efficient in the concentration estimation. Unlike the basic neural network model, the regression model has a summation layer which performs a weighted summation before the output layer. In another example, Gulbag *et al.* [115] applied an adaptive neuro-fuzzy inference system to the ANN model. Training methods such as Quasi-Newton and Levenberg-Marquardt were trialled. It was also concluded that the performance of the neuro-fuzzy system was better than the simple ANN structure. Figure. 2.6 shows a typical ANN structure with one hidden layer. It is also the method that is used in the later chapter for regression analysis.

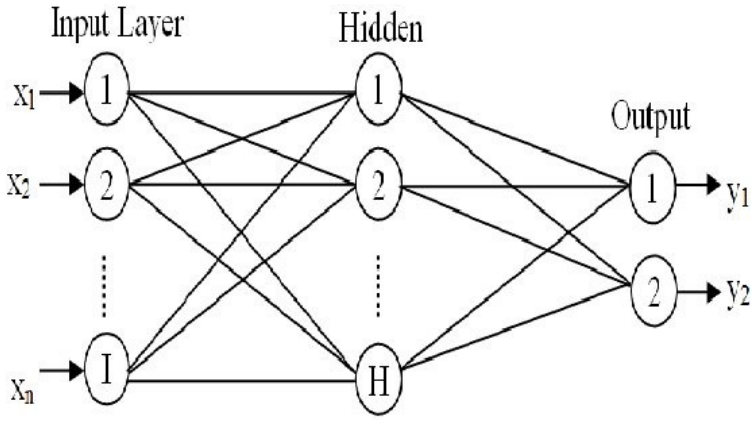

Figure 2.6: A typical ANN structure with three layers (input layer: I neurons, hidden layer: H neurons and output layer: 2 classes) (reproduced from [116]).

Support vector machine is another method that can be used for both classification and regression analyses. It has a plane structure, as shown in Figure 2.7, and a line dividing the plane into two or more different sections or classes. Shmilovici *et al.* [117] used a support vector regressor with a gas sensor array to predict a mixture of carbon monoxide, methane and ethanol. It was reported that the SVM regression analysis was better than the partial least square method, and the mean square error was much smaller with the SVM model. The downside of this model, according to Shmilovici, was the lack of compatibility towards different gases and the model needed to be reformulated. A similar study was mentioned by Ni *et al.* [118] using a support vector regressor in an automatic gas mixture recognition system, and up to three gas mixtures could be identified. Other studies, such as [119], [120] and [121] all used the support vector regressor or a modified version to predict gas concentrations successfully.

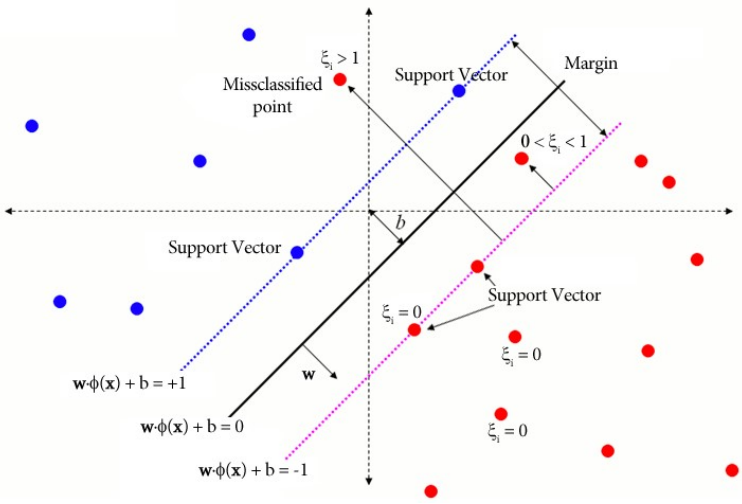

Figure 2.7: An example structure of a soft-margin support vector machine (reproduced from [122]).

The third method is the partial least square (PLS). PLS is one of the most used linear techniques for quantitative analysis in chemical sensors. It can also be used in non-linear problems by adding additional latent variables, such as Poly-PLS and Kernal PLS, but they are not common for chemical sensors [123]. Gutierrez-Osuna *et al.* [124] proposed a partial least square regression algorithm for drift compensation in MOX sensors. It was noted that the algorithm could reduce drift-related sensor variance, and at the same time, increase the class discrimination and prediction accuracy. However, this algorithm was only limited to linear dependencies, and non-linear extension was required. Niebling *et al.* [125] adapted the PLS linear regression method to be used for 'non-linear' sensor arrays. The non-linear components were interpreted into a linear format using summation and Taylor series. This reduced the average prediction error remarkably for both acetone and methanol results. In other studies, PLS can be used alongside other techniques, to improve model accuracies. For instance, Kim *et al.* [126] applied PLS algorithm to the principal component regression analysis for concentration predictions, and Campbell *et al.* [127] built a neural network based on the least square and partial least square algorithms to estimate oxygen, water vapour and temperature.

2.3.4 Classification Techniques

Classification analysis is a popular topic for gas sensors. Due to the cross sensitivity of chemical sensors, classification algorithms are necessary to distinguish different gas types. Apart from the ANN and SVM mentioned in the previous section that can also be used for classification problems, other commonly used methods including principal component analysis (PCA), k-nearest neighbours (KNN), self-organising maps (SOM), and deep neural networks.

Principal component analysis can reduce the dimensions [128] of the original data to a few principal components that can be plotted on a 2D or 3D figure, and the data clusters on the figure indicate the class information. It is easy to implement and has been used in many researches. Gardner [129] applied PCA to an array of sensors and successfully identified five alcohols clusters; Schweizer-Berberich *et al.* [130] used both PCA and principal component regression techniques to calibrate the sensor response at different gas concentrations and temperatures for food freshness monitoring; and similarly, PCA scheme was employed in the study conducted by Li *et al.* [131] using indium oxide and zinc oxide sensors for carbon monoxide, nitrogen oxide and propane detections.

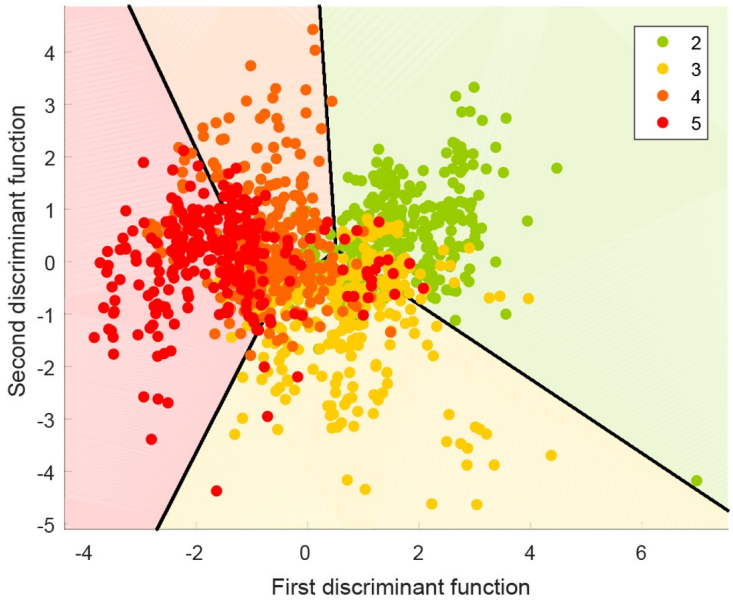

Figure 2.8: An example KNN result plot: hyperplane classifier (reproduced from [132]).

Both KNN and SOM are instance based methods that use distance functions

to assign class information. For KNN, the input data are compared with k numbers of neighbouring points, and the data with closer proximities are clustered together as the same class. It is a popular way for the non-linear gas response analysis, and can be used on it own [133, 134] or with other algorithms. Sobanski *et al.* [135] used a combined wavelet transform (dynamic response) and KNN algorithm to classify different orange juices with three gas sensors. The authors concluded that this algorithm could lead to a high correct classification ratio for both static and dynamic sensor data, as well as an immunity to noise signals. In other studies, the standard KNN model was adapted, such as clustering KNN [136], KNN with SVM [137] and KNN with PLS [138]. Figure. 2.8 shows an example KNN result plot with 2 elements (x- and y- axis).

SOM is another approach that compresses the multi-dimensional sensor dataset into a 2D format. Marco *et al.* [139] conducted a thorough research on the practical application of a SOM network with gas sensors. Six sensors were used and both static and adaptive SOM were explored. A network size of 8×8 was found to have the highest accuracy with the success rate in the adaptive model better than that of the static model. This model was also robust against non-linearities, drifts and time effect, which was suited for long term usage. In other studies, SOM was also found to be an accurate method for classification [140, 141, 142, 143], even better than a back-propagation neural network in one study [144]. These two methods can produce high success rates with gas sensors, but the downsides are the high computation power and memory space.

Deep neural network (DNN) is an extension of the shallow artificial neural

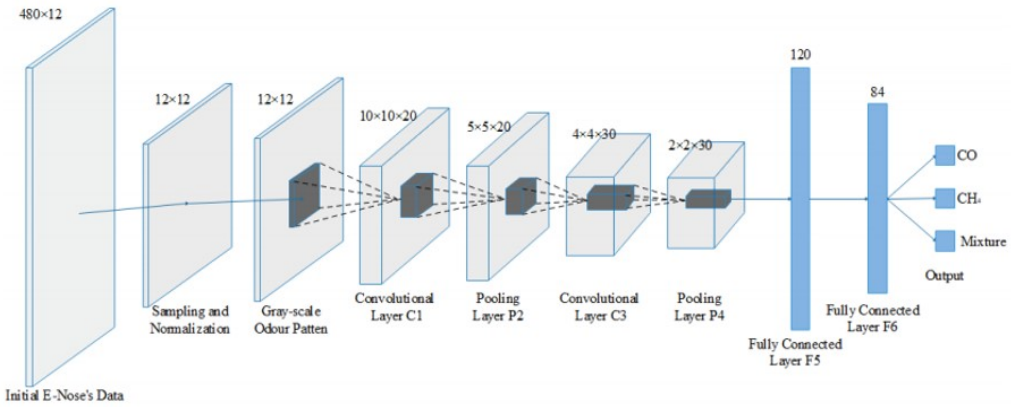

Figure 2.9: The LeNet-5 CNN structure (reproduced from [145]).

network, and has more hidden layers between the input nodes and output nodes. One popular DNN is the convolutional neural network (CNN). Despite the fact that CNN is mainly used for image processing, it can also be adopted for gas sensing applications. Lekha *et al.* [146] applied a modified 1D CNN network to classify real-time breath samples from diabetic patients. 1D Gaussian kernel filter was used for the convolution layers and max-pooling for the pooling layers. A low misclassification rate and mean square error were achieved. 1D CNN is often found to process time series data with filters acting as sliding windows to process and pass on to the next layer, such as [147], [148] and [149]. In another study, Wei *et al.* [145] proposed a novel gas identification method using LeNet-5 CNN structure and an array of 12 sensors. Instead of the 1D time series data, the sensor data were reorganised into a 2D format with greyscale patterns, similar to an image with pixels. The structure of the network is shown in Figure. 2.9, which is similar to a standard CNN topology. As compared to other algorithms, such as multilayer perceptrons and support vectors machine, this CNN model has accuracy over 98%. Wang *et al.* [78] combined a CNN with a deep Q network (DQN) by using the DQN output for the CNN classification. The overall accuracy for this model was 88% for all five analytes with good adaptability using small samples and labelled data. Similarly, Navaneeth *et al.* [150] integrated an 1D CNN model with SVM for disease classifications. Another popular DNN is the recurrent neural network (RNN). It is used for handwriting and speech recognition as it can access its memory to process a sequence of inputs. Bilgera *et al.* [151] applied a variance of RNN to an array of MOX sensors for gas source localisation. Despite the distance limitation and density mismatch on some occasions, the model can provide a high accuracy with a small error. In this thesis, only CNN is studied as an example of deep learning.

2.4 Conclusions

In this chapter, a literature review is conducted on both the plasmonic metamaterial and various sensor signal processing techniques. Plasmonic metamaterial has the advantage of tailoring the electromagnetic wavelength, which can be applied to the emitter or detector of an NDIR sensor for tunable narrowband emissions/absorptions. It is based on Maxwell's law on electromagnetic interactions in free space, which are used to deduce the wave equations for metal and dielectric materials. The electromagnetic wave that travels through the dielectric-metal interface is known as surface plasmons. It is excited by photons, and together with coupling

medium, it can generate frequencies at particular ranges. The coupling medium can be gratings, such as slots, holes and dots. The dimensions of the grating structure (width, gap) affect the wavelengths. In addition, various plasmonic materials were studied, for instance silver, gold, aluminium and tungsten. Both plasmonic structures an d materials were studied in literature as emitters and detectors. A table is provided to summarise some recent researches.

The second part of this chapter describes different signal processing methods, including the temperature modulation technique and different machine learning algorithms. Temperature modulation is a dynamic signal processing technique that finds the sensor characteristics both in the time domain and the frequency domain. Instead of the conventional constant temperature operation mode of a MOX sensor, two operating temperatures are used in a periodic order. It can be from a lower temperature to a higher temperature, from a standard temperature to a shut-down phase, or an occasional higher temperature operation as a cleaning mechanism. The collected data from this dynamic operation mode were then processed with feature extraction methods, such as Fourier transform and wavelet transform. The results can be used directly to show sensor characteristics or processed further with regression/classification techniques. Regression analysis can provide a relationship between a set of independent variables and dependent variables. Such methods include neural network, support vector machine and partial least squares. Similar algorithms can also be applied to a classification problem. Furthermore, principal component analysis, k-nearest neighbours, self-organising map and deep neural networks can also be used. All the above algorithms were mentioned in this chapter. Later in the thesis, a neural network is applied to a gas sensor regression problem, and principal component analysis, k-nearest neighbours, self-organising maps and deep neural network are used for classification analysis.

References

[1] J. C. Maxwell, *A Treatise on Electricity and Magnetism*, 3rd ed. New York: Dover Publications, 1954.

[2] K. Shah, *Plasma and Plasmonics*. Delhi: De Gruyter, 2018.

[3] The University of Edinburgh, "Electromagnetism: waves in conductors." [Online]. Available: https://www2.ph.ed.ac.uk /playfer/EMlect15.pdf

[4] M. G. Blaber, M. D. Arnold, and M. J. Ford, "Search for the ideal plasmonic nanoshell: the effects of surface scattering and alternatives to gold and silver," *The Journal of Physical Chemistry C*, vol. 113, no. 8, pp. 3041–3045, 2009.

[5] M. A. Ordal, R. J. Bell, R. W. Alexander, L. L. Long, and M. R. Querry, "Optical properties of fourteen metals in the infrared and far infrared: Al, Co, Cu, Au, Fe, Pb, Mo, Ni, Pd, Pt, Ag, Ti, V, and W." *Appl. Opt.*, vol. 24, no. 24, pp. 4493–4499, 1985.

[6] A. A. Maradudin, "Chapter 1 - Introduction: plasmonics and its building blocks," in *Handbook of Surface Science*, N. V. Richardson and H. Stephen, Eds. Amsterdam: North-Holland, 2014, vol. 4, pp. 1–36.

[7] S. A. Maier, *Plasmonics: Fundamentals and Applications*, 1st ed. New York: Springer US, 2007.

[8] A. Pusch, A. De Luca, S. S. Oh, S. Wuestner, T. Roschuk, Y. Chen, S. Boual, Z. Ali, C. C. Phillips, M. Hong, S. A. Maier, F. Udrea, R. H. Hopper, and O. Hess, "A highly efficient CMOS nanoplasmonic crystal enhanced slow-wave thermal emitter improves infrared gas-sensing devices," *Scientific Reports*, vol. 5, no. 1, pp. 17 451–17 455, 2015.

[9] D. L. C. Chan, M. Soljačić, and J. D. Joannopoulos, "Thermal emission and design in 2D-periodic metallic photonic crystal slabs," *Optics Express*, vol. 14, no. 19, pp. 8785–8796, 2006.

[10] V. Giannini, G. Vecchi, and J. Gómez Rivas, "Lighting up multipolar surface plasmon polaritons by collective resonances in arrays of nanoantennas," *Physical Review Letters*, vol. 105, no. 26, pp. 266 801–266 804, 2010.

[11] I. R. Hooper and W. L. Barnes, "Chapter 2 - the basics of plasmonics," in *Handbook of Surface Science*. Amsterdam: North-Holland, 2014, vol. Volume 4, pp. 37–74.

[12] M. Mehdizadeh, "Chapter 1 - the impact of fields on materials at RF/microwave frequencies," in *Microwave/RF Applicators and Probes for Material Heating, Sensing, and Plasma Generation: A Design Guide*. Boston: William Andrew Publishing, 2010, pp. 1–34.

[13] A. Argyros, A. Tuniz, S. C. Fleming, and B. T. Kuhlmey, "Drawn metamaterials," in *Optofluidics, Sensors and Actuators in Microstructured Optical Fibers*. Cambridge: Woodhead Publishing, 2015, pp. 29–54.

[14] C. M. Soukoulis and M. Wegener, "Past achievements and future challenges in the development of three-dimensional photonic metamaterials," *Nature Photonics*, vol. 5, no. 9, pp. 523–530, 2011.

[15] P. R. West, S. Ishii, G. V. Naik, N. K. Emani, V. M. Shalaev, and A. Boltasseva, "Searching for better plasmonic materials," *Laser & Photonics Reviews*, vol. 4, no. 6, pp. 795–808, 2010.

[16] P. B. Johnson and R. W. Christy, "Optical constants of the noble metals," *Physical Review B*, vol. 6, no. 12, pp. 4370–4379, 1972.

[17] T. Xu, A. Agrawal, M. Abashin, K. J. Chau, and H. J. Lezec, "All-angle negative refraction and active flat lensing of ultraviolet light," *Nature*, vol. 497, no. 1, pp. 470–474, 2013.

[18] H. Lezec, T. Xu, and J. Kohouek, "Nanoplasmonics and three-dimensional plasmonic metamaterials." [Online]. Available: https://www.nist.gov/programs-projects/nanoplasmonics-and-three-dimensional-plasmonic-metamaterials

[19] Z. Fei, G.-X. Ni, B.-Y. Jiang, M. M. Fogler, and D. N. Basov, "Nanoplasmonic phenomena at electronic boundaries in graphene," *ACS Photonics*, vol. 4, no. 12, pp. 2971–2977, 2017.

[20] K. Y. M. Yeung, J. Chee, H. Yoon, Y. Song, J. Kong, and D. Ham, "Far-infrared graphene plasmonic crystals for plasmonic band engineering," *Nano Letters*, vol. 14, no. 5, pp. 2479–2484, 2014.

[21] A. Andryieuski, I. Khromova, S. V. Zhukovsky, and A. V. Lavrinenko, "Graphene-enhanced metamaterials for THz applications," in *Fundamental and Applied Nano-Electromagnetics*. Dordrecht: Springer Netherlands, 2016, pp. 145–169.

[22] M. Ben Rhouma, M. Oueslati, and B. Guizal, "Surface plasmons on a doped graphene sheet with periodically modulated conductivity," *Superlattices and Microstructures*, vol. 96, no. 1, pp. 212–219, 2016.

[23] P. Tassin, T. Koschny, M. Kafesaki, and C. M. Soukoulis, "A comparison of graphene, superconductors and metals as conductors for metamaterials and plasmonics," *Nat Photon*, vol. 6, no. 4, pp. 259–264, 2012.

[24] F. B. Zarrabi, M. Mohaghegh, M. Bazgir, and A. S. Arezoomand, "Graphene–gold nano-ring antenna for dual-resonance optical application," *Optical Materials*, vol. 51, pp. 98–103, 2016.

[25] T. Jägeler-Hoheisel, J. Benduhn, C. Körner, and K. Leo, "Critical dimensions in small-molecule plasmonic particle solar cells," in *Elementary Processes in Organic Photovoltaics*. Cham: Springer International Publishing, 2017, pp. 327–349.

[26] I. E. Protsenko, A. V. Uskov, X.-W. Chen, and H. Xu, "Plasmonic superradiance of two emitters near a metal nanorod," *Journal of Physics D: Applied Physics*, vol. 50, no. 25, pp. 254 003–254 013, 2017.

[27] E. Paspalakis, E. Kallos, and V. Yannopapas, "Controlled interaction of a four-level quantum emitter with a plasmonic nanostructure," *Journal of Physics: Conference Series*, vol. 633, no. 1, pp. 12 063–12 068, 2015.

[28] Z. Zhang, H. Wang, Z. Chen, X. Wang, J. Choo, and L. Chen, "Plasmonic colorimetric sensors based on etching and growth of noble metal nanoparticles: strategies and applications," *Biosensors and Bioelectronics*, vol. 114, no. 1, pp. 52–65, 2018.

[29] K. Ma, L. Liu, P. Zhang, Y. He, and Q. Peng, "Optimization of angle-pixel resolution for angular plasmonic biosensors," *Sensors and Actuators B: Chemical*, vol. 283, no. 1, pp. 188–197, 2019.

[30] S. E. El-Zohary, A. A. Azzazi, H. Okamoto, T. Okamoto, M. Haraguchi, and M. A. Swillam, "Resonance-based integrated plasmonic nanosensor for lab-on-chip applications," *Journal of Nanophotonics*, vol. 7, no. 1, pp. 1–10, 2013.

[31] N. R. Jo, K. J. Lee, and Y.-B. Shin, "Enzyme-coupled nanoplasmonic biosensing of cancer markers in human serum," *Biosensors & bioelectronics*, vol. 81, no. 1, pp. 324–333, 2016.

[32] J. N. Anker, W. P. Hall, O. Lyandres, N. C. Shah, J. Zhao, and R. P. Van Duyne, "Biosensing with plasmonic nanosensors," *Nat Mater*, vol. 7, no. 6, pp. 442–453, 2008.

[33] D. Zopf, J. Jatschka, A. Dathe, N. Jahr, W. Fritzsche, and O. Stranik, "Hyperspectral imaging of plasmon resonances in metallic nanoparticles," *Biosensors & Bioelectronics*, vol. 81, no. 1, pp. 287–293, 2016.

[34] A. A. Yanik, A. E. Cetin, M. Huang, A. Artar, S. H. Mousavi, A. Khanikaev, J. H. Connor, G. Shvets, and H. Altug, "Seeing protein monolayers with naked eye through plasmonic Fano resonances," *Proceedings of the National Academy of Sciences*, vol. 108, no. 29, pp. 11 784–11 789, 2011.

[35] R. Ma, S. Ota, Y. Li, S. Yang, and X. Zhang, "Explosives detection in a lasing plasmon nanocavity," *Nat Nano*, vol. 9, no. 8, pp. 600–604, 2014.

[36] J. T. Daly, A. C. Greenwald, E. A. Johnson, W. A. Stevenson, J. A. Wollam, T. George, E. W. Jones, J. W. Perry, and A. Scherer, "Nanostructured surfaces for tuned infrared emission for spectroscopic applications," in *Symposium on Integrated Optoelectronics*, San Jose, CA, Apr 2000, pp. 80–89.

[37] H.-K. Fu, Y.-W. Jiang, M.-W. Tsai, S.-C. Lee, and Y.-F. Chen, "A thermal emitter with selective wavelength: Based on the coupling between photonic crystals and surface plasmon polaritons," *Journal of Applied Physics*, vol. 105, no. 3, p. 33505, 2009.

[38] J. Yu-Wei, M.-W. Tsai, Y. Yi-Han, T. Dah-Ching, C. Chia-Yi, and S.-C. Lee, "Enhancement of thermal radiation in plasmonic thermal emitter by surface plasmon resonance," in *2008 8th IEEE Conference on Nanotechnology*, Arlington, TX, USA, Aug 2008, pp. 104–107.

[39] M.-W. Tsai, T.-H. Chuang, Y.-T. Chang, and S.-C. Lee, "Two color squared-lattice plasmonic thermal emitter," in *2006 Sixth IEEE Conference on Nanotechnology*, vol. 2, Cincinnati, OH, USA, Jul 2006, pp. 746–748.

[40] H. Yan, T. Low, W. Zhu, Y. Wu, M. Freitag, X. Li, F. Guinea, P. Avouris, and F. Xia, "Damping pathways of mid-infrared plasmons in graphene nanostructures," *Nat Photon*, vol. 7, no. 5, pp. 394–399, 2013.

[41] H. Yan, X. Li, B. Chandra, G. Tulevski, Y. Wu, M. Freitag, W. Zhu, P. Avouris, and F. Xia, "Tunable infrared plasmonic devices using graphene/insulator stacks," *Nat Nano*, vol. 7, no. 5, pp. 330–334, 2012.

[42] J. Young Chul and B. Igal, "Electrically tunable infrared metamaterials based on depletion-type semiconductor devices," *Journal of Optics*, vol. 14, no. 11, pp. 114 013–114 021, 2012.

[43] S. Tay, A. Kropachev, I. E. Araci, T. Skotheim, R. A. Norwood, and N. Peyghambarian, "Plasmonic thermal IR emitters based on nanoamorphous carbon," *Applied Physics Letters*, vol. 94, no. 7, pp. 71 113–71 115, 2009.

[44] K. Ikeda, H. T. Miyazaki, T. Kasaya, K. Yamamoto, Y. Inoue, K. Fujimura, T. Kanakugi, M. Okada, K. Hatade, and S. Kitagawa, "Controlled thermal emission of polarized infrared waves from arrayed plasmon nanocavities," *Applied Physics Letters*, vol. 92, no. 2, pp. 21 117–2119, 2008.

[45] H. Feng Lu, S. Mokkapati, L. Fu, G. Jolley, H. Hoe Tan, and C. Jagadish, "Plasmonic quantum dot solar cells for enhanced infrared response," *Applied Physics Letters*, vol. 100, no. 10, pp. 103 505–103 508, 2012.

[46] B. Zhu, M. Chen, S. V. Kershaw, A. L. Rogach, N. Zhao, and H. K. Tsang, "Polarization sensitive plasmonic photodetector based on HgTe quantum dots," in *2018 IEEE Photonics Conference (IPC)*, Reston, VA, USA, Sept 2018, pp. 1–2.

[47] F. Li, H. San, C. Li, Y. Li, and X. Chen, "MEMS-based plasmon infrared emitter with hexagonal hole arrays perforated in the Al-SiO_2-Si structure," *Journal of Micromechanics and Microengineering*, vol. 21, no. 10, pp. 105 023–105 029, 2011.

[48] J. Xinming, Z. Xin, J. Peng, X. Fang, and H. Yiping, "Narrow-band midinfrared thermal emitter based on photonic crystal for NDIR gas sensor," in *2010 10th IEEE International Conference on Solid-State and Integrated Circuit Technology (ICSICT)*, Shanghai, China, Nov 2010, pp. 1459–1461.

[49] I. E. Araci, V. Demir, A. Kropachev, T. Skotheim, R. A. Norwood, and N. Peyghambarian, "Mechanical and thermal stability of plasmonic emitters on flexible polyimide substrates," *Applied Physics Letters*, vol. 97, no. 4, pp. 41 102–41 104, 2010.

[50] I. E. Araci, V. Demir, and A. V. Kropachev, "Tunable infrared emitter," U.S. Patent US20 120 235 067A1, 2011.

[51] G. R. Lahiji and K. D. Wise, "A batch-fabricated silicon thermopile infrared detector," *IEEE Transactions on Electron Devices*, vol. 29, no. 1, pp. 14–22, 1982.

[52] F. Udrea, J. W. Gardner, S. Z. Ali, M. F. Chowdhury, and I. Poenaru, "IR detector," U.S. Patent US8 552 380B1, 2012.

[53] N. I. Zheludev, E. Plum, and J. Y. Ou, "Tunable metamaterials and related devices," U.S. Patent US8 717 659B, 2014.

[54] M. Zohar, M. Auslender, L. Faraone, and S. Hava, "Novel resonant cavity-enhanced absorber structures for high-efficiency midinfrared photodetector application," *Journal of Nanophotonics*, vol. 5, no. 1, pp. 51 815–51 824, 2011.

[55] S. Bauer, S. Bauer-Gogonea, W. Becker, R. Fettig, B. Ploss, W. Ruppel, and W. von Münch, "Thin metal films as absorbers for infrared sensors," *Sensors and Actuators: A. Physical*, vol. 37-38, no. 1, pp. 497–501, 1993.

[56] X. Hu, M. Li, Z. Ye, W. Y. Leung, K.-M. Ho, and S.-Y. Lin, "Design of midinfrared photodetectors enhanced by resonant cavities with subwavelength metallic gratings," *Applied Physics Letters*, vol. 93, no. 24, pp. 241 108–241 110, 2008.

[57] U. Palanchoke, S. Boutami, and J. Hazart, "CMOS-compatible metallic nanostructures for visible and infrared filtering," *Proc. Photonic and Phononic Properties of Engineered Nanostructures IV*, vol. 8994, no. 1, pp. 67 – 72, 2014.

[58] J. Hendrickson and J. Guo, "Plasmonic perfect light absorber has a wide IR spectral band," *Laser Focus World*, vol. 48, no. 8, pp. 58–59, 2012.

[59] W. Chihhui, N. Burton III, J. Jeremy, M. Andrew, Z. Byron, S. Steve, and S. Gennady, "Metamaterial-based integrated plasmonic absorber/emitter for solar thermo-photovoltaic systems," *Journal of Optics*, vol. 14, no. 2, pp. 24 005–24 011, 2012.

[60] K. Aydin, V. E. Ferry, R. M. Briggs, and H. A. Atwater, "Broadband polarization-independent resonant light absorption using ultrathin plasmonic super absorbers," *Nat. Commun.*, vol. 2, no. 1, pp. 517–513, 2011.

[61] Y. Li, L. Su, B. Wang, Y. Guo, Z. Zhu, and Z. Zhou, "Multiplex-bands spectral characteristics of infrared perfect absorber metamaterials," *Proceedings Metamaterials: Fundamentals and Applications VI*, vol. 8806, no. 1, pp. 12–21, 2013.

[62] Y. Li, B. Wang, X. Xu, and L. Su, "Polarization sensitivity contributes to multiple band spectra of one mid-infrared absorber," *Chinese Optics Letters*, vol. 12, no. 10, pp. 101 603–101 613, 2014.

[63] S. C. Lee, S. Krishna, and S. Brueck, "Plasmonic detectors," U.S. Patent US8 835 851B2, 2014.

[64] K. Ziouche, G. Savelli, Z. Bougrioua, D. Hauser, P. Lejeune, P.-M. Michon, T. Lasri, and D. Leclercq, "Thermoelectric infrared microsensors based on a periodically suspended thermopile integrating nanostructured Ge/SiGe quantum dots superlattice," *Journal of Applied Physics*, vol. 116, no. 4, pp. 43 701–43 707, 2014.

[65] J. P. Long, J. D. Caldwell, J. C. Owrutsky, and O. J. Glembocki, "Actively Tunable Polar-Dielectric Optical Devices," U.S. Patent US20 140 224 989, 2014.

[66] S. Z. Ali, F. Udrea, J. W. Gardner, R. H. Hooper, A. De Luca, M. F. Chowdhury, and I. Poenaru, "Plasmonic IR devices," U.S. Patent US9 214 604B2, 2015.

[67] W. Yue, V. Kravets, M. Pu, C. Wang, Z. Zhao, and Z. Hu, "Multiple-resonant pad-rod nanoantennas for surface-enhanced infrared absorption spectroscopy," *Nanotechnology*, vol. 30, no. 46, pp. 5206–5216, 2019.

[68] Z. Liu, X. Liu, G. Fu, and G. Liu, "Tunable, large-scale and low-cost Si infrared absorbers," *Journal of Physics D: Applied Physics*, vol. 52, no. 46, pp. 5107–5114, 2019.

[69] A. Ali, F. A. Mangrio, X. Chen, Y. Dai, K. Chen, X. Xu, R. Xia, and L. Zhu, "Ultrathin MoS_2 nanosheets for high-performance photoelectrochemical applications via plasmonic coupling with Au nanocrystals," *Nanoscale*, vol. 11, no. 16, pp. 7813–7824, 2019.

[70] F. Zhao, C. Zhang, H. Chang, and X. Hu, "Design of plasmonic perfect absorbers for quantum-well infrared photodetection," *Plasmonics*, vol. 9, no. 6, pp. 1397–1400, 2014.

[71] V. J. Gokhale, P. D. Myers, and M. Rais-Zadeh, "Subwavelength plasmonic absorbers for spectrally selective resonant infrared detectors," in *2014 IEEE Sensors Conference*, Valencia, Spain, Nov 2014, pp. 982–985.

[72] P. Bouchon, C. Koechlin, F. Pardo, R. Haïdar, and J.-L. Pelouard, "Wideband omnidirectional infrared absorber with a patchwork of plasmonic nanoantennas," *Optics Letters*, vol. 37, no. 6, pp. 1038–1040, 2012.

[73] K. Gorgulu, A. Gok, M. Yilmaz, K. Topalli, N. Bıyıklı, and A. K. Okyay, "All-silicon ultra-broadband infrared light absorbers," *Scientific Reports*, vol. 6, no. 1, pp. 38 589–38 595, 2016.

[74] A. Lefebvre, D. Costantini, I. Doyen, Q. Lévesque, E. Lorent, D. Jacolin, J. J. Greffet, S. Boutami, and H. Benisty, "CMOS compatible metal-insulator-metal plasmonic perfect absorbers," *Optical Materials Express*, vol. 6, no. 7, pp. 2389–2396, 2016.

[75] M. F. Chowdhury, S. Z. Ali, S. Boual, R. Hopper, and F. Udrea, "Development of plasmonic MEMS CMOS infrared sensors for occupancy detection," in *2016 46th European Solid-State Device Research Conference (ESSDERC)*, Lausanne, Switzerland, Sept 2016, pp. 97–100.

[76] S. M. Sherif and M. Swillam, "Silicon-plasmonic-integrated mid-infrared sensor using CMOS technology," *Proceedings: Photonic and Phononic Properties of Engineered Nanostructures VII*, vol. 10112, no. 1, pp. 1–7, 2017.

[77] J. A. Briggs, G. V. Naik, T. A. Petach, B. K. Baum, D. Goldhaber-Gordon, and J. A. Dionne, "Fully CMOS-compatible titanium nitride nanoantennas," *Applied Physics Letters*, vol. 108, no. 5, pp. 51 110–51 114, 2016.

[78] Y. Wang, A. C. Overvig, S. Shrestha, R. Zhang, R. Wang, N. Yu, and L. Dal Negro, "Tunability of indium tin oxide materials for mid-infrared plasmonics applications," *Optical Materials Express*, vol. 7, no. 8, pp. 2727–2739, 2017.

[79] M. Mirotznik, W. Beck, K. Olver, and J. Little, "Passive infrared sensing using plasmonic resonant dust particles," *International Journal of Optics*, vol. 2012, no. 651563, pp. 1–8, 2012.

[80] S. Huang, H. Chen, H. Hsiao, P. Chang, Y. Chang, C. Chen, Y. Jiang, H. Chang, and S. Lee, "Triple peaks plasmonic thermal emitter with selectable wavelength using periodic block pattern as top layer," *IEEE Photonics Technology Letters*, vol. 24, no. 10, pp. 833–835, 2012.

[81] J. Liu, U. Guler, A. Lagutchev, A. Kildishev, O. Malis, A. Boltasseva, and V. M. Shalaev, "Quasi-coherent thermal emitter based on refractory plasmonic materials," *Optical Materials Express*, vol. 5, no. 12, pp. 2721–2728, 2015.

[82] A. Vergara, S. Vembu, T. Ayhan, M. A. Ryan, M. L. Homer, and R. Huerta, "Chemical gas sensor drift compensation using classifier ensembles," *Sensors and Actuators B: Chemical*, vol. 166-167, pp. 320–329, 2012.

[83] K. R. Kashwan and M. Bhuyan, "Robust electronic-nose system with temperature and humidity drift compensation for tea and spice flavour discrimination," in *2005 Asian Conference on Sensors and the International Conference on*

New Techniques in Pharmaceutical and Biomedical Research, Kuala Lumpur, Malaysia, Sept 2005, pp. 154–158.

[84] S. Di Carlo, M. Falasconi, E. Sanchez, A. Scionti, G. Squillero, and A. Tonda, "Increasing pattern recognition accuracy for chemical sensing by evolutionary based drift compensation," *Pattern Recognition Letters*, vol. 32, no. 13, pp. 1594–1603, 2011.

[85] L. Zhang and D. Zhang, "Domain adaptation extreme learning machines for drift compensation in E-Nose systems," *IEEE Transactions on Instrumentation and Measurement*, vol. 64, no. 7, pp. 1790–1801, 2015.

[86] J. W. Gardner, P. K. Guha, F. Udrea, and J. A. Covington, "CMOS interfacing for integrated gas sensors: a review," *IEEE Sensors Journal*, vol. 10, no. 12, pp. 1833–1848, 2010.

[87] SGX Sensortech, "Signal processing for infrared gas sensors," 2014. [Online]. Available: https://www.sgxsensortech.com/content/uploads/2014/08/AN2-—Signal-Processing-for-Infrared-Gas-Sensors.pdf

[88] J. Burgués and S. Marco, "Low power operation of temperature-modulated metal oxide semiconductor gas sensors," *Sensors*, vol. 18, no. 2, pp. 339–353, 2018.

[89] A. P. Lee and B. J. Reedy, "Temperature modulation in semiconductor gas sensing," *Sensors and Actuators B: Chemical*, vol. 60, no. 1, pp. 35–42, 1999.

[90] J. Burgués, J. Fonollosa, and S. Marco, "Discontinuously operated MOX sensors for low power applications," in *2017 ISOCS/IEEE International Symposium on Olfaction and Electronic Nose (ISOEN)*, Montreal, Canada, Jul 2017, pp. 1–3.

[91] D. Oletic, V. Jelicic, D. Antolovic, and V. Bilas, "Energy-efficient atmospheric CO concentration sensing with on-demand operating MOX gas sensor," in *2014 IEEE Sensors Conference*. Valencia, Spain: IEEE, Nov 2014, pp. 795–798.

[92] V. Jelicic, D. Oletic, T. Sever, and V. Bilas, "Evaluation of MOX gas sensor transient response for low-power operation," in *2015 IEEE Sensors Applications Symposium (SAS)*. Zadar, Croatia: IEEE, Apr 2015, pp. 1–5.

[93] I. Sayhan, A. Helwig, T. Becker, G. Muller, I. Elmi, S. Zampolli, M. Padilla, and S. Marco, "Discontinuously operated metal oxide gas sensors for flexible tag microlab applications," *IEEE Sensors Journal*, vol. 8, no. 2, pp. 176–181, 2008.

[94] S. Bicelli, A. Depari, G. Faglia, A. Flammini, A. Fort, M. Mugnaini, A. Ponzoni, V. Vignoli, and S. Rocchi, "Model and experimental characterization of the dynamic behaviour of low-power carbon monoxide MOX sensors operated with pulsed temperature profiles," *IEEE Transactions on Instrumentation and Measurement*, vol. 58, no. 5, pp. 1324–1332, 2009.

[95] A. Shaposhnik, P. Moskalev, E. Sizask, S. Ryabtsev, and A. Vasiliev, "Selective detection of hydrogen sulfide and methane by a single MOX sensor," *Sensors*, vol. 19, no. 5, pp. 1135–1149, 2019.

[96] G. Korotcenkov and B. K. Cho, "Instability of metal oxide-based conductometric gas sensors and approaches to stability improvement (short survey)," *Sensors and Actuators B: Chemical*, vol. 156, no. 2, pp. 527–538, 2011.

[97] P. Dufresne, "Hydroprocessing catalysts regeneration and recycling," *Applied Catalysis A: General*, vol. 322, no. 1, pp. 67–75, 2007.

[98] O. Wurzinger and G. Reinhardt, "CO-sensing properties of doped SnO_2 sensors in H_2-rich gases," *Sensors and Actuators B: Chemical*, vol. 103, no. 1, pp. 104–110, 2004.

[99] Y. Kato and T. Mukai, "A real-time intelligent gas sensor system using a nonlinear dynamic response," *Sensors and Actuators B: Chemical*, vol. 120, no. 2, pp. 514–520, 2007.

[100] H. Ding, H. Ge, and J. Liu, "High performance of gas identification by wavelet transform-based fast feature extraction from temperature modulated semiconductor gas sensors," *Sensors and Actuators B: Chemical*, vol. 107, no. 2, pp. 749–755, 2005.

[101] R. Ionescu, E. Llobet, J. Brezmes, X. Vilanova, and X. Correig, "Dealing with humidity in the qualitative analysis of CO and NO_2 using a WO_3 sensor and dynamic signal processing," *Sensors and Actuators B: Chemical*, vol. 95, no. 1, pp. 177–182, 2003.

[102] E. Llobet, R. Ionescu, S. Al-Khalifa, J. Brezmes, X. Vilanova, X. Correig, N. Barsan, and J. W. Gardner, "Multicomponent gas mixture analysis using

a single tin oxide sensor and dynamic pattern recognition," *IEEE Sensors Journal*, vol. 1, no. 3, pp. 207–213, 2001.

[103] E. Martinelli, A. Catini, and C. D. Natale, "An active temperature modulation of gas sensor based on a self-adaptive strategy," in *2013 Transducers & Eurosensors XXVII: The 17th International Conference on Solid-State Sensors, Actuators and Microsystems (TRANSDUCERS & EUROSENSORS XXVII)*. Barcelona, Spain: IEEE, Jun 2013, pp. 2045–2048.

[104] J. Burgués and S. Marco, "Multivariate estimation of the limit of detection by orthogonal partial least squares in temperature-modulated MOX sensors," *Analytica Chimica Acta*, vol. 1019, no. 1, pp. 49–64, 2018.

[105] G. Huyberechts, P. Szecówka, J. Roggen, and B. W. Licznerski, "Simultaneous quantification of carbon monoxide and methane in humid air using a sensor array and an artificial neural network," *Sensors and Actuators B: Chemical*, vol. 45, no. 2, pp. 123–130, 1997.

[106] H. Baha and Z. Dibi, "A novel neural network-based technique for smart gas sensors operating in a dynamic environment," *Sensors*, vol. 9, no. 11, pp. 8944–8960, 2009.

[107] A. Heilig, N. Bârsan, U. Weimar, M. Schweizer-Berberich, J. W. Gardner, and W. Göpel, "Gas identification by modulating temperatures of SnO_2S-based thick film sensors," *Sensors and Actuators B: Chemical*, vol. 43, no. 1, pp. 45–51, 1997.

[108] S. Nakata, E. Ozaki, and N. Ojima, "Gas sensing based on the dynamic nonlinear responses of a semiconductor gas sensor: dependence on the range and frequency of a cyclic temperature change," *Analytica Chimica Acta*, vol. 361, no. 1, pp. 93–100, 1998.

[109] R. Ionescu and E. Llobet, "Wavelet transform-based fast feature extraction from temperature modulated semiconductor gas sensors," *Sensors and Actuators B: Chemical*, vol. 81, no. 2, pp. 289–295, 2002.

[110] X.-J. Huang, Y.-K. Choi, K.-S. Yun, and E. Yoon, "Oscillating behaviour of hazardous gas on tin oxide gas sensor: Fourier and wavelet transform analysis," *Sensors and Actuators B: Chemical*, vol. 115, no. 1, pp. 357–364, 2006.

[111] R. Gutierrez-Osuna, "Pattern analysis for machine olfaction: a review," *IEEE Sensors Journal*, vol. 2, no. 3, pp. 189–202, 2002.

[112] L. Spinelle, M. Gerboles, M. G. Villani, M. Aleixandre, and F. Bonavitacola, "Field calibration of a cluster of low-cost available sensors for air quality monitoring. Part A: ozone and nitrogen dioxide," *Sensors and Actuators B: Chemical*, vol. 215, no. 1, pp. 249–257, 2015.

[113] T. Eklöv, P. Mårtensson, and I. Lundström, "Selection of variables for interpreting multivariate gas sensor data," *Analytica Chimica Acta*, vol. 381, no. 2, pp. 221–232, 1999.

[114] K. Huang, Z. Liu, and D. Huang, "Fault Diagnosis for Methane Sensors using Generalized Regression Neural Network," *International Journal of Online Engineering (iJOE)*, vol. 12, no. 3, pp. 42–47, 2016.

[115] A. Gulbag and F. Temurtas, "A study on quantitative classification of binary gas mixture using neural networks and adaptive neuro-fuzzy inference systems," *Sensors and Actuators B: Chemical*, vol. 115, no. 1, pp. 252–262, 2006.

[116] M. Aydın, M. S. Yıldırım, O. Karpuz, and K. Ghasemlou, "Modeling of driver lane choice behavior with artificial neural networks (ANN) and linear regression (LR) analysis on deformed roads," *Computer Science & Engineering: An International Journal (CSEIJ)*, vol. 4, no. 1, pp. 47–57, 2014.

[117] A. Shmilovici, G. Bakir, S. Marco, and A. Perera, "Finding the best calibration points for a gas sensor array with support vector regression," *Proceedings: 2004 2nd International IEEE Conference on 'Intelligent Systems'.*, vol. 1, no. 1, pp. 174–177, 2004.

[118] N. Ni and C. C. Chan, "Identification and measurement of gas mixture by using the support vector regression technique," *Measurement Science and Technology*, vol. 20, no. 11, pp. 5601–5611, 2009.

[119] A. W. Dougherty, E. Beach, P. A. Morris, and B. R. Patton, "Efficient orthogonalization in gas sensor arrays using reciprocal kernel support vector regression," *Sensors and Actuators B: Chemical*, vol. 149, no. 1, pp. 264–271, 2010.

[120] H. Ge and J. Liu, "Identification of gas mixtures by a distributed support vector machine network and wavelet decomposition from temperature modulated semiconductor gas sensor," *Sensors and Actuators B: Chemical*, vol. 117, no. 2, pp. 408–414, 2006.

[121] C. Pace, L. Fragomeni, and W. Khalaf, "Developments and applications of electronic nose systems for gas mixtures classification and concentration estimation," in *Applications in Electronics Pervading Industry, Environment and Society*, 1st ed., Cham, 2016, pp. 1–7.

[122] S. Dey, "Implementing a soft-margin kernelized support vector machine binary classifier with quadratic programming in R and Python," 2018. [Online]. Available: https://www.datasciencecentral.com/profiles/blogs/implementing-a-soft-margin-kernelized-support-vector-machine

[123] S. Marco and A. Gutierrez-Galvez, "Signal and data processing for machine olfaction and chemical sensing: A review," *IEEE Sensors Journal*, vol. 12, no. 11, pp. 3189–3214, 2012.

[124] R. Gutierrez-Osuna, "Drift reduction for metal-oxide sensor arrays using canonical correlation regression and partial least squares," in *Proceedings of the 7th International Symp. On Olfaction and Electronic Nose*, Brighton, UK, Jul 2000.

[125] G. Niebling and R. Mu¨ller, "Non-linear signal evaluation with linear regression techniques for redundant signals," *Sensors and Actuators B: Chemical*, vol. 25, no. 1, pp. 805 – 807, 1995.

[126] B. H. Kim, F. E. Prins, D. P. Kern, S. Raible, and U. Weimar, "Multicomponent analysis and prediction with a cantilever array based gas sensor," *Sensors and Actuators B: Chemical*, vol. 78, no. 1, pp. 12–18, 2001.

[127] S. R. Campbell, E. A. Mendoza, and E. Fiesler, "Neural-network-enhanced small low-cost low-power sensor for atmospheric gases," *Proceedings of the society of photo-optical instrumentation engineers*, vol. 4120, no. 1, pp. 190–197, 2000.

[128] M. Shi, B. Guo, and A. Bermak, "Redundancy analysis for tin oxide gas sensor array," in *Third IEEE International Workshop on Electronic Design, Test and Applications (DELTA'06).* Kuala Lumpur, Malaysia: IEEE, Jan 2006, pp. 448–454.

[129] J. W. Gardner, "Detection of vapours and odours from a multisensor array using pattern recognition Part 1. principal component and cluster analysis," *Sensors and Actuators B: Chemical*, vol. 4, no. 1, pp. 109–115, 1991.

[130] P.-M. Schweizer-Berberich, S. Vaihinger, and W. Göpel, "Characterisation of food freshness with sensor arrays," *Sensors and Actuators B: Chemical*, vol. 18, no. 1, pp. 282–290, 1994.

[131] F.-a. Li, J. Zou, X. Zhang, D. Zhang, H. Jin, J. Wang, and J. Jian, "Discriminating hazardous gas mixture via a zirconia-based amperometric gas sensor," *Ionics*, vol. 24, no. 5, pp. 1451–1456, 2018.

[132] M. Bastuck, T. Baur, and A. Schütze, "Dav^{3}e – a matlab toolbox for multivariate sensor data evaluation," *Journal of Sensors and Sensor Systems*, vol. 7, no. 2, pp. 489–506, 2018.

[133] L. Chambon, J. P. Germain, A. Pauly, V. Demarne, and A. Grisel, "A metallic oxide gas sensor array for a selective detection of the CO and NH_3 gases," *Sensors and Actuators B: Chemical*, vol. 60, no. 2, pp. 138–147, 1999.

[134] R. Gutierrez-Osuna and H. T. Nagle, "A method for evaluating data-preprocessing techniques for odour classification with an array of gas sensors," *IEEE Transactions on Systems, Man, and Cybernetics, Part B (Cybernetics)*, vol. 29, no. 5, pp. 626–632, 1999.

[135] T. Sobanski, I. Modrak, K. Nitsch, and B. W. Licznerski, "Application of sensor dynamic response analysis to improve the accuracy of odour-measuring systems," *Measurement Science and Technology*, vol. 17, no. 1, pp. 1–5, 2005.

[136] J. Yang, Z. Sun, and Y. Chen, "Fault detection using the clustering-kNN rule for gas sensor arrays," *Sensors*, vol. 16, no. 12, pp. 1–21, 2016.

[137] F. Rabeb, "Enhancing WO_3 gas sensor selectivity using a set of pollutant detection classifiers," *Sensor Review*, vol. 38, no. 1, pp. 65–73, 2018.

[138] O. Tomic, T. Eklöv, K. Kvaal, and J.-E. Haugen, "Recalibration of a gas-sensor array system related to sensor replacement," *Analytica Chimica Acta*, vol. 512, no. 2, pp. 199–206, 2004.

[139] S. Marco, A. Ortega, A. Pardo, and J. Samitier, "Gas identification with tin oxide sensor array and self-organizing maps: adaptive correction of sensor drifts," *IEEE Transactions on Instrumentation and Measurement*, vol. 47, no. 1, pp. 316–321, 1998.

[140] A. B. Far, F. Flitti, B. Guo, and A. Bermak, "A bio-inspired pattern recognition system for tin-oxide gas sensor applications," *IEEE Sensors Journal*, vol. 9, no. 6, pp. 713–722, 2009.

[141] U. Siripatrawan, "Self-organizing algorithm for classification of packaged fresh vegetable potentially contaminated with foodborne pathogens," *Sensors and Actuators B: Chemical*, vol. 128, no. 2, pp. 435–441, 2008.

[142] A. Ortega, S. Marco, A. Perera, T. Šundic, A. Pardo, and J. Samitier, "An intelligent detector based on temperature modulation of a gas sensor with a digital signal processor," *Sensors and Actuators B: Chemical*, vol. 78, no. 1, pp. 32–39, 2001.

[143] H. Men, X. Li, J. Wang, and J. Gao, "Applies of neural networks to identify gases based on electronic nose," in *2007 IEEE International Conference on Control and Automation*. Guangzhou, China: IEEE, May 2007, pp. 2699–2704.

[144] M. Xiaomin, "Recognition of toxic gases emission in power plant based on artificial neural network," *Energy Procedia*, vol. 17, no. B, pp. 1578–1584, 2012.

[145] G. Wei, G. Li, J. Zhao, and A. He, "Development of a LeNet-5 gas identification CNN structure for electronic noses," *Sensors*, vol. 19, no. 1, pp. 217–233, 2019.

[146] S. Lekha and M. S., "Real-time non-invasive detection and classification of diabetes using modified convolution neural network," *IEEE Journal of Biomedical and Health Informatics*, vol. 22, no. 5, pp. 1630–1636, 2018.

[147] P. Qi, Q. Meng, and M. Zeng, "A CNN-based simplified data processing method for electronic noses," in *2017 ISOCS/IEEE International Symposium on Olfaction and Electronic Nose (ISOEN)*. Montreal, QC, Canada: IEEE, May 2017, pp. 1–3.

[148] P. Peng, X. Zhao, X. Pan, and W. Ye, "Gas classification using deep convolutional neural networks," *Sensors*, vol. 18, no. 1, pp. 157–167, 2018.

[149] W. Zhu, Y. Ma, Y. Zhou, M. Benton, and J. Romagnoli, "Deep learning based soft sensor and its application on a pyrolysis reactor for compositions predictions of gas phase components," *Computer Aided Chemical Engineering*, vol. 44, no. 1, pp. 2245–2250, 2018.

[150] B. Navaneeth and M. Suchetha, "PSO optimized 1-D CNN-SVM architecture for real-time detection and classification applications," *Computers in Biology and Medicine*, vol. 108, no. 1, pp. 85–92, 2019.

[151] C. Bilgera, A. Yamamoto, M. Sawano, H. Matsukura, and H. Ishida, "Application of convolutional long short-term memory neural networks to signals collected from a sensor network for autonomous gas source localization in outdoor environments," *Sensors*, vol. 18, no. 4484, pp. 1–12, 2018.

Chapter 3

Design and Fabrication of Micro-hotplate Based CMOS Devices

3.1 Introduction

Two types of devices are discussed in this thesis, infra-red emitters and metal oxide semiconductors. Both types are based on micro hotplate structures. A hotplate, as the name suggests, converts electric energy into thermal energy, and it is an important component in micro sensors. The development of microelectromechanical systems (MEMS) allows for the miniaturisation of hotplates. This can greatly reduce the power consumption and thermal mass, hence have a faster response time and a higher temperature with the same or lower power consumption. Despite the advantages of micro hotplates, the structure design and the fabrication process are important to achieve the thermal uniformity and performance optimisation for their versatile applications. To choose an appropriate design, various parameters need to be considered. Spruit *et al.* [1] conducted a detailed review of the optimisation of micro hotplate designs. He suggested a suitable design flow chart based on a target application. The steps consist of requirements and restrictions, performance parameters, available materials and fabrication processes, design guideline and application restrictions, refinement from state-of-the-art and finally the desired micro hotplate. In this chapter, the application of the micro hotplate based device is either as an

infra-red source or a gas sensor. Therefore, the scope of the study will be limited to these two areas only, with different micro hotplate designs explored and described. The fabrication process, which has advanced notably in the past decade, is also included. Complementary metal oxide semiconductor (CMOS) process is preferred as it can be produced in bulk with high repeatability. Detailed process steps will be provided later in this chapter.

The purpose of a micro hotplate is to elevate the operating temperature which then activates the sensing mechanism of the device. Because it often operates in a high temperature condition (250 – 700°C), there are a few key concerns when designing a suitable micro hotplate:

- the response and recovery speed of the micro hotplate,
- thermal distribution over the micro hotplate and the sensing area,
- structural integrity, such as the material thermal expansion/deflection due to the operating temperature,
- thermal isolation of the micro hotplate to minimise the power consumption (low thermal loss), and
- suitability for mass production with high reproducibility, especially when used in commercial settings, and high stability.

To address those concerns, a literature review is conducted with regards to different structure designs, hotplate materials and fabrication processes.

3.2 Micro-hotplate design

A micro hotplate design generally consists of a membrane (isolation layer) on top of a substrate. There are two popular designs in literature: closed type and suspended type. The closed type membrane commonly employs a multi-stack structure with a back-etch step to remove unwanted silicon. It can provide better heat dissipation and mechanical support, but it will also consume more power. The suspended type structure, on the other hand, uses cantilever beams or bridges to support and suspend the heater over a cavity. The beams or bridges can be processed from the front side. It has a smaller thermal mass, hence lower power consumption,

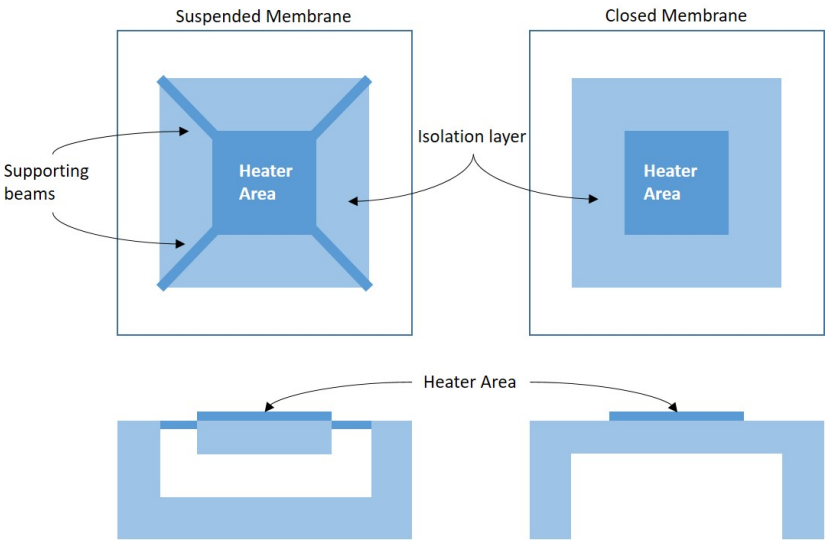

Figure 3.1: Example schematic for suspended (right) and closed (right) membrane, both top views (top) and side views (bottom).

and also has better thermal isolation. Figure. 3.1 shows the front and side views of a closed and suspended membrane design. Both designs can be micromachined and have been studied extensively in literature. Furthermore, the materials properties, heater geometry patterns and the membrane-to-heater ratio will be discussed in this section.

3.2.1 Closed Type Membrane

The closed membrane design has the hotplate structure embedded with electrodes either vertically or horizontally placed relative to the hotplate [2]. Horizontal displacement is when the heater and electrodes are on the same layer, and vertical displacement indicates difference layers (i.e. on top of the heater). Roy *et al.* described both types in his work, and suggested that the electrodes could also use catalytic metals to improve gas interaction kinetics, thus enhance the sensitivity and response time [3, 4]. This membrane is commonly formed through a post-CMOS back etching process. It has good mechanical support for further processing steps, such as micromachining and sensing material deposition. Residual stress occurs with the mechanical fabrication process as well as the thermal mismatch. For thermal stress that is caused by thermal expansion, the structure may deform or deflect at higher operating temperatures [5]. An example of mechanical and thermal stress distribution is provided by Spruit *et al.* [1] as shown in Figure. 3.2. The mechanical

stress is evenly distributed and the thermal stress is concentrated at the centre. But residual stress can be worse than thermal deflection.

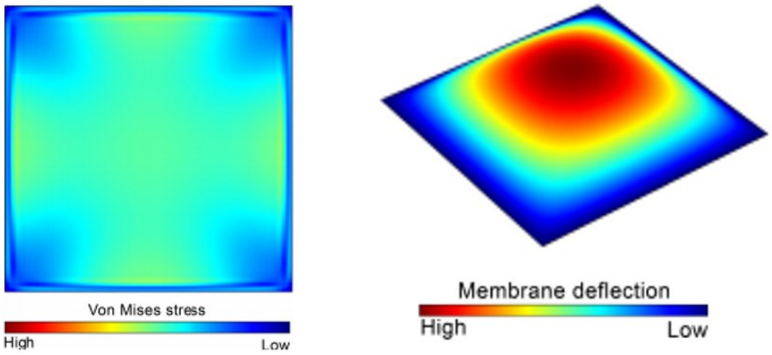

(a) Mechnical stress distribution.

(b) Thermal stress distribution ($<$ 1 μm).

Figure 3.2: Typical mechanical and thermal stress distribution of a closed type membrane (adapted from [1]).

3.2.2 Suspended Type Membrane

The suspended type membrane, also known as the spider type structure, has bridges supporting the heater area. The beams or bridges are usually formed through a front etching process. Compare to the closed membrane design, it has a smaller thermal mass and better thermal isolation as the heat conduction occurs on the beams only. There are usually two or four supporting beams which need to withstand most of the stress. Depending on the width and thickness of the beams,

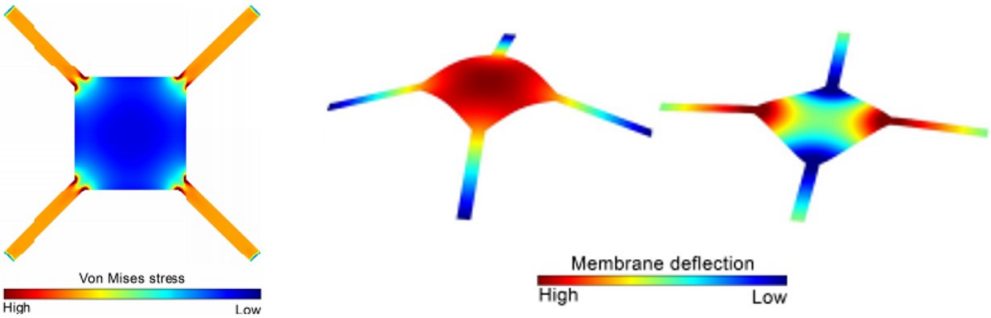

(a) Mechnical stress distribution.

(b) Thermal stress distribution.

Figure 3.3: Typical mechanical and thermal stress distribution of a suspended type membrane (adapted from [1]).

some of them can even be too fragile for sensing material deposition. Similar mechanical and thermal stress distribution was provided by Spruit *et al.* [1] and shown in Figure 3.3. Under high temperature conditions, the heater area either concaves or convexs which also puts stress on the supporting beams. When the heater is convexed with temperature, the beams suffer from high junction temperature, which can lead to temperature changes, drifts or change of resistances. One important factor is the material thermal expansion coefficient. A larger thermal expansion coefficient will lead to higher stress developed with rising temperatures. Different layer compositions also need to be considered in the stacked layer design, as a larger deviation in the material properties (mismatched thermal expansion coefficient [6]) will cause or accelerate deflections. The design often leads to favouring either convex or concave configurations. The material properties will be discussed further in the next section.

3.2.3 Material Properties

In order to have a CMOS design, the material choices are limited. For instance, gold (Au) has been mentioned in literature [7, 8] as the heater and electrodes material, but it is not a standard CMOS metal material. Another example is platinum (Pt) which compensates the problems of gold, such as low resistivity and poor adhesion [7]. However, it is not commonly used in CMOS metallisation process, thus not ideal for low-cost, high reproducibility micro hotplates. There have been many studies using platinum only or platinum mixture as the hotplate material. For example, Liu *et al.* [9] proposed a suspended SiO_2 membrane with platinum heater which can operate up to 430 °C with only 40 mW power consumption. Similar examples can be found in papers such as [10], [11], [12], and [13] with a single compound membranes (Si_3N_4, SiO_2) or a stacked membrane and a platinum heater. There are also studies on platinum mixtures such as platinum silicide (PtSi) [14] or Pt/Ti thin film [6]. However, due to the fabrication limitation, these materials will not be considered. CMOS conductive materials, such as polysilicon, aluminium and tungsten are preferred. In additional to heater materials, different membrane materials are also investigated to ensure easy accessibility and fabrication compatibility.

The desirable properties for an appropriate heating material including high electrical resistivity, high thermal conductivity, low thermal expansion coefficient, high melting point, low Poisson's ratio, large Young's modulus and compatibility to the required fabrication technology [15]. These requirements aim to select a

material that can heat up quickly and uniformly with minimum stress influences at a high temperature (> 100 °C). Popular materials mentioned in literature, apart from platinum and gold, including aluminium [16], nickel [17], nickel alloys [18, 19, 4], polysilicon [20, 21, 22], titanium nitride [23, 24], tungsten [25, 26, 27] and molybdenum [28, 29]. The material information for all the above properties is listed in Table. 3.1.

For CMOS materials, aluminium is one of the most popular metallisation materials, but it has disadvantages such as low resistivity and easy oxidation. Polysilicon (without doping) also has a relatively low electric resistivity to use as a micro hotplate, although it has a low thermal expansion coefficient. For materials with high melting points, such as titanium nitride, tungsten and molybdenum, tungsten has the lowest thermal expansion coefficient and the lowest Poisson's ratio, which suggests minimum stress deflection and thermal drift in high temperature operations.

Electrodes are used to power the heater and provide device information. As mentioned with the closed membrane design, it can be either vertically or horizontally placed. The vertical placement allows more freedom, especially with the integration of a thermometer, while the horizontal placement can save processing steps. The choice of materials can either be the same or different as the heater. With CMOS process, the same material is preferred to reduce manufacturing complexity, in particular with the same layer arrangement. However, the electrodes can be plated with materials such as gold or platinum as an additional post CMOS fabrication step [30].

The membrane is used for thermal isolation. It holds the heater, electrodes, and a thermometer in place. A commonly used material for such purpose in CMOS fabrication is silicon nitride or silicon dioxide. In an SOI wafer, the membrane is formed with an additional buried oxide layer as the etching stop. This wafer provides distinctive advantages such as improved temperature uniformity along the membrane from the thin silicon-on-isolator layer, and utilisation of an integrated readout circuitry [2]. Other materials, such as bulk silicon [31], silicon carbide [32], porous silicon [33] and non-silicon ceramic [34] have also been mentioned in various studies. Their properties, especially thermal conductivities and thermal expansion coefficients, are listed in Table. 3.2.

Table 3.1: Heater material properties [2].

Materials	**Electric Resistivity at Room Temperature** ($\Omega m \times 10^{-10}$)	**Thermal Conductivity at 300K** ($Wm^{-1}K^{-1}$)	**Thermal Expansion Coefficient** ($10^{-6}m.m^{-1}K^{-1}$)	**Melting Point** (°C)	**Poisson's Ratio**	**Young's Modulus (GPa)**
Au	221.4	318	14.2	1064	0.44	79
Ti	4200	21.9	8.6	1668	0.32	116
Pt	1050	71.6	8.8	1768	0.38	168
Al	282	237	23.1	660	0.334	70
Ta	1300	57	6.3	3017	0.34	186
Cr	1250	93.9	4.9	1907	0.21	279
Ni	693	90.9	13.4	1455	0.31	200
Ni Alloy (DilverP1)	4900	17.5	4–5.2	1450	0.30	207
Polysilicon	322	16–34	2.8	1412	0.22	169
TiN	2000	19.2	9.35	2930	—	79–250
W	528	173	4.5	3422	0.28	411
Mo	534	138	4.8	2623	0.307	329

Table 3.2: Membrane material properties.

Materials	**Thermal Conductivity in Room Temperature** ($Wm^{-1}K^{-1}$)	**Thermal Expansion Coefficient** ($10^{-6}m.m^{-1}K^{-1}$)	**Ref.**
Silicon Oxide	1.1–1.4	5.6	[35]
Silicon Nitride	10–43	1.4–3.7	[36], [37]
Silicon	1.3	2.6	[38]
Silicon Carbide	5	4.0	[39], [40]
Porous Silicon	1.2	–	[33]
Non-silicon Ceramic	2.5	10.3	[34]

Overall, the material selection for a micro hotplate design is based on the application requirement, such as operating temperatures, the size of the active area, fabrication conditions, etc. The above material properties provide general guidelines in choosing and designing a suitable micro hotplate.

3.2.4 Heater Patterns

Apart from the material properties, the heater geometry is another important factor that will affect the stress distribution and heater performance. Carefully designed heater patterns can not only provide uniform thermal distributions but also support the structural integrities. For a plane heating area (e.g. Fig. 3.2b), the centre part always has the highest temperature and gradually gets cooler towards the edges. This design will limit the active area, provide an uneven temperature

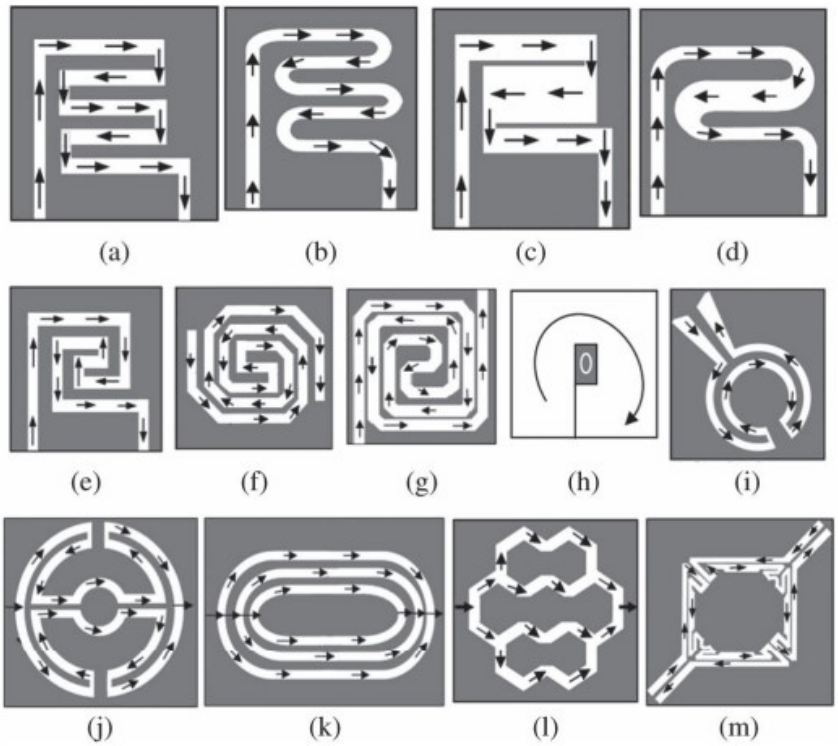

Figure 3.4: Example heater geometries: (a, b) square meander, (c, d) S-shape, (e, f, g) double spiral, (h) plane plate with hole, (i, j) circular rings, (k) elliptical rings, (l) honeycomb shape and (m) irregular shape (arrows do not represent absolute current, merely indications for current flow. Figure is reproduced from: [2]).

(a) Honeycomb (b) Drive-wheel

Figure 3.5: Two micro hotplate designs.

distribution and possibly waste the supply power. Therefore, a better design will incorporate various meander structures that can heat the entire active area to the desired temperature and minimise the central hot spot.

In a review conducted by Bhattacharyya [2], he broadly divided the design geometries into five categories: (1) square, (2) rectangular, (3) circular, (4) irregular shape and (5) 3D structures. Some example structures of each type are presented in Figure. 3.4. Instead of increasing the thermal conductivity of the entire membrane which could lead to an increase in the thermal loss, optimising the heater structure can only increase the conductivity of the selected part (i.e. the active area) hence locally improve the temperature uniformity [41]. The heater tracks and corners can be adjusted to improve the overall performance. Different track widths and lengths can be used. Mele *et al.* [42] reported an improved double spiral design with a thicker track width at the centre and thinner towards the edge. By doing so, the thermal uniformity was greatly increased from previous 13% temperature variation (constant track thickness) to 3% with the improved design. The heater corner can also be modified. Instead of the sharp turning point, a rounded/smooth corner can increase the electron mobility which is somewhat obstructed [43], and at the same time, reduce current crowding. Lee *et al.* [44] studied four heater designs to reduce central hot spot and improve thermal uniformity, namely, square meander, elliptical rings, honeycomb (vary lengths) and drive-wheel, as shown in Figure. 3.5. Those four designs were investigated with thermal images and the drive-wheel design had the best temperature homogeneity and no visible hot spot. The drive-wheel design has circular tracks with the distance increases at the centre. In addition, the centre of the design is unheated to eliminate the central hot spot and achieve uniform distribution through the outer tracks.

The heater pattern also determines the number of supporting beams or

bridges required. The most used number is 2 beams or 4 beams. Two-beam designs have less heat dissipation, but may compromise the mechanical integrity. Four-beam designs are more robust in supporting the heater but may need a higher power consumption. The heater used in this work is similar to the drive-wheel design with an empty centre, and two beams for support.

3.2.5 Membrane-to-Heater Ratio

The membrane-to-heater ratio (MHR) is another critical factor in optimising the power consumption and the robustness of the device. Sureshkannan *et al.* [45] reported an numerical relationship between the estimated power consumption (P_e, unit: mW) and MHR as :

$$P_e = l \times (65.6 - 22.5 \times \ln(\text{MHR})) \tag{3.1}$$

where l is the length of the device in mm. Therefore, the bigger the ratio the smaller the power consumption. A bigger membrane and a smaller heating area can also provide better thermal isolation, hence a better thermal efficiency. This approach was applied in various micro hotplate studies [31, 44, 46, 47]. Saxena *et al.* [48] studied in details the effect of MHR based on the simulations of one heater design. It was found that the thermal resistance increased with the increase of MHR, which contributed to the reduced power consumption. The power consumption dropped from 33.23 mW to 18.6 mW with tripled MHR at the operating temperature of 694K. Furthermore, larger MHR values can also increase the thermal uniformity of the device and reduce the temperature difference between the central area and the outer edges. The downsides, however, are the increase in the displacement and response time. In another study reported by Chiou *et al.*, the power consumption varied very little when the increase in the MHR was small (i.e. from 2.5 to 3). Therefore, it can be concluded that the benefit of low power consumption can only be observed when the MHR value is significantly bigger. This can help in design trade-offs when the improvement in the power consumption is not worth the structural deformation and slow response time.

3.3 Fabrication Process

3.3.1 Substrate Preparation

The fabrication of a micro hotplate device starts with a substrate material, such as silicon. Typical material properties of silicon are provided in Table. 3.2, but depends on the processing steps and material purities, its properties may vary. This single-crystalline silicon material can either be grown or using a float zone technique. The most commonly used method is the Czochralski process, where a seed crystal is used to dip into molten silicon and form an mono-crystal silicon ignot that can used the further processing steps. The ignot is then sliced into thin wafers (for instance, 400 μm thickness [15]) and doped either with n-type or p-type impurities to form n-substrates or p-substrates. On top of the silicon, an epitaxial layer can be added using gaseous or liquid precursors. This extra step can provide high quality substrates for many applications such as GaN on Si devices [49], power electronics, etc.

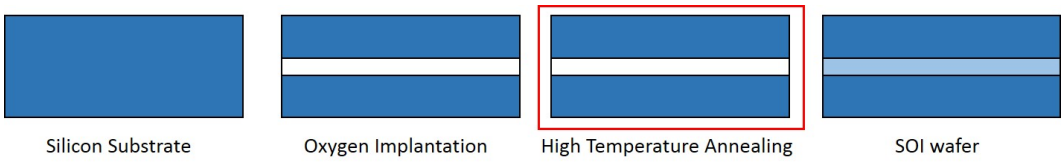

(a) SIMOX method.

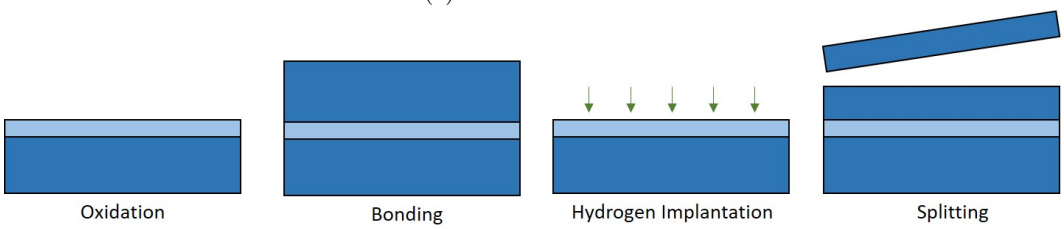

(b) Wafer bonding method.

Figure 3.6: Two SOI wafer fabrication methods.

For an SOI wafer, a silicon oxide layer is grown on top of the substrate. Oxygen is implanted into the silicon substrate which is then annealed at a high temperature to allow oxygen ions to interact with the silicon, thus forms a SiO_2 layer [50]. This process is achieved through ion-implantation at the temperature ranging from 700 °C to 1100 °C [51]. This method is known as separation by implantation of oxygen (SIMOX). Another method to form the SOI wafer is the wafer bonding technique that directly bonds the silicon oxide to the second substrate.

One example is the Smart Cut technique which uses hydrogen implantation and cuts away the implantation wafer [52]. Figure. 3.6 shows the processing steps of these two methods. The buried layer can act as an etching stop and the top doped silicon layer can be used as the heater material. The top silicon layer can have a thickness around 0.4 μm [53].

3.3.2 Dielectric Layer

The dielectric layer provides the electric isolation for the circuit or components on the same chip. In the CMOS process, it is made either using silicon oxide or silicon nitride through thermal oxidation or deposition process. The thermal oxidation is realised with an oxidizing agent (i.e. oxygen for dry oxidation and water for wet oxidation) at a high temperature over 800 °C. For instance, Prasad *et al.* [57] grew a 0.6 μm layer of SiO_2 through thermal oxidation at 1050 °C for 90 mins with constant O_2 flow. It also can be grown through plasmon-enhanced chemical vapour

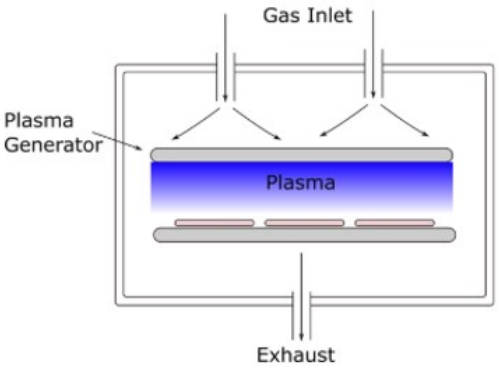

(a) PECVD [54].

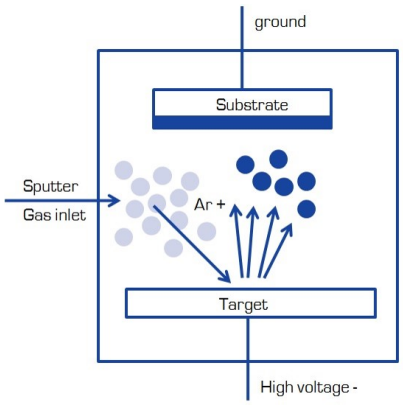

(b) Sputtering Method [55].

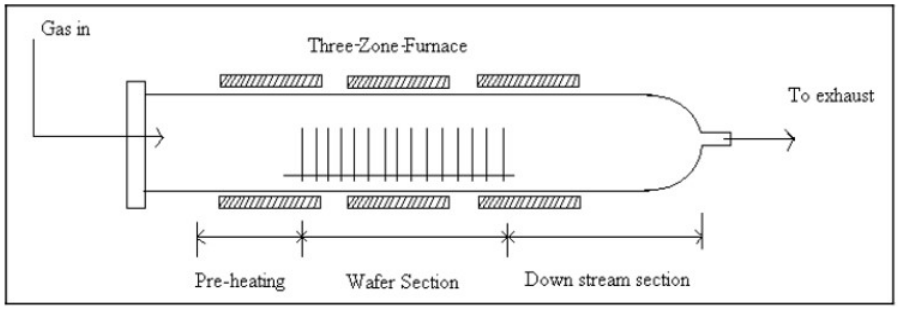

(c) LPCVD Chamber [56].

Figure 3.7: Popular deposition methods (reproduced from sources as stated).

deposition (PECVD) as mentioned in [58]. Chemical vapour deposition (CVD) uses gas vapour to form a thin film uniformly on top of a solid substrate. PECVD uses plasma generated from powering the electrodes with RF power to enhance the chemical reaction rate of the precursors [59]. The common precursors are organosilanes which are monomeric silicon-based materials [60], such as silane (SiH_4) [58], tetraethoxysilane (TEOS) [61] and tetramethoxysilane (TMOS) [62]. Similarly, the silicon nitride (Si_3N_4) layer can also be deposited through CVD. Though CVD is often conducted under atmosphere pressure, low-pressure CVD (LPCVD) is another popular way to grow low-stress silicon nitride [63]. Compare to the standard atmospheric pressure at $\sim$ 101,000 Pa, LPCVD is performed at 10–1000 Pa [64]. Another deposition technique used for silicon nitride is the sputtering deposition, which is a physical vapour deposition (PVD) method. The sputtering technique uses positive ions to bombard the cathode, which then coats the surface [51]. These three methods are illustrated in Figure. 3.7. The same process can be applied to the passivation layer, which is the last layer that protects the device. A common material is silicon nitride which is relatively chemically inert.

3.3.3 Metal Layer

The micro heater is formed using the metal materials mentioned previously, such as tungsten and aluminium. The material is deposited through either a CVD or a PVD method and then etched using photolithography to form the desired pattern. Photolithography is a process that transfers an image from a photomask to a wafer [51]. The photomask consists of the pattern that can either be negative, where the pattern does not exist, or positive, where the pattern exists. The photomask is constructed with chrome covered quartz glass [65]. The wafer with the metal layer is first coated with a photoresist material. It is a light sensitive polymer that either hardens (negative photoresist) or becomes soluble (positive photoresist) when in contact with ultraviolet light. Such materials include DNQ-Novolac photoresist (positive) and epoxy based polymer (negative) [66, 67]. After UV exposure, the photoresist is removed with solvents and the metal layer is etched to only leave the protected pattern structure. For instance, aluminium can be etched by solutions such as hydrochloric acid (HCl) or potassium hydroxide (KOH). The last step is to remove the photoresist protection layer and reveal only the metal layer. This process is shown in Figure. 3.8.

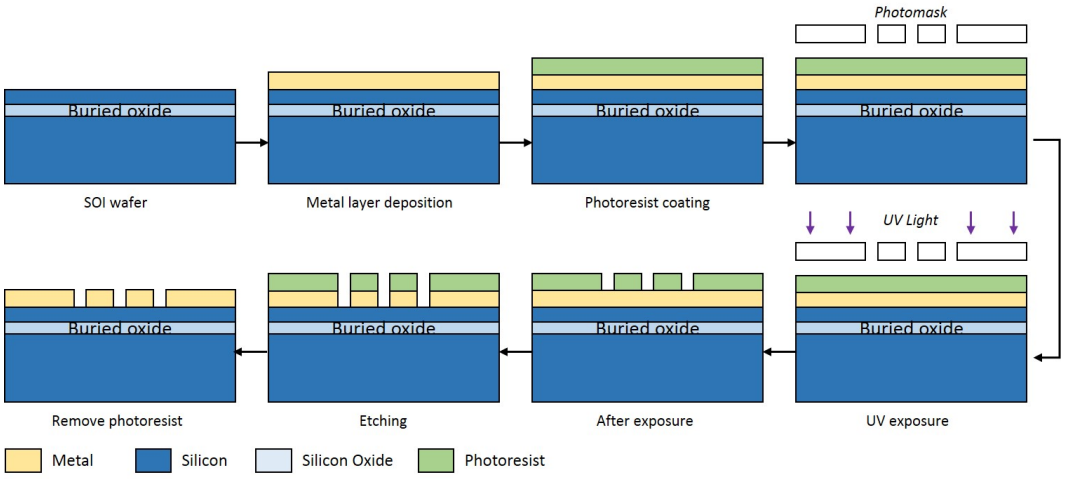

Figure 3.8: Process of photolithography to form the heater pattern.

3.3.4 Etching Process

The post-CMOS etching process is used to form the membrane structure. It can be conducted either from the front or the back. A mask is used similarly to the photolithography process to protect the structure, and the open area is then etched. The etching process has three parameters: etch rate, etch geometry and etch selectivity [68]. The etch rate is in unit μm/min which is in the perpendicular direction. It is also dependent on the etch geometry at different orientations. The etch selectivity is the ratio of the etch rate to the etching mask. Two types of etching processes are described here, wet etching and dry etching.

Wet etching uses an etchant solution to remove unwanted materials. Solutions such as KOH [69], ethylene di-amine pyro-catechol (EDP) [70] and tetra-methyl ammonium hydroxide (TMAH) [71] are suitable to etch silicon based substrate. Figure. 3.9 shows a wet etching process when the wafer is dipped into a solution container. The chemical reaction will dissolve the un-masked substrate. Dutta *et al.* [72] conducted a study to compare the characteristics of these three etching solutions at different concentrations and temperatures. It was concluded that the maximum etching rate was achieved at 15.06 μm/min with 20wt% KOH (typically 30wt%); the etching rate increases with the increase of TMAH concentration ($<$ 25wt%) and the decrease of EDP concentration ($>$ 71wt%). At an elevated temperature, i.e. 120 °C for KOH, a smoother surface could be realised. Similar results can also be achieved with two steps etching: KOH first and EDP second. Wet etching is relatively low cost and simple, but it has disadvantages such as poor resolution [2]. Therefore, for

the modern fabrication technology, a dry etching technique is preferred.

Dry etching technique uses chemical vapour, plasma or ion bombardment. It can provide finer patterns and better results, especially when vertical sidewalls are required. Plasma etching involves a gas source and an RF power source. Plasma is induced from the RF magnetic field, thus activates the gas molecules to react with the substrate. Different gases are used for different materials. A commonly used gas source is a mixture containing tetrafluoromethane (CF_4), which can be used to etch materials such as silicon and tungsten [68]. For the ion etching process, two popular ways are reactive ion etching (RIE) and deep reactive ion etching (DRIE). Unlike plasma etching, which is predominately isotropic, both RIE and DRIE are anisotropic processes [50]. Isotropic etching suggests the same etching rate in all directions while anisotropic etching is orientation dependent. Figure. 3.10 shows the difference between these two processes. In the RIE process, the wafer is placed on the cathode and ions are accelerated towards it. It typically has a higher etching rate than plasma, and due to the nature of the electromagnetic field, the etching can be perpendicular. Deep RIE is an extension of the RIE process. DRIE uses passivation and etching cycles (Bosch process) to achieve sidewall passivation and

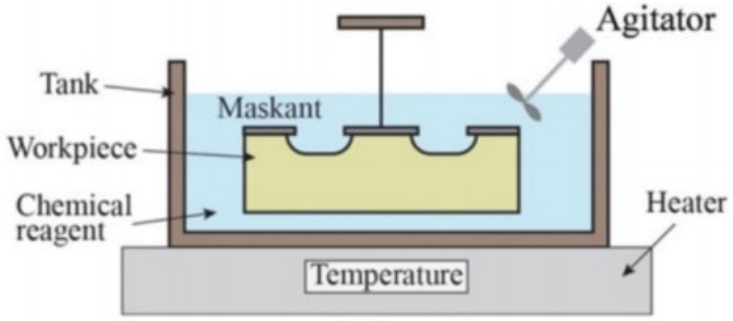

Figure 3.9: A wet etching process (reproduced from [68]).

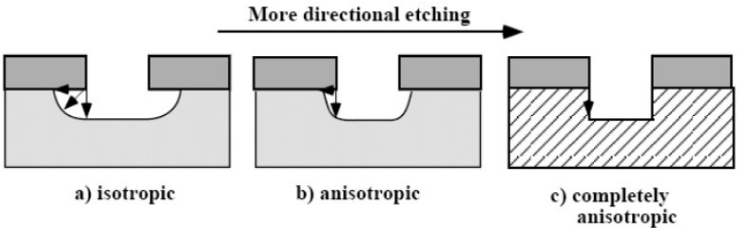

Figure 3.10: Isotropic etching versus anisotropic etching(reproduced from [73]).

clear trench bottom with high mask selectivity, or cooling the wafer (Cyro-DRIE) to improve anisotropy [74]. Both RIE and DRIE use fluorine-based chemical vapours.

The micro hotplate used in this work is based on a back-etch membrane. In order to achieve a near perpendicular sidewall, DRIE is used. Therefore, the final micro hotplate design is presented in Figure. 3.11.

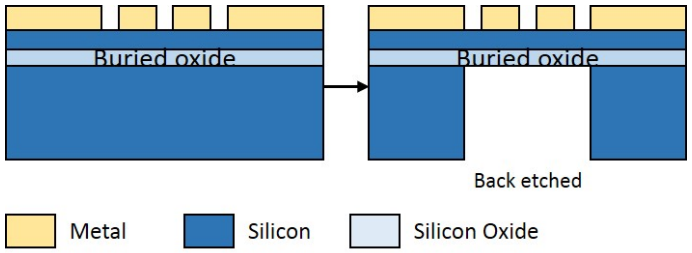

Figure 3.11: The micro hotplate design with back etched membrane.

3.4 Micro-hotplate in Gas Sensor Applications

Micro hotplates are used in many applications, such as chemical sensors [75], thermal actuators [76], nanoreactors [77], micro-fluidics [78], space applications [79], *it situ* studies [1], and etc. This work only focuses on its application in the gas sensing area, especially as infrared emitter sources and metal oxide based sensors.

3.4.1 Infrared Source

Infrared has a growing need especially in the infrared sensing and spectroscopy applications. Therefore, an infrared source as a key component in a spectroscopic measurement requires an intense and stable emission with high reliability. Instead of the conventional filament bulb, a micro hotplate provides better performance in terms of power consumption, noise reduction, miniaturisation, and tunable designs. Different micro hotplate designs and materials were explored to increase the operating temperature and emissivity of the device. For instance, Hildenbrand *et al.* [80] presented different suspension structures with a platinum and ceramic coating for an enhanced emission at wavelengths above 5 μm. Platinum, as mentioned earlier in the material section, has a high melting point, which allows a high operating temperature over 650 °C [81, 14]. For CMOS materials, tungsten can be used as the IR micro hotplate metal, which is reliable at a temperature of 600

°C [27]. The power consumption for such device is usually in milliwatts with miniaturised devices below 100 mW, such as 44mW in [81], 70mW in [27] and 90mW in [82].

The emissivity for a micro hotplate based infrared source is generally broadband, i.e. varied emissions over a range of wavelengths. The range of interest is the mid-infrared range, from 2.5 μm to 25 μm. But the enhancement in the emissivity is typically located within a smaller range. Ali *et al.* [27] designed a CMOS micro hotplate infrared emitter which had a close to black body emission at wavelengths over 8.5 μm. This can be improved with additional coatings on top of the micro hotplate, such as carbon nanotubes (CNT) or nanostructures. De Luca *et al.* [83] reported an increase of 130% in emission radiation at wavelengths below 8 μm with additional CNT coatings. Similarly, Muller *et al.* presented a micro hotplate with non-periodic microstructures that can greatly enhance the emissivity in the near to mid-infrared range ($0.8 \sim 2.5$ μm) to 97% [84]. More recently, with the development of metamaterials, plasmonic structures have received great interest with their capabilities in tuning emission wavelengths, thus realise a narrow band infrared source. This will be discussed further in the next two chapters where a plasmonic structure is employed. The background knowledge of the plasmonic technology and its application in sensing are presented in Chapter 2.

3.4.2 Metal Oxide Semiconductors

Metal oxide (MOX) gas sensor is one of the most studied micro hotplate applications. The sensor is micro hotplate based with metal oxide deposited on top. The sensing mechanism is trapping electrons with adsorbed molecules and depletion induced by those charged electrons, hence a change in the conductivity [85]. The oxygen species, such as O_2^- and O^{-2}, can tie up electronic carriers and lead to a gas sensitive depleted surface [15]. The depletion decreases when the chemisorbed oxygen is removed from the surface and increases with oxidizing. In other words, gas molecules interact with the surface oxide either as donors or acceptors. Two types of materials are used on the surface, namely, n-type and p-type. N-type materials (donor) can give away free electrons to the gas molecules (acceptor), while p-type materials (acceptor) require more electrons from the gas molecules (donor). Because of that, the conductivity increases with n-type materials (a decrease in the resistance) and decreases with p-type (an increase in the resistance). The chemical

reaction equation of this process can be expressed for n-type as:

$$\frac{1}{2}mO_2 + \{\text{vacancy}\} + e^- \overset{k_1}{\longleftrightarrow} \{O_m^-\} \tag{3.2}$$

and

$$X + \{O_m^-\} \xrightarrow{k_2} \{XO_m\} + e^- \tag{3.3}$$

when the molecule X reacts with the chemisorbed oxygen species [50].

N-type materials are more investigated as compared to p-type materials. One explanation is that the p-type material conduction mainly occurs along the semiconductor shell layer, which limits the gas response. The n-type material, however, can enhance the gas response considerably by reducing the material particle size [86]. Another explanation is that the porous structure on the surface, which can trap gas molecules, is more easily formed with n-type crystals. Popular n-type materials including zinc oxide (ZnO) [87], hematite ($\alpha - Fe_2O_3$) [88], tin oxide (SnO_2), indium oxide (In_2O_3) [89] and tungsten trioxide (WO_3) [90], and p-type materials including copper oxide (CuO) [91], nickel oxide (NiO) [92], chromium oxide (Cr_2O_3) [93] and cobalt oxide (Co_3O_4) [86]. All of them show gas responses with some selectivities. The selectivity in MOX sensors is not as good as the NDIR sensors, but researches show some gases can be distinguished. For instance, WO_3 shows good responses towards NO_2 at ppb levels with low cross-sensitivity to CO, methane, hydrogen and acetone [94], and SnO_2 is sensitive to pollutant gas such as CO, CO_2, NO_x [95], and ammonia [96]. Overall, MOX sensors can respond to multiple gases, therefore, it is difficult to identify the gas type based on just one MOX sensor. In the later chapter, signal processing methods are introduced to compensate for this drawback and classify target gases.

The MOX sensors mentioned in this work are n-type SnO_2 and WO_3, and p-type NiO and CuO. All of them are deposited through a manual drop coating technique. The SnO_2 is doped with 2wt% Palladium and 0.4wt% Platinum, which can enhance the sensor response. The WO_3 has a smaller grain size, thus more reactive and likely to adsorb the ionised oxygen species [94]. Both NiO and CuO are pure without any doping metals.

3.5 Conclusions

This chapter provides a review of the design and fabrication of the micro hotplate devices. The primary concerns in designing a suitable micro hotplate are the stress distribution (both thermal and mechanical), device integrity, thermal isolation, the response and recovery speed, and fabrication processes. These concerns were addressed in this chapter. Two main heater structures were described, closed type and suspended type. A closed membrane provides better structure integrity while a suspended membrane has a smaller thermal mass, hence better thermal isolation. Both can be achieved through a back or front etching process. In addition, various heater and membrane materials were explored. Heater materials such as gold, platinum, nickel, polysilicon, titanium nitride, tungsten and molybdenum were studied. However, due to the preference for using the CMOS process, material choice is limited. For instance, materials such as platinum has high conductivity and melting point, but it is a post-CMOS process. The membrane materials were silicon based such as bulk silicon, silicon oxide and silicon nitride. The materials properties were listed and compared. Furthermore, the heater geometries were investigated as it would also contribute to the device integrity and stress distribution. The meander patterns can be divided into five categories, square, rectangular, circular, irregular shape and 3D structures. Factors such as track width and track gap were also mentioned that could affect the device performance. On top of that, the membrane-to-heater ratio was introduced which was closely linked to the device power consumption and operating speed.

Following the micro hotplate design, the fabrication processes were described. In the CMOS process, silicon is the starting point. A wafer was prepared either as bulk silicon or with an isolator layer (SOI). Two methods were introduced to prepare the SOI wafer, the SIMOX method and the wafer bonding method. After the wafer preparation, the dielectric layer was deposited or oxidized on the top. Chemical vapour deposition was explained here, in particular the plasma-enhanced (PE) CVD and the low pressure (LP) CVD. This same method could also be used for the next metallisation step that requires photolithography to generate patterned structures. The final step was the post-CMOS etching process, either dry or wet etchings. In wet etchings, chemical solutions such as TMAH and KOH could be used to dissolve the unwanted material. In dry etchings, reactive ion etching was mainly introduced and the enhanced version, deep reactive ion etching as the way to achieve near perpendicular sidewalls.

The last section described the two applications for the micro hotplate devices in this thesis, infrared emitter source and metal oxide gas sensor. Both employed a drive-wheel tungsten heater pattern embedded in a silicon oxide membrane backed etched using DRIE post process. This is the foundation for the following chapters of which the plasmonic structure and signal processing methods are based.

References

[1] R. G. Spruit, J. T. van Omme, M. K. Ghatkesar, and H. H. P. Garza, "A review on development and optimization of microheaters for high-temperature in situ studies," *Journal of Microelectromechanical Systems*, vol. 26, no. 6, pp. 1165–1182, 2017.

[2] P. Bhattacharyya, "Technological journey towards reliable microheater development for MEMS gas sensors: A review," *IEEE Transactions on Device and Materials Reliability*, vol. 14, no. 2, pp. 589–599, 2014.

[3] S. Roy, C. Sarkar, and P. Bhattacharyya, "A highly sensitive methane sensor with nickel alloy microheater on micromachined Si substrate," *Solid-State Electronics*, vol. 76, no. 1, pp. 84–90, 2012.

[4] D. S. Roy, C. Sarkar, and P. Bhattacharyya, "Low temperature fabrication of a highly sensitive methane sensor with embedded co-planar nickel alloy microheater on MEMS platform," *Sensor Letters*, vol. 10, no. 1, pp. 760–769, 2012.

[5] Y. W. Lai, N. Koukourakis, N. C. Gerhardt, M. R. Hofmann, R. Meyer, S. Hamann, M. Ehmann, K. Hackl, E. Darakis, and A. Ludwig, "Integrity of micro-hotplates during high-temperature operation monitored by digital holographic microscopy," *Journal of Microelectromechanical Systems*, vol. 19, no. 5, pp. 1175–1179, 2010.

[6] J. Puigcorb, D. Vogel, B. Michel, A. Vil, I. Gracia, C. Can, and J. R. Morante, "High temperature degradation of Pt/Ti electrodes in micro-hotplate gas sensors," *Journal of Micromechanics and Microengineering*, vol. 13, no. 4, pp. S119–S124, 2003.

[7] K. Zhang, S. Chou, and S. Ang, "Fabrication, modeling and testing of a thin film Au/Ti microheater," *International Journal of Thermal Sciences*, vol. 46, no. 6, pp. 580–588, 2007.

[8] X. Yi, J. Lai, H. Liang, and X. Zhai, "Fabrication of a MEMS micro-hotplate," *Journal of Physics: Conference Series*, vol. 276, no. 12098, pp. 1–10, 2011.

[9] Q. Liu, G. Ding, Y. Wang, and J. Yao, "Thermal performance of micro hotplates with novel shapes based on single-layer SiO_2 suspended film," *Micromachines*, vol. 9, no. 514, pp. 1–12, 2018.

[10] M. Prasad and P. S. Dutta, "Development of micro-hotplate and its reliability for gas sensing applications," *Applied Physics A*, vol. 124, no. 788, pp. 1–11, 2018.

[11] S. Fatemeh, "Implementation of high-performance MEMS platinum micro-hotplate," *Sensor Review*, vol. 35, no. 1, pp. 116–124, 2015.

[12] J. Dennis, A. Ahmed, and N. Mohamad Mohamad, "Design, simulation and modeling of a micromachined high temperature microhotplate for application in trace gas detection," *International Journal of Engineering & Technology*, vol. 10, no. 2, pp. 67–74, 2010.

[13] L. Xu, T. Li, and Y. Wang, "A novel three-dimensional microheater," *IEEE Electron Device Letters*, vol. 32, no. 9, pp. 1284–1286, 2011.

[14] J. Spannhake, O. Schulz, A. Helwig, A. Krenkow, G. Müller, and T. Doll, "High-temperature MEMS heater platforms: long-term performance of metal and semiconductor heater materials," *Sensors*, vol. 6, no. 4, pp. 405–419, 2006.

[15] I. Simon, N. Bârsan, M. Bauer, and U. Weimar, "Micromachined metal oxide gas sensors: opportunities to improve sensor performance," *Sensors and Actuators B: Chemical*, vol. 73, no. 1, pp. 1–26, 2001.

[16] G. Yan, Z. Tang, P. C. Chan, J. K. Sin, I.-M. Hsing, and Y. Wang, "An experimental study on high-temperature metallization for micro-hotplate-based integrated gas sensors," *Sensors and Actuators B: Chemical*, vol. 86, no. 1, pp. 1–11, 2002.

[17] P. Bhattacharyya, P. Basu, B. Mondal, and H. Saha, "A low power MEMS gas sensor based on nanocrystalline ZnO thin films for sensing methane," *Microelectronics Reliability*, vol. 48, no. 11-12, pp. 1772–1779, 2008.

[18] B. Kantha and S. Sarkar, "The design of a low power MEMS based micro-hotplate device using a novel nickel alloy for gas sensing applications," *Journal of Nano- and Electronic Physics*, vol. 6, no. 1, pp. 01 004–01 009, 2014.

[19] A. A. Monika, "Design and simulation of MEMS based microhotplates as gas sensor," *International Journal of Advanced Research in Computer Engineering & Technology (IJARCET)*, vol. 2, no. 8, pp. 2487–2492, 2013.

[20] M. Afridi, C. Montgomery, E. Cooper-Balis, S. Semancik, K. G. Kreider, and J. Geist, "Microhotplate temperature sensor calibration and BIST," *Journal of research of the National Institute of Standards and Technology*, vol. 116, no. 6, pp. 827–838, 2011.

[21] A. N. Nordin, I. Voiculescu, and M. Zaghloul, "Micro-hotplate based temperature stabilization system for CMOS SAW resonators," *Microsystem Technologies*, vol. 15, no. 8, pp. 1187–1193, 2009.

[22] J. Puigcorbé, A. Vilà, I. Gràcia, C. Cané, and J. R. Morante, "Dielectric micro-hotplate for integrated sensors: an electro-thermo-mechanical analysis," in *Transducers '01 Eurosensors XV*. Berlin, Heidelberg: Springer, Jun 2001, pp. 312–315.

[23] J. Creemer, D. Briand, H. Zandbergen, W. van der Vlist, C. de Boer, N. de Rooij, and P. Sarro, "Microhotplates with TiN heaters," *Sensors and Actuators A: Physical*, vol. 148, no. 2, pp. 416–421, 2008.

[24] M. R. Venkatesh, S. Sachdeva, B. El Mansouri, J. Wei, A. Bossche, D. Bosma, L. C. P. M. de Smet, E. J. R. Sudhölter, and G. Q. Zhang, "A low-power MEMS IDE capacitor with integrated microhotplate: application as methanol sensor using a metal-organic framework coating as affinity layer," *Sensors*, vol. 19, no. 4, pp. 888–906, 2019.

[25] S. Z. Ali, F. Udrea, W. I. Milne, and J. W. Gardner, "Tungsten-based SOI microhotplates for smart gas sensors," *Journal of Microelectromechanical Systems*, vol. 17, no. 6, pp. 1408–1417, 2008.

[26] S. Z. Ali, A. De Luca, Z. Racz, P. Tremlett, T. Wotherspoon, J. W. Gardner, and F. Udrea, "Low power NDIR CO_2 sensor based on CMOS IR emitter for boiler applications," in *2014 IEEE SENSORS*. Valencia, Spain: IEEE, Nov 2014, pp. 934–937.

[27] S. Z. Ali, A. De Luca, R. Hopper, S. Boual, J. W. Gardner, and F. Udrea, "A low-power, low-cost infra-red emitter in CMOS technology," *IEEE Sensors Journal*, vol. 15, no. 12, pp. 6775 – 6782, 2015.

[28] L. L. R. Rao, M. K. Singha, K. M. Subramaniam, N. Jampana, and S. Asokan, "Molybdenum microheaters for MEMS-based gas sensor applications: Fabrication, electro-thermo-mechanical and response characterization," *IEEE Sensors Journal*, vol. 17, no. 1, pp. 22–29, 2017.

[29] L. Mele, F. Santagata, E. Iervolino, M. Mihailovic, T. Rossi, A. Tran, H. Schellevis, J. Creemer, and P. Sarro, "A molybdenum MEMS microhotplate for high-temperature operation," *Sensors and Actuators A: Physical*, vol. 188, no. 1, pp. 173–180, 2012.

[30] J. W. Gardner, P. K. Guha, F. Udrea, and J. A. Covington, "CMOS interfacing for integrated gas sensors: a review," *IEEE Sensors Journal*, vol. 10, no. 12, pp. 1833–1848, 2010.

[31] T. Iwaki, J. A. Covington, J. W. Gardner, F. Udrea, C. S. Blackman, and I. P. Parkin, "SOI-CMOS based single crystal silicon micro-heaters for gas sensors," in *2006 IEEE SENSORS*. Daegu, South Korea: IEEE, Oct 2006, pp. 460–463.

[32] A. Harley-Trochimczyk, A. Rao, H. Long, A. Zettl, C. Carraro, and R. Maboudian, "Low-power catalytic gas sensing using highly stable silicon carbide microheaters," *Journal of Micromechanics and Microengineering*, vol. 27, no. 4, pp. 45 003–45 012, 2017.

[33] C. Tsamis, A. G. Nassiopoulou, and A. Tserepi, "Thermal properties of suspended porous silicon micro-hotplates for sensor applications," *Sensors and Actuators B: Chemical*, vol. 95, no. 1, pp. 78–82, 2003.

[34] A. A. Vasiliev, A. V. Pisliakov, A. V. Sokolov, N. N. Samotaev, S. A. Soloviev, K. Oblov, V. Guarnieri, L. Lorenzelli, J. Brunelli, A. Maglione, A. S. Lipilin, A. Mozalev, and A. V. Legin, "Non-silicon MEMS platforms for gas sensors," *Sensors and Actuators B: Chemical*, vol. 224, no. 1, pp. 700–713, 2016.

[35] L. Filipovic, "Topography simulation of novel processing techniques," Ph.D. dissertation, Vienna University of Technology, 2012.

[36] AZO Materials, "Silicon nitride (Si_3N_4) properties and applications," 2001. [Online]. Available: https://www.azom.com/properties.aspx?ArticleID=53

[37] Accuratus, "Silicon nitride, Si_3N_4 ceramic properties," 2013. [Online]. Available: https://www.accuratus.com/silinit.html

[38] The Ioffe Physical-Technical Institute of the Russian Academy of Sciences, "Si-silicon thermal properties." [Online]. Available: http://www.ioffe.ru/SVA/NSM/Semicond/Si/thermal.html

[39] R. Maboudian, C. Carraro, D. G. Senesky, and C. S. Roper, "Advances in silicon carbide science and technology at the micro- and nanoscales," *Journal of Vacuum Science & Technology A*, vol. 31, no. 5, pp. 50 805–50 822, 2013.

[40] Accuratus, "Silicon carbide, SiC ceramic properties," 2013. [Online]. Available: https://www.accuratus.com/silicar.html

[41] G. Saxena and R. Paily, "Performance improvement of square microhotplate with insulation layer and heater geometry," *Microsystem Technologies*, vol. 21, no. 11, pp. 2331–2338, 2015.

[42] L. Mele, T. Rossi, M. Riccio, E. Iervolino, F. Santagata, A. Irace, G. Breglio, J. F. Creemer, and P. M. Sarro, "Electro-thermal analysis of MEMS microhotplates for the optimization of temperature uniformity," *Procedia Engineering*, vol. 25, no. 1, pp. 387–390, 2011.

[43] J. Lee and W. P. King, "Microcantilever hotplates: design, fabrication, and characterization," *Sensors and Actuators A: Physical*, vol. 136, no. 1, pp. 291–298, 2007.

[44] S. M. Lee, D. C. Dyer, and J. W. Gardner, "Design and optimisation of a high-temperature silicon micro-hotplate for nanoporous palladium pellistors," *Microelectronics Journal*, vol. 34, no. 2, pp. 115–126, 2003.

[45] G. Sureshkannan and G. Mohan Kumar, "Experimental investigation and 2-D thermal analysis of high temperature microtubular heaters," *European Journal of Scientific Research*, vol. 74, no. 1, pp. 403–411, 2012.

[46] F. Naumann, M. Ebert, J. Hildenbrand, E. Moretton, C. Peter, and J. Wollenstein, "Thermal and mechanical design optimisation of a micro machined mid-infrared emitter for optical gas sensing systems," in *EuroSimE 2009 - 10th International Conference on Thermal, Mechanical and Multi-Physics Simulation and Experiments in Microelectronics and Microsystems*. Delft, Netherlands: IEEE, Apr 2009, pp. 1–5.

[47] J. Courbat, M. D. Canonica, D. Briand, N. F. de Rooij, D. Teyssieux, L. Thiery, and B. Cretin, "Thermal simulation and characterization for the design of ultra-

low power micro-hotplates on flexible substrate," in *2008 IEEE SENSORS*. Lecce, Italy: IEEE, Oct 2008, pp. 74–77.

[48] G. Saxena and R. Paily, "Effect of membrane to heater ratio on the performance of square microhotplate," in *2013 Annual International Conference on Emerging Research Areas and 2013 International Conference on Microelectronics, Communications and Renewable Energy*. Kanjirapally, India: IEEE, Jun 2013, pp. 1–5.

[49] J. Mach, J. Piastek, J. Maniš, V. Čalkovský, T. Šamořil, J. Damková, M. Bartošík, S. Voborný, M. Konečný, and T. Šikola, "Low temperature selective growth of GaN single crystals on pre-patterned Si substrates," *Applied Surface Science*, vol. 497, no. 1, pp. 143 705–12, 2019.

[50] J. W. Gardner, V. K. Varadan, and O. O. Awadelkarim, *Microsensors, MEMS, and smart devices*, 1st ed., ser. Wiley Online Books. Chichester: John Wiley & Sons, Intd, 2001.

[51] P. E. Allen and D. R. Holberg, *CMOS analog Circuit Design*, 3rd ed. New York: Oxford University Press, 2012.

[52] M. Bruel, B. Aspar, and A.-J. Auberton-Hervé, "Smart-cut: a new silicon on insulator material technology based on hydrogen implantation and wafer bonding," *Japanese Journal of Applied Physics*, vol. 36, no. 1-3B, pp. 1636–1641, 1997.

[53] F. Udrea, J. W. Gardner, D. Setiadi, J. A. Covington, T. Dogaru, C. C. Lu, and W. I. Milne, "Design and simulation of SOI CMOS micro-hotplate gas sensors," *Sensors and Actuators B: Chemical*, vol. 78, no. 1, pp. 180–190, 2001.

[54] PV-Manufacturing.org, "PECVD of silicon nitride." [Online]. Available: https://pv-manufacturing.org/pecvd-of-silicon-nitride/

[55] Thin Film Consulting, "Physical vapor deposition: PVD." [Online]. Available: http://www.thfc.de/fundamentals-of-sputtering

[56] N. Chawla, R. Nagarajan, and E. Bhattacharya, "Experimental and theoretical investigation of thermodynamic and transport phenomena in polysilicon and silicon nitride CVD," *ECS Transactions*, vol. 19, no. 23, pp. 53–68, 2009.

[57] M. Prasad, D. S. Arya, and V. K. Khanna, "Fabrication and reliability study of a double spiral platinum-based MEMS hotplate," *Journal of Micro/Nanolithography, MEMS, and MOEMS*, vol. 14, no. 2, pp. 1–9, 2015.

[58] A. Tommasi, M. Cocuzza, D. Perrone, F. C. Pirri, R. Mosca, M. Villani, N. Delmonte, A. Zappettini, D. Calestani, and L. S. Marasso, "Modeling, fabrication and testing of a customizable micromachined hotplate for sensor applications," *Sensors*, vol. 17, no. 62, pp. 1–18, 2017.

[59] D. A. Boyd, L. Greengard, M. Brongersma, M. Y. El-Naggar, and D. G. Goodwin, "Plasmon-assisted chemical vapor deposition," *Nano Letters*, vol. 6, no. 11, pp. 2592–2597, 2006.

[60] M. Dawood, "Durability of steel components strengthened with fiber-reinforced polymer (FRP) composites," *Rehabilitation of Metallic Civil Infrastructure Using Fiber Reinforced Polymer (FRP) Composites*, pp. 96–114, 2014.

[61] C. Martinet, V. Paillard, A. Gagnaire, and J. Joseph, "Deposition of SiO_2 and TiO_2 thin films by plasma enhanced chemical vapor deposition for antireflection coating," *Journal of Non-Crystalline Solids*, vol. 216, no. 1, pp. 77–82, 1997.

[62] K. H. A. Bogart, N. F. Dalleska, G. R. Bogart, and E. R. Fisher, "Plasma enhanced chemical vapor deposition of SiO_2 using novel alkoxysilane precursors," *Journal of Vacuum Science & Technology A*, vol. 13, no. 2, pp. 476–480, 1995.

[63] S. L. Marasso, A. Tommasi, D. Perrone, M. Cocuzza, R. Mosca, M. Villani, A. Zappettini, and D. Calestani, "A new method to integrate ZnO nanotetrapods on MEMS micro-hotplates for large scale gas sensor production," *Nanotechnology*, vol. 27, no. 38, pp. 385 503–385 509, 2016.

[64] R. Curley, T. McCormack, and M. Phipps, "Low-pressure CVD and plasma enhanced CVD," 2011. [Online]. Available: http://classweb.ece.umd.edu/enee416/GroupActivities/LPCVD-PECVD.pdf

[65] N. H. E. Weste and D. M. Harris, *Integrated Circuit Design*, 4th ed. Boston, MA: Pearson Education, Inc., 2011.

[66] D. Roy, P. K. Basu, and S. V. Eswaran, "Photoresists for microlithography," *Resonance*, vol. 7, no. 7, pp. 44–53, 2002.

[67] S. R. Turner and R. C. Daly, "The chemistry of photoresists," in *Photopolymerisation and Photoimaging Science and Technology*, N. S. Allen, Ed. Dordrecht: Springer Netherlands, 1989, pp. 75–113.

[68] H.-P. Phan, D. V. Dao, and N.-T. Nguyen, "Silicon micro-/nanomachining and applications," in *Micro and Nanomanufacturing Volume II*, M. J. Jackson and W. Ahmed, Eds. Cham: Springer International Publishing, 2018, pp. 225–261.

[69] W. Shin, M. Nishibori, L. F. Houlet, T. Itoh, N. Izu, and I. Matsubara, "Fabrication of thermoelectric gas sensors on micro-hotplates," *Sensors and Actuators B: Chemical*, vol. 139, no. 2, pp. 340–345, 2009.

[70] R. E. Cavicchi, J. S. Suehle, K. G. Kreider, B. L. Shomaker, J. A. Small, M. Gaitan, and P. Chaparala, "Growth of SnO_2 films on micromachined hotplates," *Applied Physics Letters*, vol. 66, no. 7, pp. 812–814, 1995.

[71] J. Wang, Z. Tang, J. Li, and F. Zhang, "A micropirani pressure sensor based on the tungsten microhotplate in a standard CMOS process," *IEEE Transactions on Industrial Electronics*, vol. 56, no. 4, pp. 1086–1091, 2009.

[72] S. Dutta, M. Imran, P. Kumar, R. Pal, P. Datta, and R. Chatterjee, "Comparison of etch characteristics of KOH, TMAH and EDP for bulk micromachining of silicon (110)," *Microsystem Technologies*, vol. 17, no. 10, pp. 1621–1628, 2011.

[73] M. Ostling, "Lecture 7: etching," 2013. [Online]. Available: https://www.kth.se/social/upload/510f795cf276544e1ddda13f/Lecture 7 Etching.pdf

[74] F. Laermer, S. Franssila, L. Sainiemi, and K. Kolari, "Chapter 21: deep reactive ion etching," in *Micro and Nano Technologies*. Boston: William Andrew Publishing, 2015, pp. 444–469.

[75] S. Semancik, R. E. Cavicchi, M. C. Wheeler, J. E. Tiffany, G. E. Poirier, R. M. Walton, J. S. Suehle, B. Panchapakesan, and D. L. DeVoe, "Microhotplate platforms for chemical sensor research," *Sensors and Actuators B: Chemical*, vol. 77, no. 1, pp. 579–591, 2001.

[76] D. Briand, S. Colin, A. Gangadharaiah, E. Vela, P. Dubois, L. Thiery, and N. F. de Rooij, "Micro-hotplates on polyimide for sensors and actuators," *Sensors and Actuators A: Physical*, vol. 132, no. 1, pp. 317–324, 2006.

[77] J. F. Creemer, S. Helveg, P. J. Kooyman, A. M. Molenbroek, H. W. Zandbergen, and P. M. Sarro, "A MEMS reactor for atomic-scale microscopy of nanomaterials under industrially relevant conditions," *Journal of Microelectromechanical Systems*, vol. 19, no. 2, pp. 254–264, 2010.

[78] D. N. Pagonis, G. Kaltsas, and A. G. Nassiopoulou, "Fabrication and testing of an integrated thermal flow sensor employing thermal isolation by a porous

silicon membrane over an air cavity," *Journal of Micromechanics and Microengineering*, vol. 14, no. 6, pp. 793–797, 2004.

[79] D. Briand, O. Guenat, B. van der Schoot, T. Hirata, and N. F. de Rooij, "Microhotplate, a useful concept for gas sensing, fluidics and space applications," *Electrochemical Society Proceedings*, vol. 19, no. 1, pp. 151–157, 2000.

[80] J. Hildenbrand, J. Korvink, J. Wollenstein, C. Peter, A. Kurzinger, F. Naumann, M. Ebert, and F. Lamprecht, "Micromachined mid-infrared emitter for fast transient temperature operation for optical gas sensing systems," *Sensors Journal, IEEE*, vol. 10, no. 2, pp. 353–362, 2010.

[81] P. Barritault, M. Brun, S. Gidon, and S. Nicoletti, "Mid-IR source based on a free-standing microhotplate for autonomous CO_2 sensing in indoor applications," *Sensors and Actuators A: Physical*, vol. 172, no. 2, pp. 379–385, 2011.

[82] A. A. Vasiliev, R. G. Pavelko, S. Y. Gogish-Klushin, D. Y. Kharitonov, O. S. Gogish-Klushina, A. V. Sokolov, A. V. Pisliakov, and N. N. Samotaev, "Alumina MEMS platform for impulse semiconductor and IR optic gas sensors," *Sensors and Actuators B: Chemical*, vol. 132, no. 1, pp. 216–223, 2008.

[83] A. De Luca, M. T. Cole, R. H. Hopper, S. Z. Ali, F. Udrea, J. W. Gardner, and W. I. Milne, "SOI CMOS MEMS infra-red thermal source with carbon nanotubes coating," *Procedia Engineering*, vol. 87, no. 1, pp. 839–842, 2014.

[84] L. Müller, I. Käpplinger, S. Biermann, W. Brode, and M. Hoffmann, "Infrared emitting nanostructures for highly efficient microhotplates," *Journal of Micromechanics and Microengineering*, vol. 24, no. 3, pp. 35 014–35 022, 2014.

[85] C. Wang, L. Yin, L. Zhang, D. Xiang, and R. Gao, "Metal oxide gas sensors: Sensitivity and influencing factors," *Sensors*, vol. 10, no. 3, pp. 2088–2106, mar 2010.

[86] B. Zhang, M. Cheng, G. Liu, Y. Gao, L. Zhao, S. Li, Y. Wang, F. Liu, X. Liang, T. Zhang, and G. Lu, "Room temperature NO_2 gas sensor based on porous Co_3O_4 slices/reduced graphene oxide hybrid," *Sensors and Actuators B: Chemical*, vol. 263, no. 1, pp. 387–399, 2018.

[87] N. Hongsith, E. Wongrat, T. Kerdcharoen, and S. Choopun, "Sensor response formula for sensor based on ZnO nanostructures," *Sensors and Actuators B: Chemical*, vol. 144, no. 1, pp. 67–72, 2010.

[88] J. Chen, L. Xu, W. Li, and X. Gou, "α-Fe_2O_3 nanotubes in gas sensor and lithium-ion battery applications," *Advanced Materials*, vol. 17, no. 5, pp. 582–586, 2005.

[89] I. Boehme, S. Herrmann, A. Staerz, H. Brinkmann, U. Weimar, and N. Barsan, "Understanding the sensing mechanism of Rh_2O_3 loaded In_2O_3," *Proceedings of Eurosensors*, vol. 2, no. 13, pp. 754–757, 2018.

[90] A. Staerz, T. Russ, U. Weimar, and N. Barsan, "Understanding the sensing mechanism of WO_3 based gas sensors," in *2019 IEEE International Symposium on Olfaction and Electronic Nose (ISOEN)*. Fukuoka, Japan: IEEE, May 2019, pp. 1–3.

[91] Y. M. Choi, S.-Y. Cho, D. Jang, H.-J. Koh, J. Choi, C.-H. Kim, and H.-T. Jung, "Ultrasensitive detection of VOCs using a high-resolution CuO/Cu_2O/Ag nanopattern sensor," *Advanced Functional Materials*, vol. 29, no. 9, p. 1808319, 2019.

[92] T. P. Mokoena, H. C. Swart, and D. E. Motaung, "A review on recent progress of p-type nickel oxide based gas sensors: Future perspectives," *Journal of Alloys and Compounds*, vol. 805, pp. 267–294, 2019.

[93] B. K. Miremadi, R. C. Singh, Z. Chen, S. Roy Morrison, and K. Colbow, "Chromium oxide gas sensors for the detection of hydrogen, oxygen and nitrogen oxide," *Sensors and Actuators B: Chemical*, vol. 21, no. 1, pp. 1–4, 1994.

[94] B. Urasinska-Wojcik, T. A. Vincent, M. F. Chowdhury, and J. W. Gardner, "Ultrasensitive WO_3 gas sensors for NO_2 detection in air and low oxygen environment," *Sensors and Actuators B: Chemical*, vol. 239, no. 1, pp. 1051–1059, 2017.

[95] B. Yuliarto, G. Gumilar, and N. Septiani, "SnO_2 nanostructure as pollutant gas sensors: Synthesis, sensing performances, and mechanism," *Advances in Materials Science and Engineering*, vol. 2015, no. 12, pp. 1–14, 2015.

[96] M. Shahabuddin, A. Sharma, J. Kumar, M. Tomar, A. Umar, and V. Gupta, "Metal clusters activated SnO_2 thin film for low level detection of NH_3 gas," *Sensors and Actuators B: Chemical*, vol. 194, no. 1, pp. 410–418, 2014.

Chapter 4

Modelling and Simulation of Plasmonic IR Emitter

4.1 Introduction

A NDIR gas sensor, as mentioned previously in Chapter 2, can be greatly improved with the help of plasmonic technology, which can be applied to both emitters and detectors. A miniaturised NDIR emitter based on a micro hotplate was introduced in Chapter 3. Unlike emitters, detectors normally are pyroelectric based. This chapter will limit the scope on the design and simulation of the emitters only. Different designs were explored and suitable structures were modelled and simulated. Software model was built based on the finite element method (FEM) using COMSOL Multiphysics v5.1 to aid this process. Fine tuned structures were used for different gases of interests, and finalised designs were laid out in Tanner EDA L-edit v16 and fabricated in a commercial foundry (XFAB) as a part of the multi-project wafer.

4.1.1 IR spectroscopy

Because molecules absorb infra-red radiation at their specific wavelengths, IR spectroscopy is a common method for chemical analysis (i.e. solid, liquid or gas). There are three regions on the IR spectrum (700 nm–1 mm) [1], near, mid and far, are used for identifying different substances. Near Infra-Red Spectroscopy (NIRS),

ranged from 700 nm to 2.5 μm, is used in pharmaceutical and biomedical applications [2], such as monitoring and diagnosis of brain functions [3, 4], neuroimaging [5, 6], brain computer interfaces for neuro-prosthetics [7], sports medicine [8] and cardiovascular support [9, 10]. Far Infra-Red (FIR), in the region from 25 μm to 1 mm, can be found in applications like therapeutic intervention with Far Infra-red (FIR) lamp or sauna [11]. It is also used in astronomical community [12, 13]. But most of the research interest in determining organic compound structures is on Mid Infra-Red (MIR) area, which lies from 2.5 μm (4000 cm^{-1}) to 25 μm (400 cm^{-1}). The infra-red spectrum, an example shown in Fig. 4.1, is used to analyse the absorption from molecule vibration as the peak value always correlates to a specific molecular structure. The plot shows the absorption/transmission of the infra-red radiation against the wavelength for ethyl acetate molecules. It is normal for a compound to have more than one absorption peak (as seen in Fig. 4.1), with some weaker and some stronger signals, as it may have several different vibrating motions (i.e.: stretching or bonding [14]). For molecules with multiple frequency peaks, the highest one is often used as a reference. Compounds with similar molecular structures, such as ethyl acetate ($C_4H_8O_2$) and methyl benzoate ($C_8H_8O_2$), both in the ester family, tend to have absorption peaks within the same range that is around 1750 cm^{-1} to 1735 cm^{-1} wavenumbers [15]. Fig. 4.2 is an overview of some typical IR absorption windows for compounds with similar structures.

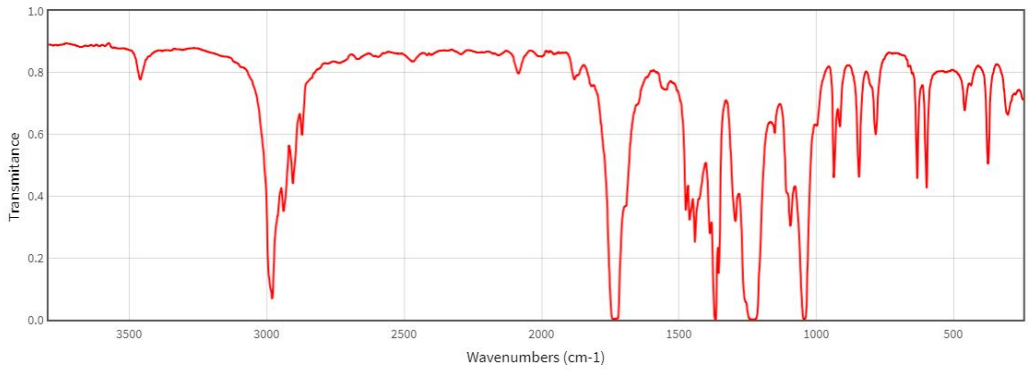

Figure 4.1: Example of an IR absorption spectrum (ethyl ecetate)(reproduced from [16]).

To obtain an IR spectrum for a particular chemical compound, a FTIR spectrometer is often used. The main components including an IR source, a detector and an interferometer. The interferometer is used to split the IR beam into two with different paths, which transmit through mirrors (fixed and moving) and re-combined later to measure intensity differences. This process is shown as a simplified sketch

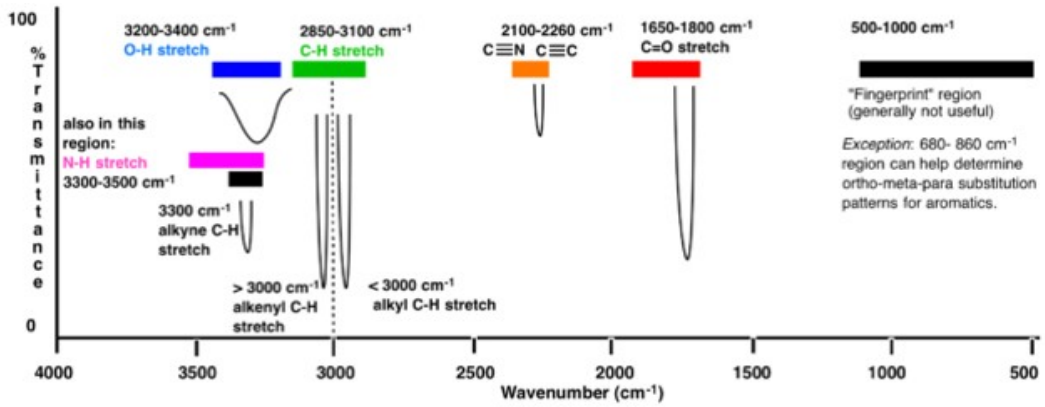

Figure 4.2: Typical IR absorption windows for compounds with similar molecular structures(reproduced from [15]).

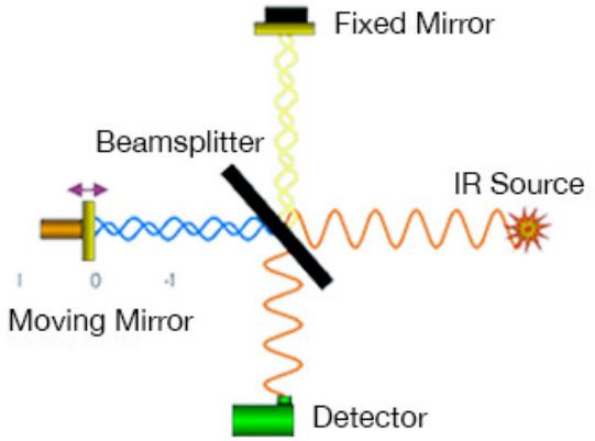

Figure 4.3: Schematic of an optical interferometer for the FTIR spectrometer(adapated from [17]).

in Fig. 4.3. It is able to provide a full spectrum within a short period of time with minimum noise, but it is costly to use outside laboratory condition. In particular with gas measurement, adding gas lines to FTIR spectrometer is complicated and expensive. Therefore, cost-effective and possibly even handheld setup is needed. An appropriate device for such requirement is NDIR gas sensor.

4.1.2 Non-dispersive Infra-red (NDIR) gas sensor

Optical sensors, such as NDIR sensors, generally have advantages of high stability, sensitivity and selectivity [18]. Unlike chemical sensor, it is less likely to

get poisoned or decay over long term. Because it is based on the physical absorption of the infra-red radiation, the sensor response is also a lot faster than chemical sensor. An in-depth sensor technology comparison was described in Chapter 2. A typical NDIR gas sensor contains an emitter and a detector inside a sampling chamber [19, 20], as the assembly shown in Fig. 4.4. The emitter and the detector can sit on the opposite side of the chamber, or could have an reflective optical path as waveguide for a more complex design. The path length relates to the concentration levels at which the target gas can be detected. The sensor response is based upon the Beer-Lambert absorption law [21] as:

$$I = I_o e^{-\alpha l} \tag{4.1}$$

where I is the light transmitted through the sensor cell, I_o is the light incident on the sensor cell, l is the cell length, and α is the absorption coefficient of the target gas, which is the product of gas concentration and specific absorptivity [22]. Therefore, a shorter path length is used for high concentrations (i.e. 10 mm path length for detecting concentrations at percentage levels), and a longer path length is used for lower concentrations (i.e. 100 mm path length for detecting concentrations at tens of ppm levels).

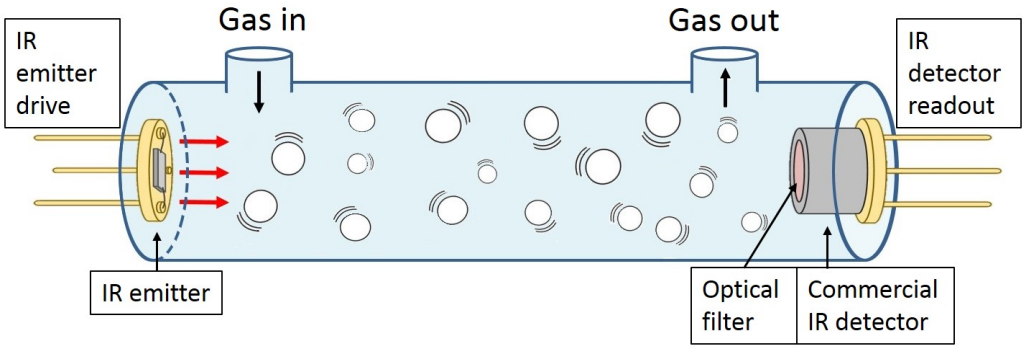

Figure 4.4: Schematic of a typical NDIR gas sensor.

Instead of detecting the full spectrum, an NDIR sensor can only detect a narrow wavelength range. This is due to the optical filter located on the detector side. The filter, commercially has a band-gap of 90 nm or 180 nm, is often centred to a known wavelength of the target gas. One of the most popular commercial NDIR sensors is the carbon dioxide (CO_2) sensor, which has a strong IR absorption peak at 4.26 μm. Absorption peaks for other gases within the mid-infrared region are plotted in Fig. 4.5. The gases of interest in this work are: carbon dioxide (CO_2), carbon

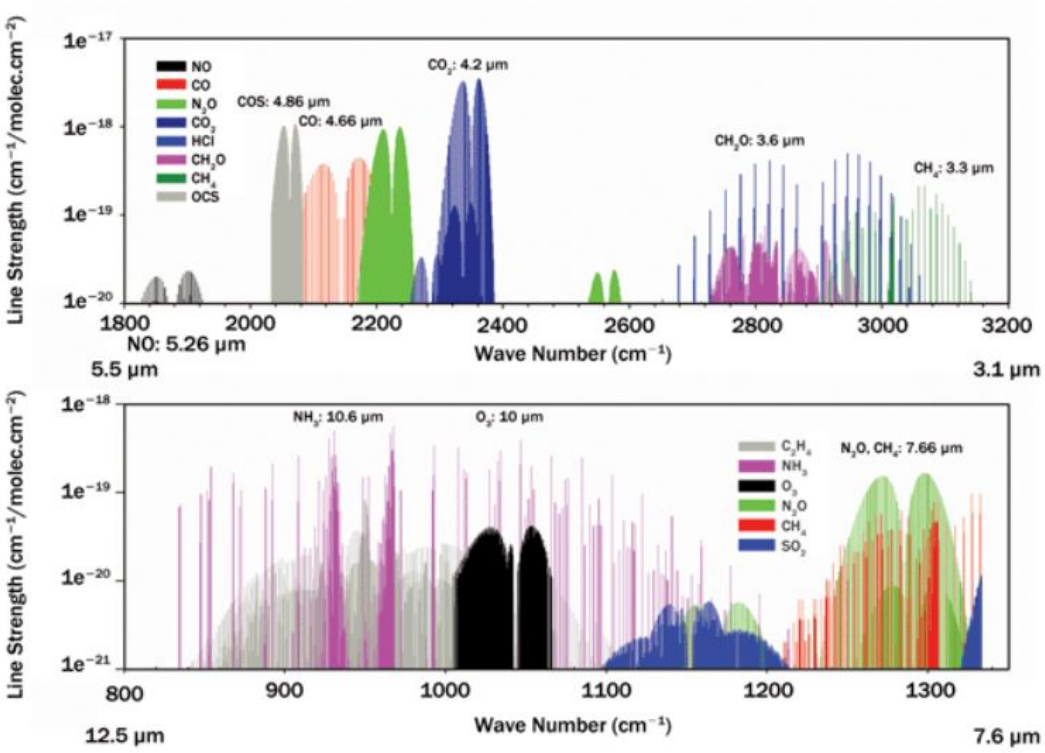

Figure 4.5: Mid-IR molecular absorption spectra from 3.1 μm to 12.5 μm(reproduced from [23]).

monoxide (CO), hydrogen sulfide (H_2S), ammonia (NH_3) and acetone (C_3H_6O), which have their main peaks at 4.26 μm, 4.6 μm, 7.3 μm, 10.6 μm and 8.26 μm, respectively.

These particular gases are selected to cover a long range of values on the mid infra-red spectrum, from 4.0 μm up to 11 μm, and at the same time, are useful for various gas monitoring applications. Carbon dioxide and carbon monoxide are two of the main air pollutants. An increase in CO_2 is caused by deforestation and emissions, which contributes to the greenhouse effect and global warming [24]. CO is a product of fuel combustions (such as vehicles), which can react with other pollutants in the air to form harmful ground level ozone [25]. It is also important for indoor air quality control, as leaks from home combustion appliances are associated with the deaths of hundreds of non-fire related CO poisoning [26]. Ammonia is another natural gas that can be emitted by human activity e.g. in chemical and automotive sectors. In atmosphere, it can react with oxides of nitrogen and sulfur to form secondary particulates [27]. Acetone is a VOC that can cause acute irritation and minor neurological disturbances when exposed or inhaled [28, 29]. It can also

be found in human breath as a warming sign for diabetes [30]. Hydrogen sulfide is a toxic gas that has received an increasing attention due to the replacement of normal combustion engine with hydrogen fuel cell. It is a common impurity that can be found in the hydrogen fuel [31, 32].

The infra-red spectrum of those selected gases is presented in Fig. 4.6. The spectrum for water is also plotted with a prominent peak occur around 3.00 μm and a less prominent peak at 6.10 μm (as compare to other gases' absorbance values). Therefore, the water inference, that is common for gas sensors, is expected to have less effect on the NDIR sensor at wavelengths of interest, in terms of sensor response and sensitivity.

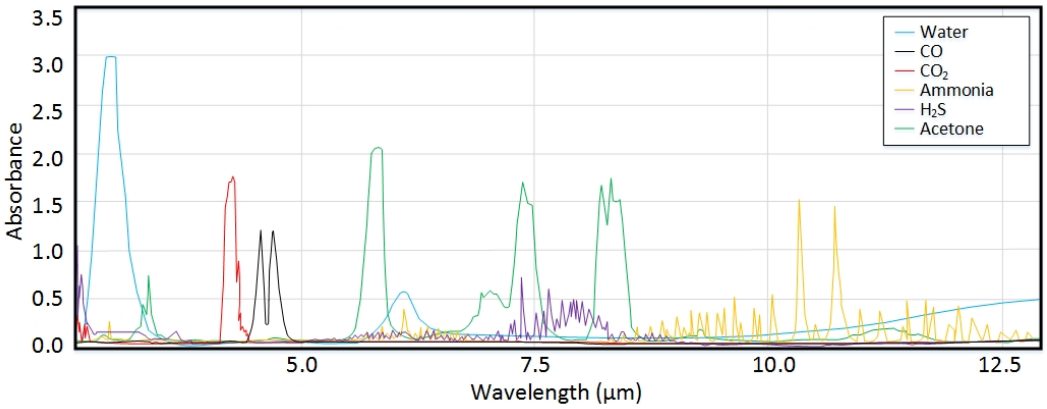

Figure 4.6: Mid-IR molecular absorption spectra for gases of interest and water.

4.1.3 IR emitters and detectors

A black body is defined as a body which absorbs all incident rays without any reflection, regardless of frequencies or angles. Kirchhoff's law states the thermal equilibrium of an object with respect to the surrounding radiation area [33]. So for an object to maintain a black body distribution, the energy (E) for absorption and emission must be equal, for every frequency, radiation, and polarization [34]. The intensity of absorption $\mathrm{I}_\alpha(\lambda, T)$ at wavelength λ and temperature T is equals to:

$$I_\alpha(\lambda, T) = \alpha_\lambda I_O(\lambda, T) \tag{4.2}$$

and for emission $\mathrm{I}_\varepsilon(\lambda, T)$ is equals to

$$I_\varepsilon(\lambda, T) = \varepsilon_\lambda I_O(\lambda, T), \tag{4.3}$$

where α_λ is the absorptivity of the object at wavelength λ and ε_λ is the emissivity. $I_O(\lambda, T)$ is the free-space black-body radiation intensity at wavelength λ and temperature T. To maintain a thermal equilibrium, the absorption and emission must be equal, hence:

$$\alpha_\lambda = \varepsilon_\lambda \tag{4.4}$$

Therefore, one could say only a good absorber makes a good emitter, and their techniques and designs are interchangeable.

The intensity value follows Planck's law for radiation calculation. Max Planck [35] described the spatial radiance B_v of a physical body at wavelength λ and temperature T as

$$B_v(\lambda, T) = \frac{2hc^2}{\lambda^5} \frac{1}{e^{\frac{hc}{\lambda k_B T}} - 1} \tag{4.5}$$

where h is the Planck constant (6.626×10^{-34} Js), c is the speed of light (2.998×10^8 ms^{-1}), and k_B is the Boltzmann constant (1.381×10^{-23} JK^{-1}). The equation states the mathematical relation between wavelength and temperature in regard to radiation energy, which increases more rapidly with temperature at shorter wavelength. This could also be observed using Wien's displacement law as the Wien's displacement constant ($b = 2.989 \times 10^{-3}$ mK) is the product of peak frequency (λ_{peak}) and temperature (T). The peak also shifts with temperature. The distribution curve is presented in Figure. 4.7.

To design an emitter, based on the infra-red radiation requirement and miniaturised sizing, a micro hotplate can be used [36, 37]. The micro hotplate is a resistor, which can be heated up to over 300 °C or higher, depends on the materials, to emit infra-red. Structures such as encapsulated filament were studied in the early years of research in the literature, those including suspended structures [38, 39, 40], free-standing structures [41, 42], and micro-bridge structures [43, 44]. They were later implemented onto the silicon technology with micro-machining as MEMS or CMOS compatible devices for commercialization. The hotplate, introduced in Chapter 3 was used as the base in this work for a new generation of infra-red emitters.

Commercial NDIR emitters generally use bulbs as they are very cheap and have a broadband spectrum for different gas testing requirements. Example emitters available on the market are shown in Fig. 4.8 from Heimann Sensors. But they are low efficient, short life time ($\sim$ 5000 hrs), high thermal time constant (need longer

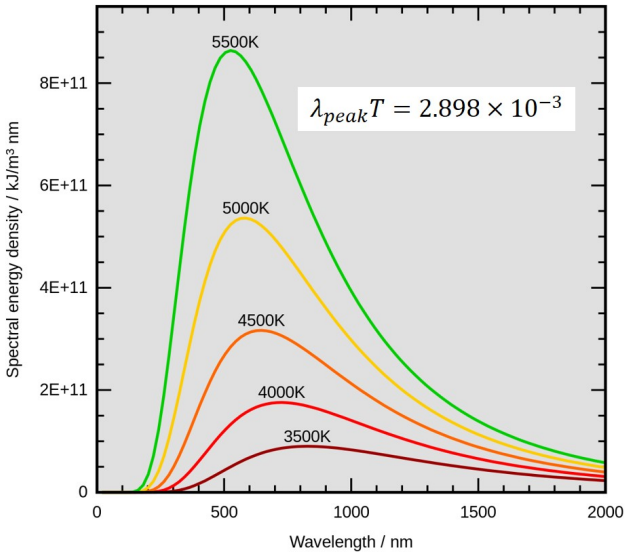

Figure 4.7: Spectral radiation distribution based on Wein's displacement law.

time to heat up, not ideal for thermal modulation), cover more than required wavelengths with the light disperse in different angles, and bulky. An ideal source would be a laser source, but it is too expensive for gas sensing, especially for applications outside laboratory or industrial conditions. To compensate for those disadvantages, plasmonic structure is employed.

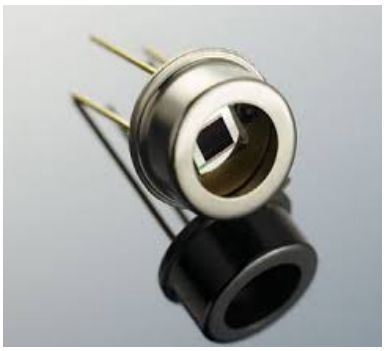

(a) HSL EMIRS series [45]

(b) HSL series [46]

Figure 4.8: Examples of commercial IR emitters, both from Heimann Sensor GmbH.

The plasmonic technology, as an emerging area nowadays, has shown promising results in manipulating lights for sensing. By incorporating plasmonic design with the micro hotplate, it is possible to tune the emitter to emit at a specific wavelength. This can concentrate the infra-red radiation without any wasted wavelengths (such as in broadband source), which means lower power consumption for the same

or better radiation intensity. This narrowband design also has the potential to improve sensitivity and selectivity. On the detector side, same plasmonic structure can be applied with a tuned narrow absorption band. By doing so, it could enable removing the relatively large optical filter from the sensor chamber in the future.

4.2 Design of the IR emitter

4.2.1 Emitter structure

The basic structure of the emitter comprises a micro hotplate and a plasmonic layer. The micro hotplate itself, can emit a broadband infra-red radiation by converting thermal power into optical power. The plasmonic layer is used to fine-tune the radiation wavelength. It was also found to enhance the thermo-optical transduction efficiency without degrading its original performance. The cross-section of the structure is shown in Fig. 4.9. The design is built upon a silicon handle wafer that can be either with or without the buried oxide layer (only present in the SOI process). The buried oxide acts as an etch-stop for the membrane. The structure has three metal layers, the middle layer (M2) is optional as it acts as a heat sink to help with the thermal uniformity across the membrane. Metal 1 (M1) layer has the circular multi-ring micro hotplate design and metal 3 (M3) has the plasmonic structure. The design also includes a passivation layer at the top for post-processing/handling protection.

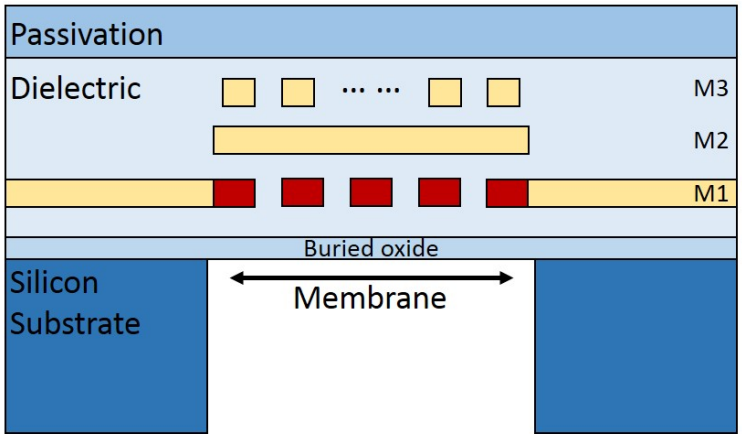

Figure 4.9: The cross-section of the infra-red emitter with the plasmonic M3 layer in SOI process (not to scale).

A membrane structure is used for better thermal isolation, so the heater area could reach a temperature of 600 °C or higher. A back-etch is carried out with a dry etching technique. Deep Reactive-Ion Etching (DRIE) post-processing step is an isotropic (non-directional) etching process that can etch perpendicularly in one direction and its preferred. The near perfect vertical side-walls means bigger membrane with minimal chip size. The circular membrane also serves as a mechanical support with a even stress distribution.

The layer thickness, as provided by the foundry, various with different materials. More details will be mentioned later in the modelling section.

4.2.2 Plasmonic structure

The plasmonic layer is located on the M3 layer on top of the micro hotplate. As the area is being heated, plasmon is induced. Within the two modes: plasmon polariton or gap plasmon mode (GPM) and surface lattice resonance (SLR) mode [47], SLR is the design focus as it controls the wavelength and emissivity whilst GPM relates to the emitting direction. Polarization sensitivity in the design has been studied and reported in literatures such as [48], but the aim of this work is to have an emitter with high emissivities in all directions, so carefully designed plasmonic layer is essential. Various designs from the literature have been discussed in details in Chapter 2. Here, the selected design of choice is patterned cylindrical dots. The circular shaped dot is helpful in constraining the resonance of surface plasmons, hence the peak radiation wavelength.

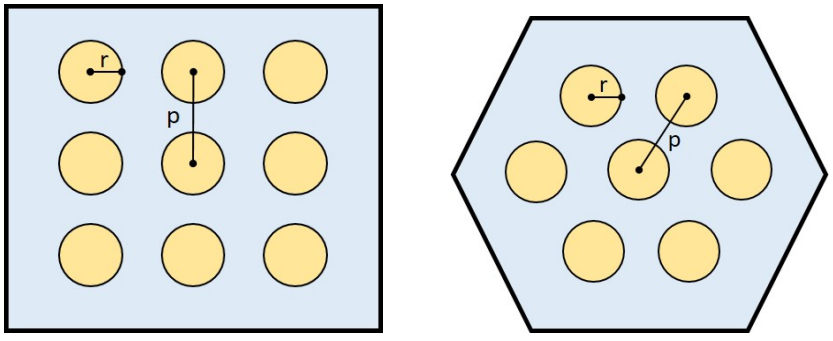

(a) (b)

Figure 4.10: Patterned plasmonic structures (a) the square lattice and (b) the hexagonal lattice.

Two periodical patterns were investigated at the beginning stage of the work: square lattice and hexagonal lattice, as depicted in Fig. 4.10. Both lattices have rounded dots with radius, r (or diameter, d) and period/pitch, p. It is possible to have different sizes of dots on the same design for a more advanced radiation manipulation, but it is not considered in this work. Because the structure controls the frequency, so it is important to tailor the pattern with appropriate sizing. Mathematical approaches can be found in the literature, and Masuda *et al.* and Ogawa *et al.* [49, 50, 51] studied the mathematical relation between the pattern's dimension and resonance frequency. They described a wavelength selectable plasmonic absorber, which could detect in the mid- and long-wavelength infra-red region. It had periodic hole arrays in a square lattice and gold sputtered on top. With the three variables, p, d and h, they came to the conclusion that the absorption wavelength was controlled mainly by the period and diameter of the structure, depth only had little effect on it. Later, Masuda *et al.* [51] introduced the concept of filling factor (d/p), which was the ratio between the cavity diameter and period. The threshold value was calculated when the resonant wavelength was equals to the period and the natural number s was equals to zero (as depth can be neglected). It was found that the sufficient absorption, over 80%, could be achieved at a filling factor value of 0.586 or higher. Despite the structure difference between square and hexagonal lattice, same maths can applied here. Therefore, it was the starting point of the model simulation, where optimum values with the highest absorption rate were expected.

To have perfect cylindrical dots in the fabricated chip, a planarization step is required. A popular way of planarization is chemical mechanical polishing (CMP), which, as the name suggests, uses both chemical and mechanical force to polish and smooth the surface. It can remove unwanted materials or fill-in gaps in a planar and uniform fashion, which is ideal when dot or hole structures are required. But this step was missing from the fabrication process, so the structure tends to be extruded (islands) instead. Therefore, both ideal (cylindrical dots) and realistic (extruded cylindrical islands) models were simulated in the COMSOL model for comparison.

4.2.3 Materials

CMOS compatible materials were chosen for this design. It has a silicon substrate with silicon dioxide (SiO_2) dielectric layers and a silicon nitride (Si_3N_4) passivation layer. A high temperature metal layer material is needed for micro hotplate application. In literature, materials such as polysilicon, tin dioxide, silver,

gold, platinum or titanium nitride were used. Platinum allows the device to reach a higher temperature (above 650 °C [52]) as compares to the polysilicon. For an even higher operating temperature, the highly doped tin dioxide could be used as the heater material together with platinum to reach over 1000 °C [53]. Titanium nitride has a very high melting temperature (2950°C), higher than platinum and polysilicon [54], but it is quite resistive and not currently available for small modules. Silver [55] and gold [56] metal layers have also been mentioned. All those materials can be manufactured at a relatively low cost using micro machining. But for CMOS processing, the choice of metal is limited. The fabrication process, provided by XFAB, Germany, has a choice of aluminium and tungsten (high temperature materials) for metallization. The properties of these two materials with typical values are presented in Table 4.1.

4.3 COMSOL Simulation Models

4.3.1 Structures

The thickness of each CMOS layer is given in Table 4.2, which was provided by the CMOS process foundry, XFAB, Germany. Accordingly to the mathematical model mentioned earlier, the thickness of each layer, especially the plasmonic layer, plays an insignificant role in the performance. Therefore, the thickness influence was not considered in the work, and default layer thicknesses from the manufacturer were used throughout all the simulations.

Table 4.1: Material properties for aluminium and tungsten (at room temperature).

Properties	**Aluminium**	**Tungsten**
Chemical Symbol	Al	W
Density (g/cm^3)	2.70	19.25
Resistivity (Ωm)	2.65×10^{-8}	5.60×10^{-8}
Thermal Conductivity (W/mK)	205	180
Temperature Coefficient $\Omega(/°C)$	0.0043	0.0045
Melting Point (°C)	600.3	3422.0

Table 4.2: Typical layer thicknesses ($\pm 15 \sim 20\%$) with aluminium and tungsten metal layer .

Layers	**Aluminium (nm)**	**Tungsten (nm)**
Passivation (Si_3N_4)	550	550
SiO_2	200	200
Metal 3 (M3)	940	500
SiO_2 (M2-M3)	650	900
Metal 2 (M2)	650	300
SiO_2 (M1-M2)	650	650
Metal 1 (M1)	720	300
SiO_2	2250	2250

Some initial work on this subject has been conducted previously by a team at Cambridge University, UK, so as a continuance of that work, only the hexagonal lattice was considered, both for simulation and fabrication. An trial wafer run was also conducted with various geometries [57], which will be referred to as Batch 0. As an improved version of Batch 0, COMSOL Multiphysics v5.1 software was used to find the optimum structure for the desired frequency. Because of the periodic lattice structure, only one unit was reproduced in the model, which contains the minimum required patterns for simulation, to reduce computation load.

Apart from the layers in fabrication process, an additional air and two perfectly matched layers (PML) were added to confine the simulation boundaries. The simulation structure is presented in Fig. 4.11 with the side view and top view. PML is commonly used to solve wave simulations, as it is assume to perfectly absorb electromagnetic waves at all frequencies and angles. The extruded cylindrical model was also simulated as seen in Figure. 4.12.

4.3.2 Model

The radio frequency module with electromagnetic wave solver provided by COMSOL was used for simulations. A 3D FEM was built as describe above. It is frequency domain based that is used for the time-harmonic electromagnetic field

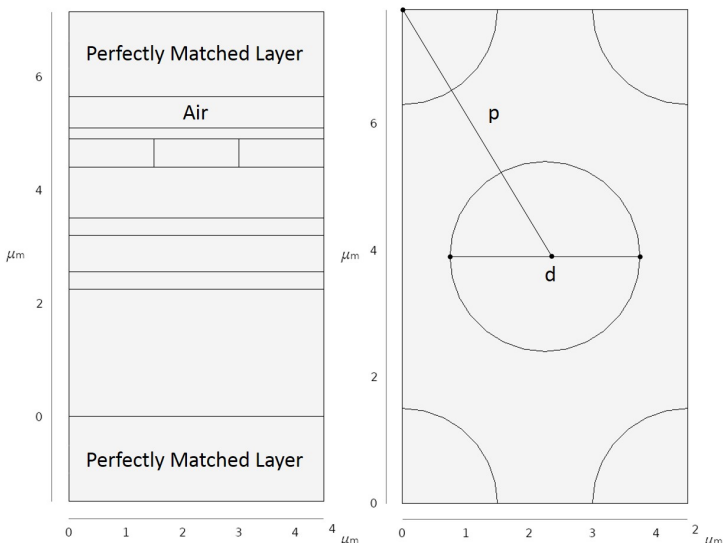

Figure 4.11: An example of the simulated structure with one unit of plasmonic lattice, the side view (left) and top view (right).

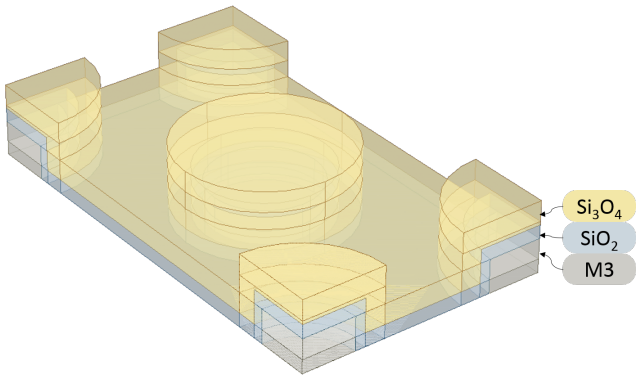

Figure 4.12: An example of the simulated extruded plasmonic layer.

distribution. The solver follows Maxwell's law and Faraday's law as:

$$\nabla \times \mathbf{H} = \mathbf{J} + \frac{\delta \mathbf{D}}{\delta t} \tag{4.6}$$

and

$$\nabla \times \mathbf{E} = -\frac{\delta \mathbf{B}}{\delta t} \tag{4.7}$$

where $\mathbf{H}$ is the magnetic field (unit: A/m), $\mathbf{J}$ is the current density (unit: A/m^2), $\mathbf{E}$ is the electric field (unit: V/m), and $\mathbf{B}$ is the magnetic flux density (unit: T). In the electric field, to solve the time-harmonic and eigenfrequency problem, the

equation is writted in the form as:

$$\nabla \times (\mu_r^{-1} \nabla \times \mathbf{E}) - k_o^2 \varepsilon_r \mathbf{E} = 0 \tag{4.8}$$

where μ_r is the relative permeability, ε_o is the permittivity of vacuum and $\varepsilon_r c$ is the relative permittivity. k_o is the free space wave number, which is defined as:

$$k_o = \omega \sqrt{\varepsilon_o \mu_o} = \frac{\omega}{c_o} \tag{4.9}$$

where ω is the angular frequency, c_o is the speed of light in vacuum and μ_o is the permeability in vacuum.

Because the simulated unit is repeated in reality, to have a more comprehensive understanding of the entire design, an appropriate boundary condition is applied. Floquet periodicity is chosen, which has the numerical expression of:

$$\mathbf{E}_{dst} = \mathbf{E}_{src} e^{-jk_F \cdot (r_{dst} - r_{src})} \tag{4.10}$$

where $\mathbf{E}_{dst}$ and $\mathbf{E}_{src}$ represent the electric field in destination (dst) and source (src) boundary selections, r is the radius vector and k_F is the k-vector (unit: rad/m) for Floquet periodicity. It is defined in the x and y directions as:

$$k_x = k_o \text{sin}\alpha_1 \text{cos}\alpha_2 \tag{4.11}$$

$$k_y = k_o \text{sin}\alpha_1 \text{sin}\alpha_2 \tag{4.12}$$

where α_1 and α_2 are the evaluation and azimuthal angle of the incidence. k_z is also defined in the model as:

$$k_z = k_o \text{cos}\alpha_1 \tag{4.13}$$

but is not included in the periodic condition as the simulated unit only repeats in the x and y directions.

COMSOL software provides a wide selection of materials for simulations. As the properties of the manufacturing materials were unknown, default properties in the COMSOL material library were used in simulations. A custom mesh option was selected as oppose to the default meshing sequence to reduce computation elements, while providing accurate results. Free triangular mesh element was applied to the whole model, which defines the surfaces and edges of the structure. Figure. 4.13 shows the FEM model with meshed elements.

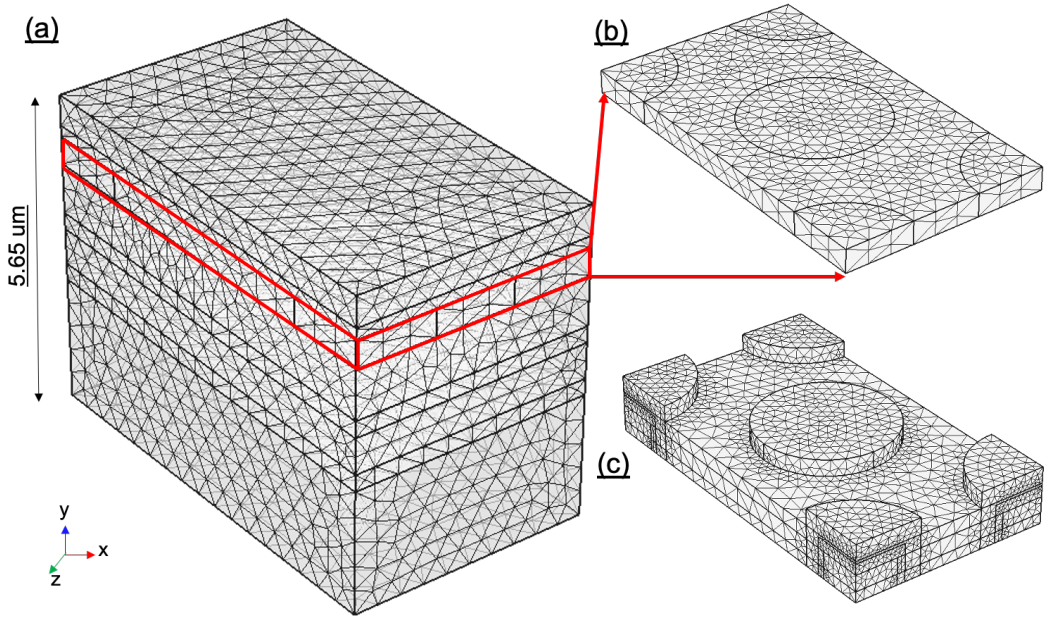

Figure 4.13: The 3D FEM model with meshed elements of the (a) entire structure (without PML) and the enlarged plasmonic layer both (b) ideal and (c) extruded.

The mathematical model mentioned in section. 4.2.2 provides a starting point in the parameter swept analysis. The two main factors, pitch and diameter, were varied one at a time. Because the filling factor introduced by Masada K. *et al.* was calculated when pitch equals to the resonance frequency, therefore, pitch was fixed first. For example, CO has a resonant frequency at 4.6 μm, then the swept analysis was conducted with p = 4.6 μm and the diameter centred at 1.4 μm (= p $\times$ 0.6) with +40% variation (i.e: 1.4 μm to 2.0 μm). When necessary, values for pitch were also varied by 5-10 % as a following step. Those steps were repeated until the optimum geometry was found for each design.

4.3.3 Fabrication Variance

The wafer Batch 0, provided by Cambridge University, has various diameter/pitch designs. The whole list of patterned geometries is attached in the appendix. To investigate the possible fabrication variance, the same design on different reticles were examined under a scanning electron microscope (SEM). The selected chip were measured with five dots each. Figure. 4.14 shows an example of the SEM measurement and the averaged results for the 25 selected chips are summarised in

Table. 4.3.3.

The measurements show slight fluctuations in both pitch and diameter values, especially in the x and y directions of the diameter measurements. The deviation is around 10%. A more accurate measurement is preferred with profile measuring function, but the equipment is limited.

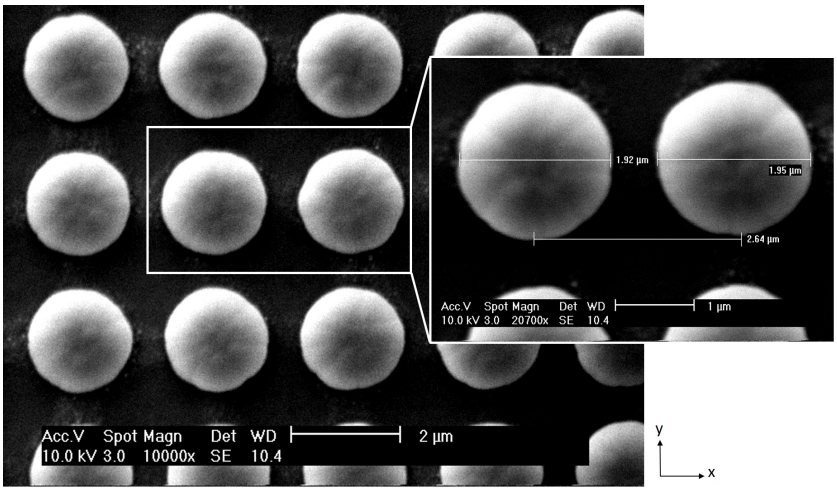

Figure 4.14: An example of a SEM image of the plasmonic dots with measurements.

Thermal expansion is another variation that need to be considered. The linear expansion coefficients for aluminium and tungsten at 20 °C are 23.1 ($\times 10^{-6}\mathrm{K}^{-1}$) and 4.5 ($\times 10^{-6}\mathrm{K}^{-1}$), respectively. Therefore, when the heater temperature reaches 400 °C, the metal material will expand by 0.9% for aluminium and 0.18% for tungsten.

Table 4.3: Wafer Batch 0 plasmonic pattern geometries measured under the SEM (averaged over five dots.)

Chip Order	**Pitch**	**Diameter (x direction, μm)**	**Diameter (y direction, μm)**
1	2.61	1.04	1.16
2	2.61	1.02	1.12
3	2.56	0.99	1.10
4	2.59	1.00	1.10
5	2.61	1.04	1.13

Continued on next page

Table 4.3 – *Continued from previous page*

Chip Order	**Pitch**	**Diameter (horizontal (x))**	**Diameter (vertical (y))**
6	2.60	1.04	1.16
7	2.60	1.01	1.12
8	2.60	1.01	1.08
9	2.59	0.98	1.10
10	2.60	1.01	1.13
11	2.59	1.03	1.13
12	2.61	1.00	1.20
13	2.63	1.07	1.13
14	2.61	1.00	1.06
15	2.61	1.02	1.09
16	2.58	1.03	1.15
17	2.58	1.01	1.15
18	2.59	0.96	1.08
19	2.59	1.01	1.09
20	2.59	0.99	1.09
21	2.60	1.02	1.07
22	2.60	1.02	1.13
23	2.60	1.00	1.08
24	2.60	1.01	1.07
25	2.56	1.04	1.12

4.3.4 Simulation Results

The selected values, after parameter swept, were simulated across the entire frequency spectrum of interest (i.e. 4 μm to 11 μm). The aim is to have the prominent peak at the desired frequency and relatively inactive at the rest of the spectrum. A 5-10% manufacturing tolerance is included. Both ideal (planar) and realistic (non-planar, extruded) model were simulated for all gases of interest: carbon dioxide (4.26 μm), carbon monoxide (4.6 μm), hydrogen sulfide (7.3 μm), acetone (8.26 μm) and ammonia (10.6 μm). Table. 4.4 shows the selected values for both planar and non-planar designs with tungsten metal layers.

Table 4.4: Planar and non-planar plasmonic geometries used in simulations with tungsten metal layers (unit: μm).

Gas of Interest	**IR Absorption Band**	**Planar**		**Non-planar**	
		Diameter	**Pitch**	**Diameter**	**Pitch**
CO	4.6	3.2	4.45	2.4	4.0
CO_2	4.26	3.6	4.2	1.6	4.3
H_2S	7.3	2.6	6.5	2.6	7.5
Acetone	8.2	4.0	8.2	4.0	8.2
Ammonia	10.6	3.6	10.8	3.6	10.8

Simulations were conducted from wavelength 4 μm to 11 μm with 200 sampling points. The results are presented in Figure. 4.15 for all gases of interest with both structures (fabrication tolerance not shown). The model was simulated across the entire spectrum of interest to study cross correlations between the target gas and the other gases. The shaded areas represent the commercial optical filter with a band-gap of 180 nm. The darker area is where the target peak should be for each gas and the lighter areas are for the other gases. All five designs show high emissivity with CO, CO_2 and acetone have close to black-body emissions. Cross-correlation among these five gases of interest is relative small, apart from the higher wavelength range, such as ammonia. It was found difficult to fine-tune the emission peak at the higher wavelength range (above 7.5 μm), in which case a different mathematical model needs to be explored as a further work.

Aluminium was another metal of choice, as this multi-project wafer has no aluminium run, only preliminary simulations were performed. Results are included in the appendix.

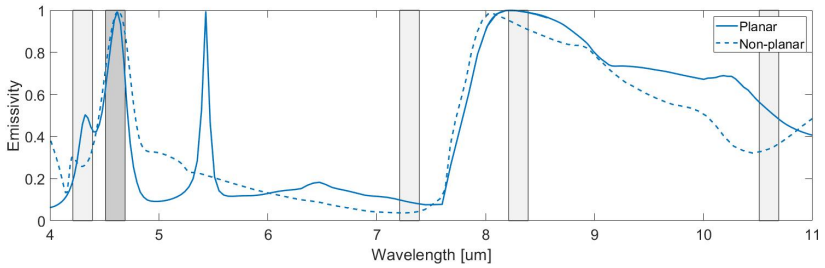

(a) Carbon Monoxide

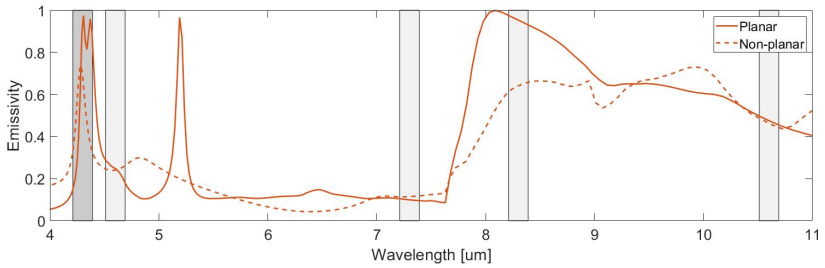

(b) Carbon Dioxide

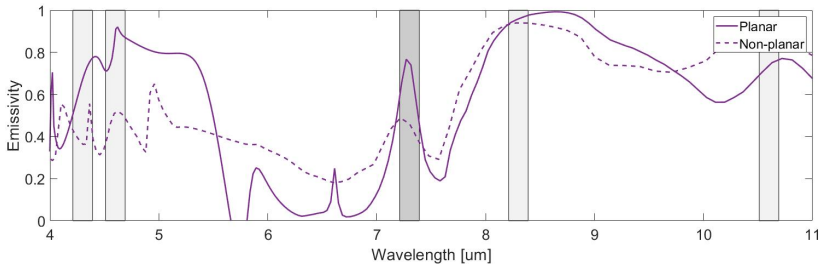

(c) Hydrogen sulfide

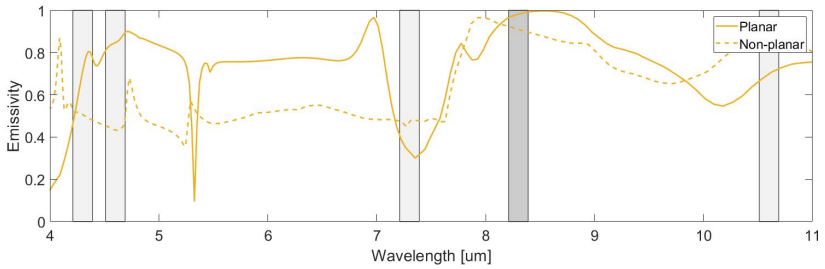

(d) Acetone

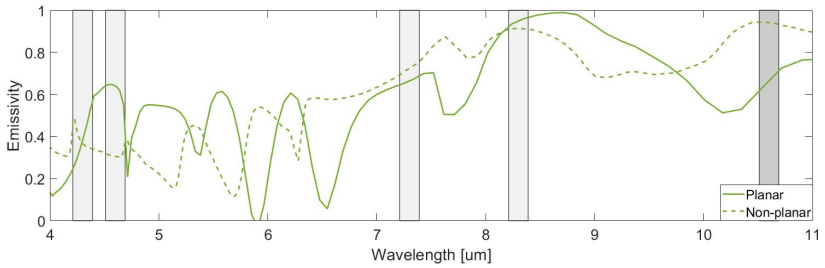

(e) Ammonia

Figure 4.15: COMSOL simulation results for the plasmonic structure and tungsten metal layers from 4 μm to 11 μm.

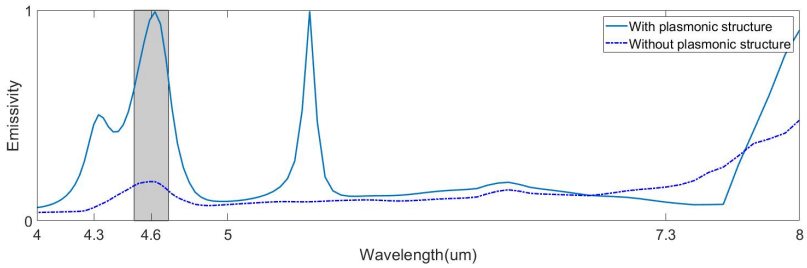

(a) Plasmonic versus Non-plasmonic

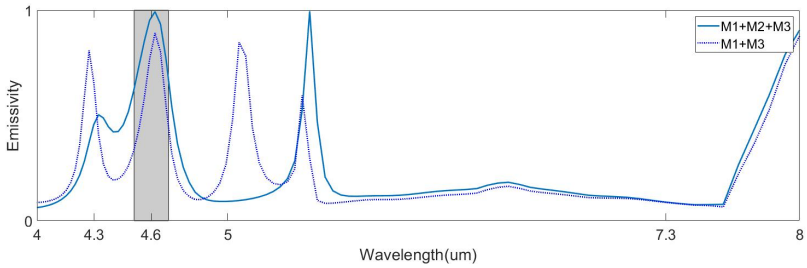

(b) With versus Without M2

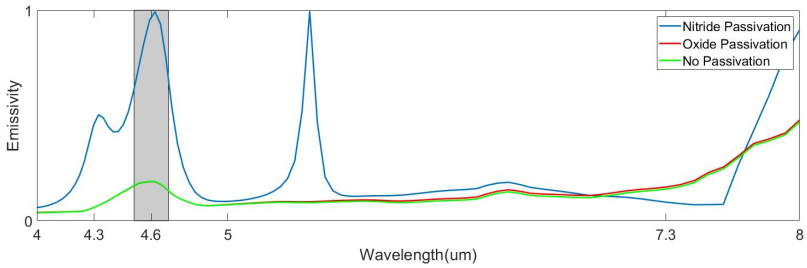

(c) Passivation layer comparison

Figure 4.16: COMSOL simulation for different comparison studies with plasmonic geometry for carbon monoxide.

In order to demonstrate the emission enhancement by the plasmonic structure, the performance comparison was also studied. Plasmonic versus non-plasmonic was simulated with the same structure for CO, which is shown in Figure. 4.16(a). Though a peak is observed for the non-plasmonic structure, it is less significant in the emissivity value at ~ 0.2 as compare to the plasmonic structure with a close to a black body emission at 1. Other comparisons, such as with/without metal 2 layer for thermal uniformity and different passivation materials, were also studied and presented in Figure. 4.16. The frequency spectrum shifted with silicon oxide as passivation and no passivation layer. Similar feature was also observed with other patterned geometries for different gases. Depending on the manufacturing process and materials, such variation can be tailored and eliminated by varying the geometries.

Alongside the frequency spectrum simulation, electric field distribution was also plotted in Figure. 4.17 showing the field intensity at the resonance frequency. At the peak wavelength, electric charges are more concentrated in the proximity of the plasmonic structure which leads to a stronger localized electric field, hence enhanced emissivity.

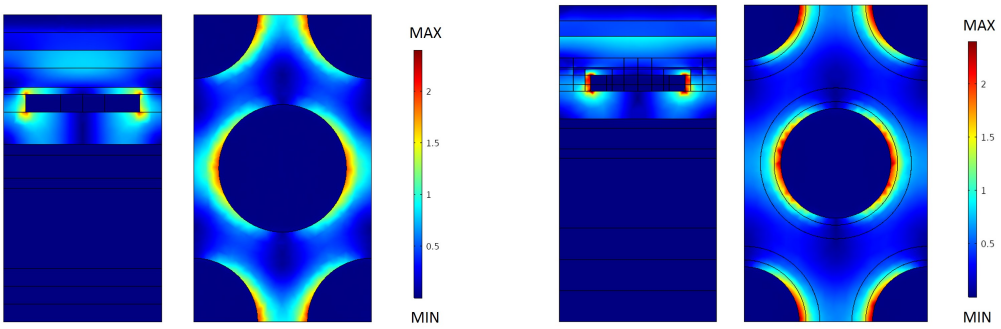

(a) Planar (b) Non-planar

Figure 4.17: Electric field intensity for planar and non-planar plasmonic designs.

4.4 Fabrication Process

4.4.1 Mask Layout

After the geometries for the plasmonic structure were fixed, masks were designed for fabrication. The fabrication process was provided by XFAB Germany, though XI10 1.0 μm CMOS process for both bulk and SOI wafers. Mentor Graphics Tanner EDA L-edit v16 was used to design masks for the plasmonic pattern. The micro hotplate was based on the existing design provided by Cambridge University (UK), with metal multi-rings on M1 layer (as Figure. 4.18).

The ratio between the micro hotplate and the membrane determines the operation speed of the sensor, i.e. the operation frequency in PWM or AC mode. The bigger membrane and smaller micro hotplate means faster speed, and vice versa. The membrane size depends on the chip size, which in this case has a size of 1.6 mm $\times$ 1.6 mm. Therefore, the biggest possible membrane size, without affects the structural integrity and with space for tracks and pads, is 1.2 mm diameter. Heater sizes vary for different designs and the full list is provided in Table. 4.5. The design for CO_2 has the smallest heater size of 60 μmm diameter. CO_2 NDIR sensor

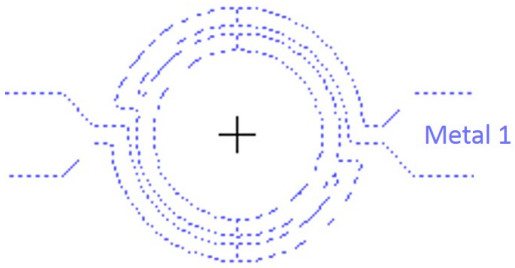

Figure 4.18: The micro hotplate with multi-ring structure on M1.

Table 4.5: Membrane and heater sizes of the designs.

Designs	**Membrane Size** (μm)	**Heater Diameter** (μm)
CO	1200	250
CO + 3%	1200	250
CO − 3%	1200	250
CO_2	1200	60
Acetone	1200	150
H_2S	1200	150
Ammonia	1200	150

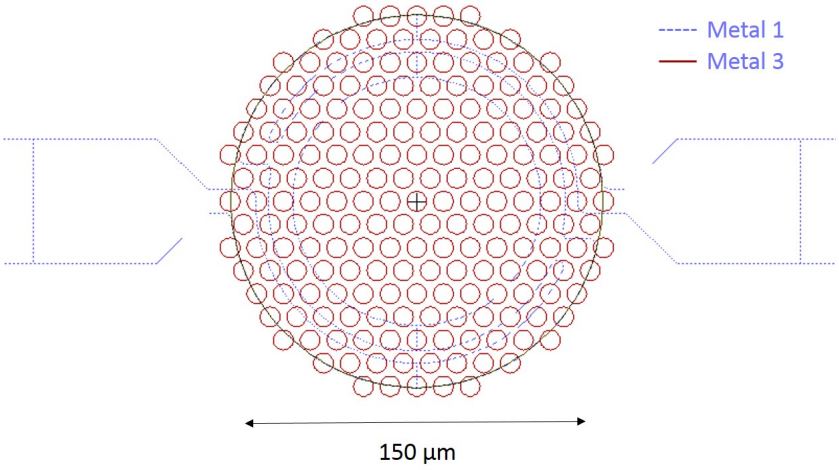

Figure 4.19: An example of the M3 plasmonic structure on the M1 micro hotplate.

is widely available in commercial products, therefore the aim for designing a CO_2 sensor is to increase the switching speed. For other designs, 150 μmm and 250 μmm diameters are standard heater sizes and selected for trial and error. CO_2 plus and

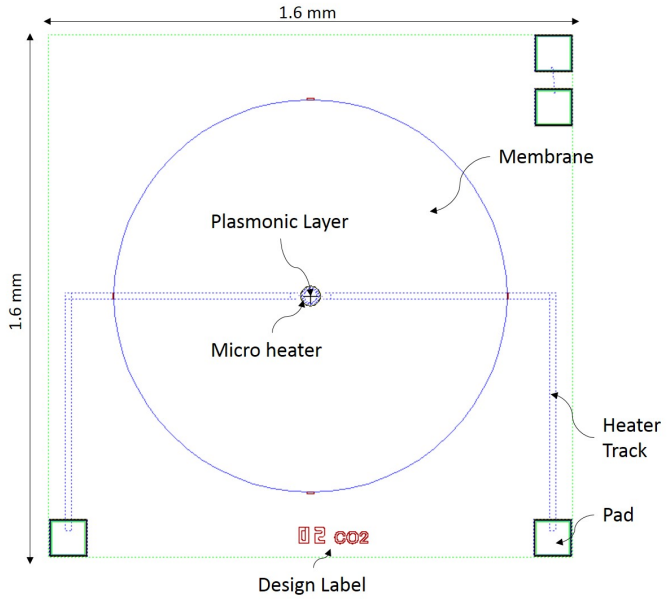

Figure 4.20: An example of the finished chip layout (plasmonic structure not shown).

minus were included in the design for manufacturing tolerance check.

Tanner L-edit v16 has the capability to generate structures with code instructions, a.k.a macros. A macro file was then written to create the plasmonic layer with rounded dots on metal 3 based on the simulated diameter and pitch values within the heater diameter. An example structure is shown in Figure. 4.19 and the final chip is shown in Figure. 4.20. All designs were created in the same manner. In total, 7 designs were submitted to XFAB for fabrication.

4.4.2 Tape-out

The fabrication steps follows the standard XFAB XI10 process. The fabrication of micro hotplate was described previously based on a 6-inch silicon handle wafer. On top of the micro hotplate layer, additional layers were deposited to form the plasmonic layer. Figure. 4.21 briefly explains those steps.

After the deposition of the silicon dioxide layer, either through thermal oxides or chemical vapour deposition (CVD), a metal layer (M2) is deposited. One of the common metallisation method is physical vapour deposition (PVD) using sputtering or evaporation technique. Then another layer of silicon oxide is deposited before moving on to the final metallisation layer with plasmonic structure. The metal structure is deposited and etched for the periodic pattern. On top of that, a layer of silicon was deposited and oxidised as the dielectric layer. Without the help of CMP for planarization, the oxide layer together with metal layer became extruded islands and the shape carried on to the passivation layer. Silicon nitride is the material for passivation layer, which can be deposited via CVD. It also acts as a protection layer for further processing.

The last step was back-etching to form the membrane. Deep reactive ion etching was used to create a near-perfect vertical wall. It is an isotropic plasma dry etching process that uses chemical reactions to turn the material into volatile, which is then removed later. This post-processing step was performed in the same foundry. The finished wafer was then send off for dicing into 1.6 mm $\times$ 1.6 mm chips.

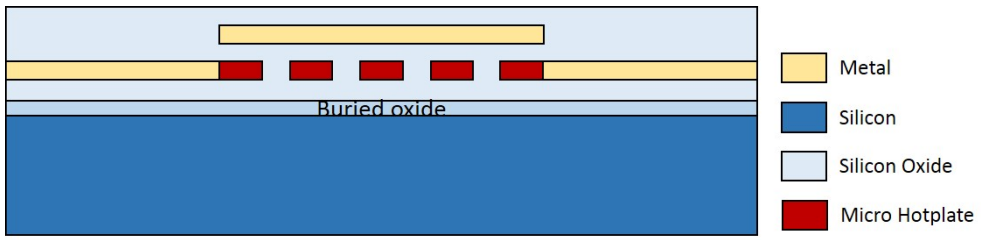

(a) SOI wafer with micro hotplate.

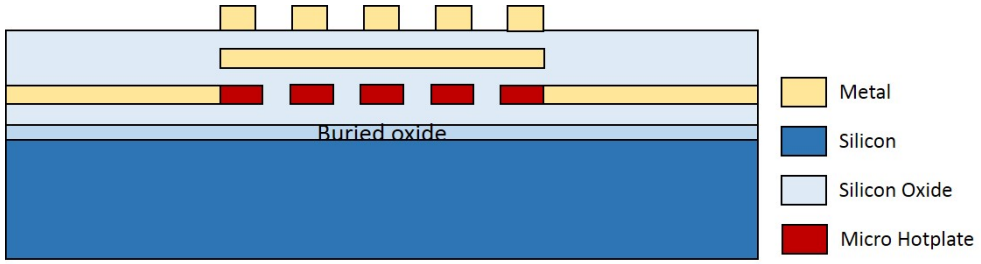

(b) Plasmonic pattern deposition.

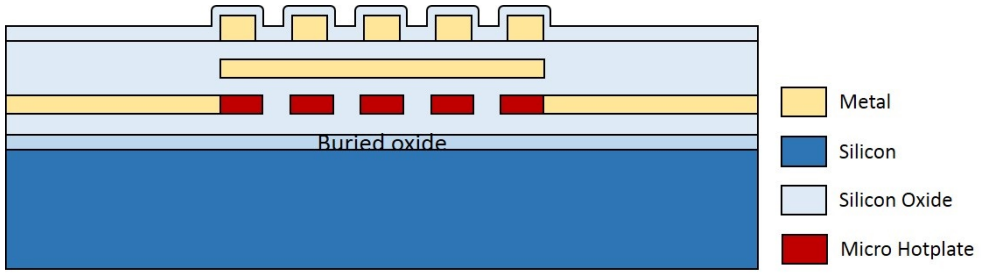

(c) Silicon oxide as dielectric layer.

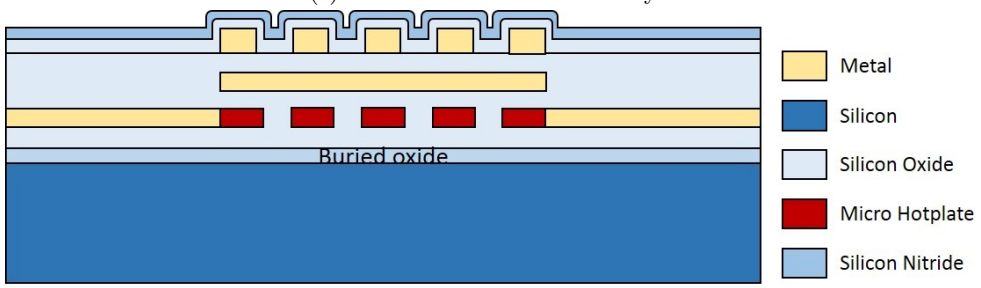

(d) Passiviation layer deposited.

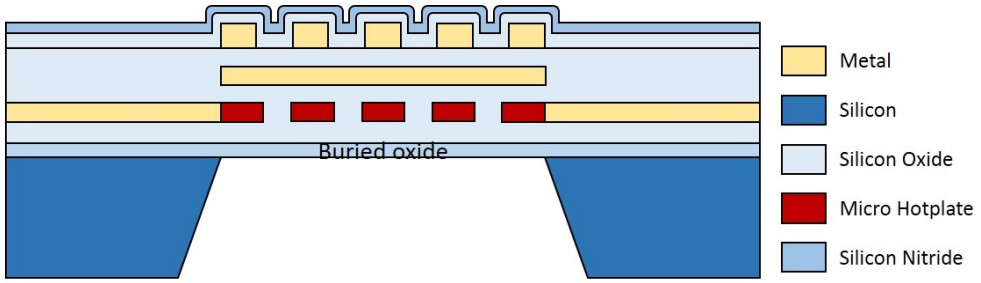

(e) Post-processing using DRIE to form membrane.

Figure 4.21: Fabrication process for plasmonic patterns (not to scale).

4.5 Conclusions

In this chapter, a new generation of plasmon enhanced CMOS infra-red emitters were presented to be used in NDIR gas sensors. Conventional NDIR sensor has limitations such as bulky, low sensitivity and high power consumption with a broadband infra-red emission (more than 5 μm range). This novel emitter with plasmonic structure helps to overcome those limitations with a tuned emission peak for high sensitivity and low power consumption ($\sim$ 30 mA), and the CMOS process for miniaturized sizing and low production cost.

The designed emitter has three metal layers on top of a back-etched membrane structure for mechanical support and thermal isolation. Metal 1 layer has a circular multi-ring micro hotplate, metal 2 is a plain metal layer for thermal uniformity, and metal 3 is the plasmonic patterned layer. The metal of choice was either aluminium or tungsten (high temperature CMOS metal), both were investigated. A patterned plasmonic structure was introduced with periodic arrays of cylindrical dots. The design is based on hexagonal lattices with the pitch and diameter of the dot control the plasmon resonance frequency, i.e. emission wavelength. The ideal structure has cylindrical dots embedded within the dielectric layer (planar design), but with the missing processing step (planarization), extruded dots (non-planar design) are more realistic. Both structures were considered in the modelling and simulation.

Simulations were performed using the COMSOL Multiphysics v5.1 software and electromagnetic wave functions. Five gases of interest were selected for the scope of study: carbon monoxide, carbon dioxide, hydrogen sulfide, acetone and ammonia, which have their unique absorption wavelengths at 4.26 μm, 4.6 μm, 7.3 μm, 10.6 μm, and 8.26 μm, respectively. All target wavelengths were simulated for both planar and non-planar structures to obtain their optimum geometries, and results were presented. The fabrication tolerance was investigated and considered in the simulation process, which is shown to be 5$\sim$10%. The result shows a close to black body radiation can be achieved at wavelengths for almost all of the target gases, but at the higher wavelength range ($> 7.5\mu m$), single emission peak was harder to achieve. The performance enhancement with the designed plasmonic structure was also studied. Compared with the design without plasmonic structure, the emissivity increased almost four times more. Different layer-structures and passivation materials were also explored, proving the existing design was the best available one.

The tailored structure was then send off for fabrication. Masks were designed in Tanner EDA L-edit v16 and CMOS process from commercial foundry XFAB, Germany, with multi-project wafer run was used for the tape-out. The returned wafer, both bulk and SOI, will be presented in the next chapter together with their experimental results.

References

[1] M. Tasumi and A. Sakamoto, *Introduction to experimental infrared spectroscopy: fundamentals and practical methods.* Chichester: Wiley, 2015.

[2] D. A. Burns and E. W. Ciurczak, *Handbook of near-infrared analysis.* Boca Raton: CRC Press, 2008.

[3] J. C. Ye, S. Tak, K. E. Jang, J. Jung, and J. Jang, "NIRS-SPM: Statistical parametric mapping for near-infrared spectroscopy," *NeuroImage*, vol. 44, no. 2, pp. 428–447, Jan 2009.

[4] B. S. Lin, C. C. Wang, M. H. Chang, and C. C. Chio, "Evaluation of traumatic brain injury by optical technique," *BMC Neurology*, vol. 15, no. 205, pp. 1–9, 2015.

[5] S. Lloyd-Fox, A. Blasi, and C. Elwell, "Illuminating the developing brain: The past, present and future of functional near infrared spectroscopy," *Neuroscience & Biobehavioral Reviews*, vol. 34, no. 3, pp. 269–284, Feb 2010.

[6] X. Cui, D. M. Bryant, and A. L. Reiss, "NIRS-based hyperscanning reveals increased interpersonal coherence in superior frontal cortex during cooperation," *NeuroImage*, vol. 59, no. 3, pp. 2430–2437, Feb 2012.

[7] S. Fazli, J. Mehnert, J. Steinbrink, G. Curio, A. Villringer, K.-R. Müller, and B. Blankertz, "Enhanced performance by a hybrid NIRS–EEG brain computer interface," *NeuroImage*, vol. 59, no. 1, pp. 519–529, Jan 2012.

[8] M. Ferrari, M. Muthalib, and V. Quaresima, "The use of near-infrared spectroscopy in understanding skeletal muscle physiology: recent developments," *Philosophical Transactions of the Royal Society A: Mathematical, Physical and Engineering Sciences*, vol. 369, no. 1955, pp. 4577–4590, Nov 2011.

[9] T. W. L. Scheeren, P. Schober, and L. A. Schwarte, "Monitoring tissue oxygenation by near infrared spectroscopy (NIRS): background and current applications," *Journal of Clinical Monitoring and Computing*, vol. 26, no. 4, pp. 279–287, Aug 2012.

[10] S. Chakravarti, S. Srivastava, and A. J. C. Mittnacht, "Near infrared spectroscopy (nirs) in children," *Seminars in Cardiothoracic and Vascular Anesthesia*, vol. 12, no. 1, pp. 70–79, 2008.

[11] F. Vatansever and M. R. Hamblin, "Far infrared radiation (FIR): its biological effects and medical applications," *Photonics & lasers in medicine*, vol. 4, pp. 255–266, Nov 2012.

[12] M. J. Kaufman, M. G. Wolfire, D. J. Hollenbach, and M. L. Luhman, "Far-Infrared and Submillimetre Emission from Galactic and Extragalactic Photodissociation Regions," *The Astrophysical Journal*, vol. 527, no. 2, pp. 795–813, 1999.

[13] G. L. Pilbratt, J. R. Riedinger, T. Passvogel, G. Crone, D. Doyle, U. Gageur, A. Heras, C. Jewell, L. Metcalfe, S. Ott, and M. Schmidt, "Herschel space observatory - an esa facility for far-infrared and submillimetre astronomy," *Astronomy and Astrophysics*, vol. 518, pp. 1–7, July 2010.

[14] Royal Society of Chemistry, "Infrared Spectroscopy (IR)," 2009. [Online]. Available: www.rsc.org/learn-chemistry/resource/download/res00000940/cmp00001320/pdf

[15] J. ASHENHURST, "Infrared Spectroscopy: A Quick Primer On Interpreting Spectra," 2016. [Online]. Available: https://www.masterorganicchemistry.com/2016/11/23/quick_analysis_of_ir_spectra/

[16] National Institute of Standards and Technology (NIST), "Ethyl Acetate." [Online]. Available: https://webbook.nist.gov/cgi/cbook.cgi?ID=C141786&Type=IR-SPEC&Index=2

[17] Thermo Fisher, "Introduction to FTIR spectroscopy." [Online]. Available: https://www.thermofisher.com/uk/en/home/industrial/spectroscopy-elemental-isotope-analysis/spectroscopy-elemental-isotope-analysis-learning-center/molecular-spectroscopy-information/ftir-information/ftir-basics.html

[18] X. Liu, S. Cheng, H. Liu, S. Hu, D. Zhang, and H. Ning, "A Survey on Gas Sensing Technology," *Sensors*, vol. 12, no. 7, p. 9635, 2012.

[19] E. L. Tury, K. Kaste, R. E. Johnson, and D. O. Danielson, "Non-dispersive infrared gas analyzer system," U.S. Patent US5 060 505A, 1991.

[20] R. E. Passaro and K. Williams, "Non-dispersive infrared gas analyzer," U.S. Patent US4 346 296A, 1982.

[21] G. Wypych, *Handbook of Material Weathering*. Ontaria: ChemTec Publishing, 2013.

[22] J. Hodgkinson, R. Smith, W. O. Ho, J. R. Saffell, and R. P. Tatam, "Non-dispersive infra-red (NDIR) measurement of carbon dioxide at 4.2 μm in a compact and optically efficient sensor," *Sensors and Actuators B: Chemical*, vol. 186, pp. 580–588, 2013.

[23] F. Tittel, "Mid-ir semiconductor lasers enable sensors for trace-gas-sensing applications," *Photonics spectra*, vol. 48, pp. 52–56, June 2014.

[24] C. D. Rogers, "The Effects of Carbon Dioxide on Air Pollution," 2018. [Online]. Available: https://sciencing.com/list-5921485-effects-carbon-dioxide-air-pollution.html

[25] Scottish Pollutant Release Inventory, "Carbon Monoxide." [Online]. Available: http://apps.sepa.org.uk/spripa/Pages/SubstanceInformation.aspx?pid=4

[26] P. W. Francisco, S. Pigg, D. Cautley, W. B. Rose, D. E. Jacobs, and S. Cali, "Carbon monoxide measurements in homes," *Science and Technology for the Built Environment*, vol. 24, no. 2, pp. 118–123, Feb 2018.

[27] L. Int Panis, "The Effect of Changing Background Emissions on External Cost Estimates for Secondary Particulates," *Open Environmental Sciences*, vol. 2, pp. 47–53, May 2008.

[28] Toxico-Logic Consulting Inc., "Assessment report on acetone for developing ambient air quality objectives," 2004. [Online]. Available: https://open.alberta.ca/publications/0778539460

[29] H. Hansen and S. B. Wilbur, "Toxicological profile for acetone," 1994. [Online]. Available: https://www.atsdr.cdc.gov/ToxProfiles/tp21.pdf

[30] S. Park, "Acetone gas detection using TiO_2 nanoparticles functionalized In_2O_3 nanowires for diagnosis of diabetes," *Journal of Alloys and Compounds*, vol. 696, pp. 655–662, 2017.

[31] B. M. Besancon, V. Hasanov, R. Imbault-Lastapis, R. Benesch, M. Barrio, and M. J. Mølnvik, "Hydrogen quality from decarbonized fossil fuels to fuel cells," *International Journal of Hydrogen Energy*, vol. 34, no. 5, pp. 2350–2360, Mar 2009.

[32] P. Bakonyi, F. Bogdán, V. Kocsi, N. Nemestóthy, K. Bélafi-Bakó, and G. Buitrón, "Investigating the effect of hydrogen sulfide impurities on the separation of fermentatively produced hydrogen by PDMS membrane," *Separation and Purification Technology*, vol. 157, pp. 222–228, Jan 2016.

[33] R. Carminati, M. Nieto-Vesperinas, and J.-J. Greffet, "Reciprocity of evanescent electromagnetic waves," *Journal of the Optical Society of America A*, vol. 15, no. 3, pp. 706–712, 1998.

[34] D. L. C. Chan, M. Soljačić, and J. D. Joannopoulos, "Thermal emission and design in 2D-periodic metallic photonic crystal slabs," *Optics Express*, vol. 14, no. 19, pp. 8785–8796, 2006.

[35] M. Planck, *The theory of heat radiation / Authorised translation by Morton Masius.* New Tork: Dover Publications, 1914.

[36] S. M. Lee, D. C. Dyer, and J. W. Gardner, "Design and optimisation of a high-temperature silicon micro-hotplate for nanoporous palladium pellistors," *Microelectronics Journal*, vol. 34, no. 2, pp. 115–126, 2003.

[37] A. De Luca, M. T. Cole, A. Fasoli, S. Z. Ali, F. Udrea, and W. I. Milne, "Enhanced infra-red emission from sub-millimetre microelectromechanical systems micro hotplates via inkjet deposited carbon nanoparticles and fullerenes," *Journal of Applied Physics*, vol. 113, no. 214907, pp. 1–6, 2013.

[38] M. Parameswaran, A. M. Robinson, D. L. Blackburn, M. Gaitan, and J. Geist, "Micromachined thermal radiation emitter from a commercial CMOS process," *Electron Device Letters, IEEE*, vol. 12, pp. 57–59, 1991.

[39] D. Bauer, M. Heeger, M. Gebhard, and W. Benecke, "Design and fabrication of a thermal infrared emitter," *Sensors and Actuators A: Physical*, vol. 55, no. 1, pp. 57–63, 1996.

[40] J. Hildenbrand, J. Korvink, J. Wollenstein, C. Peter, A. Kurzinger, F. Naumann, M. Ebert, and F. Lamprecht, "Micromachined Mid-Infrared Emitter for Fast Transient Temperature Operation for Optical Gas Sensing Systems," *IEEE Sensors Journal*, vol. 10, no. 2, pp. 353–362, 2010.

[41] R. S. Muller and C. H. Mastrangelo, "Vacuum-sealed silicon incandescent light," 1994. [Online]. Available: https://www.google.com/patents/US5285131

[42] H. Rogne, D. T. Wang, T. A. Hansen, S. T. Moe, and A. Ferber, "Infrared source," 2010. [Online]. Available: https://patents.google.com/patent/US7741625

[43] H. Yuasa, S. Ohya, S. Karasawa, K. Akimoto, S. Kodato, and K. Takahashi, "Single crystal silicon micromachined pulsed infrared light source," in *Proceedings of International Solid State Sensors and Actuators Conference (Transducers '97)*, vol. 2, June 1997, pp. 1271–1274.

[44] T. Watanabe, H. Hara, and N. Kishi, "Infrared light source," European Patent EP2 056 337A3, 2011.

[45] Heimann Sensor GmbH, "HSL EMIRS Series: IR Sources for broad range Gas Analysis." [Online]. Available: https://www.heimannsensor.com/Datasheets/Datasheet-6-EMIR_rev1.pdf

[46] Heimann Sensor GmbH, "HSL Series: IR-Lamps." [Online]. Available: https://www.heimannsensor.com/Datasheets/Datasheet-3b-HSL_lamps_rev1.pdf

[47] A. Pusch, A. De Luca, S. S. Oh, S. Wuestner, T. Roschuk, Y. Chen, S. Boual, Z. Ali, C. C. Phillips, M. Hong, S. A. Maier, F. Udrea, R. H. Hopper, and O. Hess, "A highly efficient CMOS nanoplasmonic crystal enhanced slow-wave thermal emitter improves infrared gas-sensing devices," *Scientific Reports*, vol. 5, no. 17451, pp. 1–7, 2015.

[48] J. Rosenberg, R. V. Shenoi, S. Krishna, and O. Painter, "Design of plasmonic photonic crystal resonant cavities for polarization sensitive infrared photodetectors," *Optics Express*, vol. 18, no. 4, pp. 3672–3686, 2010.

[49] S. Ogawa, J. Komoda, K. Masuda, and M. Kimata, "Wavelength selective wideband uncooled infrared sensor using a two-dimensional plasmonic absorber," *Optical Engineering*, vol. 52, no. 12, pp. 1–6, Dec 2013.

[50] S. Ogawa, K. Okada, N. Fukushima, and M. Kimata, "Wavelength selective uncooled infrared sensor by plasmonics," *Applied Physics Letters*, vol. 100, no. 021111, pp. 1–4, 2012.

[51] K. Masuda, Y. Takagawa, M. Kimata, and S. Ogawa, "Optimization of two-dimensional plasmonic absorbers based on a metamaterial and cylindrical cavity model approach for high-responsivity wavelength-selective uncooled infrared sensors," *Sensors and Materials*, vol. 26, no. 4, pp. 215–223, 2014.

[52] P. Barritault, M. Brun, S. Gidon, and S. Nicoletti, "Mid-IR source based on a free-standing microhotplate for autonomous CO2 sensing in indoor applications," *Sensors and Actuators A: Physical*, vol. 172, no. 2, pp. 379–385, 2011.

[53] J. Spannhake, O. Schulz, A. Helwig, A. Krenkow, G. Müller, and T. Doll, "High-temperature MEMS Heater Platforms: Long-term Performance of Metal and Semiconductor Heater Materials," *Sensors*, vol. 6, no. 4, pp. 405–419, 2006.

[54] J. F. Creemer, D. Briand, H. W. Zandbergen, W. van der Vlist, C. R. de Boer, N. F. de Rooij, and P. M. Sarro, "Microhotplates with TiN heaters," *Sensors and Actuators A: Physical*, vol. 148, no. 2, pp. 416–421, 2008.

[55] Y. Jiang, M. Tsai, Y. Ye, D. Tzuang, C. Chen, and S. Lee, "Enhancement of thermal radiation in plasmonic thermal emitter by surface plasmon resonance," in *2008 8th IEEE Conference on Nanotechnology*, Aug 2008, pp. 104–107.

[56] K. Ikeda, H. T. Miyazaki, T. Kasaya, K. Yamamoto, Y. Inoue, K. Fujimura, T. Kanakugi, M. Okada, K. Hatade, and S. Kitagawa, "Controlled thermal emission of polarized infrared waves from arrayed plasmon nanocavities," *Applied Physics Letters*, vol. 92, no. 021117, pp. 1–3, 2008.

[57] A. De Luca, "SOI Smart Multi-Sensor Platform for Harsh Environment Applications," Ph.D. dissertation, University of Cambridge (UK), 2015.

Chapter 5

Sensor Integration, Calibration and Application

5.1 Introduction

Based on the IR emitter design and fabrication shown in Chapter 4, the returned wafers were diced and tested together with commercial thermopile IR detectors and narrowband optical filters under an automated gas testing bench. A LabView program was used to control the mass flow controllers (MFCs) and adjust the gas concentration levels. Circuit boards for both detectors and emitters were populated, and the collected data were post-processed using MATLAB. The sensors were tested with their target gases in different humidities. The integrated NDIR sensors were then included into two sensing systems for two projects: EU SmokeBot and EPSRC SuperGen. The sensing systems for both projects are microcontroller based, and can be used outside laboratory conditions as portable devices.

5.2 Experimental Setup

5.2.1 Infra-red Emitters

Six wafers (three bulk and three SOI) were fabricated (XFAB, Germany) and returned after dicing (DISCO HI-TEC Europe GmbH, Germany). Apart from

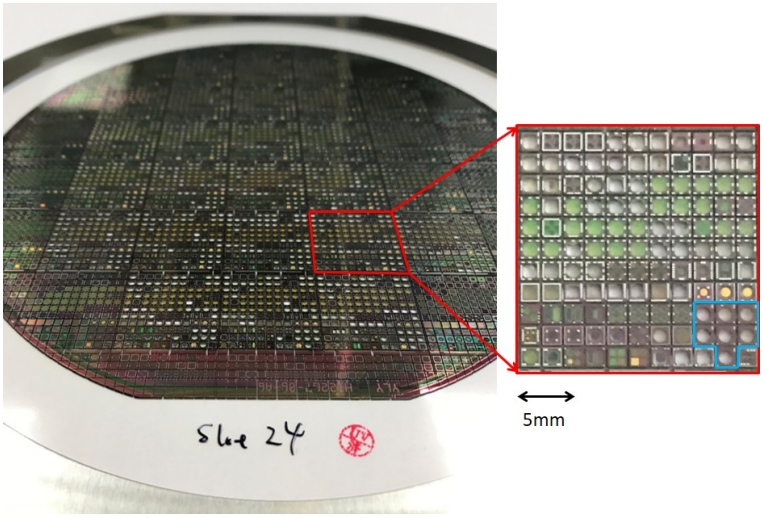

Figure 5.1: Fabricated SOI wafer with zoomed-in reticule (blue line marked the plasmonic devices).

one wafer (SOI) which was broken during the dicing test run, the other five were intact. Figure. 5.1 shows an example of the returned wafer. The wafer is 6-inch in diameter with 11 × 11 chips in each reticule. Each individual chip has the dimension of 1.6 mm × 1.6 mm. There are 26 reticules per wafer with back-etched membranes, and 7 plasmonic emitter chips in each reticule. In total, each emitter design has 76 bulk chips and 52 SOI chips. Figure. 5.2 shows the photographies of the fabricated chip with different heater sizes, both with and without a membrane.

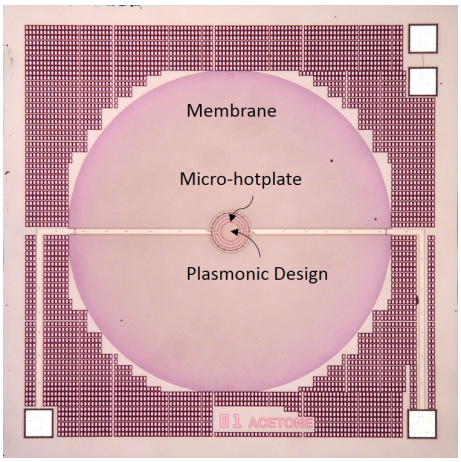

(a) IR emitter chip with 150 nm heater and membrane.

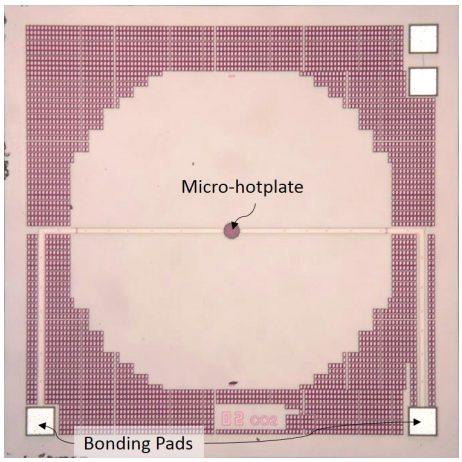

(b) IR emitter chip with 60 nm heater and no membrane.

Figure 5.2: Photographies of the top view of two fabricated emitter chips (1.6 mm × 1.6 mm).

The plasmonic structure was first examined under a scanning microscope to measure pattern geometries. A Zeiss SUPRA 55-VP SEM with a field emission electron gun (FEG) was used. This gave a more accurate measurement using its non-contact profile measurement function, compared to the SEM measurement mentioned in Chapter 4. Figure. 5.3 shows an example of the SEM measurement and Figure. 5.4 shows the cross section of the chip.

The SEM profile measurement function is suitable for structures with different heights, in this case, extruded cylindrical dots. The profile measurement of the pattern includes the passivation layer thickness as well as the silicon oxide thickness. Differences were found when comparing the measured values to the designed struc-

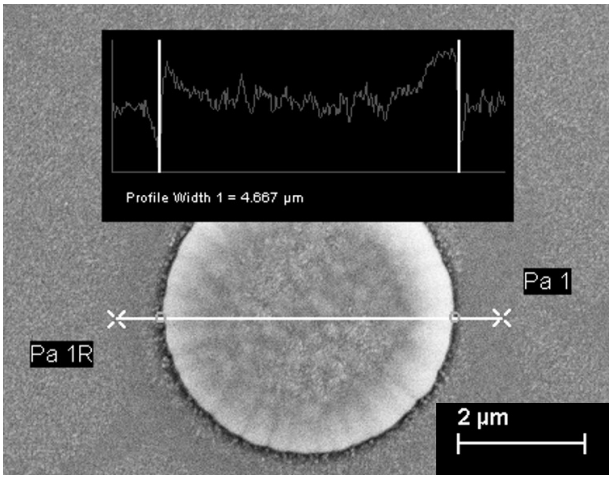

Figure 5.3: SEM measurement with non-contact profile measuring function.

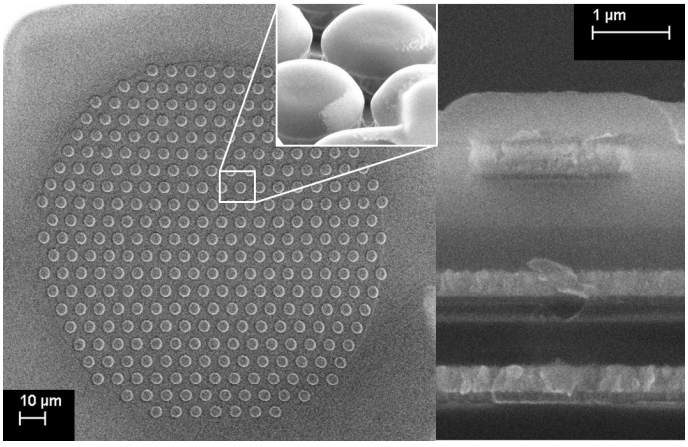

Figure 5.4: SEM images of the plasmonic structure and its side views. Left: Top view of the plasmonic pattern, and Right: cross section of the structure.

Table 5.1: Plasmonic patterns designed and measured geometries (unit: μm).

Gas of Interest	**IR Absorption Band**	**Designed**		**Actual (Bulk)**		**Actual (SOI)**	
		Diameter	Pitch	Diameter	Pitch	Diameter	Pitch
CO	4.6	2.4	4.0	1.62	4.2	1.8	4.5
CO+3%	–	2.47	4.12	1.9	4.6	1.95	4.7
CO-3%	–	2.32	3.88	1.49	4.06	1.84	4.41
CO_2	4.26	1.6	4.3	2.3	4.0	2.5	4.2
H_2S	7.3	2.6	7.5	2.0	6.2	1.95	6.3
Acetone	8.2	4.0	8.2	3.13	7.6	3.5	8.2
Ammonia	10.6	3.6	10.8	3.1	10.9	2.9	10.6

tures, as seen in Table. 5.1. Coloured text is used to indicate those with a variation higher (red) or lower (blue) than 5%.

Majority of the measured dimensions are less than the designed dimensions. These discrepancies greatly affect the resonance frequencies, as proven by the COMSOL simulation in Figure. 5.5 comparing the designed and measured geometries. In the example simulation, the fabrication variance causes the resonance peak to shift left as well as a decreasing in the emission intensity.

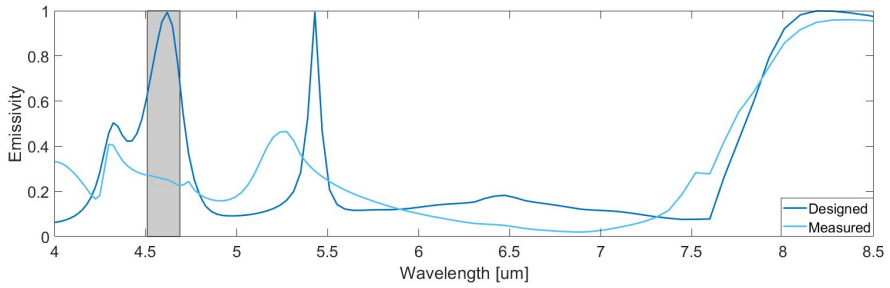

Figure 5.5: COMSOL simulation of designed and measured emitter chips for CO detection (shaded area represents the optical filter band).

The diced chips were then wire-bonded to TO-18 packages from Spectrum Semiconductor Materials Inc., which can be plugged into a socket (DAU Components Ltd.) with the same footprint on the external circuit board. This setup allows for an easy replacement of the emitter and detector for different gas testing using the same experimental setup. It is also more convenient to change if a chip is damaged or if the wire-bonding becomes loose.

5.2.2 Infra-red Detectors

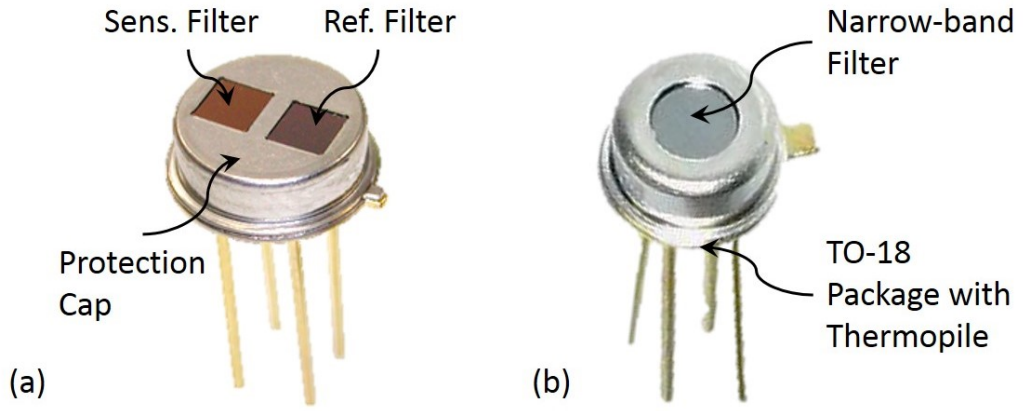

Figure 5.6: Commercial thermopile detectors with (a) dual channels and (b) single channel (Heimann Sensors GmbH).

Table 5.2: Commercial detector specifications.

Detector Type	**Target Gas**	**Centred Wavelength (μm)**	**Band-gap (nm)**
HMS J21 F4.60 (single)	CO	4.64	180
HTS A21 F4.26 (dual) HMS J21 F4.26 (single)	CO_2	4.26	180
HTS A21 F7.3 (dual) HMS J21 F7.3 (single)	H_2S	7.3	180
HTS A21 F8.26 (dual) HMS J21 F8.26 (single)	Acetone	8.26	250
HTS A21 F10.5 (dual) HMS J21 F10.5 (single)	Ammonia	10.5	240

For the first step towards a filterless NDIR sensor, a commercial thermopile detector with filter was used together with the plasmonic IR emitter. The detectors were provided by Heimann Sensors GmbH with narrow absorption bands centred at the peak frequency of the target gases. Two types of detectors are available, one with a reference channel and one without. The reference channel of the dual channel detector has a broad-band filter while the sensing channel has a narrow band. Therefore, the collected data from both channels can be processed together to remove common noise. The single channel detector is simpler with just the sensing channel. It has the advantage of smaller size (TO-18 package instead of the

TO-5 package for dual channel), and is suitable when the noise level is negligible as compared to sensing signals. Figure. 5.6 shows these two types of detectors.

The narrow pass band of the detector filter (optical film) varies from 180 nm up to 250 nm, depending on the centred frequency peak. Table. 5.2 lists the commercial detectors and their absorption band associated with their target gases.

5.2.3 External Circuit

External circuit boards are required to power and drive both emitters and detectors. They are based on circuits design by Vincent *et al.* in [1] and [2]. For the emitters operating in DC mode, a constant current circuit is used to set the micro hotplate temperature. Figure. 5.7 shows the constant current circuit consists of an operational amplifier, a transistor and a resistor to set the current value. The Molex connector, marked on the circuit as P2, is connected to the Data Acquisition system (DAQ) from National Instruments (NI) for voltage supply.

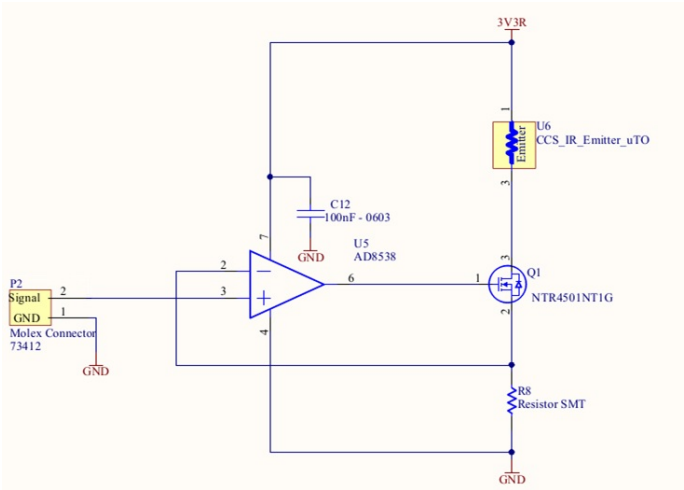

Figure 5.7: Constant current circuit for IR emitter.

The maximum operation temperature for the tungsten based micro hotplate can be as high as 600 °C. The optimum temperature should be a balance between emission intensity and sensor lifespan. Typically, 400 °C is sufficient. But because the heater-membrane ratio used in this design had never been characterised before, a trial and error approach was performed to find the heater limit. Table. 5.3 summarises the micro hotplate resistances and their operating current values.

Table 5.3: Emitter resistances and operating current in DC mode.

Heater Size (μm)	**Gas of Interest**	**Resistance** (Ω)	**Max. Current** (mA)	**Variance**
60	CO_2	65	20	$\pm 5\%$
150	Acetone, Ammonia, H_2S	100	29	$\pm 5\%$
250	CO, CO+3%, CO-3%	72	32	$\pm 5\%$

The maximum current found in DC mode was also used in AC mode as the voltage peak to set the sinusoidal amplitude. Either the DAQ or a frequency generator breakout board can be used to generate the waveform. Figure. 5.8 shows the SparkFun MiniGen breakout board. It is controlled by the serial peripheral interface (SPI) which operates as a slave to the microcontroller (master). This is also used in a portable system with NDIR sensors, which will be mentioned later in the application section.

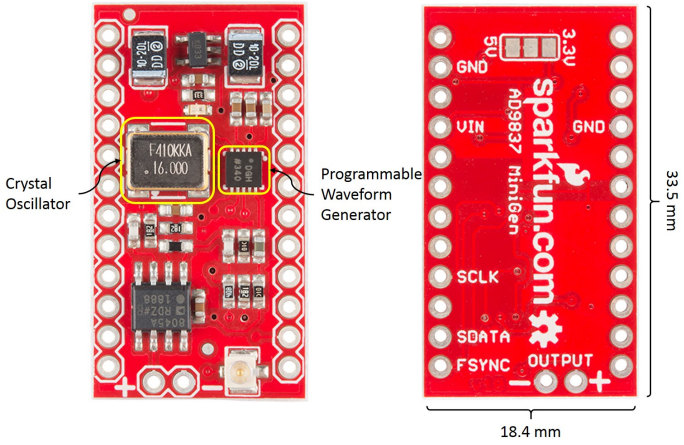

Figure 5.8: Frequency generator breakout board.

The circuit board for IR detector consists of two amplification stages for each channel (a reference channel and a sensing channel). Because the signal from the detector is really small (less than 0.1 mV), a high amplification is needed (with a gain of 4000 or higher) to get tens of millivolt of response. This gain is not possible to achieve with a single amplification stage, therefore, a two-stage circuit was used. Figure. 5.9 shows the amplification circuit for one channel (two same circuits are used for each channel of the dual-channel detector). The benefit of the amplification

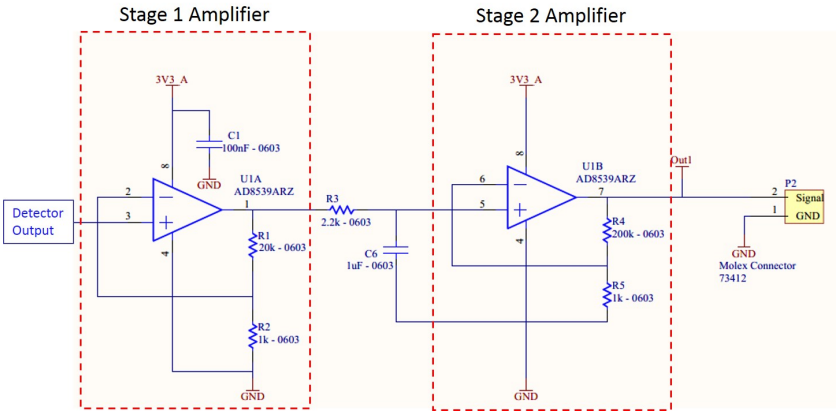

Figure 5.9: Amplification circuit for the detector.

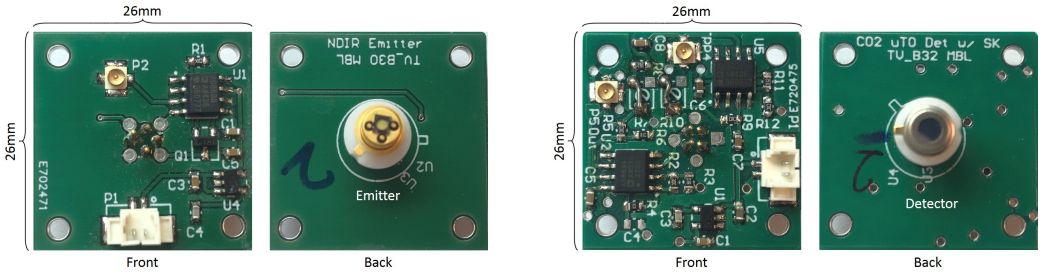

(a) Emitter circuit board.

(b) Single channel detector circuit board.

Figure 5.10: Photographies of the emitter and detector circuit boards.

is to have a visible voltage change from the gas detection, but the amplification also applies to the noise signals, hence the necessity of post-processing.

The fabricated and populated circuit boards for both emitters and detectors are shown in Figure. 5.10. They were fabricated by Eurocircuits using 4-layer boards. In the assembly, the emitter or detector was mounted on the chamber panel on one side, and the circuit board on the other side. The single channel detector is shown in the figure, and the dual channel detector has a larger size with a TO-5 packaging and socket, but the circuit board has the same size. For a more compact design, the frequency generator can be integrated with the emitter current control circuit.

5.2.4 Gas Chamber

A gas chamber is used in the NDIR sensor for the IR radiation to travel through. The optical path length of such chamber is defined as the product of the

physical distance/geometric length the light travels, which can be either straight or reflective, and the refractive index of the medium. The two ends of the chamber are the emitter and detector. The length of the optical path affects the radiation intensity throughout the chamber, and the absorption time of the gas with infra-red. Therefore, a longer optical path will allow more gas molecules to react with the IR radiation, providing a stronger detection signal even at low ppm levels.

There are two ways to improve the optical path length without comprising the compactness of the gas cell: highly reflective materials (refractive index of the medium) and a reflective path (geometric length). Coating materials for the optical path can be polished aluminium, silver [3] or gold [4], which has close to 100% reflectance at wavelengths above 700 nm as shown in Figure. 5.11. In this work, an aluminium tube with smooth gold inner coating was used. This was then inserted inside an aluminium gas chamber.

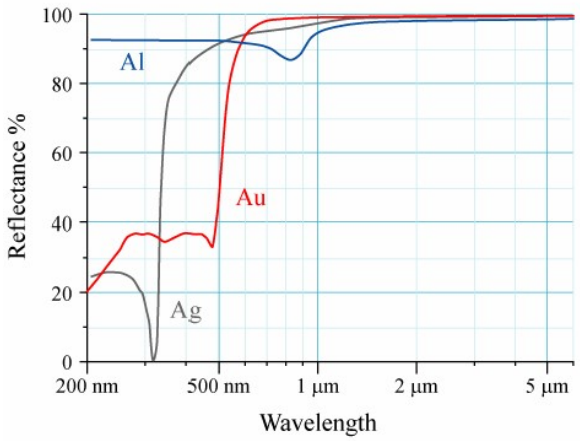

Figure 5.11: Reflectance of aluminium (Al), silver (Ag) and gold (Au) [5].

The conventional way to lengthen the optical path is to have a longer tube, which assumes a centred radiation going straight towards the other end. This is easy to implement as the field of view (FOV) of the emitter is often centred and narrow, and radiation dispersion is not considered. The disadvantage of this design is that the path length is limited by the tube length. For a reflective path, the length can be greatly increased, but is harder to control. It requires a precise placement of the emitter and detector, and the interference from dispersed radiations needs to be considered. There have been some studies in literature, such as using a cuvette [6] or reflective path [7, 8] to enhance reflection for NDIR sensors. The optical path can even be replaced by fibre as a waveguide as suggested by [9] and [10].

In this work, the conventional optical path was used, but some preliminary studies on the reflective path were conducted. One of the selected designs uses a ring-shaped gas chamber with curved inner walls. The optical path simulation shown in Figure. 5.12 was obtained using a trial version of the LensMechanix from Zemax as an add-on option to Solidworks 2016. Two emitters of the same type were used to increase the intensity of the infra-red radiation, and one detector located on the opposite side. By doing so, the path length doubled the length of the straight path (40mm). This simulated design was later adjusted for sizing (angles of the main components remained the same), and a prototyped circular gas chamber was presented in Figure. 5.13.

For this design, both the emitter and detector panels are removable for easy

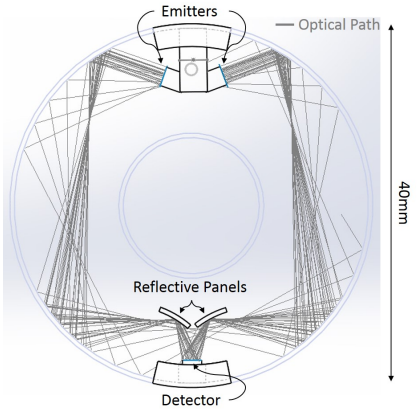

Figure 5.12: Preliminary simulation result of the reflective optical path inside a circular gas chamber.

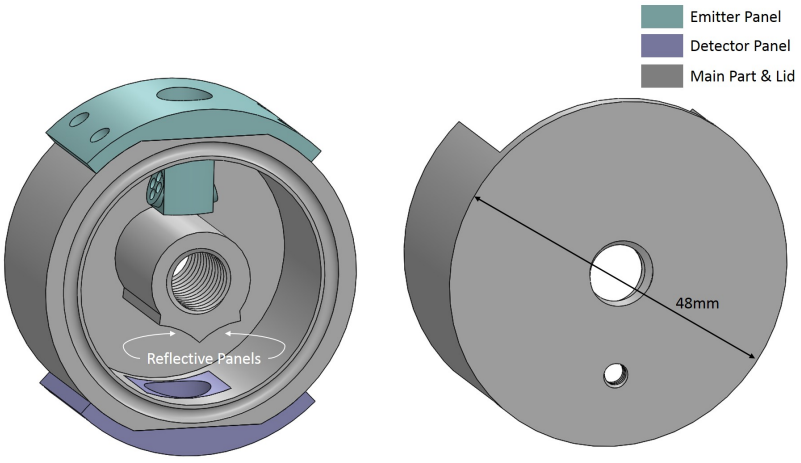

Figure 5.13: 3D model of the circular gas chamber prototype.

replacement. The lid is screwed on with nuts and bolts to the main chamber. All removable parts are sealed with o-rings to prevent leakage. The whole system has a size of 48mm in diameter, but can achieve an almost doubled optical path length. This system can be either 3D printed or machined with aluminium, and the inner wall polished and coated with silver or gold.

Another approach was trialled in [11] using an adjustable optical path. The gas chamber has multiple detector panels, which can intercept the radiation to have a shorter path. Some preliminary experiments were conducted to test this setup, but here, a more reliable system mentioned in [1] was used. Figure. 5.14 shows two gas chambers with different optical path lengths. The top smaller one uses a 3D-printed chamber with gold tubing insert. It has a length of 3 cm, which is good for detecting percentage levels. The bottom longer one was machined with an aluminium and gold tubing insert. The path length is around 12 cm, which is often used to test gas at ppm levels. Most of the experiments were performed with the bottom one, with the exception of CO_2 at percentage levels, which was tested using the smaller chamber.

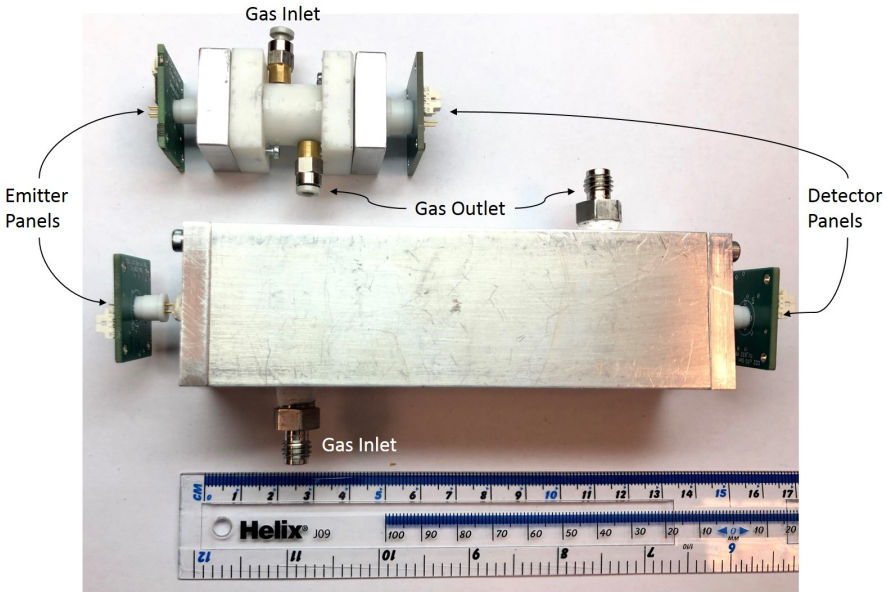

Figure 5.14: NDIR gas chamber with 3D printed (top) and aluminium (bottom) materials.

5.2.5 Gas Rig Setup

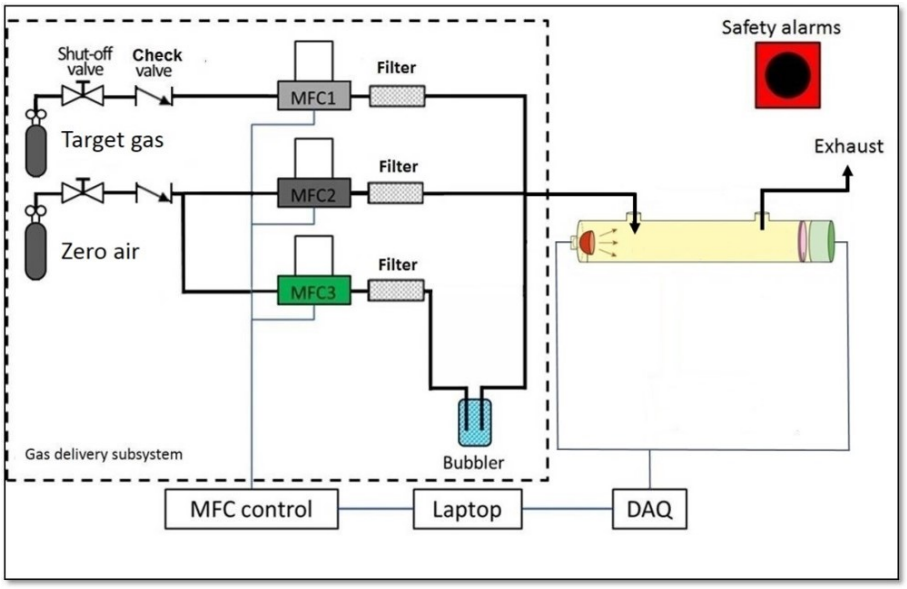

Figure 5.15: Block diagram of the gas rig setup.

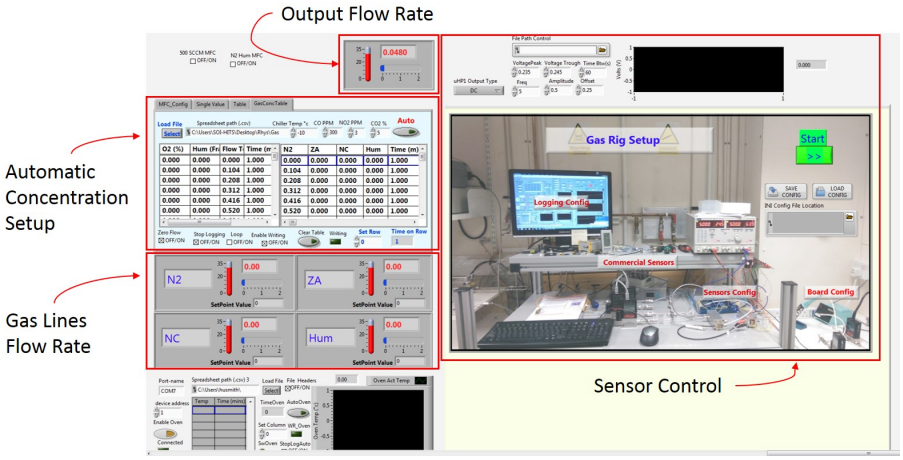

Figure 5.16: LabVIEW interface of the gas rig.

An automated gas testing rig was used to perform gas experiments. Figure. 5.15 shows the block diagram of the gas rig setup. Each gas line is controlled by a mass flow controller, which is used to adjust gas concentration levels through a LabVIEW program. One of the zero air gas line is first fed into a bubbler containing distilled water to add humidity to the system. The exhaust is also monitored by a MFC to check for gas leakage, before outputting to a fume cupboard. The system is controlled through a LabVIEW interface shown in Figure. 5.16. A NI DAQ system is used to power the sensor, sample and collect response data.

Gas bottles from BOC and CK Special Gases Ltd. were used to perform gas experiments. Table. 5.4 summarises the gas concentration information used for the following experiments.

Table 5.4: List of gas bottles and concentration levels.

Supplier	**Gas Type**	**Max. Concentration**	**Carrier Gas**
BOC	Carbon Monoxide	300ppm	Zero Air
CK Special Gases	Carbon Monoxide	400ppm	Hydrogen
BOC	Carbon Dioxide	500ppm	Zero Air
BOC	Carbon Dioxide	5%	Zero Air
CK Special Gases	Hydrogen Sulfide	30ppm	Hydrogen
BOC	Acetone	200ppm	Zero Air
BOC	Ammonia	25ppm	Zero Air

5.3 Sensor Testing and Calibration

All emitters were tested with their target gases. The maximum concentration level, based on the gas bottle limitations, was trialled first to test the functionality of the emitter with its corresponding detector. Due to the fabrication variances observed earlier, the radiation intensity at the target peak wavelength was greatly reduced. Because the detector filter only allows the target wavelength to pass through, the compromised emitters made the experiment difficult to run. Both DC and AC drive circuits were trialled to power the emitters, but the response signals were buried under the enhanced noise signals from the amplification circuit. The amplification limit of the detector board was also trialled, but no visible response could be seen. Another explanation is the low maximum gas concentration level. At a lower emission intensity, higher concentration, such as percentage level, would be easier to detect, as compared to the ppm levels available from the gas bottles.

The emitter with the designed wavelength of 4.26 μm for carbon dioxide (5% concentration) detection was trialled using the shorter gas chamber (3 cm) and an AC drive circuit to test its operating frequency. It was possible to power the emitter at a higher frequency (> 30 Hz), but no response could be observed on the detector side. Fast Fourier transform (FFT) was trialled for post-processing to extract signals at the operating frequency, but the response was not visible. Even though a shorter

gas chamber is more suited for high concentration levels, the micro hotplate size (60 μm dia.) can be too small to emit enough radiation.

The only emitters that were able to detect gas were the acetone and ammonia emitter chips, as their plasmonic designs tend to have high emission intensities at a higher wavelength range(> 7.5 μm). Therefore, the following section focuses on the results obtained for acetone and ammonia detection.

5.3.1 Experiments in Dry Air

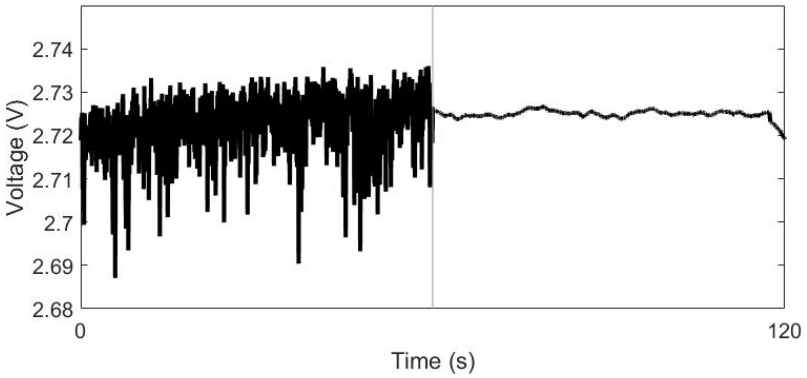

Figure 5.17: Raw (left) versus filtered (right) data.

Synthetic zero air was used to perform dry air experiments. Acetone gas at concentration levels from 50ppm up to 200ppm, and ammonia gas at concentration levels from 10ppm up to 20ppm were trialled. Various concentration steps were tested with zero air as baseline in between in each experiment run. Because NDIR can response to the target gas within a short period of time, i.e. ∼30–40ms, each concentration step was only on for 2 minutes. DC voltage supply was used and a constant flow rate of 0.5 slpm was applied throughout the experiment. The same experiment was performed for three times and the collected data in voltage was then post processed in MATLAB. The moving average and median filter were used to remove noise signals and random spikes. Figure. 5.17 shows the raw data versus the post processed data. The noise and spikes can be greatly reduced to reveal the true sensor signal changes. Figure. 5.18 and 5.19 show the post processed data averaged over three experiments of the sensor response towards acetone and ammonia, respectively.

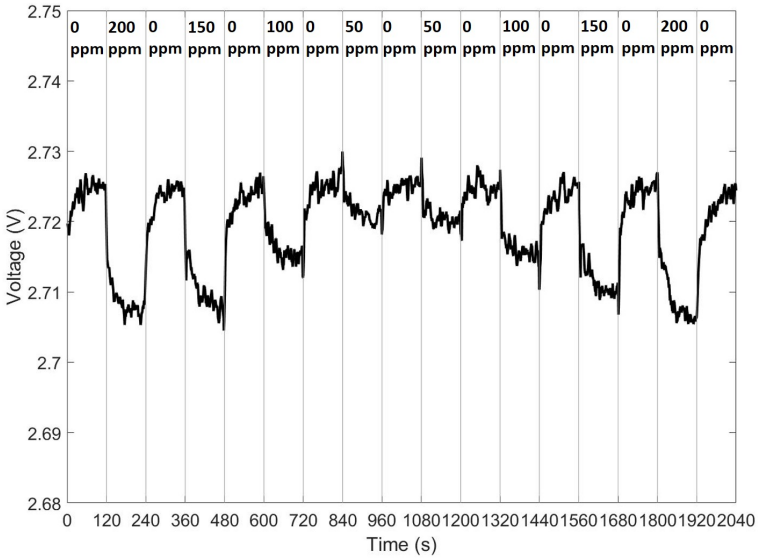

Figure 5.18: NDIR sensor experiments with acetone from 50ppm to 200ppm in dry air.

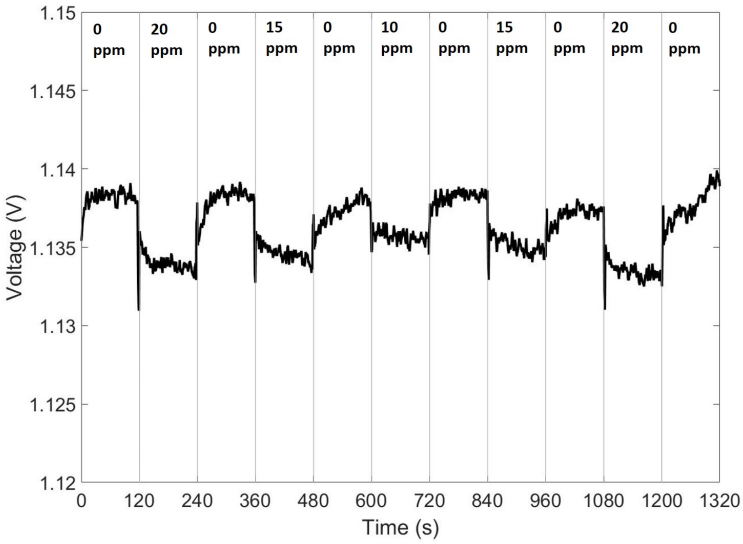

Figure 5.19: NDIR sensor experiments with ammonia from 10ppm to 20ppm in dry air.

5.3.2 Experiments in Humidity

Similar experiments were performed under humidity conditions. 25% and 50% relative humidity (RH) levels were generated through a bubbler and mixed together with the synthetic dry air as the baseline for these experiments. Same as the dry air experiments, various concentration steps were trialled for two minutes each

with a DC power supply and a constant 0.5 slpm flow rate controlled by LabVIEW and DAQ. The concentration levels were limited by the bottle concentration and total flow rate, as the humidity needs to be added as part of the flow rate. Therefore, in the acetone test, for 25% relative humidity, the concentration levels from 50ppm to 150ppm were trialled; and for 50% relative humidity, concentrations from 25ppm to 75ppm were trialled. Ammonia was only trialled under 25% relative humidity with concentration levels from 10 ppm to 20 ppm. Figure. 5.20, 5.21 and 5.22 show the experimental results averaged over three runs using the same post-processing filters as before in MATLAB.

Based on the relative humidity values, the absolute humidity can be calculated, which is defined as the mass of water vapour in a certain volume [12]. This is a more accurate way to measure the humidity level in the air as it considers both the ambient temperature and pressure. The formula used to calculate absolute humidity (A) is:

$$A = C \times P_w / T \tag{5.1}$$

where C is the constant number of 2.16679 gK/J, P_w is the vapour pressure (Pa), and T is the temperature in Kelvin. The vapour pressure (P_w) is calculated using saturated vapour pressure (P_{ws}) times the relative humidity in decimal. Therefore, the absolute humidity value under room temperature (23.5 °C) for 25% RH and

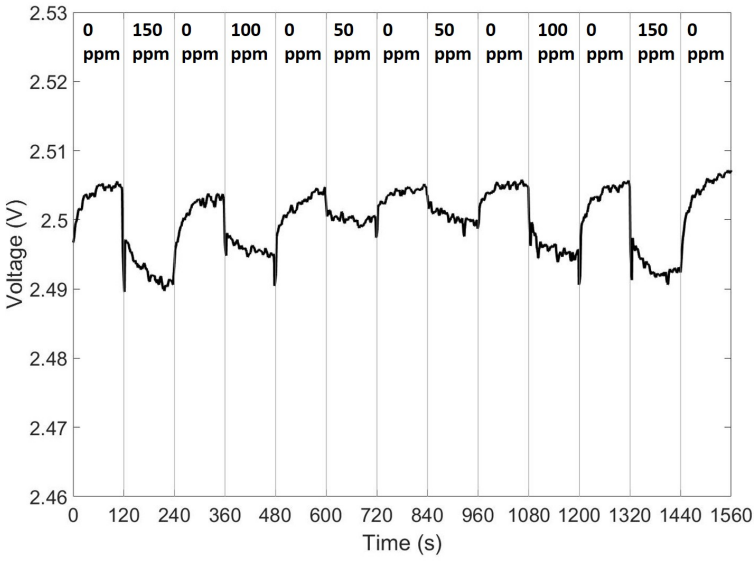

Figure 5.20: NDIR sensor experiments with acetone from 50ppm to 150ppm in 25%RH.

50% RH is 7 g/m^3 and 14 g/m^3, respectively.

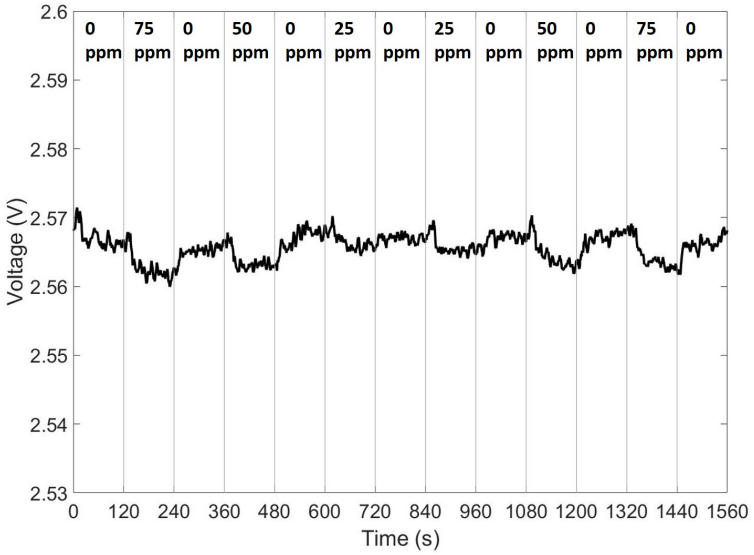

Figure 5.21: NDIR sensor experiments with acetone from 25 ppm to 75 ppm in 50% RH at room temperature.

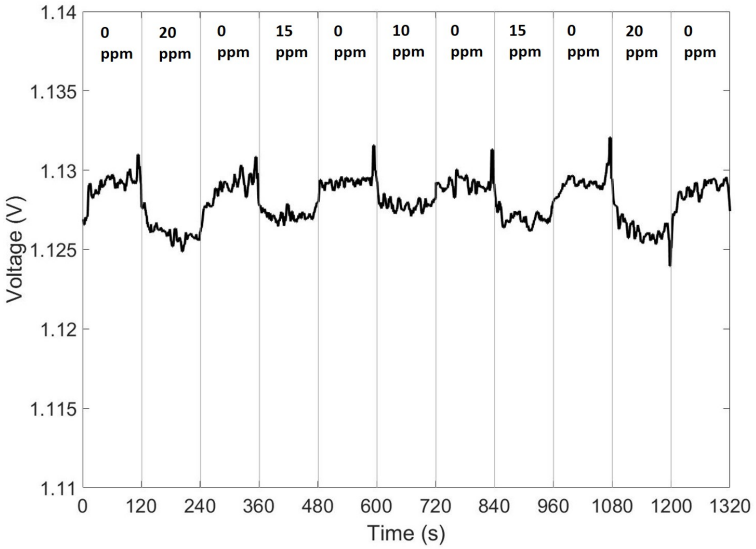

Figure 5.22: NDIR sensor experiments with ammonia from 10 ppm to 20 ppm in 25% RH at room temperature.

5.3.3 Analysis

The sensors with plasmonic enhanced emitters performed well in both acetone and ammonia tests under different humidity levels. Both sensors responded within 30 ms. Due to the low gas concentration ranges, the response signals were small, even after the amplification circuit. But after post-processing with the moving average and median filter, the signals became more visible. As different concentration levels of acetone and ammonia were trialled, it is not possible to compare the two gases together. However, it is expected that they should respond a similar manner.

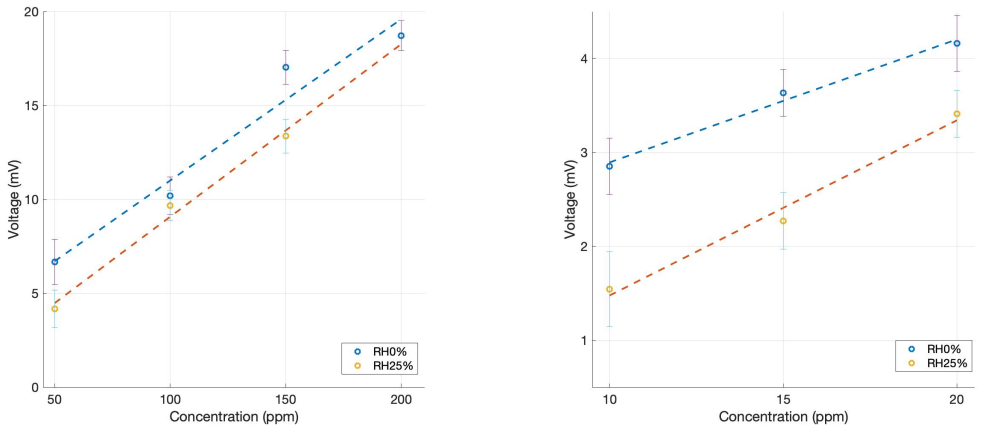

(a) Sensor in acetone.

(b) Sensor in ammonia.

Figure 5.23: Sensor response (voltage difference) in acetone and ammonia at dry and 25% RH conditions (room temperature).

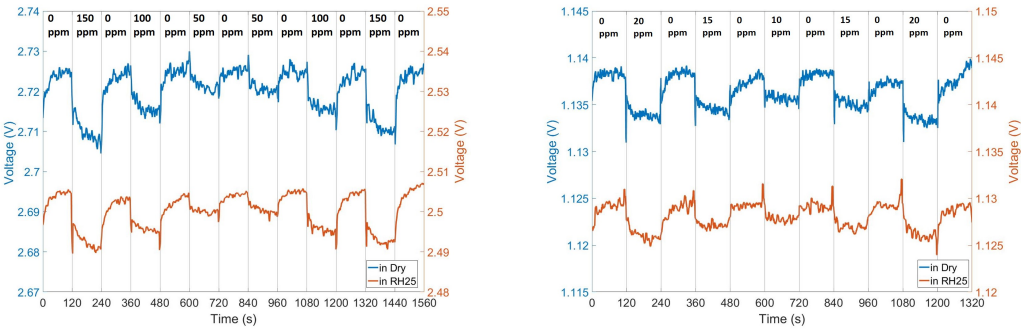

(a) Sensor in acetone.

(b) Sensor in ammonia.

Figure 5.24: Sensor response in acetone and ammonia at dry and 25% RH conditions (room temperature).

The sensor response increases with the increase of concentration levels, as more gas molecules are mixed and reacted with the infra-red. Figure. 5.23 plots the voltage changes of the sensors towards various concentration levels. The voltage to concentration change is linear as expected. Humidity affects the sensor baseline as well as the response range, which can be observed both in Figure. 5.23 and 5.24. At the same concentration level (150ppm acetone), the baseline dropped around 30%, but this can vary depending on the humidity levels.

5.4 NDIR applications

The NDIR sensor can be used in various applications. In industry, it is widely used for CO_2 detection. CO_2 can be found in our everyday life, as an important standard for air quality monitoring and ventilation system. It is also one of the greenhouse gases, and can be found in agriculture, health care, transportation, etc.. While some gas tests are stationary, in certain scenarios moveable or portable sensors are preferred. One aim of the miniaturised NDIR sensor is to make it easy to carry and suitable for various portable applications. All the experiments performed before in this chapter require of a Keithley power supply and a DAQ for control and data collection, which are not ideal to carry for outside laboratory experiments. Therefore, in this section, a portable NDIR sensor system is described. Such setup is implemented into two projects for different applications: SmokeBot to aid firefighters, and Supergen detect impurities in hydrogen.

5.4.1 Portable NDIR system

As mentioned previously, the emitters can be powered either by DC supply or AC supply. The circuit board for DC supply is the same as previously mentioned. For AC supply, a frequency generator circuit is integrated onto the emitter board, thus removing the need for an extra breakout board to achieve a more compact design. Figure. 5.25 shows the populated emitter board with a frequency generator. The same circuit on the breakout board was used, which was able to generate sinusoidal wave with a microcontroller SPI communication.

A PCB motherboard was used to connect the microcontroller with the NDIR sensor together with other sensors and electronics components. Figure. 5.26 shows

the flow chart of an example system setup, which will be explained in details for each project. The system can be portable with battery power supply, or integrated with other system (i.e. a mobile robot) for a more advanced application.

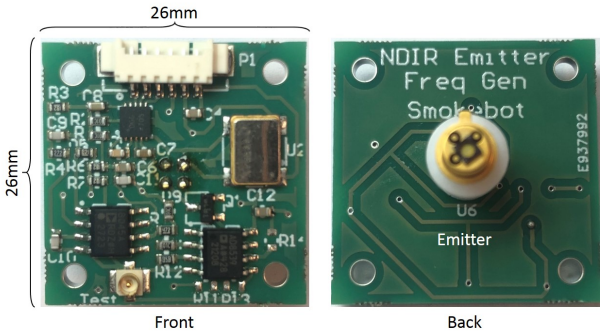

Figure 5.25: NDIR sensor emitter board with frequency generator circuit.

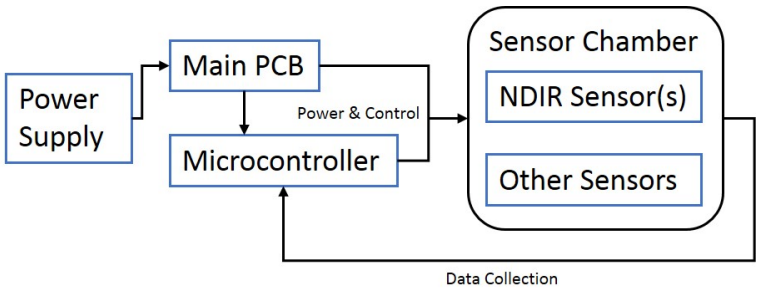

Figure 5.26: Flow chart of a portable NDIR sensor system setup.

5.4.2 NDIR on Mobile Robot

The SmokeBot project was funded under the EU Horizon 2020 Framework (project ID: 645101). The aim was to operate mobile robot in domains with restricted visibility and possible hidden danger, mainly to aid fire brigades in search and rescue missions, prior to the deployment of human team. It incorporated a fusion of sensors, including LIDAR, Radar, thermal camera and gas sensors, to provide a comprehensive environmental information. This project addressed the shortcomings of sensors in harsh conditions, which the existing commercial sensors could not cope, by developing novel sensors and prototyping them with an industrial explorer robot. The end product was demonstrated and tested in a fire training station with a burning house.

As a part of the novel RGT-V unit (radar, gas sensors, thermal cameras - vision), a gas sensing unit, namely FireNose, was developed which was able to detect

and discrimination gases in harsh conditions, i.e. high temperature, high humidity, falling debris, smoke, etc.. Four micro hotplate based sensors were used (three metal oxide sensors and one NDIR sensor) together with commercial sensors (flow sensor, particle sensor and environmental sensor), all housed inside a robust steel enclosure. Similar to the portable NDIR sensor system mentioned in the previous section, a microcontroller was used to drive sensors and collect/process data. Figure. 5.27 shows the flow chart of the FireNose, and Figure. 5.28 shows the photography of the unit.

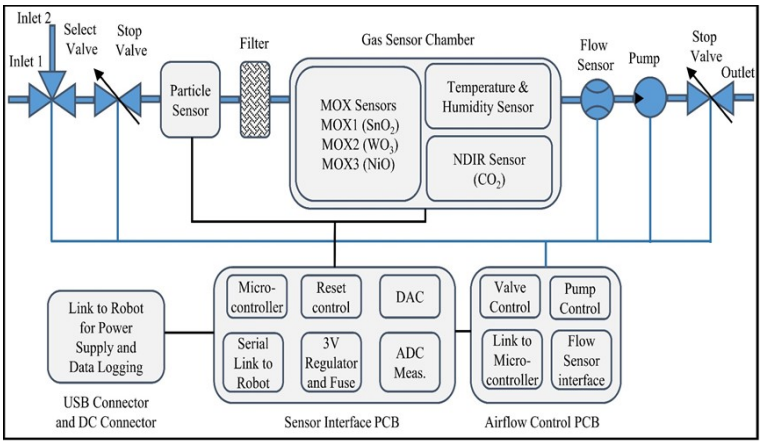

Figure 5.27: Block diagram of the FireNose.

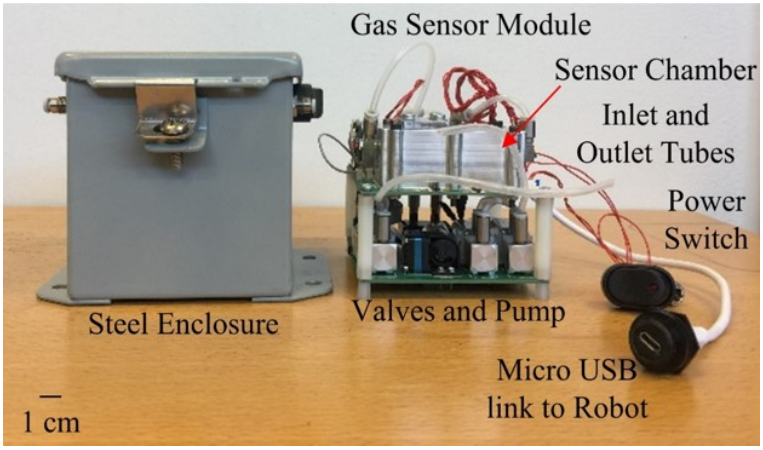

Figure 5.28: Photograph of the FireNose with enclosure (dimension: 100 mm × 100 mm × 100 mm).

Both the MOX sensors and NDIR sensor were studied and characterised with the unit. This section will focus on the performance of the NDIR sensor. The NDIR sensor, as shown in Figure. 5.29, comprises of an emitter, a detector and a gas cell. The gas cell has the length of 5 cm, which is smaller than the standard testing

chamber (i.e. $\sim$ 10 cm). It is the optimised size that can fit into the compact enclosure while keeping its detectability of the target gas. The whole sensor is screwed on to an adjustable slot on the circuit boards, so the sensor can be easily changed and replaced if necessary. The target gas in this project is CO_2 as one of the common gas found in harsh environment. But during the characterisation of the unit, acetone was used instead. Therefore the sensor was replaced with an acetone emitter and detector pair during trial runs.

An AC driven CO_2 sensor is preferred on the mobile robot, as the movement of the robot together with the operating noise from the surrounding equipments will

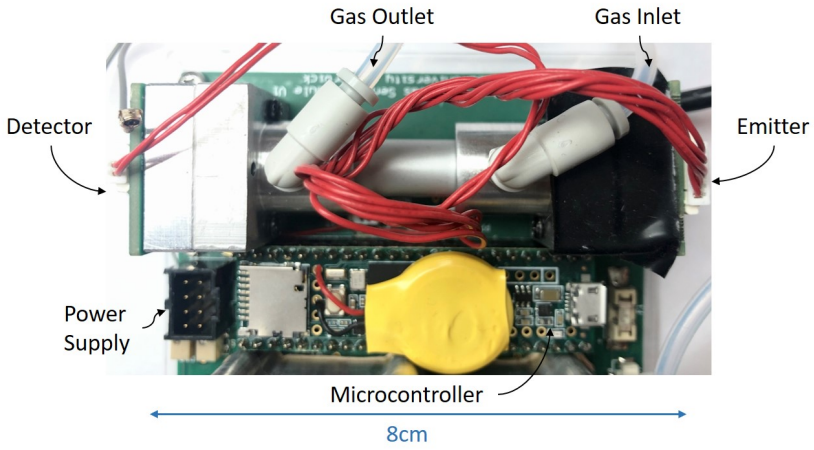

Figure 5.29: NDIR sensor with microcontroller on the main PCB of the FireNose.

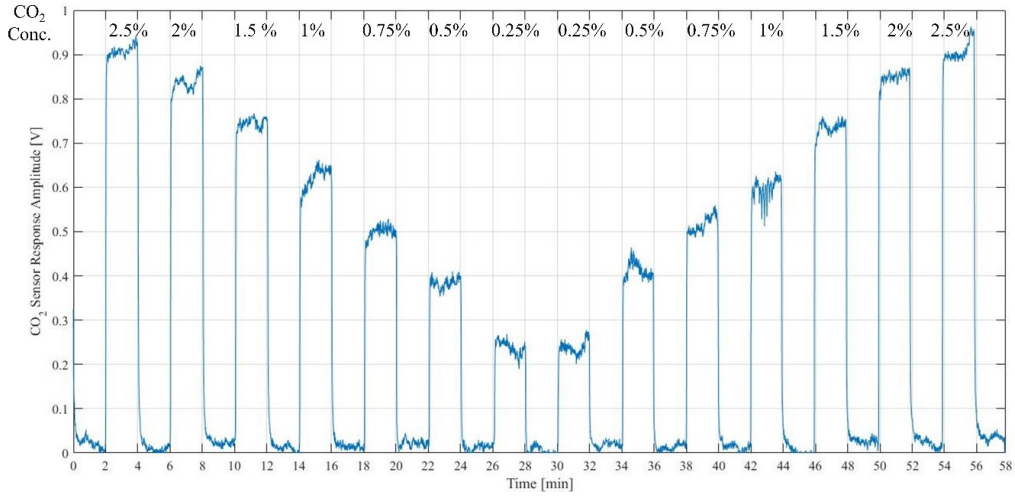

Figure 5.30: CO_2 NDIR sensor response after post-processing towards different concentration levels [13].

interfere with the DC signals. However, with AC signals, those noises can be ignored by performing FFT to extract the signal at the operating frequency. Figure. 5.30 shows the sensor response after processing with different concentration levels.

The characterisation results of acetone were demonstrated in the previous section. In the trial runs with a mobile robot, liquid with high acetone content (i.e. nail polish remover) was poured onto a piece of paper and waved in front of the inlet of the FireNose. Figure. 5.31 is the screenshot of such response transmitted wireless to a laptop. The transmitting frequency is equivalent to the data output frequency, which is 10Hz. The two peaks correspond to the two waves.

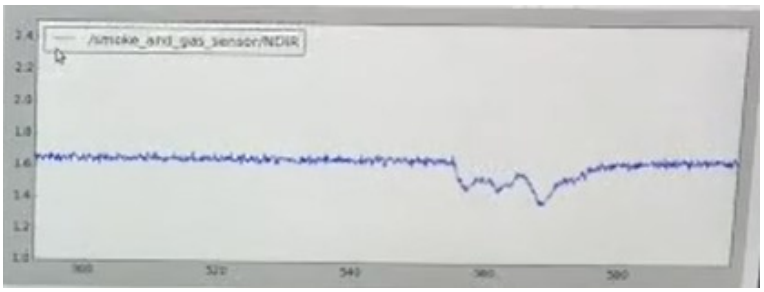

Figure 5.31: Screenshot of the acetone NDIR sensor towards liquid acetone vapour on the mobile robot.

5.4.3 NDIR for Impurity Detection

A similar design was applied for impurity detection of hydrogen in hydrogen fuel cells. Hydrogen has received a growing attention as an emerging energy source to replace the traditional diesel or petrol fuel for automobiles. It is categorised as clean energy source as the by-product of hydrogen fuel and oxygen is pure water. This pollution-free alternative can also increase the engine efficiency to 60% compared to the conventional engine efficiency of 35% [14]. One of the most promising fuel cell technologies for light-duty transportation (cars, small vans, etc.) is Polymer Electrolyte Membrane (PEM). It consists of a proton conducting membrane (electrolyte) with electrodes on each side (anode and cathode) [15]. The hydrogen fuel used in this process is produced through a reformation of natural gases, such as methane (CH_4) or other organic fuels. However, these gas sources often contain impurities such as carbon oxide (CO, CO_2), H_2S, NH_3, NO_x, SO_x and organic sulfur-carbon or carbon-hydrogen compounds [16]. Impurity is one of the most important issues in fuel cell operations, as it affects the performance of the fuel cell causing

cell degradation, membrane damage, and reducing cell life. Therefore, monitoring the impurities is a crucial task for maintaining the functionality of fuel cells.

As one of the partners in the EPSRC SuperGen project (EP/L018330/1), an impurity detection system was designed, which consists of micro-hotplate based

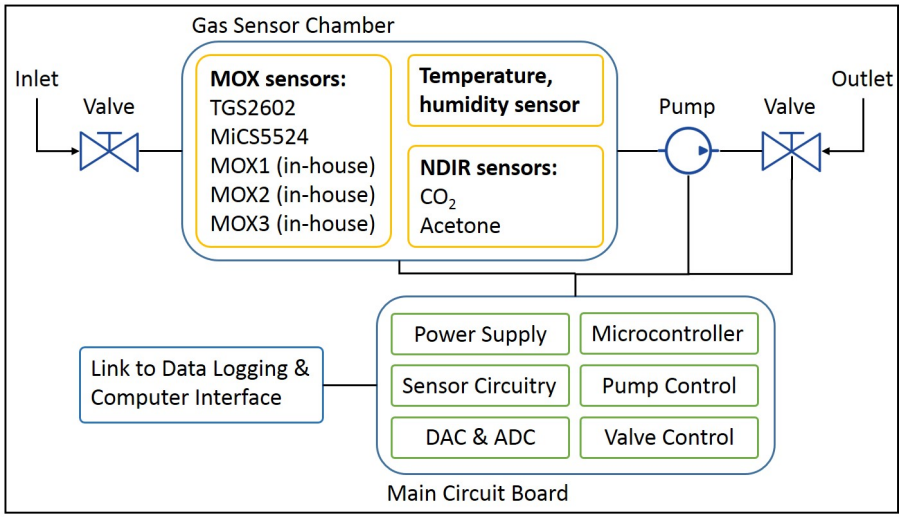

Figure 5.32: Block diagram of the hydrogen fuel cell impurity detection system.

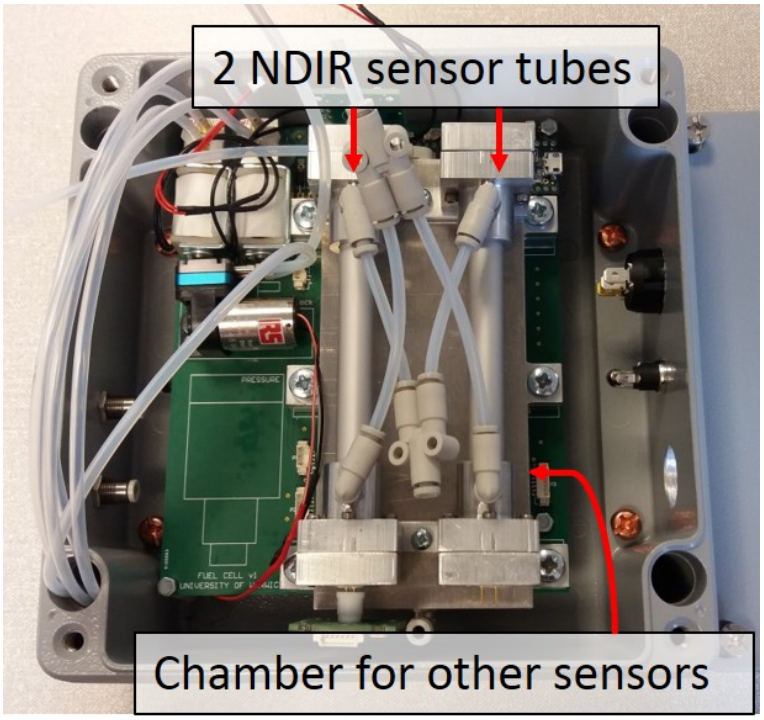

Figure 5.33: Photography of the impurity detection system.

sensors: MOXs and NDIRs. Both commercial sensors and sensors made in-house were used. In total, five MOX sensors (2 commercial and 3 in-house) and 2 NDIR sensors (in-house and plasmonic) were integrated into this system. Figure. 5.32 shows the block diagram of the system, and Figure. 5.33 is the photography of the prototype. Mox sensors were selected to detect different impurities, and the NDIR sensors were chosen to detect CO_2 and ammonia. The same emitters and detectors mentioned earlier were used in the system with a 9 cm length gas cell.

A steel enclosure was used to house this system, which can be used in harsh conditions such as high temperature, humidity or low oxygen environments. This unit is USB powered and can be adapted for more complex tasks. The system also contains an integrated environmental sensor (BME280, BOSCH) for ambient humidity, temperature and pressure monitoring. All sensors are integrated, and the unit can be used for a comprehensive air quality monitoring, harsh environment exploring, or impurities detection in hydrogen fuel. The prototyped unit can be further improved, such as better signal processing capabilities, and new methods for data logging and added display for easy readout.

5.5 Conclusions

In this chapter, the fabricated plasmonic emitter chips were assembled and tested in this chapter. Six 6-inches wafers, three bulk and three SOI process, were diced and returned from the foundry. Each wafer has 26 reticles. Apart from one wafer broken during dicing, in total, 76 bulk chips and 53 SOI chips were fabricated for each emitter design. Chips from each design were picked and measured under a scanning microscope before laboratory experiments. A variation (more than 5%) was observed in all designs, which affects the resonance peak of the emitters. Despite these variations, all emitters were tested under a gas rig. Commerical detectors from Heimann Sensors GmbH were used for the tests. They are thermopile based detectors with narrow-band optical film filter integrated on the lid. The optical film has a band-gap of $180 \sim 250$ nm centred at the target frequency peaks. Different optical cells were also discussed in terms of length and shape. The selected gas cell is a straight aluminium tube with gold inter coating.

An automated gas rig and a NI DAQ system were used to perform the gas experiment. It is controlled by a LabVIEW program which can automatically ad-

just the gas concentration levels through mass flow controllers. The sensors were driven by external circuitries with a constant current circuit for the emitters and amplifiers for the detectors. All gases of interest were trialled, carbon monoxide, carbon dioxide, hydrogen sulfide, acetone and ammonia. But due to the variation occurred in fabrication, only acetone and ammonia showed visible responses during experiments. Various concentration steps were trialled for these two gases, up to 200 ppm for acetone and 20 ppm for ammonia, in both humid (25% and 50% relative humidity) and dry air. The collected data were post-processed using MATLAB to remove noise and spikes. The processed results were then presented and compared.

Applications for the NDIR sensor were also described in this chapter, especially for two projects: SmokeBot and SuperGen. A portable, compact NDIR sensor system comprises a main circuit board with a microcontroller to drive sensors and collect data, and a power supply source. A sensor system, including NDIR sensors, was designed for both projects. In SmokeBot, the NDIR sensor was used to detect CO_2 in harsh environments to aid fire brigades, but acetone was used for trial runs. In the SuperGen, the sensor system was used to detect impurities in hydrogen for hydrogen fuel cell, therefore, impurities such as CO_2 and ammonia were the target gases for NDIR sensors.

This chapter concludes the research on plasmonic NDIR sensors. This research shows the advantages and applications of plasmonic enhanced infra-red emitters in gas detections at a low ppm range. Due to the fabrication variance, the full extent of the emitters cannot be conducted, which requires another wafer run and further work. As the functionality of the plasmonic structure has been proven, it can also be applied to the detector design, for a true filterless NDIR sensor. A preliminary study on the optical path was examined, but it deserves further study with simulation and prototyping. Overall, a novel plasmonic metamaterial was trialled and tested. The performance shows promising results and further work are needed.

References

[1] T. A. Vincent and J. W. Gardner, "A low cost MEMS based NDIR system for the monitoring of carbon dioxide in breath analysis at ppm levels," *Sensors and Actuators B: Chemical*, vol. 236, pp. 954–964, 2016.

[2] T. A. Vincent, "Development of a handheld breath analyser for the monitoring

of energy expenditure," PhD Thesis, University of Warwick, Coventry, UK, 2017.

[3] J. Peng, X. M. Ji, Y. W. Shi, Q. Liu, Z. M. Bao, and Y. P. Huang, "A novel NDIR CO_2 sensor using a mid-IR hollow fiber as a gas cell," in *2010 10th IEEE International Conference on Solid-State and Integrated Circuit Technology (ICSICT)*, 2010, pp. 1489–1491.

[4] P. Barritault, M. Brun, O. Lartigue, J. Willemin, J.-L. Ouvrier-Buffet, S. Pocas, and S. Nicoletti, "Low power CO_2 NDIR sensing using a micro-bolometer detector and a micro-hotplate IR-source," *Sensors & Actuators: B. Chemical*, vol. 182, pp. 565–570, 2013.

[5] E. Fearon, T. Sato, D. Wellburn, K. Watkins, and G. Dearden, "Thermal effects of substrate materials used in the laser curing of particulate silver inks," *Proceedings of the International Conference on Laser Assisted Net Shape Engineering*, vol. 5, pp. 379–390, 2007.

[6] R. Frodl and T. Tille, "A high-precision NDIR CO_2 gas sensor for automotive applications," *IEEE Sensors Journal*, vol. 6, no. 6, pp. 1697–1705, 2006.

[7] J. Mayrwoger, P. Hauer, W. Reichl, R. Schwodiauer, C. Krutzler, and B. Jakoby, "Modeling of infrared gas sensors using a ray tracing approach," *IEEE Sensors Journal*, vol. 10, no. 11, pp. 1691–1698, 2010.

[8] J. Hodgkinson, R. Smith, W. Ho, J. R. Saffell, and R. P. Tatam, "A low cost, optically efficient carbon dioxide sensor based on nondispersive infra-red (NDIR) measurement at 4.2 μm," in *Proceedings of the SPIE*, vol. 8439, 2012, pp. 843 910–843 919.

[9] J. Hodgkinson and R. P. Tatam, "Optical gas sensing: a review," *Measurement Science and Technology*, vol. 24, no. 1, pp. 12 004–12 063, 2013.

[10] N. Fujitsuka, M. Yonemura, K. Sakakibara, T. Taguchi, and T. Wakita, "Alcohol detection in exhaled air by NDIR method," *IEEJ Transactions on Sensors and Micromachines*, vol. 132, no. 7, pp. 219–223, 2012.

[11] A. Ganesan, "A novel high sensitivity NDIR plasmonic gas sensor for hydrogen fuel cell," Master Thesis, University of Warwick, 2015.

[12] Vaisala, "Humidity conversion formulas: calculation formulas for humidity," Vaisala Oyj, Tech. Rep., 2013. [Online]. Available: www.vaisala.com

[13] T. A. Vincent, Y. Xing, M. Cole, and J. W. Gardner, "SmokeBot WP2 periodic report 2017-2018," University of Warwick, Coventry, UK, Tech. Rep., 2018.

[14] Fuel Cell Technologies Office, "Fuel cells." [Online]. Available: https://www.energy.gov/eere/fuelcells/fuel-cells

[15] S. Litster and G. McLean, "PEM fuel cell electrodes," *Journal of Power Sources*, vol. 130, no. 1-2, pp. 61–76, 2004.

[16] X. Cheng, Z. Shi, N. Glass, L. Zhang, J. Zhang, D. Song, Z.-S. Liu, H. Wang, and J. Shen, "A review of PEM hydrogen fuel cell contamination: Impacts, mechanisms, and mitigation," *Journal of Power Sources*, vol. 165, no. 2, pp. 739–756, 2007.

Chapter 6

Signal Processing Technique with Thermal Modulation for Toxic Gas Sensing

6.1 Introduction

The following two chapters focus on micro-hotplate based metal oxide gas sensors. Metal oxide sensors (MOX) are popular for their low cost, simplicity and wide detection ranges. However, they are notoriously unstable with considerable baseline drifts and long recovery times. They also lack selectivities towards different gases. To overcome those issues, two signal processing techniques are proposed.

In this chapter, a thermal modulation technique is described to solve the baseline drift problem of MOX sensors. This micro-hotplate based sensor is powered by a pulse signal that switches the micro-hotplate temperature between two values. The collected data are then processed through a Fast Fourier Transform (FFT) to obtain the transient response information, which correlates to gas concentration level and gas type. This method is trialled both off-board as a post-processing step, and on-board for real-time signal processing. It allows the sensor to operate without the need of a prior stabilisation period and the response time can be greatly reduced. The processed information is also used in a shallow artificial neural network for regression fitting analysis.

6.1.1 Baseline Drift in MOX Sensors

Metal oxide sensors employ gas-sensing materials deposited on top of a pair of IDT and heater. The sensing principle is the change of sensor conductances when exposed to the target gas. It requires annealing prior to use, which allows the surface structure to form and stabilise. The annealing time can last from 1 hour up to 24 hours or more. This process helps to increase sensor sensitivity and reduce recovery time [1, 2]. It also helps with the baseline stabilisation and drift minimising, but drift cannot be eliminated. Drift is an issue that can be commonly found in all chemical sensors. It can be gradual, resulting in reduced sensor responses over a long time period. Holmberg *et al.* [3] categorised drifts into two types, physical drift (or sensor drift) and measurement drift. Physical drift is the drift caused by the physical or chemical interactions of the sensor, such as ageing or poisoning. Those results are irreversible, thus changing the sensor behaviour towards the same gas. The other type is measurement drift, caused by factors such as a change in the gas flow rate, temperature, humidity, air pressure, etc. Some of these aspects can be controlled and some are not. Therefore, to extend the sensor lifetime and measurement repeatability, drift compensation is essential for chemical sensor research.

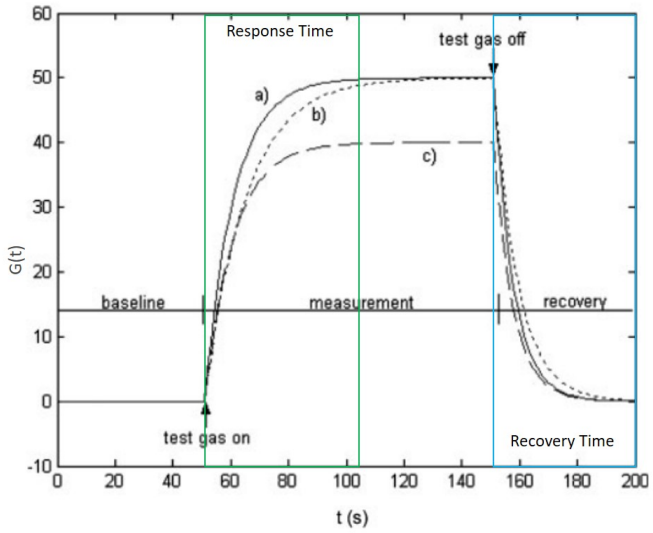

Figure 6.1: A typical n-type MOX sensor response curve to reducing gas. (a), (b) and (c) shows three possible scenarios of the same sensor response towards the same gas under the influence of different kinds of drift [3].

Figure. 6.1 shows a typical MOX sensor response towards a given gas. When

the gas is introduced, the sensor will start to respond (the sensing material interacts with gas molecules and conductance rises with a reducing gas) which can take tens of seconds (response time). After the response stage, the sensor reaches a steady-state as the gas concentration stays constant. When the gas is removed, the sensor will start to recover back to the 'no gas' baseline stage, which can be tens of seconds or even minutes (recovery time). The figure shows three curves (a), (b) and (c), which are three possible response curves for the same sensor towards the same given gas due to drifts. Presuming curve (a) is the ideal sensor response, then curve (b) is a decrease in the sensor response speed, and curve (c) is a decrease in the sensor response (at the steady-state, which is the biggest issue). Drift can also cause a difference between the baseline values before and after the gas experiment (not visible in Figure. 6.1). Figure. 6.2 shows a sensor response ($\propto$ conductance) towards a given gas at a decreasing gas concentration level. This experiment lasted for 65 minutes in total (5 mins for each concentration step), and it can be seen that the baseline drifts throughout the experiment. The concentration of the given gas decreases with zero air used as baseline in between. The sensor response decreases with concentration levels, but the zero air baseline also decreases with drifts. The plot also shows a long recovery time of the MOX sensor as compared to the response time. This could also explain the drift as the sensor has not recovered fully from the gas exposure before the next concentration level is tested.

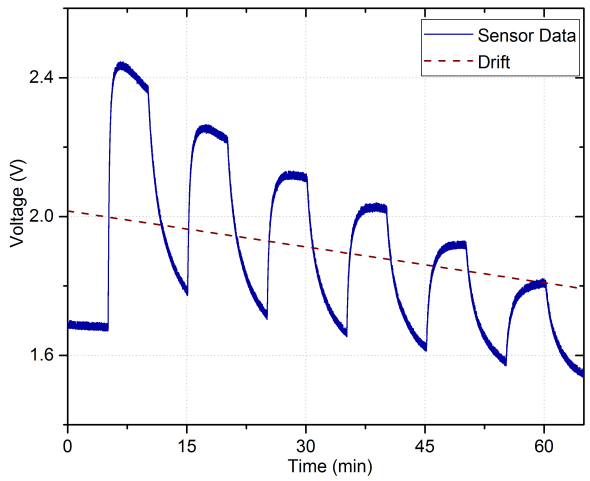

Figure 6.2: An example MOX sensor test with a given gas at different concentration levels.

6.1.2 Drift Compensation

Holmberg *et al.* [3] suggested various drift compensation methods, such as a reference gas method, sensor behaviour analysis, pattern classification, etc. Therefore, drift can be compensated either during the experiment or after in the data processing stage. For methods that can be used during gas experiments, they can either compensate the physical drift or the measurement drift. The reference gas method uses a reference gas as it assumes a strong relation between the drift and the sensor characteristics, hence a drift pattern for each sensor that can be filtered out later. This relationship can be as simple as a subtraction or division, or can be hidden requiring a pattern recognition technique. A similar approach can be applied to the measurement drift, as a change in humidity or flow rate affects more than one sensor. Therefore a similar behaviour can be observed by a reference sensor.

For drift compensation at the post-processing stage, signal processing methods can be performed, such as Principle Component Analysis (PCA), Self Organising Maps (SOM), Artificial Neural Network (ANN), etc. As a common cause for drift is related to change in humidity and temperature, an environmental sensor to monitor these two factors are preferred during the gas experiment. With the collected data, a pattern can be built showing the relationship between the sensor characteristics and environmental factors, which can then be compensated. A similar pattern can also be built when multiple sensors are used in one experiment for gas classification. More details on the pattern recognition methods will be discussed in the next chapter.

This chapter compensates the sensor response by using approaches both during the experiment and through post-processing. Thermal modulation is used during the experiment, and ANN is the post-processing approach. By combining these two methods, sensor drifts can be compensated at a faster response rate, and the response pattern can be recognised at different concentration levels. The literature review for both the thermal modulation technique and pattern recognition techniques is provided in Chapter 2.

6.2 Thermal Modulation Technique

6.2.1 Metal Oxide Sensors

In chapter 2, the technique of thermal modulation used in literature was described with its different approaches and applications. Here, this technique is incorporated into the gas experiments.

Because the MOX sensors are micro hotplate based, they are sensitive to temperature change. The micro hotplate is provided by ams Sensors Ltd, UK (formerly Cambridge CMOS Sensors). It is a circular dielectric membrane with tungsten metal layers. The device is 1 mm $\times$ 1 mm in size. The drive circuit is a current control circuit with an adjustable load resistance, as shown in Figure. 6.3. For laboratory experiments, both the circuit input and data output are connected to the NI DAQ system.

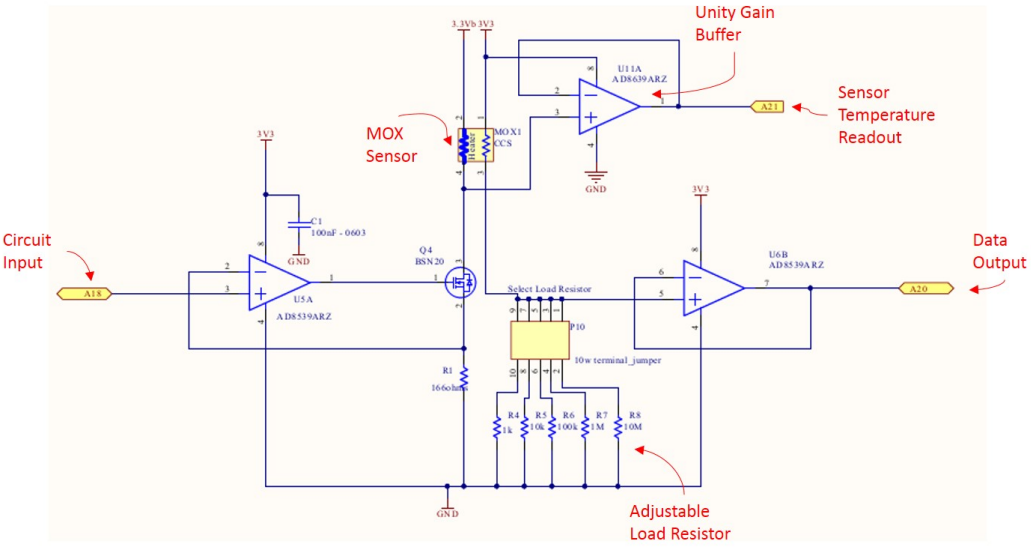

Figure 6.3: Drive circuit for MOX SOI CMOS gas sensor.

The datasheet of the micro hotplate provides the device current-temperature relationship, as shown in Figure. 6.4. The sensor can operate up to 600°C, but to achieve a balance between sensitivity (higher at higher temperature) and sensor lifetime (longer at lower temperature), the optimal operating temperature was found to be 350°C [5]. It was achieve through experiments at various temperatures to find the balance between sensitive response and long lifetime. In order to see a visible difference in the output voltage, a temperature difference of at least 50°C

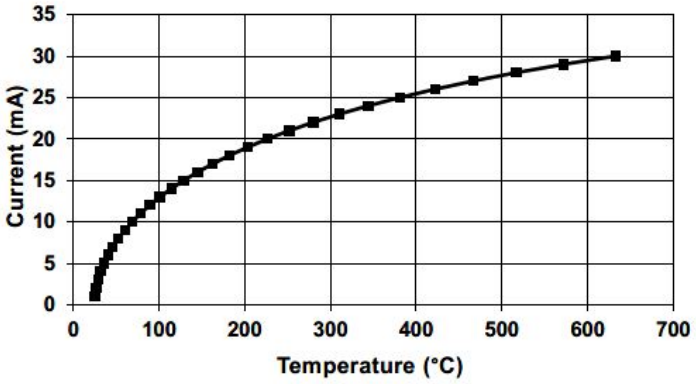

Figure 6.4: The micro-hotplate datasheet (CCS301) on current versus temperature.

was chosen for thermal modulation. Various combinations were trialled, such as 200°C and 250°C, 200°C and 300°C, 200°C and 350°C, 250°C and 300°C, and 250°C and 350°C [4]. The combination chosen here is 250°C and 300°C. For a micro hotplate temperature at 250°C and 300°C, the current needed is 21 mA and 23 mA, respectively. Therefore, the operating voltage is 0.205 V for 250°C and 0.220 V for 300 °C.

On top of the micro hotplate, gas sensitive material was deposited according to the gas detection requirement. Figure. 6.5 shows the bare micro hotplate chip and the chip with deposited material.

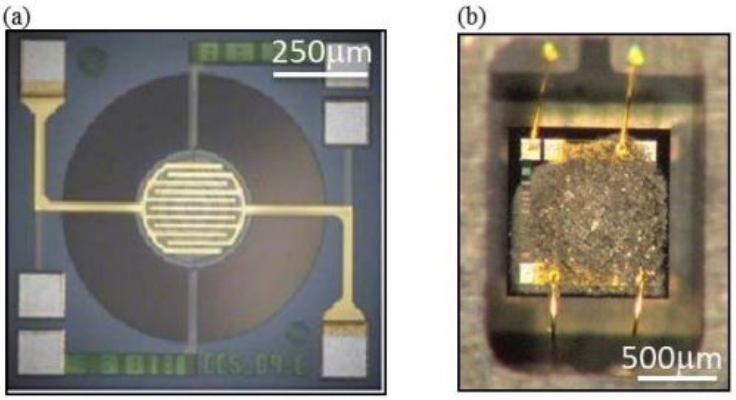

Figure 6.5: Images of (a) the bare micro hotplate and (b) with gas sensing material coating [5].

6.2.2 Processing Steps

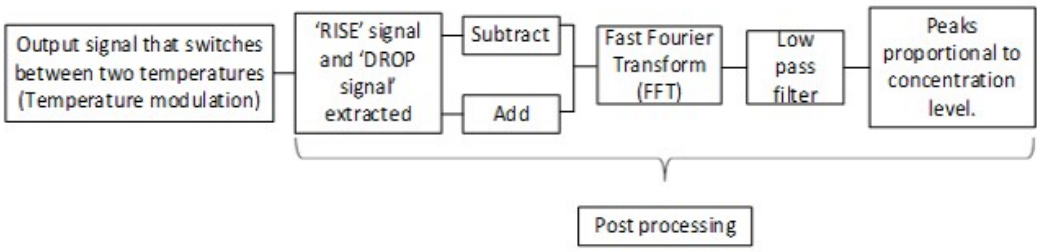

Figure 6.6: Flow chart of the thermal modulation processing steps.

Figure. 6.6 summarises the steps used in the thermal modulation signal processing method. An example of a CO experiment with a SnO_2 coated MOX sensor is used for explanation. In this experiment, the micro hotplate operating temperature was pulsed between 250°C (marked as 'LOW' state) and 300°C (marked as 'HIGH' state) for 10s each, hence a period of 20s. Five pulses were sent in total for five cycles, which were used for averaging. The sampling rate was set to 100 Hz. A 300 ppm bottle of CO gas in air was connected. Different concentration levels were explored, both in dry and wet air.

The data were collected through a NI DAQ system, and the raw data is shown in Figure. 6.7. The sensor resistance changes with different micro-hotplate

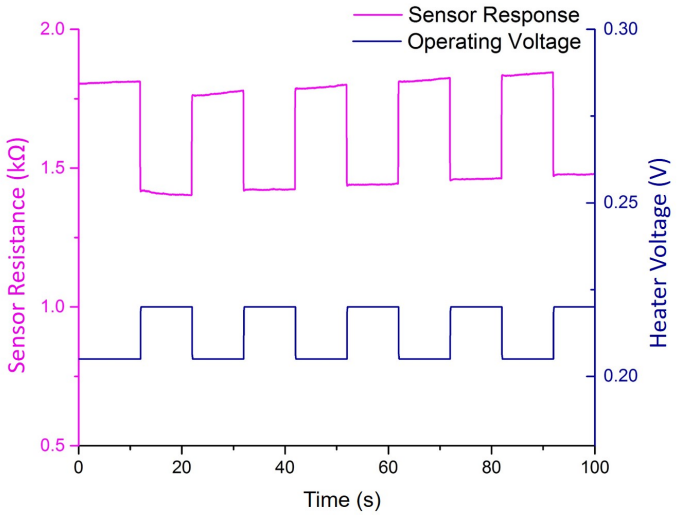

Figure 6.7: Raw sensor resistance data with thermal modulation.

temperatures. Because the MOX sensor used in this experiment is n-type, so the resistance decreases when exposed to a reducing gas. As the sensor is highly sensitive to temperature changes, so the change in resistance is almost instant. This is one of the reasons why thermal modulation is suitable for this type of sensors.

The signal post-processing was conducted using MATLAB. Each individual pulse was extracted and processed following the steps shown in Figure. 6.6. Either the sensor resistance values or the conductance values can be used for this process. These values are calculated based on the circuit, which acts as a potential divider. A 1kΩ load resistor was connected in this test. The 'detrend' function in MATLAB can remove the visible linear drift shown in Figure. 6.8(a) as an extra step, but it is not necessary. The 'HIGH' and 'LOW' transient phase of the resistance signal was extracted. The rising/dropping moment, t_0, is the dotted line in Figure. 6.8(a). The metal oxide material has different temperature coefficient towards the heating and cooling of the heater. In addition, the chemical reaction towards the target gas will also affect the thermal transient response during these two temperature conditions. Therefore, to extract these information, one of the plots (either 'HIGH' or 'LOW') was flipped to align the steady-state, and subtracted to get the difference curve.

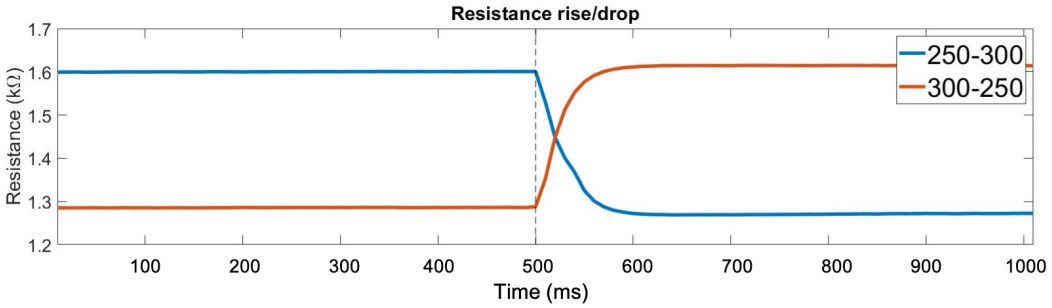

(a) Rising and falling plots aligned at t_0

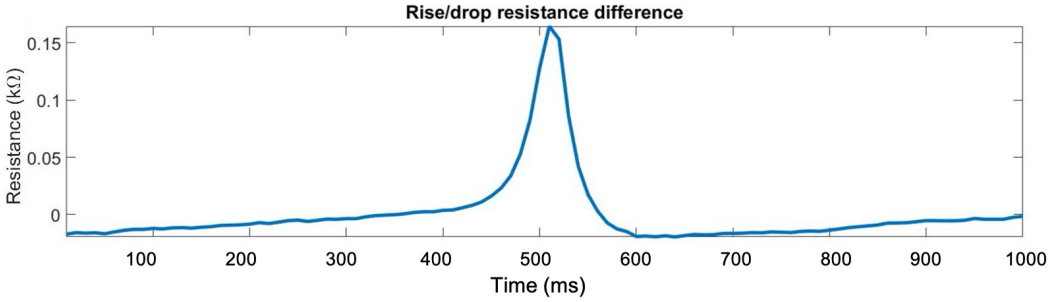

(b) Resistance difference after normalising

Figure 6.8: Temperature modulation using resistance signal in zero air.

The final step was to remove the steady-state resistance signal through subtraction to get the plot shown in Figure. 6.8(b). This difference curve various depending on the gas type and concentration levels.

Different concentration levels of the same gas were trialled. The same process was applied to signals collected at concentration levels of 0 ppm, 100 ppm, 200 ppm and 300 ppm in dry synthetic air. Their post-processing results are shown in Figure. 6.9(a). In order to study the characteristic of such peaks, a Fast Fourier Transform (FFT) was then applied to the peak window and a low pass filter to get the results shown in Figure. 6.9(b). It was found that the peaks were proportional to the concentration levels, which could be a way to characterise the sensor response and identify the gas concentration level.

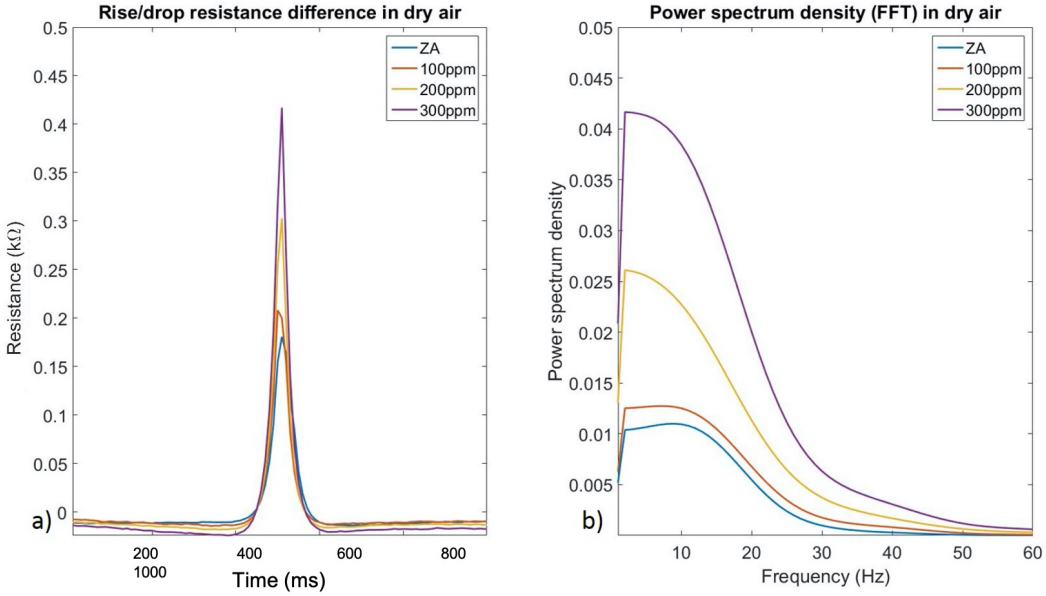

Figure 6.9: (a) Peaks of resistance difference in dry air with concentration levels of 0 ppm, 100 ppm CO, 200 ppm CO and 300 ppm carbon monoxide at room temperature. (b) Corresponding FFT power spectrum density plot with low pass filter in dry air with concentration levels of 0 ppm, 100 ppm, 200 ppm and 300 ppm carbon monoxide.

A similar experiment with 15% relative humidity was also trialled and processed. Figure. 6.10 shows the peaks of resistance differences at different concentration levels, as well as the FFT power spectra. When the humidity was introduced, the resistance differences, as well as the power densities of the FFT greatly increased.

The sensor conductance can also be used in this technique [6, 7]. The only difference is instead of subtracting the 'HIGH' and 'LOW' transient, they will be summed up as shown in Figure. 6.11. Same as before, the rising/dropping moment, t_0, was aligned first. The summed peak signals at different concentration levels were plotted in a similar manner as before for comparison (Figure. 6.12).

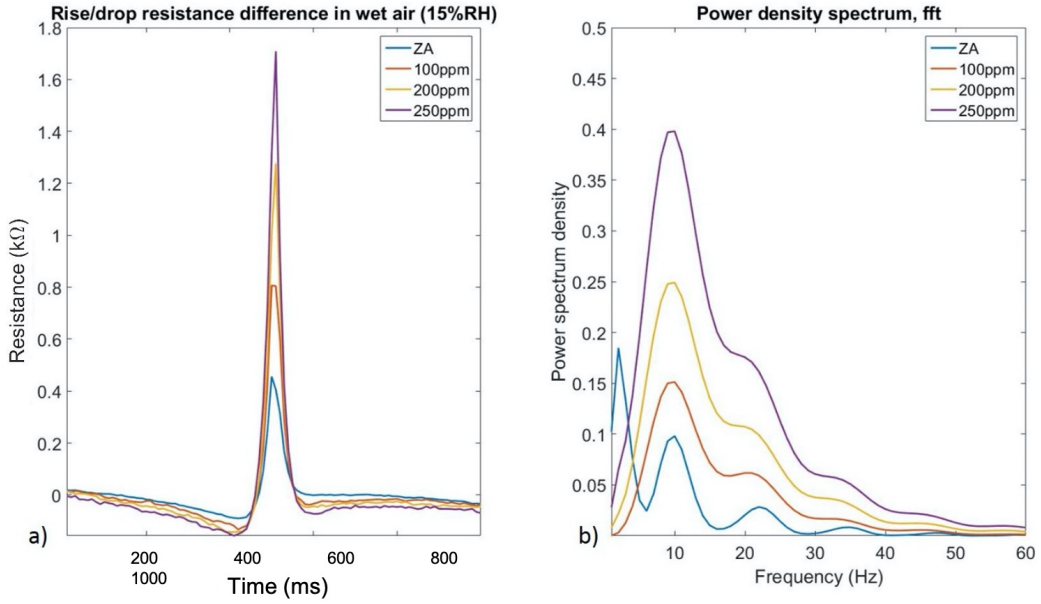

Figure 6.10: (a) Peaks of resistance difference in 15% RH (at room temperature) with concentration levels of 0 ppm, 100 ppm CO, 200 ppm CO and 250 ppm carbon monoxide. (b) Corresponding FFT power spectrum density plot with low pass filter in 15% RH with concentration levels of 0 ppm, 100 ppm, 200 ppm and 250 ppm carbon monoxide.

Both the resistance and conductance results show the relationship between the peak values/FFT power densities and the gas concentration levels. This information was obtained through this thermal modulation technique. Although five pulses of 20s were used in this trial, in reality, the pulse period can be shorter, which will be demonstrated in a later section. By doing so, the sensor response time can be greatly reduced from tens of seconds to a few seconds only (depending on the pulse period). It also has the advantage of drift compensation as the gradual baseline drift will not affect any further processing steps. The subtraction of the two transient phases will remove the drift and reveal only the relevant information, that is the peak magnitudes. The peak amplitude correlates to the gas concentration level, as well as the test condition (dry, wet, etc.). It shows a pattern that can be utilised for further processing, which will be presented in a later section. Overall, this thermal

modulation technique proves to be a feasible signal processing technique for MOX gas sensors.

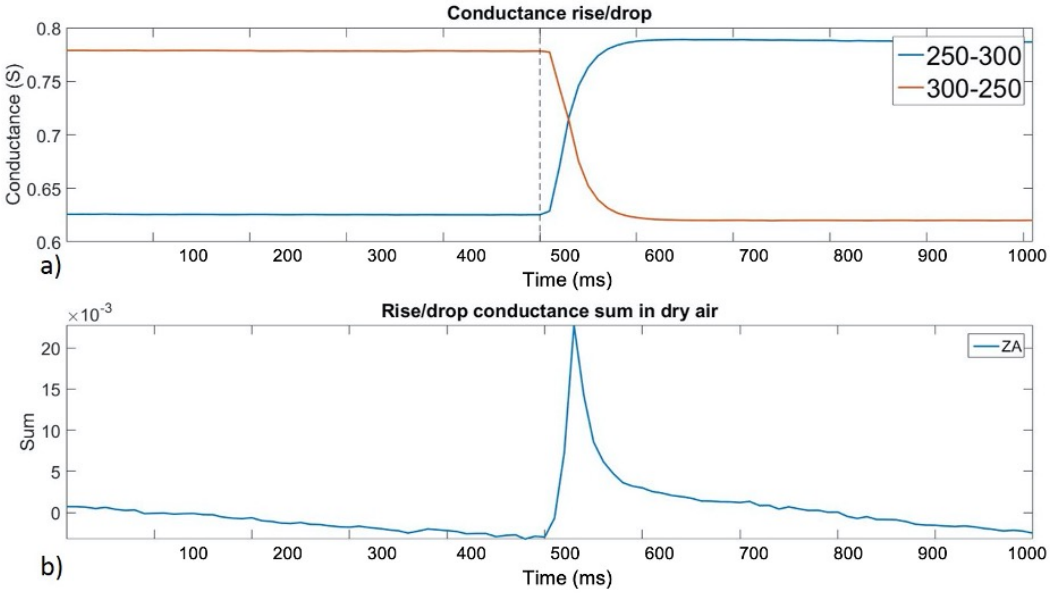

Figure 6.11: Temperature modulation using conductance signal in zero air, (a) rising and falling plot aligned at t_0, (b) conductance sum after normalising.

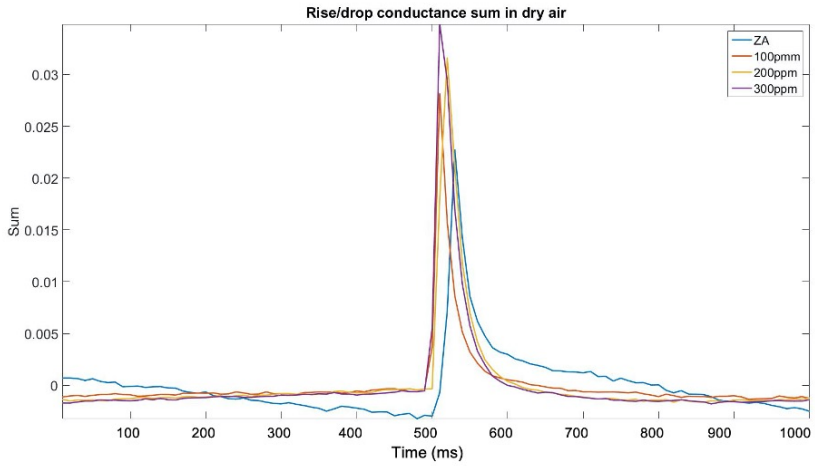

Figure 6.12: Peaks of conductance sum in dry air for: 0 ppm, and 100 ppm CO, 200 ppm CO and 300 ppm CO at room temperature.

6.3 Real-time Application Using Microcontroller

In Chapter 5.4, two sensor applications were introduced. Both consist of a portable and compact gas sensing unit. One of the applications is to aid fire fighters in search and rescue missions. For such application, a fast sensor response towards the change of gas concentrations is necessary. Furthermore, an accurate and detailed concentration indication will be of great help for gas mapping. Three MOX sensors were used in such application scenario, which had customised chemical coatings and was controlled by a microcontroller. This section focuses on the signal processing of these three sensors, in particular, the integration for an on-board thermal modulation technique to deliver a fast gas indication.

The three MOX sensors are custom-made based on the micro hotplate mentioned earlier, and coated with Pt/Pd doped n-type tin dioxide (SnO_2), n-type tungsten trioxide (WO_3) and p-type nickel oxide (NiO), respectively. These sensors have a relatively faster response speed and recovery rate than most of the commercial MOX sensors, but they do not meet the high standard of certain applications where an instant sensor response is essential. For instance, applications in medical appliances, real-time air quality detection, and emergency response. Unlike NDIR sensors, MOX sensors have a wide gas detection range and require less space than NDIR sensors (only the sensor chip and a simple external circuit are needed, instead of a dedicated chamber with a detector). All three sensors were housed inside an aluminium gas chamber. A Teensy 3.6 microcontroller was used to control the sensors and collect/process data.

6.3.1 MOX Sensor in 'Static' Mode

When the sensor is driven with a constant current and a single operating temperature, it is called 'static' DC mode. All three MOX sensors were first trialled under the 'static' condition with a 350°C constant heater temperature. The sensor circuitries were driven by the Teensy microcontroller to set current values. The unit was connected to a gas testing bench for measurements. Gas concentrations from 25 to 200 ppm of acetone and 100 ppm to 500 ppm of ethanol [1] were trialled with five minutes steps and synthetic air baseline in between. Sensor response data were visualized using a LabVIEW program at a 10 Hz sampling rate and stored to

[1] the permissible exposure limit (PEL) of both ethanol and acetone is 1,000 ppm for 8 hours [8]

an onboard microSD card at 100 Hz. Figure. 6.13 shows the change in resistances of three MOX sensors in acetone (Figure. 6.13(a)) and ethanol (Figure.X 6.13(b)), both in dry conditions.

This result demonstrates that these novel high bandwidth sensors offer a good sensitivity to gas concentration at low ppm levels. The 'static' response time is 10 s, which is superior to MOX sensors currently available on the market. The data were post-processed with a filter to remove drift. The baseline between each concentration is slightly different each time that requires a longer stabilization period between measurements, which is not realistic for a mobile robot in emergency response. As the micro-hotplate has a fast switching time (10 ms for the rise and 30 ms for the fall) and MOX sensors are more sensitive to temperature changes, thermal modulation ('dynamic' mode) is employed to improve the sensor response speed.

6.3.2 MOX Sensor in 'Dynamic' Mode

In the 'dynamic' operation, the microheater is pulsed between two temperatures to switch 'HIGH' and 'LOW', as described previously. The miniature sensors then uniquely offer the possibility to extract data during the transition period between those two temperatures. Among the various temperature ranges (from 200°C to 350°C) mentioned earlier, 225°C ('LOW') and 325°C ('HIGH') were selected, which generated an average power consumption of < 60 mW. The pulse period was 2 s with 1 s at each temperature level.

One set of data was extracted from each switching cycle. Readings were taken at both temperatures and subtracted, thus removing the effect of signal drift. Considering the conductance changes, G, of the sensor in quasi-steady-state, as the sensor in gas at a constant concentration, the output from the sensor can be approximated to:

$$G_1(t) = G_{T1} + (G_{T2} - G_{T1})(1 - e^{\frac{-t}{\tau_1}}) \tag{6.1}$$

$$G_2(t) = G_{T2} - (G_{T2} - G_{T1})(1 - e^{\frac{-t}{\tau_2}}) \tag{6.2}$$

where τ_1 and τ_2 are the rise and fall time of the conductance, T_1 and T_2 are the 'LOW' and 'HIGH' temperature, as marked in Figure. 6.14.

Equation. 6.1 represents the transition period increasing with temperature (switch 'HIGH' period) and Equation. 6.2 represents the period when the temper-

ature is decreased (switch 'LOW' period). These periods are represented as exponential changes. To calculate the response of the sensor to the target gas, remove

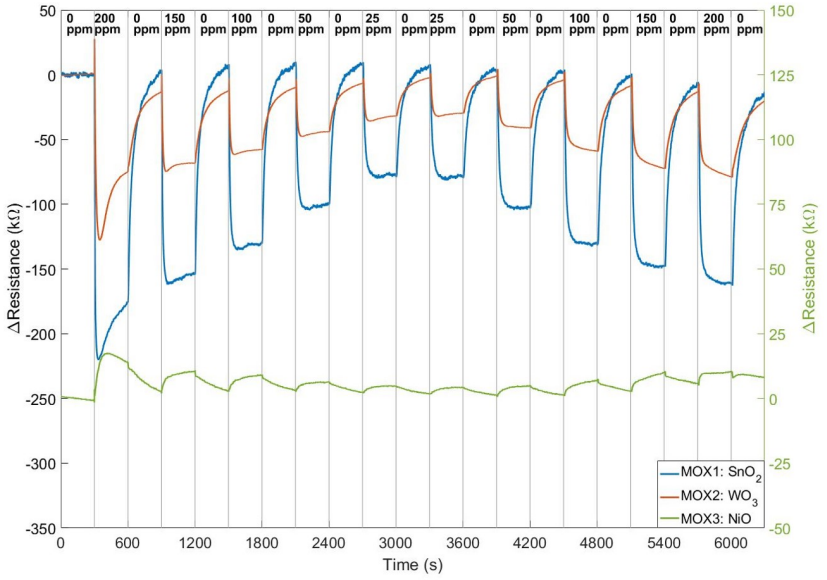

(a) Acetone from 25 ppm to 200 ppm in 5 mins steps.

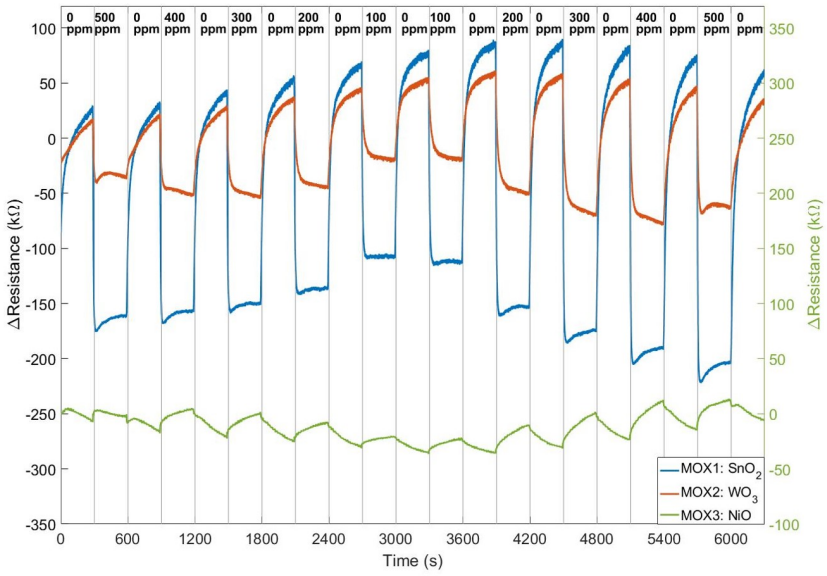

(b) Ethanol from 100 ppm to 500 ppm in 5 mins steps.

Figure 6.13: Change of resistances of three MOX sensors (Pt/Pd doped SnO_2, WO_3 and NiO) towards acetone and ethanol under dry conditions with synthetic air baseline between gases.

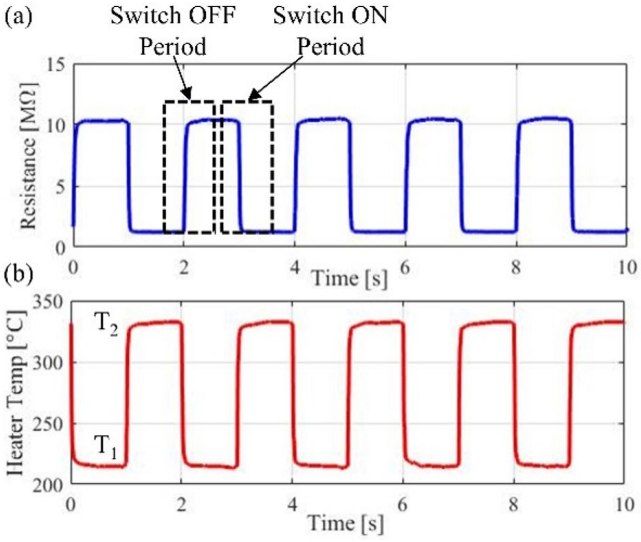

Figure 6.14: Peaks of conductance sum in dry air for: 0 ppm, and 100 ppm CO, 200 ppm CO and 300 ppm CO.

drift and eliminate the change in resistance due to heater temperature, the 'LOW' period was inverted and subtracted from the 'HIGH' period. A fast Fourier transform (FFT) was then performed on the subtracted data to find the peak magnitude, which was different for gases at different concentration levels. Those steps had been performed offline in MATLAB initially before implemented into a Teensy 3.6 microcontroller for a real time data output. The LabVIEW program was used to visualize the signal processing steps as shown in Figure. 6.15.

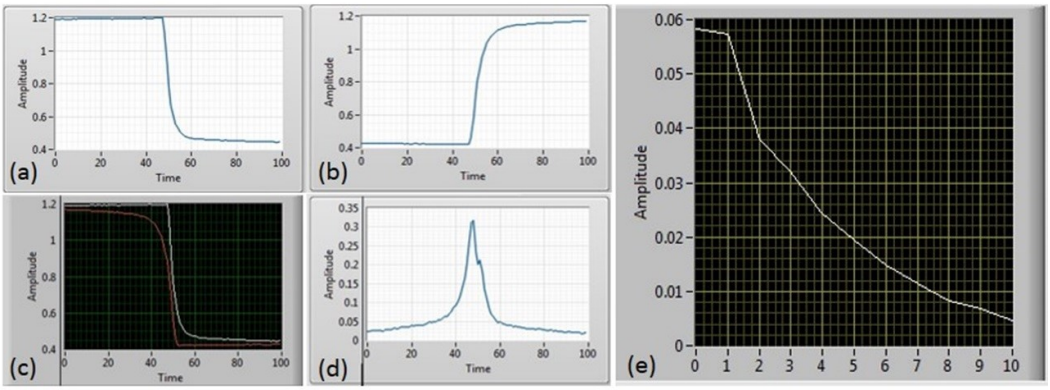

Figure 6.15: Thermal modulation steps visualized in LabVIEW. One sensor pulse is used as an example, the (a) falling and (b) rising part (c) inverted, and (d) subtracted. Results are then processed through FFT to get (e) amplitude readings.

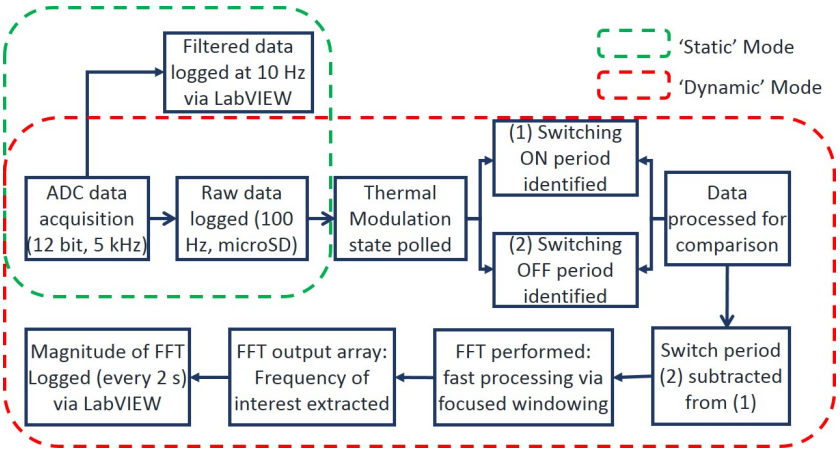

Figure 6.16: Block diagram of the Teensy microcontroller program under 'static' and 'dynamic' mode.

Teensy code was written and optimized to perform those steps in real time. To increase the efficiency of the data processing, a reduced select number of samples was processed (128 data points) per cycle. The FFT processing stage was focused on analysing the frequency range of interest (defined by initial experiments using the MATLAB interface described above). A block diagram is presented below in Figure. 6.16 to show the difference in the code for 'static' and 'dynamic' operation. The raw sensor data were recorded at a 100 Hz sampling frequency and stored onto a microSD card, and the FFT results were also stored while displaying in LabVIEW.

The 'dynamic' operation of sensors was trialled using the same gas testing bench with the same two gases: acetone and ethanol. Five concentration levels were tested for each gas: acetone in 0 ppm, 50 ppm, 100 ppm, 150 ppm and 200 ppm; ethanol in 0 ppm, 100 ppm, 200 ppm, 400 ppm and 500 ppm. Sensors were warmed up for a few minutes prior to the experiments, no need for a long stabilization period. Each concentration was trialled for 2 min as this is sufficient to provide concentration information of the target gas. FFT results were presented every 2s correlates to the 2s period of the pulse. The magnitude changes to different concentration levels were visualized in the LabVIEW program. This can be further adapted to be displayed on a handheld device for end-users. To present the results, the FFT magnitudes averaged over 10 pulses (20 s) were shown in Figure. 6.17. A period of ten pulses was chosen as it can represent an averaged result instead of a singular value. In real time for a faster indication, a shorter time period can be used for averaging.

The FFT output data demonstrate the response to the target gas can be

represented by the magnitude of the FFT. The peak magnitudes, which occur at 2 Hz, were extracted and the ratio FFT_{gas}/FFT_{air} is plotted in Figure. 6.18. Both

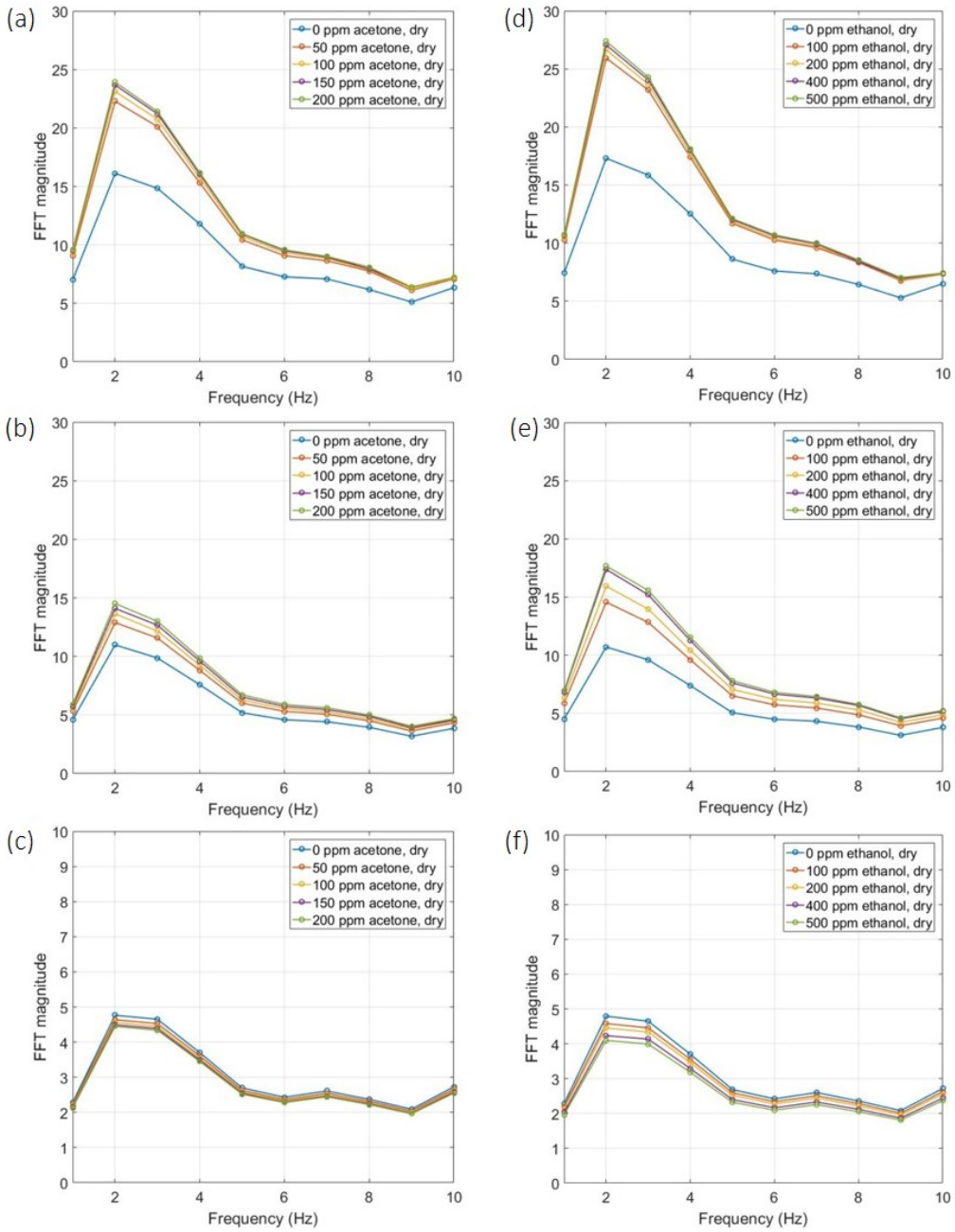

Figure 6.17: Real-time thermal modulation results of three metal oxide sensors towards acetone (a—c) and ethanol (e—g). Response of MOX1 SnO_2 sensor in (a) acetone and (d) ethanol; response of MOX2 WO_3 sensor in (b) acetone and (e) ethanol; response of MOX3 NiO sensor in (c) acetone and (f) ethanol.

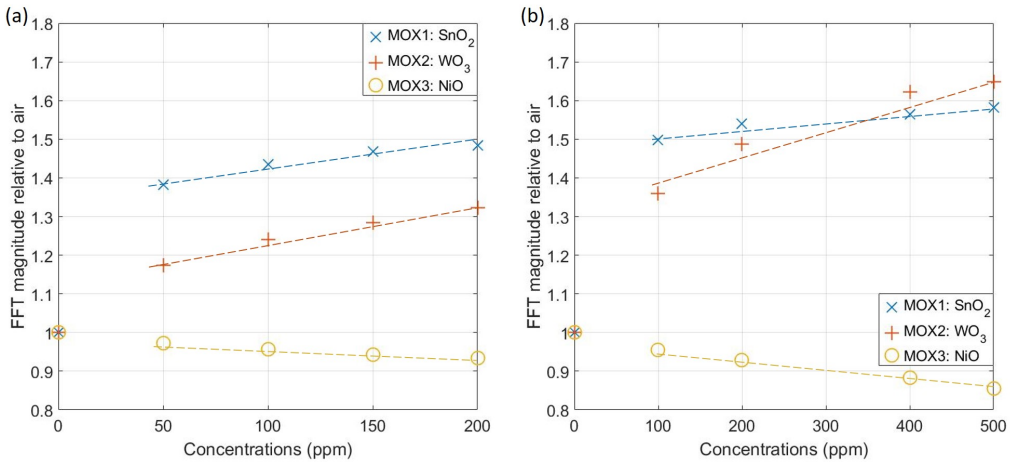

Figure 6.18: FFT magnitude relative to air results of three sensors: SnO_2, WO_3 and NiO in acetone (a) and ethanol (b).

SnO_2 and WO_3 device magnitudes increase with concentrations and WO_3 sensor has greater response towards ethanol. NiO sensor has a smaller response to both gases, which is possible as the NiO sensor is more sensitive to gases such as ammonia.

These presented results demonstrate the working mechanism of this novel temperature modulation technique in real-time applications, which is vital for the mobile robot application. An on-board signal processing algorithm has been adapted and optimized for a microcontroller to be used on a gas sensing unit with a sensor array. Three gas sensors can be used at the same time with raw data transmitted at 100 Hz sampling rate and FFT results every 2 s, which can potentially be faster with a smaller 'HIGH' and 'LOW' period. The sensors, housed inside a robust steel enclosure were tested using a gas testing bench towards acetone and ethanol gas. Both 'static' and 'dynamic' modes were trialled. In 'static' DC mode, sensors were operated with a current control circuit and a constant micro-heater temperature at 350 °C. The sensors show great sensitivities to both gases at low concentration levels with a response speed at 10 s, which are superior to other MOX sensors currently available on the market. Due to the nature of MOX sensor, a warming-up period is required before experiments for at least 60 to 90 min, and longer stabilization period (more than 5 mins) is necessary between measurements for a more accurate result. By operating sensors in 'dynamic' mode, those imperfections can be compensated. These MOX sensors cannot be installed on a mobile exploration robot when operated in 'static' mode, as the robot must be ready for deployment with little or no notice.

In 'dynamic' mode, the magnitudes of FFT results corresponding to the increase of concentration levels (as seen in Figure. 6.18). The peak frequency for acetone and ethanol was found to be at 2 Hz. It is worth noticing that with different gases, the FFT peaks at different frequencies. This information can have the potential to be used to distinguish gases. The distinct peak frequencies identified for each gas can be caused by the speed of the chemical reactions occurring in the film layer differs depending on the gas present and in turn, this affects the response of the sensor when a temperature shift is implemented. The experiments were also repeated, and the sensors produced a stable output during the measurements, with any baseline signal drift, existed in 'static' operation mode, removed through this signal processing technique. The system is able to operate independently from the baseline, which is critical in a hazardous environment, where it is unlikely a stable baseline will be acquired. Figure. 6.19 shows the variance of normalized FFT values over 30 datasets, which is within ±2% variation.

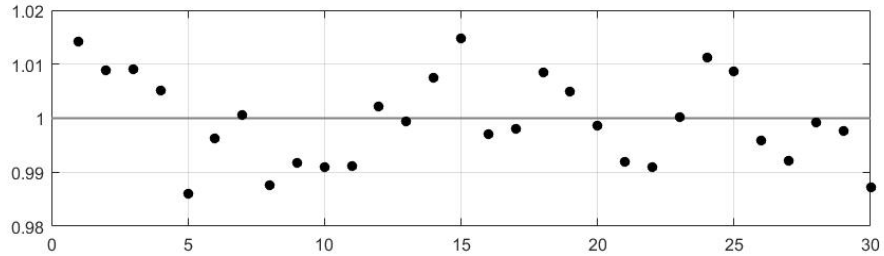

Figure 6.19: Variance plot of normalized FFT results over 30 datasets.

Different metal oxide coatings respond to gases differently. The SnO_2 coated device has a high response towards both ethanol and acetone, but a greater response was observed to ethanol. For the same concentration of acetone and ethanol at 200 ppm, the SnO_2 sensor has ∼5% more response towards ethanol. The WO_3 sensor also has a smaller response to acetone with a magnitude increase of 30% for 200 ppm acetone, but an increase for 200 ppm of ethanol is close to 50%. The NiO sensor has a smaller response towards both gases with less than 1% change at 200 ppm concentration level. The SnO_2 sensor has an increase close to 38% whilst WO_3 has a 17% increase for 50 ppm acetone. In 100 ppm ethanol, SnO_2 and WO_3 sensors have 50% and 37% increase in response, respectively. For a gas in higher concentrations, such as ethanol at 500 ppm, WO_3 has a slightly larger response of 65% increase compared to SnO_2 with 60% increase. The visible exponential trend on the plots indicates the devices can get saturated at higher concentrations. These distinctive characteristics of sensors toward different gases can contribute to gas discrimination

process alongside the peak frequency changes for a more accurate understanding.

A Teensy microcontroller was incorporated to drive the circuit and process the data. The output from the microcontroller, which was connected over a USB connection for real-time plotting, can directly show the exact gas present and its concentrations (i.e., from the frequency and magnitude of the FFT result). Importantly, this output can directly be used to assess the hazardous nature of the gas detected (from its magnitude) and thus reduces the processing load on the host computer (i.e., for an application involving a mobile robot). This allows the development of a new generation of smart, low-cost gas sensors to be used for applications where fast readings (in few seconds or less) are required. The potential applications including, but not limited to, mobile robot, indoor/outdoor air quality monitoring, portable wearable devices, and the internet of things. This measurement system can also be used alongside an extensive gas mapping and discrimination algorithm, to improve the accuracy and speed notably as compared to using the raw sensor data.

6.4 Post-processing with Artificial Neural Network

The FFT power spectra of the thermally modulated data show that the peak magnitudes correlate to the gas concentration levels. The magnitude increases with the increase of gas concentration, but it is also related to other factors such as temperature, humidity, gas type, sensor type, etc. Previous section studied the outputs with regard to three different sensors and two gases. Here, the influence of humidity levels is studied using one gas sensor under one gas of interest. The sensor data published in [4] and [9] are used in this section. A regression artificial neural network model is then applied to find the pattern for numerical predictions.

6.4.1 Sensor Raw Data

The data were collected using a MOX sensor coated with CuO sensing material. It is a p-type material that increases the resistance value when exposed to the given gas. It is less popular than the n-type sensors, such as SnO_2 and WO_3, but it has received a growing attention due to its ability to detect toxic gases like hydrogen sulfide (H_2S) [10, 11] or carbon monoxide [12] in harsh conditions. Therefore, a CuO based MOX sensor is used here to detect H_2S in hydrogen carrier gas. The

material is pure p-type CuO, and the paste was dropped onto the micro hotplate which was then left to dry in air at room temperature for ∼12 hours [4]. The substrate was then annealed for 2 hours at 450 °C before performing any gas sensing measurements.

The measurement system is similar to the rig mentioned in the previous chapter, which consists of an automated LabVIEW program with mass flow controllers, a NI DAQ and a gas chamber. A mixture of H_2S and H_2 was introduced with various concentration levels: 0 ppm, 1 ppm, 5 ppm, and 10 ppm, at four relative humidity levels: 0%. 25%, 50% and 75%. Similarly, the micro hotplate was switched between two voltages levels for two operating temperatures. Two combinations were trialled: 200°C to 300°C (denoted as 'LOW' temperature range) and 200°C to 350°C (denoted as 'HIGH' temperature range), at the supply voltage of 0.185 V to 0.220 V and 0.185 V to 0.239 V, respectively. Five pulses of each temperature range were performed for each concentration and humidity level. Apart from 10 ppm in 75% relative humidity, which was not available due to flow limitation, a total of 19 datasets was obtained with 10 pulses in each dataset (5 'LOWs' and 5 'HIGHs'). Each pulse has a period of 10 seconds with 5 seconds on each temperature level. The total flow rate and the ambient temperature was monitored throughout the experiments, which was 300 sccm for flow rate and 23.2°C for ambient temperature. Figure. 6.20 shows an example of one collected dataset.

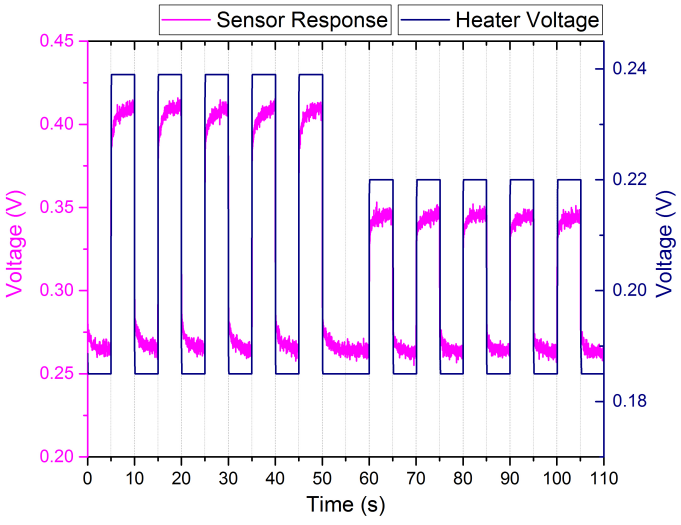

Figure 6.20: An example plot of the CuO sensor with pure hydrogen under dry conditions and room temperature.

6.4.2 Data Pre-processing

The collected datasets were first pre-processed using the thermal modulation steps described earlier. Because the alignment of 'HIGH' and 'LOW' transient phase is critical for the following steps, each pulse was examined to make sure the turning point was recorded properly. The data sampling rate was 100 Hz, and occasional, the turning point would be missed and the next point in the middle of the curve was collected instead. In such case, the pulse would be discarded as the further processed data would be an inaccurate reflection of the humidity and gas concentration level. Increasing the data sampling rate can reduce the occurrences of such situation. Therefore, the same experiments were performed twice, hence 10 pulses, then five valid pulses were extracted from each temperature range.

The thermal modulation processing steps including turning point alignment, subtraction and FFT. The results at the 'HIGH' and 'LOW' temperature range are presented in Figure. 6.21 for four different humidity levels. The peak magnitude increases with concentrations and humidity levels. Based on the plots, the peaks occur at the frequency of 1 Hz. The peak magnitude values are plotted in Figure. 6.22. Apart from the 75% relative humidity, the zero gas baseline increases with humidity levels. The linear relationship between the concentrations and magnitudes is more visible at the higher temperature range, as well as the proportionality with the increasing humidity levels.

The processed data were then compressed to only have a single value per FFT spectrum. This is to reduce the computation load by only using the valuable data that contain the valid sensor information. Therefore, the power density values of each FFT spectrum at 1 Hz were extracted and organised as the input to the neural network model. Five values from five pulse for each concentration and humidity level were selected and appended into a matrix.

All data were auto-ranged (between minimum and maximum) to make sure an even spread. Both humidity and concentration levels were auto-ranged between [0, +1] with 0 for the lowest concentration/humidity, and +1 for the highest. The FFT magnitude was auto-ranged between [-1, +1] for the whole dataset before splitting into training and testing data group. Out of the five pulses, four were used for network training and one for testing. Each dataset was tested in turns until all had been tested independently. The two temperature ranges were tested separately, as well as together for a more comprehensive comparison.

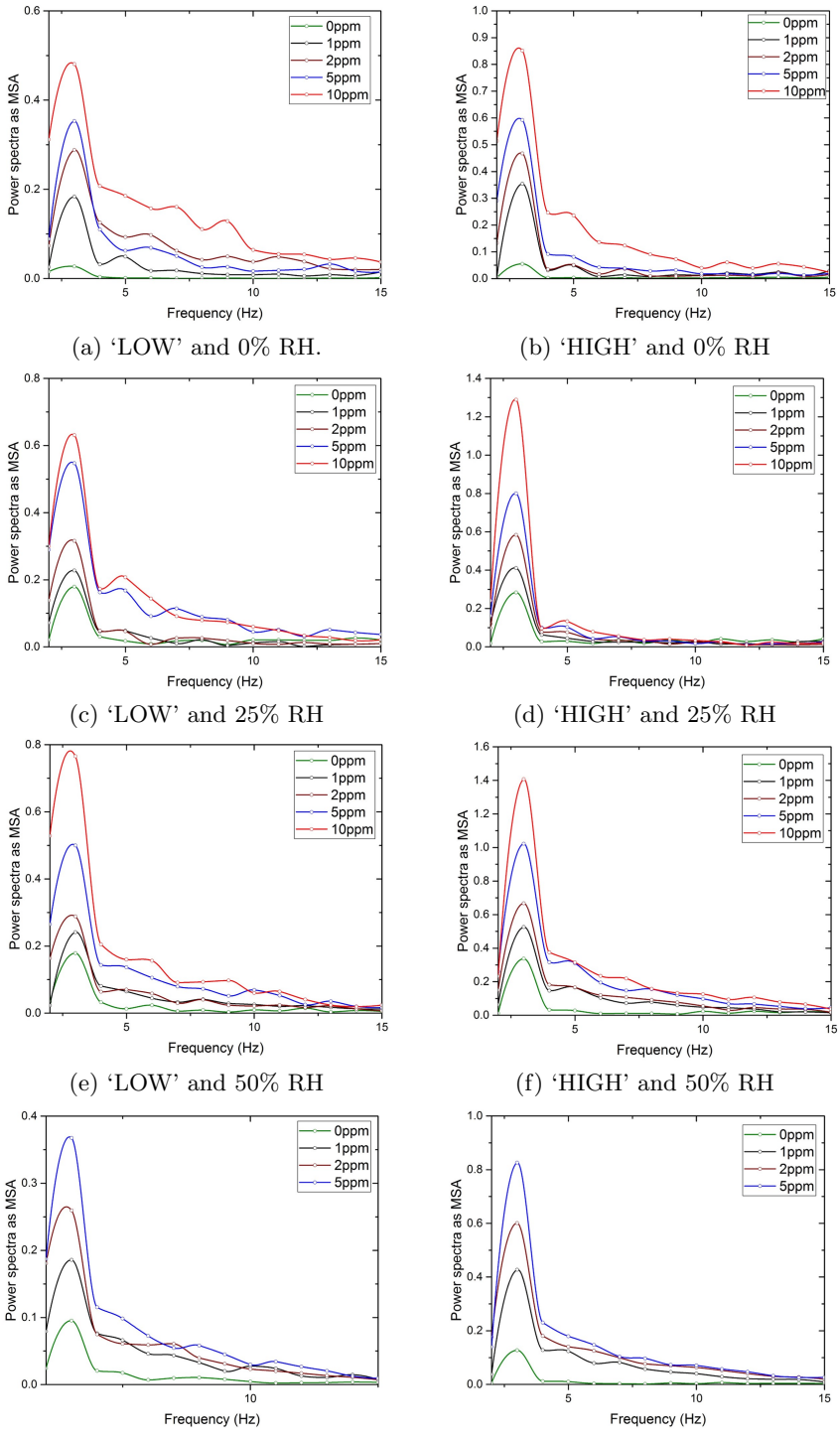

(a) 'LOW' and 0% RH.

(b) 'HIGH' and 0% RH

(c) 'LOW' and 25% RH

(d) 'HIGH' and 25% RH

(e) 'LOW' and 50% RH

(f) 'HIGH' and 50% RH

(g) 'LOW' and 75% RH

(h) 'HIGH' and 75% RH

Figure 6.21: Power spectra of the FFT results for CuO MOX sensor towards H_2S at different concentrations and humidity levels.

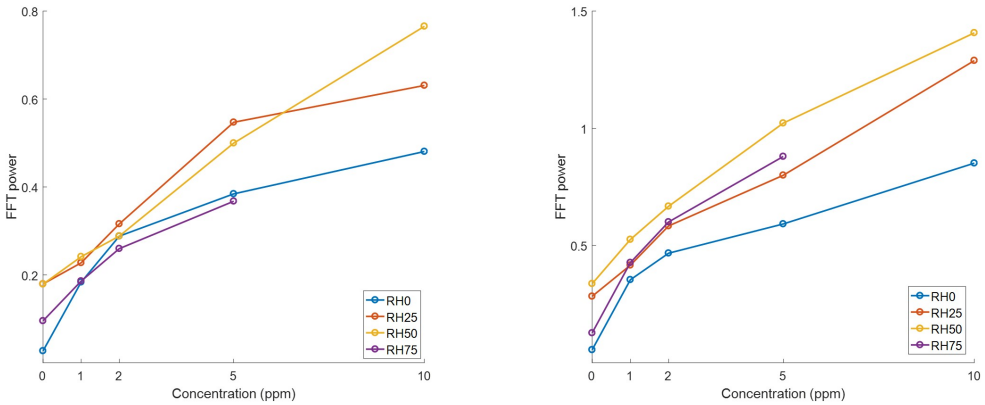

(a) Averaged results at 'LOW' temperature range.

(b) Averaged results at 'HIGH' temperature range.

Figure 6.22: Averaged FFT peak magnitude results.

6.4.3 Artificial Neural Network: Prediction

An artificial neural network (ANN) is a simple way to process non-linear data that involve a certain pattern or model. It is a computational method that mimics the human brain based on the collected data and neural perceptrons. An introduction and literature review of ANNs was provided in Chapter 2.

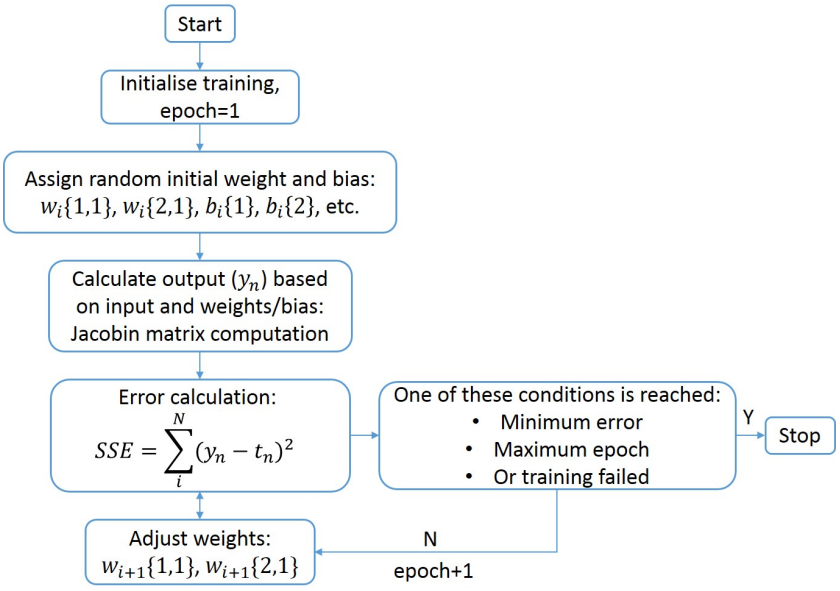

Figure 6.23: Flow chart of the Levenberg-Marquardt algorithm.

The neural network toolbox in MATLAB R2017 was used to carry out the data training and testing process. The model is a feed-forward backpropagation network with a customisable training function. One of the fastest training algorithms is the Levenberg-Marquardt optimisation. It is also a popular solver for fitting problems. The network randomly assigns weights at the initial stage and then adjusts them during training epochs. Figure. 6.23 is the training process of the network.

In the figure, w, b and t represent the weight, bias and target output value, respectively. The Jacobian matrix functions are given as:

$$jj = j_X * j_X \tag{6.3}$$

$$j_e = j_X * E \tag{6.4}$$

$$dX = \frac{-(jj + \mu I)}{j_e} \tag{6.5}$$

where the Jacobian j_x is calculated for each variable X based on the weights and bias. E is all errors, I is the identity matrix and μ is the combination coefficient or an adaptive value. The weight is adjusted using:

$$w_{i+1} = w_i - (j_i^T j + \mu I)^{-1} j_i e_i \tag{6.6}$$

where e is the error, w_i is the current weight and w_{i+1} is the next weight.

From the pre-processed matrix, auto-ranged humidity levels, FFT magnitudes and the operating temperature in binary form ('LOW' as '0' and 'HIGH' as '1') were used as inputs, and concentration levels as the output. The network has a two-layered structure with 1 hidden layer of 10 neurons and one output layer, as shown in Figure. 6.24. The model used four pulses for training and one pulse for concentration prediction. Five training repeats were performed for each testing pulse. The predicted concentration levels were then categorised with the desired concentration values. For prediction within the 5% difference to the target concentration level, it was categorised as correct; between 5 $\sim$ 15% difference as incorrect, and any difference bigger than 15% as unknown. The five repeats of the five pulses results were then summed up as the confusion table shown below (Table. 6.1).

The correct prediction rate for concentration levels at 0 ppm, 1 ppm, 2 ppm, 5ppm and 10 ppm is 86.5%, 84.0%, 59.0%, 37.5% and 95.8%, respectively. The averaged success rate is 72.6% with the highest rate at 10 ppm classification and

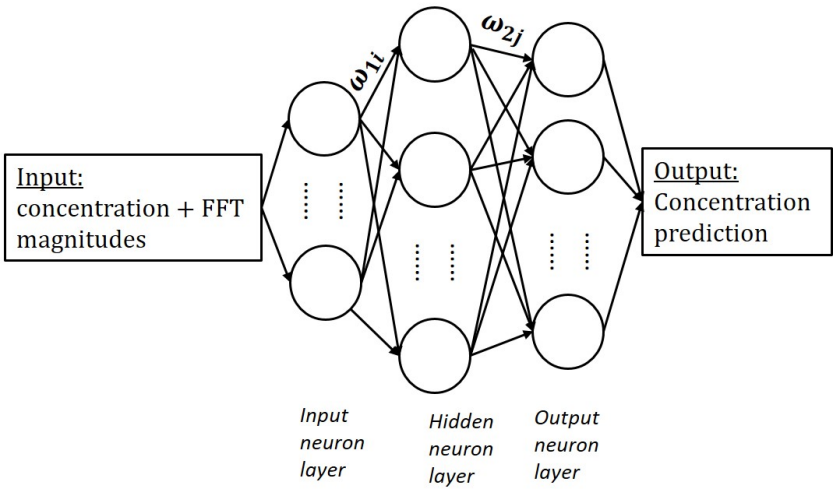

Figure 6.24: The ANN model topology.

Table 6.1: Confusion table for gas concentration prediction results (sum of five repeats).

Predicted Output	**Target Output**				
	0 ppm	**1 ppm**	**2 ppm**	**5 ppm**	**10 ppm**
0 ppm	173	17	0	0	0
1 ppm	26	168	33	0	0
2 ppm	0	14	118	35	0
5 ppm	0	0	29	75	20
10 ppm	0	0	0	25	115
Unknown	1	1	20	65	15
Total	*200*	*200*	*200*	*200*	*150*

the lowest rate at 5 ppm classification. The epoch for the model was around 6∼150. A maximum epoch of 200 was set, and it was varied with different datasets. It was found that more epochs were needed for a bigger dataset (i.e. datasets with both 'LOW' and 'HIGH'), and 'HIGH' datasets required fewer epochs than 'LOW' datasets.

'LOW' and 'HIGH' temperature ranges were then studied separately using a similar approach. Instead of the 10 hidden neurons, 6 was found to provide the best outcome. Five pulses were tested independently with five repeats each. The predicted results were categorised in the same manner, and summarised as shown in the confusion tables (Table. 6.2 and Table. 6.3) for both 'LOW' and 'HIGH'.

Table 6.2: Confusion table for gas concentration prediction results at 'LOW' operating temperature (sum of five repeats).

Predicted Output	**Target Output**				
	0 ppm	**1 ppm**	**2 ppm**	**5 ppm**	**10 ppm**
0 ppm	70	12	0	0	0
1 ppm	30	76	24	0	0
2 ppm	0	12	32	25	0
5 ppm	0	0	27	20	21
10 ppm	0	0	0	14	35
Unknown	0	0	17	41	19
Total	*100*	*100*	*100*	*100*	*75*

Table 6.3: Confusion table for gas concentration prediction results at 'HIGH' operating temperature (sum of five repeats).

Predicted Output	**Target Output**				
	0 ppm	**1 ppm**	**2 ppm**	**5 ppm**	**10 ppm**
0 ppm	95	10	0	0	0
1 ppm	5	83	7	0	0
2 ppm	0	7	76	17	0
5 ppm	0	0	15	69	1
10 ppm	0	0	0	7	70
Unknown	0	0	2	7	4
Total	*100*	*100*	*100*	*100*	*75*

The overall prediction accuracy is better at the 'HIGH' temperature range with 82.7% correct rate as compared to the 49.1% at the 'LOW' temperature range. This suggests that the sensor response data are more distinctive at a higher operating temperature, which are more suitable for pattern recognition. Sum squared error (SSE) was used to evaluate the network performance, which has the equation of:

$$\mathrm{SSE} = \sum_{\mathrm{i}=1}^{\mathrm{i}} (y(i) - t(i))^2 \tag{6.7}$$

The averaged SSE result for the model with both 'LOW' and 'HIGH' datasets is 0.3666, for only 'LOW' datasets is 0.3661 and 0.1055 for only 'HIGH' datasets. This also suggests better performance with 'HIGH' datasets.

6.4.4 Artificial Neural Network: Regression Analysis

Similar neural network models were then explored as regression analysis to find the best linear regression fitting between predicted concentrations and target concentrations. As found out in the previous section, the 'HIGH' temperature range is more suited for the pattern recognition then the 'LOW' one, and these two temperature ranges were studied separately again in this section. Because the data for 10 ppm in 75% relative humidity were unavailable, for the accuracy purpose, the 10 ppm data at all humidity level were ignored in the section. Therefore, the input nodes for the model were: relative humidity (0%, 25%, 50% and 75%) and FFT magnitude values, and output node was the concentration value (0 ppm, 1 ppm, 2 ppm, 5 ppm). Out of the five datasets (pulse 1 to pulse 5), three were used for training and two for testing, hence a total of 10 combinations were trialled. The same feed-forward backpropagation network with Levenberg-Marquardt optimisation was used. Three ANN models were trained and tested for each combination: 1 hidden layer of 4 neurons, 1 hidden layer of 8 neurons, and 2 hidden layer of 4 neurons.

The predicted results were then plotted against the target output in a linear fitting format. Ideally, the fitted line is $y(n) = t(n)$ with $y(n)$ as the predicted results and $t(n)$ as the target results. But in reality, the fitted line is in the format of $y(n) = a \times t(n) + b$ with a and b as constants. The closer a is to 1 the better, which means a higher fitting accuracy. Figure. 6.25 shows an example of the best fitting line with the ANN of 1 hidden layer of 8 neurons and 'HIGH' operating temperature. The axes show the auto-ranged concentration level, with 0 as 0 ppm, 0.2 as 1 ppm, 0.4 as 2 ppm and 1 as 5 ppm. This fitting was performed for all 10 datasets under three ANN structures, the fitted lines were then averaged to obtain the overall results. The averaged plots for both 'LOW' and 'HIGH' with three structures are shown in Figure. 6.26.

The network performance was analysed using sum squared errors. The summarised SSE of all three ANN structures averaged over 10 datasets is presented in Table. 6.4.

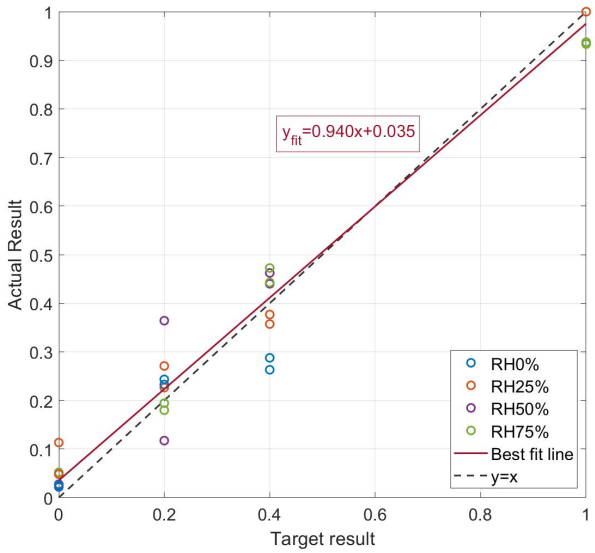

Figure 6.25: An example of the fitted line for predicted output versus target output ('HIGH' temperature range; ANN: 1 hidden layer of 8 neurons).

Table 6.4: Summarised model comparison with best-fitting line and SSE values.

ANN Structure	**Temperature Range**	**Best-fitting Line y(n)**	**Avg. SSE**
1 hidden layer 4 neurons	'LOW'	$0.809t(n) + 0.081$	0.9192
	'HIGH'	$0.898t(n) + 0.040$	0.2090
1 hidden layer 8 neurons	'LOW'	$0.836t(n) + 0.065$	0.8554
	'HIGH'	$0.925t(n) + 0.032$	0.2812
2 hidden layer 4 neurons each	'LOW'	$0.886t(n) + 0.052$	0.9206
	'HIGH'	$0.938t(n) + 0.031$	0.2109

By comparing the performance between the 'LOW' and 'HIGH' datasets, 'HIGH' is generally better in terms of the best fitting lines and sum squared errors, which is the same observation as seen in the last section. The gradient value for 'LOW' temperature range is ∼0.8 with the highest at 0.88, but the value for 'HIGH' temperature range is closer to 1 at ∼0.9 or higher. The SSE values for 'HIGH' temperature range are much smaller than those of the 'LOW' temperature ranges, which are tripled. This behaviour is consistent over three ANN models. These models provide similar results when compared among themselves, with the 2 hidden layers of 4 neurons each as the best one for both temperature ranges. When using the model with 2 hidden layers, the gradients of the best fitting lines for 'LOW' and

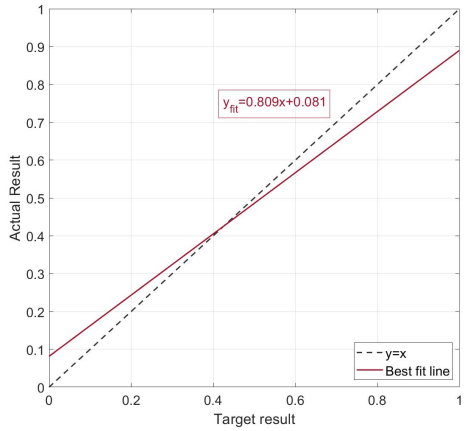

(a) 'LOW': 1 hidden layer of 4 neurons

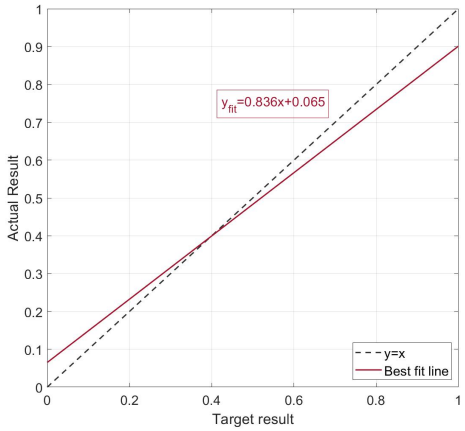

(b) 'LOW': 1 hidden layer of 8 neurons

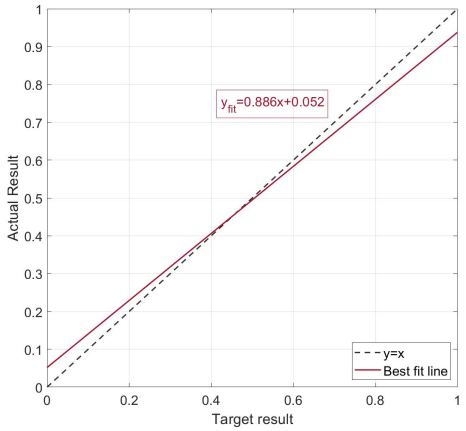

(c) 'LOW': 2 hidden layers of 4 neurons each

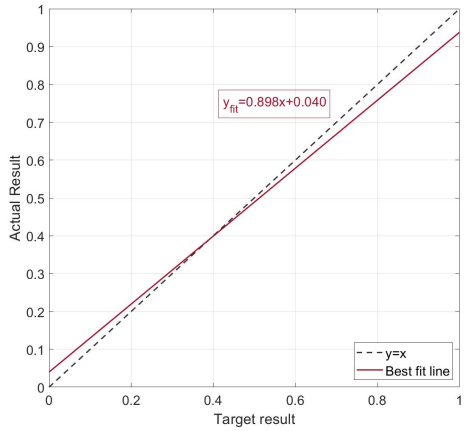

(d) 'HIGH': 1 hidden layer of 4 neurons

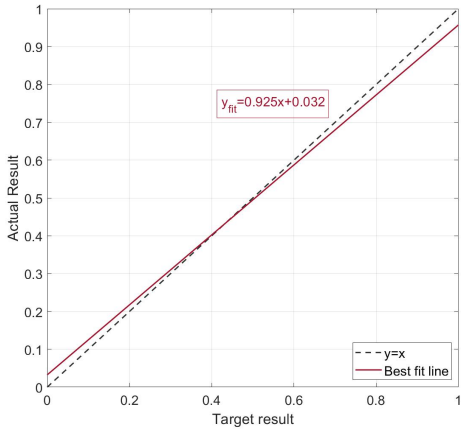

(e) 'HIGH': 1 hidden layer of 8 neurons

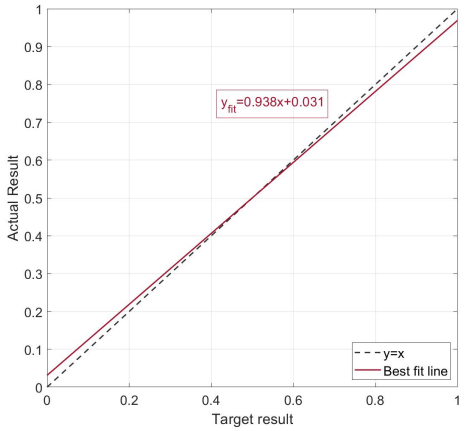

(f) 'HIGH': 2 hidden layer of 4 neurons each

Figure 6.26: Fitting results for three ANN models in both 'LOW' and 'HIGH' operating temperature range, averaged over 10 datasets.

'HIGH' are close to each other, which suggest both temperature ranges are suitable for the regression analysis. Therefore, this ANN model is preferred as 2 layers can obtain a more complex mathematical relationship among each neuron and greatly increase the analysis accuracy.

6.5 Conclusions

In this chapter, a thermal modulation signal processing technique was investigated with data collected using metal oxide gas sensors. One of the most important issues with MOX sensors is the baseline drift, which requires a long stabilisation period prior to the experiment and between gas exposures. To compensate this flaw, a thermal modulation technique is developed. Instead of using the 'static' response of the sensor, the 'dynamic' mode is used. As the MOX sensor is micro hotplate based, in 'static' mode, the heater is set to one operating temperature, i.e. 300°C or higher. But in the 'dynamic' mode, the heater temperature is switching between two pre-set operating temperatures. The MOX sensor is highly sensitive towards the heater temperature, so the change in the sensor resistance is almost instant. By doing so, the collected data have hidden information that can be further processed and extracted. The further processing steps involve finding the transient phases of the temperature ('HIGH-LOW' and 'LOW-HIGH'), which are then subtracted and filtered using the fast Fourier transform. The end results are the FFT spectra with magnitude peaks at a specific frequency, i.e. 1 Hz. It was found that the peak magnitudes correlate with the gas concentration levels, and varied with gas types and experimental conditions, such as humidity levels. Both humid and dry air conditions were studied for comparison.

This method was later implemented with a gas sensing unit which contains a microcontroller for on-board real time signal processing. The same sensing unit as mentioned in the previous chapter was used, which has three MOX sensors with customised coatings of SnO_2, WO_3 and NiO, respectively. These sensors were both experimented in 'static' and 'dynamic' mode, results were presented. The thermal modulation algorithm was optimised to perform in real-time using a Teensy 3.6 microcontroller and visualised through a LabVIEW program. All three sensors were modulated and processed at the same time, and their results matched the 'static' mode experiments, i.e. the sensor response towards different concentration levels. This method allows the dynamic sensor data to be used, which only requires 2 s of

sensor data (or even less) to indicate gas exposure instead of the tens of seconds in the 'static' mode. It greatly improved the sensor response time, and the drift is compensated as no long stabilisation or recovery period is needed. The magnitude peak information can be used directly to indicate the gas exposure, or can be used for further processing to reveal its relationship towards concentration and humidity levels, i.e. a pattern can be found.

In order to find the pattern, data collected from one MOX sensor were trialled, which contained various humidity and concentration levels. An artificial neural network was implemented using MATLAB. The model includes input neurons, hidden layers and output neurons. The Levenberg-Marquardt algorithm was used for weight adjustments and optimisations, and sum squared error was used for network performance analysis. The sensor was operated with two operating temperature range, a.k.a 'LOW' and 'HIGH'. Both datasets were considered, either separately or together. When considered together, the input neurons of the model included humidity levels, FFT peak magnitudes, and temperature ranges in binary form. When considered separately, the input neurons only included the humidity levels and FFT magnitudes. The output neuron for both cases was concentration levels. All values were auto-ranged and evenly spread between the maximum and minimum value of the dataset. Data were separated for training and testing, and the model outputted the predicted concentration values. Both prediction analysis with confusion tables and regression analysis with best-fitting lines were trialled. Various model combinations were also tested, i.e. the number of hidden layers and neurons. It was found that the 'HIGH' temperature range data were more suited for both the prediction and regression analysis. In the prediction analysis, the averaged accuracy is at 82.7% for 'HIGH' dataset and 49.1% for 'LOW' dataset. In the regression analysis, the gradient for the best fit line of the 'HIGH' dataset is averaged at 0.95 as compared to the 'LOW' at 0.84. The performance is also better with 'HIGH' datasets and smaller SSE values. This proves the feasibility to use thermal modulated data for regression fitting and prediction problems, which is useful for the development of smart sensors. More machine learning methods are explored in the next chapter, especially for the detection of odours.

References

[1] S. Ozturk, N. Kilinc, and Z. Ozturk, "The effects of annealing on gas sensing properties of ZnO nanorod sensors coated with Pd and Pt," *Procedia Engineering*, vol. 47, no. 1, pp. 434–437, Jan 2012.

[2] G. E. Patil, D. D. Kajale, S. D. Shinde, R. Bari, D. Chavan, V. Gaikwad, and G. H. Jain, "Effect of annealing temperature on gas sensing performance of SnO_2 thin films prepared by spray pyrolysis," *Sens. Transducers J.*, vol. 9, pp. 96–108, 2010.

[3] M. Holmberg and T. Artursson, "Drift compensation, standards, and calibration methods," in *Handbook of Machine Olfaction*. Weiheim: Wiley-VCH, 2004, ch. 13, pp. 325–346.

[4] B. Urasinska-Wojcik and J. W. Gardner, "Identification of H_2S impurity in hydrogen using temperature modulated metal oxide resistive sensors with a novel signal processing technique," *IEEE Sensors Letters*, vol. 1, no. 4, pp. 1–4, 2017.

[5] B. Urasinska-Wojcik and J. W. Gardner, "H_2S sensing in dry and humid H_2 environment with p-type CuO thick-film gas sensors," *IEEE Sensors Journal*, vol. 18, no. 9, pp. 3502–3508, 2018.

[6] T. Iwaki, J. A. Covington, and J. W. Gardner, "Identification of different vapors using a single temperature modulated polymer sensor with a novel signal processing technique," *IEEE Sensors Journal*, vol. 9, no. 4, pp. 314–328, 2009.

[7] T. Iwaki, J. A. Covington, F. Udrea, and J. W. Gardner, "Identification and quantification of different vapours using a single polymer chemoresistor and the novel dual transient temperature modulation technique," *Sensors and Actuators B: Chemical*, vol. 141, no. 2, pp. 370–380, 2009.

[8] United States Department of Labor, "Permissible exposure limits: annotated tables," 2019. [Online]. Available: https://www.osha.gov/dsg/annotated-pels/

[9] W. Xing, A. A. Shah, B. Urasinska-Wojcik, and J. W. Gardner, "Prediction of impurities in hydrogen fuel supplies using a thermally-modulated CMOS gas sensor: Experiments and modelling," in *2017 IEEE SENSORS*, Glasgow, UK, Oct 2017, pp. 1–3.

[10] E. Llobet, J. Brunet, A. Pauly, A. Ndiaye, and C. Varenne, "Nanomaterials for the selective detection of hydrogen sulfide in air," *Sensors*, vol. 17, no. 2, pp. 391–409, 2017.

[11] S. Park, S. Kim, H. Kheel, S. K. Hyun, C. Jin, and C. Lee, "Enhanced H_2S gas sensing performance of networked CuO-ZnO composite nanoparticle sensor," *Materials Research Bulletin*, vol. 82, no. 1, pp. 130 – 135, 2016.

[12] M. Hübner, C. Simion, A. Tomescu-Stănoiu, S. Pokhrel, N. Bârsan, and U. Weimar, "Influence of humidity on CO sensing with p-type CuO thick film gas sensors," *Sensors and Actuators B: Chemical*, vol. 153, no. 2, pp. 347 – 353, 2011.

Chapter 7

Signal Processing with Machine Learning Algorithms for Odour Detection

7.1 Introduction

An electronic nose (e-nose) instrument comprises of two parts, the hardware such as sensors and circuit boards, and the software such as data collection and signal processing. Therefore, to enhance the functionality of an e-nose, both hardware and software need to be studied. As a continuance of the previous chapter, this chapter focuses on the software improvement of the e-nose system. Such enhancements include developing new algorithms or optimising existing ones for gas sensing. In Chapter 2 Literature Review, different approaches of signal processing algorithms were discussed with examples. This chapter is based on various machine learning algorithms, especially their applications in time-series gas sensor data.

Three types of algorithms are studied here: dimensionality reduction algorithms, instance based learnings, and neural networks. A dimensionality reduction algorithm is to reduce the number of variables, such as Principal Component Analysis (PCA), and an instance based learning compares the new instance with training instance, for example, k-Nearest Neighbour (KNN) or Self-Organising Maps (SOM). Neural network can be divided into shallow networks, as used in the previous chapter and deep networks, i.e. Convolutional Neural Networks (CNN). All models men-

tioned above will be explored using the datasets collected from a gas sensing unit. The sensing unit is MOX sensors based with a microcontroller. Different gases were trialled, including synthetic urine for odour detection. The work aims to use the sensing system as well as the machine learning algorithms to detect and discriminate urine odour.

7.1.1 Odour Detection

An odour is a distinctive smell that is caused by volatile molecules. The smell can be a simple odour, i.e. a single compound or structure, or a complex odour, i.e. mixtures of molecule components [1]. Simple odours refer to a well-defined compound, such smells were defined by Amoore [2] into seven 'primary' odour categories, for instance, musky and floral. Complex odours, on the other hands, can be a combination of multiple molecules with each molecule has its distinctive smell. Both humans and animals can sense odours, either pleasant or unpleasant. This is because odour molecules stimulate olfactory receptors, thus sending information to the brain which can identify the odour based on experiences and memories (known information). The biological olfaction system was briefly introduced in Chapter 1. An e-nose works on a similar approach. To detect an odour, the vapour molecules 'react' with the sensor which is then triggered with response information. The information is then passed on to the 'brain', the microcontroller, that processes this information. Unlike gas detection, which generally requires a high sensitivity towards one specific gas, complex odour detection needs sensitivity towards various compounds. The metal oxide sensor is a suitable candidate because it responds to a wide range of gases/odours. However, in order to identify a complex odour smell, one MOX sensor is not enough. Similar to the mammalian olfactory system with multiple receptors triggered by one odour, multiple sensors are needed, hence a sensor array. Each sensor will be different from each other, which mimics the olfactory receptors, but they should all respond to the target odour. Therefore, in this chapter, three non-specific MOX sensors with different chemical coatings are used to identify the complex odour smell of synthetic urine.

7.1.2 Application Background

Synthetic urine is the chosen target odour for its application to aid incontinent individuals. Involuntary loss of urine is one of the most distressing and chal-

lenging problems. It can be caused by ageing, physical disabilities, and for women, after pregnancy. According to the World Health Organization, there are over 200 million people worldwide with urinary incontinence [3], and the National Health Service (NHS), UK, has estimated about 6 million people in the UK have some degree of urinary incontinence [4]. Individuals who suffer from this symptom often find it has detrimental effects on their quality of life [5]. Adult incontinence will lead to the loss of self-esteem, depression, loss of independence, even social isolation and loneliness [6]. One key reason is the malodour of waste products. Continence products, like absorbent pants/pads, are available on the market, but the fear of leakage may still restrain one's activities. An affected person often cannot perceive the odour of their own excretions (or perceived too late) [7], delayed incontinence care can cause physical problems such as skin breakdown and infections [8, 9]. It is also a significant concern that the unpleasant smell can be detected by others. To avoid such embarrassment, odour detection technologies, for instance a sensor device, could relieve the psychological pressure and potentially improve the quality of life.

The sensor device mainly serves as an odour detection and warning system. It should be able to detect the leaked urine smell before anyone else noticing, thus saving the individual from any social embarrassment. The aim is to have the device close to the groin area, such as on a belt, and only provides warning mechanisms (such as vibration) when urine is detected. Therefore, the device should be compact and wearable and able to identify urine odour only. To achieve that, the gaseous headspace of urine is studied here. The headspace consists of the urine vapour with a mixture of odour molecules. Smith [10] studied the gases headspace of urine samples using mass spectrometry and identified a total of 232 volatile compounds. These compounds can be used as biomarkers for non-invasive disease diagnosis, such as diabetes [11, 12], urinary tract infection [13], and prostate cancer [14]. All of these compounds contribute to the distinctive smell that urine has, which most people will consider unpleasant. To identify urine odour correctly, it is important to distinguish it from the smells of these individual compounds. Therefore, three of the individual compounds are selected for study alongside the urine odour. These compounds are ammonia, ethyl acetate and acetone, as they can interfere with the urine smell [15].

The sensor system contains sensors that can detect and respond to the target compounds. However, to identify urine and distinguish it from its similar compounds, signal processing methods are required. Here, different methods are explored off-board with the aim for an optimised on-board classification algorithm as

further work, therefore a stand-alone urine identification and warning device in the future.

7.2 Data acquisition and Pre-processing

7.2.1 Test Setup

As a prototype of this urine sensing and warning system, an existing sensing unit was used first to collect data for processing. The same unit as mentioned in Chapter. 5.4.3 was used under a gas testing rig. Four gases of interest were measured, which were acetone, ammonia, ethyl acetate and the gaseous headspace of synthetic urine. Acetone, ammonia and ethyl acetate were based on gas cylinders with the maximum concentration levels of 200 ppm, 25 ppm and 20 ppm, respectively. They all have zero air carrier gas. The synthetic urine sample was in liquid form provided by Pickering Laboratories, Inc., and its constituents are listed below in Table. 7.1. This was bubbled using a bubbler and the headspace vapour was fed into a gas line. Figure. 7.1 shows the testing bench setup, which is similar to the one used in previous chapters with an additional urine line.

Table 7.1: Constituents of the synthetic urine (Pickering Laboratories, Inc.).

Compounds	**Concentration (g/L)**	**Compounds**	**Concentration (g/L)**
Urea	25.0	Ammonium Chloride	3.0
Sodium Chloride	9.0	Creatinine	2.0
Disodium Hydrogen Orthophosphate, anhydrous	2.5	Sodium Sulphite, hydrated	3.0
Potassium Dihydrogen Orthophosphate	2.5		

Custom-made metal oxide sensors were used to perform gas experiments. The coatings for these three MOX sensors are n-type WO_3, Pd/Pt doped SnO_2 and p-type CuO, respectively, for enhanced specificity. The characteristics of the sensors have been studied and published previously [16, 17]. They were all placed inside the aluminium chamber of the gas sensing unit. A small low-cost Teensy 3.6 microcontroller was integrated inside the unit to drive the sensors and collect data. All sensors were driven with constant current circuits and the microhotplate temperatures were set to 400°C for optimum performance. A commercial environmental

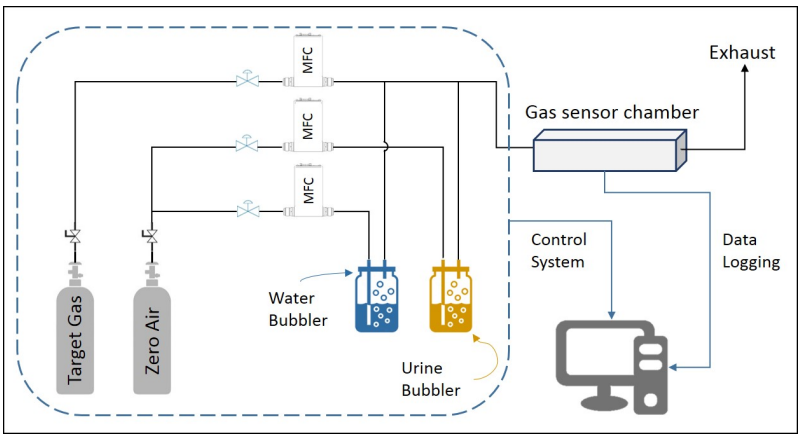

Figure 7.1: Screenshot of the acetone NDIR sensor towards liquid acetone vapour on the mobile robot.

sensor (BME 280, BOSCH) was also included for ambient humidity, temperature and pressure monitoring. Due to the high humid nature of the urine headspace, relative humidity (RH) and temperature were monitored to make sure all experiments were carried out under the same conditions.

7.2.2 Results Pre-processing

In order to collect a variety of data samples for further processing, different concentration and humidity levels were trialled. Ammonia was tested at concentrations of 1 ppm, 3 ppm, 5 ppm, 8 ppm, and 10 ppm. The same concentrations were applied to ethyl acetate. Concentrations for acetone were 1 ppm, 5 ppm, 10 ppm, 30 ppm, and 50 ppm. For synthetic urine, percentage levels were trialled at 1%, 2%, 3%, 4%, and 5% (at standard atmosphere). Three relative humidity levels were selected for experiments: 0%, 25% and 50%. Each experiment was performed with 5-minute steps of the target gas and synthetic air baseline in between. For instance, the steps for ammonia experiment were: 1 ppm, 3 ppm, 5 ppm, 8 ppm, 10 ppm, 8 ppm, 5 ppm, 3 ppm, and 1 ppm, a total of 9 steps. Similar step experiments were trialled for other gases based on their concentration settings. Five repeats were conducted for each gas at each humidity level. The raw sensor response plots are similar to Figure. 6.13 shown in Chapter 6.

Pre-processing steps were then implemented. The data used for algorithms include three sensor responses, gas concentration levels, humidity levels and gas types. The raw sensor responses were in voltages, which were converted into resis-

tance values using the same method mentioned in Chapter 6. To obtain the sensor response, instead of directly using the resistance values, an extra step was used. In literature [18], common pre-processing algorithms to describe the sensor response are:

- Absolute response: R_g,
- Difference response: $(R_g - R_b)$,
- Relative Difference: (R_g/R_b) or (R_b/R_g),
- Fractional Difference: $(R_g - R_b)/R_b$,

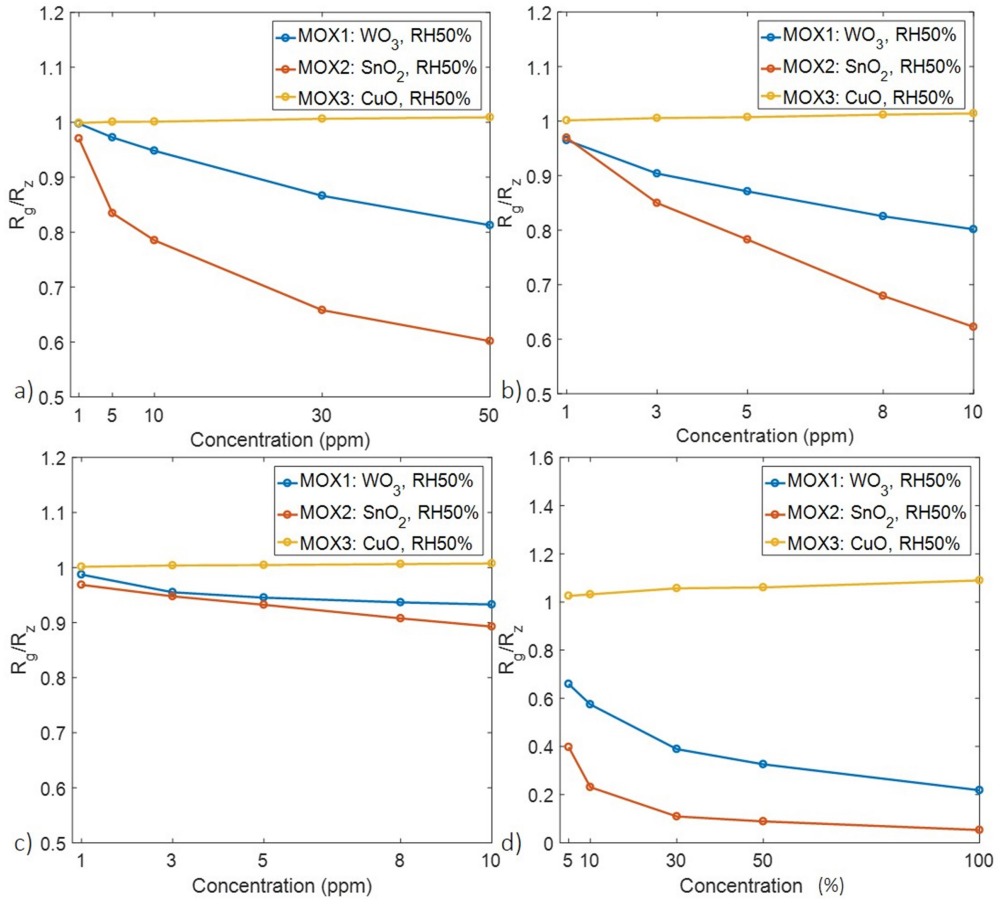

Figure 7.2: Sensor response in relative difference of three MOX sensors (MOX1: WO_3, MOX2: SnO_2, MOX3: CuO) towards (a) acetone, (b) ammonia, (c) ethyl acetate and (d) synthetic urine, at five concentration levels, all in 50% relative humidity condition.

where R_b is the resistance value at synthetic air baseline, and R_g is the resistance value with the response to the given gas. The relative difference was used as the response data, which was averaged and compressed to a single data point per concentration level. Therefore, 9 data points were extracted for one experiment at one humidity level. With five repeats, a total of 135 (9 data points $\times$ 5 repeats $\times$ 3 RH) data points were acquired for one given gas. Figure. 7.2 shows the acquired data plotted at each humidity level against concentrations for each gas of interest. For repeated data points, i.e. 1 ppm at the beginning and end of the experiment, only one data point was shown.

The same auto-ranging method was applied to the rest of the datasets, which was to normalise the data between the minimum and maximum value. This allows the data to spread evenly across all sensors and contribute proportionately in the training model. Sensor response data were auto-ranged between [-1, +1], and concentration and humidity levels were auto-ranged between [0, 1]. The gas type information was presented either in binary form or class numbers depending on the algorithms, such as '0' for not gas and '1' for gas, or '1' to '4' for four gases. The detailed data information for each algorithm will be given later.

7.3 Principal Component Analysis (PCA)

7.3.1 Algorithm Introduction and Steps

The first signal processing method trialled was the principal component analysis. It is one of the dimensionality reduction algorithms, where the input variables are reduced to a set of principal variables. This statistical procedure was first invented by Karl Pearson in 1901 and improved later by Harold Hotelling [19]. The algorithm transforms a large dataset into a new set of variables that contains only the critical information. The high dimensionality of the large dataset is reduced to two (2D) or three (3D) variables, which can be plotted against each other to form data clusters correlating to the data classes. This is one of the most common linear methods used for gas sensor array analysis.

The pre-processed data were used instead of the raw sensor data as the initial input of the algorithm. This is to minimise the data range so that the larger values will not dominate the results. The input dataset contains the three sensor responses,

the concentration and humidity levels, and the output dataset is the four classes. These five inputs were first processed to find correlations for feature elimination and extraction. This was achieved using covariance matrices. Covariance is a measure to find how much each of the dimensions/inputs varies from the mean value with respect to each other, i.e. the relationship between dimensions. For the dataset with five input dimensions (a to e), the matrix looks like:

$$C = \begin{pmatrix} \text{cov(a,a)} & \text{cov(a,b)} & \text{cov(a,c)} & \text{cov(a,d)} & \text{cov(a,e)} \\ \text{cov(b,a)} & \text{cov(b,b)} & \text{cov(b,c)} & \text{cov(b,d)} & \text{cov(b,e)} \\ \text{cov(c,a)} & \text{cov(c,b)} & \text{cov(c,c)} & \text{cov(c,d)} & \text{cov(c,e)} \\ \text{cov(d,a)} & \text{cov(d,b)} & \text{cov(d,c)} & \text{cov(d,d)} & \text{cov(d,e)} \\ \text{cov(e,a)} & \text{cov(e,b)} & \text{cov(e,c)} & \text{cov(e,d)} & \text{cov(e,e)} \end{pmatrix} \tag{7.1}$$

where each covariance is calculated through:

$$\text{cov(a, b)} = \frac{\sum_{i=1}^{n}(a_i - \overline{a})(b_i - \overline{b})}{(n-1)} \tag{7.2}$$

for the data length of n and mean values of $\overline{a}$ and $\overline{b}$. A negative covariance indicates one value increases with the decrease of the other (inversely correlated); a positive covariance indicates one value increases with the increase of the other; and a zero covariance indicate independent inputs. Similarly, the correlation value can be found through:

$$\text{cor(a, b)} = \frac{\text{cov(a, b)}}{\sigma_a \sigma_b} \tag{7.3}$$

where σ_a and σ_b are the standard deviation of input a and b, respectively.

The covariance values determine the relationships between each dimension, then eigenvectors and eigenvalues of the matrix are found. The purpose of this step is to identify the principal components (features) of the dataset, which are independent to each other and carry the most important information, i.e. the five inputs can be compressed into two or three components. Typically, the first component accounts for the maximum possible information, and the last one accounts for the least. Each eigenvector has its corresponding eigenvalue, and the calculated eigenvalues are arranged in descending order with the largest one as the first principal component, the second one as the second, and so on. The percentage of each component is also obtained by dividing the individual eigenvalues by the sum of all eigenvalues. The percentage and descending order show the significance of each component, and

lesser ones are discarded. The remaining ones become a matrix with key features. Figure. 7.3 shows the algorithm steps in a flow chart.

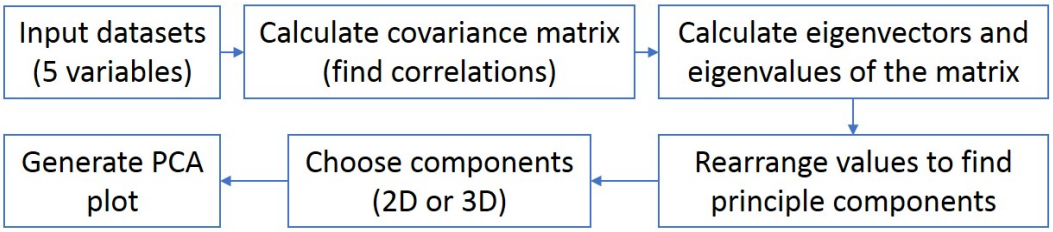

Figure 7.3: The flow chart of PCA algorithm steps.

7.3.2 Results

A Python script was written to perform the PCA analysis with the help of the scikit-learn library. Both 2D and 3D plots were trialled, as shown in Figure. 7.4. The first three components contain more than 98% of the important information.

In the 2D plot, no visible clusters can be observed and data are spread within three parallel regions (relates to three humidity levels). The first component and the second component have inverse correlations where one increases and the other one decreases. However, in the 3D plot, each gas correlates to a plane. This indicates the importance of the third component in the cluster discrimination. Acetone, ammonia and synthetic urine have a similar distribution pattern, and their planes are close together. Ethyl acetate has a wider distribution pattern, hence a more distinctive sensor behaviour. When a new dataset is introduced, based on the coordinates, it can be classified to the gas plane it is closest to. Though 3D planes can be observed for different target gases, the principal component analysis is not a suitable classification algorithm and harder to implement onto a microcontroller.

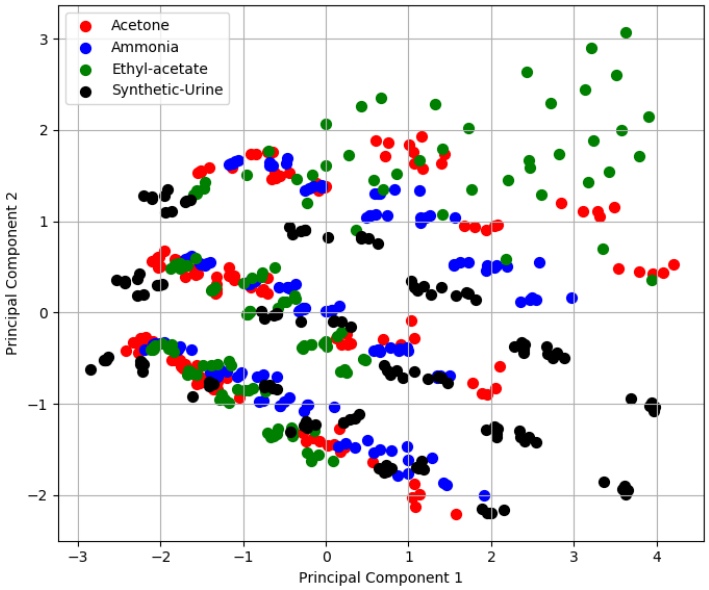

(a) 2 principal components.

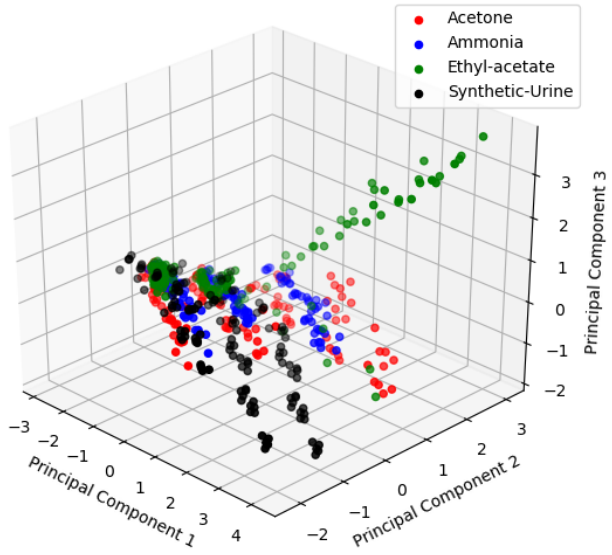

(b) 3 principal components.

Figure 7.4: Results using PCA analysis.

7.4 Instance Based Algorithms

The second method trialled is the instance based clustering algorithm, in particular, the k-nearest neighbour (KNN) and self-organising maps (SOM). The model is trained and adapted based on the input dataset, and class clusters are formed. It stores the known data, or instances, that the new data are compared to. KNN compares the new data with the known data using distance equations, while SOM compares the new data based on the most suitable weight neuron. These two methods are introduced in this section and realised through python and MATLAB programs.

7.4.1 k-Nearest Neighbours (KNN)

The k-Nearest neighbour algorithm assumes the proximity of a class in n-dimensional space. In another words, it assumes similar data points are closer to each other. It is a non-parametric, instance-based method that does not assume a function for the variables. This algorithm finds the similarity, or proximity of date points under the same class, then groups them together in one location.

The k value in KNN is defined as the number of neighbour instances that the new data point is compared to, commonly it is an odd integer. Therefore, when $k = 1$, the new data point is assigned to a class based on a single nearest neighbour. This number is pre-defined before training starts. It is important to optimise the k value to prevent over-fitting and under-fitting. The appropriate number of neighbours will result in a smooth class boundary and an accurate classification with minimum errors. The similarity between the new data point and its neighbours is calculated using distance measurement methods, such as Euclidean distance, Hamming distance, Manhattan Distance, Minkowski distance (a combination of Euclidean and Manhattan), etc.. The Euclidean distance calculation is the most commonly used one, and is linear. It calculates the straight-line between two points in the Euclidean space, so the distance between point x and point y follows the Pythagorean formula as:

$$d(x,y) = \sqrt{(x_1 - y_1)^2 + (x_2 - y_2)^2 + ... + (x_n - y_n)^2} = \sqrt{\sum_{i=1}^{n}(x_i - y_i)^2} \tag{7.4}$$

The equations for the other popular distance measurement methods are listed below.

- Hamming distance: $d(x,y) = \sum_{i=1}^{n} \mid x_i - y_i \mid$ (if $x = y$, $d = 0$, else $d = 1$)
- Manhattan distance: $d(x,y) = \sum_{i=1}^{n} \mid x_i - y_i \mid$
- Minkowski distance: $d(x,y) = (\sum_{i=1}^{n}(\mid x_i - y_i \mid)^k)^{\frac{1}{k}}$

The calculated distances are then sorted in ascending order and the top k numbers from the array are used for the next step. The probability is obtained using the most frequent class of these k values as the class label for the new/unknown data point. Figure. 7.5 shows the flow chart of these processing steps.

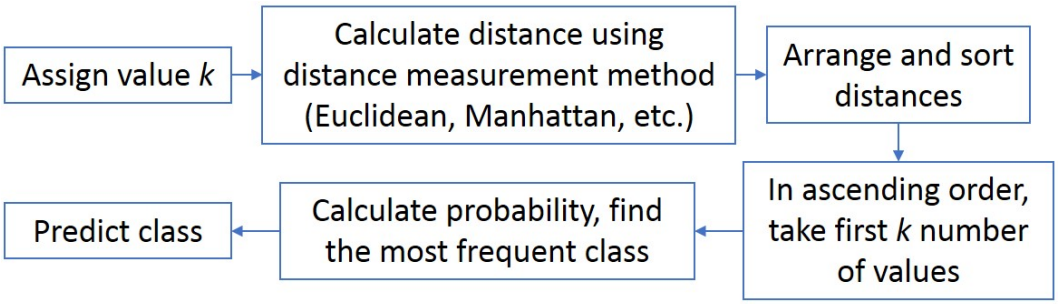

Figure 7.5: The flow chart of KNN steps.

KNN is an easy to implement algorithm that requires no stastical assumptions. It is accurate and versatile, and all the data are stored and used without any data compressions or eliminations. But it needs high computation power and high memory for large datasets. It can also be affected by the curse of dimensionality [20], which occurs in high-dimensional data (lots of input variables) as the increase of dimensionality can cause an increase in data space. The sparse data will negatively influence the classification results.

The dataset used in this work contains five input variables and four class labels. The input variables are the auto-ranged humidity levels, the concentration levels, and the three MOX sensor response data. The output classes are acetone, ammonia, ethyl acetate and synthetic urine. Within the five repeated test data,

four sets were used for training and one for testing. A python script was written based on the scikit-learn machine learning library. First, the optimised k value was found by calculating the accuracy of the model. An accuracy against k value plot is shown in Figure. 7.6. The accuracy of the model increases initially with the increase of k value (under-fitting), but after reaching the limit, the accuracy decreases with the increase of k (over-fitting). The optimum value, $k = 5$, was then defined for the model to train and test all datasets.

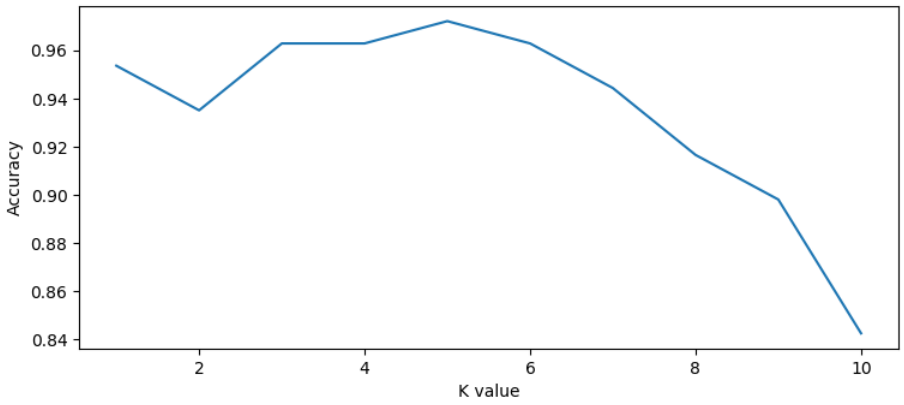

Figure 7.6: The model accuracy against k value.

The training process allows the model to form five classes. The testing dataset was then calculated using the same distance measurement function, Euclidean distance, to assign its classes. A confusion table is used to demonstrate the prediction results versus target results. Table. 7.2 to 7.6 are the confusion tables for the five datasets (dataset 1 to 5) and their corresponding accuracies in percentage. Accuracy is defined as the true positives over total positives.

Table 7.2: Confusion table obtained using the KNN algorithm (dataset 2–5 for training, dataset 1 for testing).

Predicted Outputs	**Target Outputs**			
	Acetone	**Ammonia**	**Ethyl Acetate**	**Synthetic Urine**
Acetone	26	0	0	0
Ammonia	1	27	0	0
Ethyl Acetate	0	0	25	0
Synthetic Urine	0	0	0	27
Total Number	*27*	*27*	*27*	*27*
Total Accuracy: 97.22%				

Table 7.3: Confusion table obtained using the KNN algorithm (dataset 1 & 3–5 for training, dataset 2 for testing).

Predicted Outputs	**Target Outputs**			
	Acetone	**Ammonia**	**Ethyl Acetate**	**Synthetic Urine**
Acetone	26	1	7	0
Ammonia	0	24	6	0
Ethyl Acetate	0	2	14	0
Synthetic Urine	1	0	0	27
Total Number	*27*	*27*	*27*	*27*
Total Accuracy: 84.26%				

Table 7.4: Confusion table obtained using the KNN algorithm (dataset 1–2 & 4–5 for training, dataset 3 for testing).

Predicted Outputs	**Target Outputs**			
	Acetone	**Ammonia**	**Ethyl Acetate**	**Synthetic Urine**
Acetone	26	0	0	0
Ammonia	0	27	2	0
Ethyl Acetate	0	0	25	0
Synthetic Urine	1	0	0	27
Total Number	*27*	*27*	*27*	*27*
Total Accuracy: 97.22%				

Table 7.5: Confusion table obtained using the KNN algorithm (dataset 1–3 & 5 for training, dataset 4 for testing).

Predicted Outputs	**Target Outputs**			
	Acetone	**Ammonia**	**Ethyl Acetate**	**Synthetic Urine**
Acetone	27	0	0	0
Ammonia	0	24	1	0
Ethyl Acetate	0	3	26	0
Synthetic Urine	0	0	0	27
Total Number	*27*	*27*	*27*	*27*
Total Accuracy: 92.30%				

Table 7.6: Confusion table obtained using the KNN algorithm (dataset 1–4 for training, dataset 5 for testing).

Predicted Outputs	**Target Outputs**			
	Acetone	**Ammonia**	**Ethyl Acetate**	**Synthetic Urine**
Acetone	27	0	0	0
Ammonia	0	21	1	0
Ethyl Acetate	0	1	26	0
Synthetic Urine	0	5	0	27
Total Number	*27*	*27*	*27*	*27*
Total Accuracy: 93.52%				

The averaged overall accuracy is 92.90%. Apart from dataset 2, all the other four datasets have accuracies over 92 % with the highest at 97.22% for dataset 1 & 3. It is possible that dataset 2 is not a good experiment result, or the k value for this particular dataset needs to be optimised further. Because the k value was only optimised based on one dataset (dataset 1), so a higher accuracy can be achieved if the k value is optimised for all datasets separately. In all five datasets, synthetic urine can be successfully classified with no error, which is what the application requires.

A classification report with each dataset was also generated, Table. 7.7 shows an example with dataset 1. This report is defined using true and false positives and negatives, and it is a representation of the main classification metrics on a per-class basis. There are four key metrics: precision, recall, f1 score and support. They are

Table 7.7: The classification report with dataset 1.

	Precision	**Recall**	**F1-score**	**Support**
Acetone	1	0.96	0.98	27
Ammonia	0.9	1	0.95	27
Ethyl Acetate	1	0.93	0.96	27
Synthetic Urine	1	1	1	27

defined as:

- Precision is the accuracy of positive predictions.
  P = TP/(TP+FP)
- Recall is the fraction of positives that are correctly classified.
  R = TP/(TP+FN)
- F1-score is a weighed harmonic mean of precision and recall (1.0 as best score and 0.0 as the worst).
  F1 = 2 × (R × P)/(R + P)
- Support is the number of occurrences of the given class, i.e. 27 per class in the testing model.

Those abbreviations used above, TP, FP, FN represent true positive, false positive and false negative, respectively.

PCA sometimes is used as a pre-processing step for KNN to reduce date dimensions and avoid the curse of dimensionality. Therefore, the PCA processed data in section. 7.3 were trialled with the KNN model and compared with the results without the PCA process. However, this extra step did not improve the classification results, and the data without PCA pre-processing step provides a better classification accuracy (at 92.9%). The overall averaged accuracy for KNN with PCA is 88.89%. The confusion tables and classification reports for the KNN with PCA pre-processed data are presented in the appendix.

KNN is a simple algorithm that gives a high prediction accuracy with the given training data. It is a suitable training method for this dataset to distinguish urine odour from its similar compounds. The main disadvantage is the amount of memory it requires. As one of the end goals is to implement an appropriate algorithm

onto a microcontroller for real-time odour classification, the high computation power and memory requirements may not be the best solution for such application. Overall, KNN is a good method for off-line supervised odour classification.

7.4.2 Self-Organising Maps (SOM)

Another instance based algorithm trialled is the self-organising maps, also known as the Kohonen Map. It was first introduced by Teuvo Kohonen in 1980s [21]. It allows a visualisation of a high dimensional dataset in a low dimensional (2D) format. The visualisation is achieved through a map space, with nodes or neurons in a rectangular or hexagonal grid. Unlike KNN, SOM is an unsupervised training algorithm, as it learns the model through training without prior knowlegde of the class labels. The class information is learned through trainings.

The algorithm starts by initializing a map topology. The map consists of nodes/neurons that will be linked with input nodes, for instance a 10×10 grid for 100 nodes. An example map is shown in Figure. 7.7. SOM is developed based on an adaptive learning model, and the nodes are competing to represent the input nodes (competitive learning). The number of nodes for the map is depending on the dataset and more nodes give a bigger map. For a more advanced model, a growing/adaptive map can be used, but here, the map nodes are fixed.

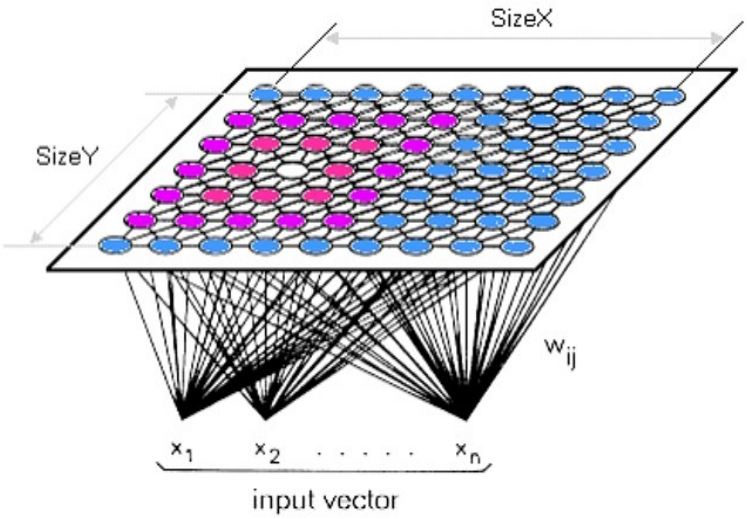

Figure 7.7: An example SOM topology.

The weight for each node is then initialised with a random value. A sample

input is selected to test and find the weights best represent the input to its output. These weights and their corresponding nodes are the winning neurons that become a meaningful coordinate system. The competition process is based on a discriminant function as:

$$d_j(x) = \sum_{i=1}^{N}(x_i - w_{ji})^2 \tag{7.5}$$

where x is the input vector, N is the number of input dimensions, w is the weight vector, i is the input number and j is the neuron number [22]. This function is the squared Euclidean distance between the input vector (x) and the weight vector (w) for each neuron. The winning neuron (best matching unit, BMU) has the smallest discriminant function value. This neuron and its surrounding neighbours are updated with weight equation:

$$\Delta w_{ji} = \eta(t)T_{j,I(x)}(t)(x_i - w_{ji}) \tag{7.6}$$

where $I(t)$ is the index of the winning neuron, t is the epoch, $\eta(t)$ is the learning rate and $T_{j,I(x)}$ is the topological neighbourhood [22]. The weights are then adjusted to pull the neighbouring nodes closer towards the input vector. These steps are repeated and the nodes with a similar pattern are then clustered together to form a class. The end result is a feature map with the coordination information for each class. Figure. 7.8 shows the flow chart of this process.

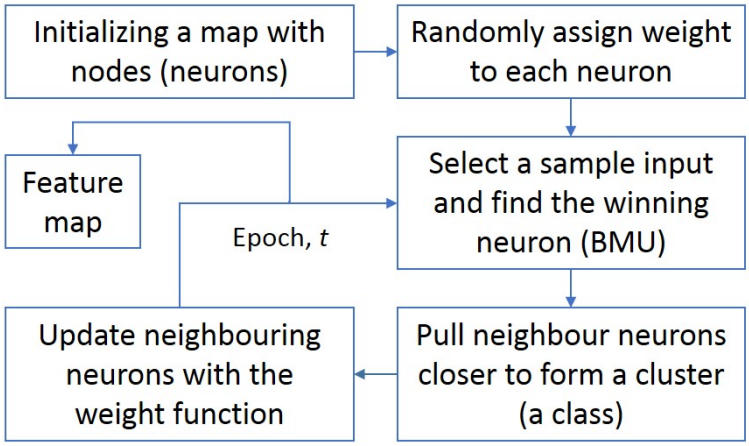

Figure 7.8: Flow chart of the SOM algorithm.

This method was trialled using the same dataset and the MATLAB neural network clustering toolbox. A 10 × 10 neuron map was generated first on a rectangular grid. Five input variables were trained without class information, and each

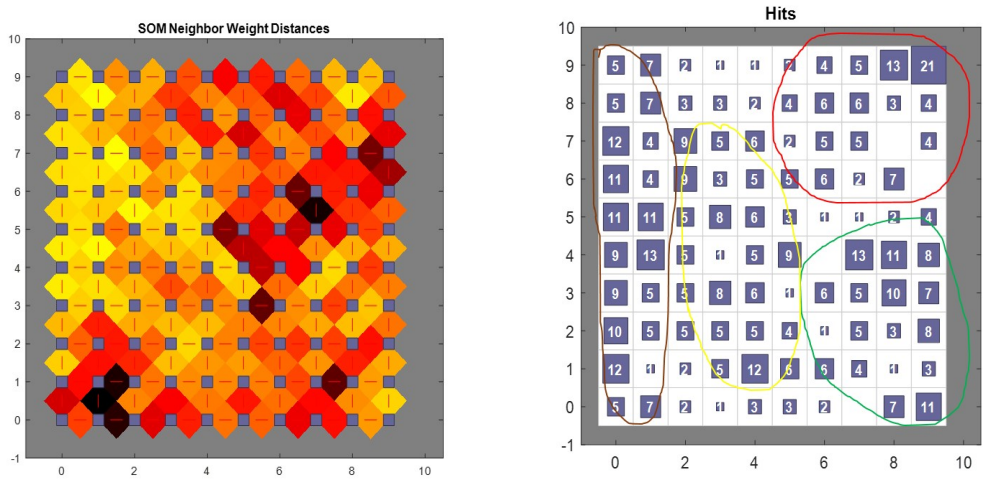

(a) SOM feature map with weight distance.

(b) SOM sample hits.

Figure 7.9: Temperature modulation using resistance signal in zero air.

neuron was adjusted based on the input data. After training, the feature map was created with blue squares as neurons and gradient colours as distances between neurons, as shown in Figure. 7.9a. The darker colour indicates a larger distance, which is also the borderline between classes, and the brighter colour indicates a closer distance of similar features, and a smooth distribution of sample hits. The sample hit distribution in Figure. 7.9b can be used to compare with the weight distance map and identify classes. From these figures, classes can be identified such as one class on the left (the brighter colour region), a cluster of hits on the bottom right corner, one class at the top right with most hits, and one cluster in the middle, as marked.

The weight of each input was also plotted to show dependency, as shown in Figure. 7.10. Inputs with similar coloured maps suggest dependency, and less similarity suggests independent features. No obvious similarity can be observed which means all inputs are independent and essential for the classification process. The weight position plot in Figure. 7.11 shows the weight clusters. This plot is originally in a 5D (5 input variables) format, which is compressed to present in 2D instead. Overall, SOM is a great way to present the data classification clusters visually. This result shows the feasibility of using this algorithm with this dataset.

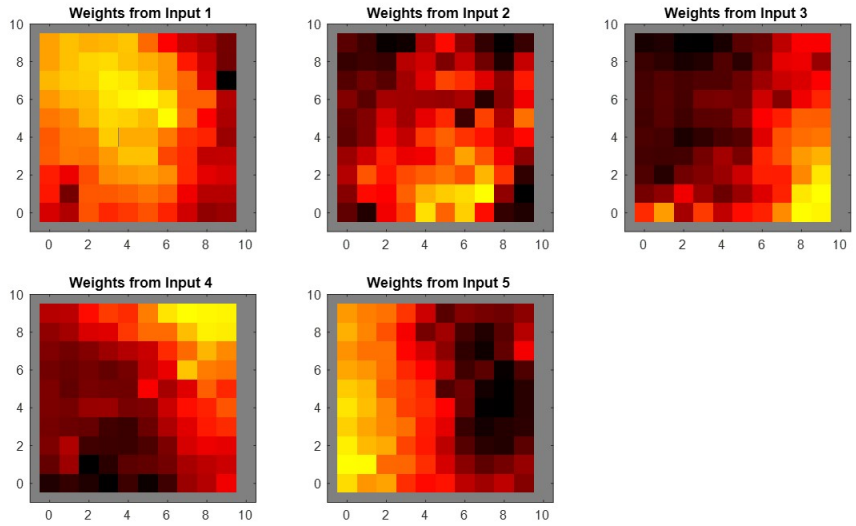

Figure 7.10: Weight map for input variables.

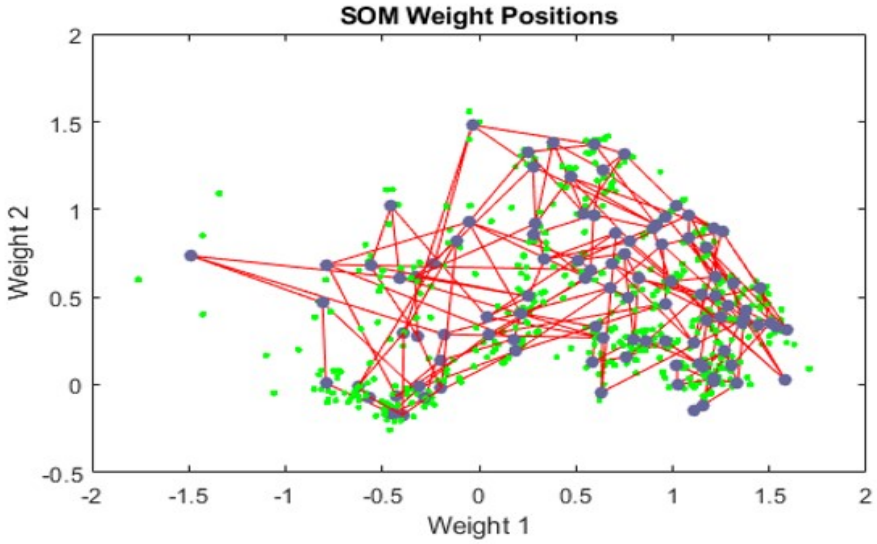

Figure 7.11: The weight position plot of the SOM model.

7.5 Shallow Neural Network

The artificial neural network is a method inspired by the biological neural system. This method was introduced in Chapter 6 to analyse the thermally modulated sensor data. When the network model has 1 or 2 hidden layers, it is considered as a shallow neural network; for a more complex system, it is known as a deep neural

network. This section focuses on the shallow neural network with a similar method used previously, and the next section will discuss the deep neural network.

7.5.1 Algorithm Introduction and Steps

The shallow neural network can provide a simple and understandable insight into the neural network learning model. It consists of an input layer, hidden layer(s) and an output layer. The last chapter introduced the Levernberg-Marquardt optimisation algorithm, which is more suited for the regression analysis. Here, the scaled conjugate gradient algorithm is used for the classification problem. It is a supervised feed-forward backpropagation learning method based on the Levernberg-Marquardt approach. Compare to the other conjugate gradient methods, it avoids the line search per iteration, which is needed to determine the step size. [23]. The step size is the length of the weight update, which is determined by the learning rate. In a standard backpropagation algorithm, the step size is based on the steepest descent direction. In the conjugate gradient algorithm, the step size is determined through the search along the conjugate gradient direction. In the scaled conjugate gradient, the step size is found through a scaling mechanism, which reduces the time consumption of the algorithm and a super-linear convergence [24].

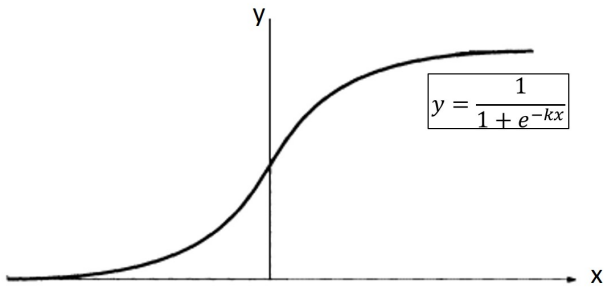

Figure 7.12: Sigmoid function plot and its formula.

The model uses the sigmoid function in the hidden layers and the softmax function for the output layer. Unlike the step function, the sigmoid function gives a smoother output with the change in the input only causes a small change in the output. Figure. 7.12 shows the curve and formula for the sigmoid function. The softmax function normalises the values following the probability distribution that

sums to 1. The function is defined as:

$$softmax(x_i) = \frac{e^{x_i}}{\sum_{j=1}^{n} e^{x_j}} \tag{7.7}$$

and the output is in the range of [0, 1].

The model performance is evaluated using the cross entropy. It is a method to analysis the loss function of the model, especially for classification problems. The cross entropy (CE) is calculated using:

$$CE(t, y) = -t \times log(y) \tag{7.8}$$

where y is the estimated output value and t is the target value. Each output is evaluated and the total performance of the given dataset is:

$$CE_{total} = \frac{\sum_{i=1}^{n} CE(t_i, y_i)}{n} \tag{7.9}$$

for a total of n output values. The full algorithm step is presented in Figure. 7.13.

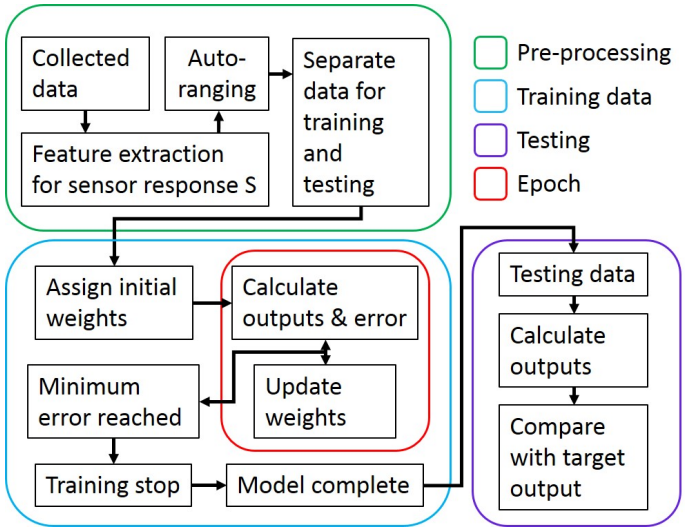

Figure 7.13: Block diagram of the data processing steps.

7.5.2 Data with Concentration Input

The first attempt used the same input dataset as the previous algorithms, which are the concentration level, the humidity level and the three sensor responses.

The neural network model has two hidden layers with 8 neurons each. The output neurons are in binary form with '1' for gas and '0' for no gas. The topology of the network is shown in Figure. 7.14.

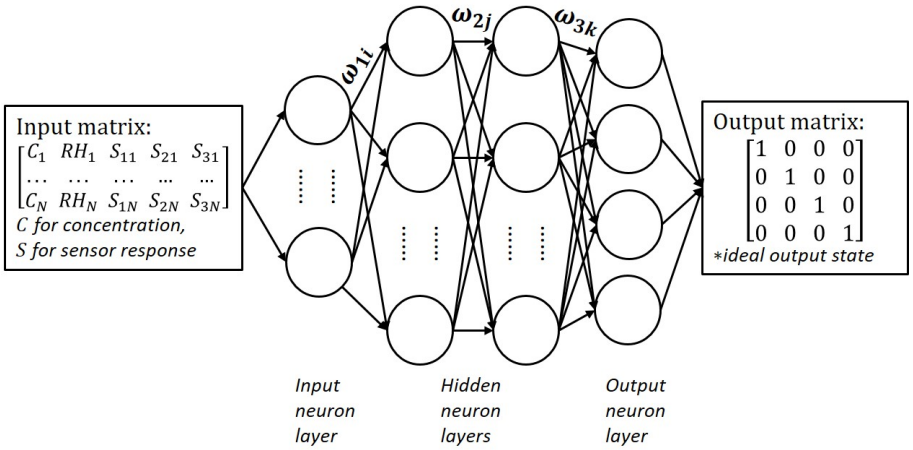

Figure 7.14: The topology of the shallow neural network model with 5 input neurons, 2 hidden layers of 8 neurons each, and 4 output neurons.

Same as the KNN model, different combinations of the five datasets were used for training and testing. The model performance was determined using both the classification accuracy and the cross entropy value. Table. 7.8 to 7.12 are the classification results in confusion tables using these five datasets.

Base on the confusion tables, the ANN model is not as good as the KNN model in terms of classification accuracy. In KNN, 100% synthetic urine can be identified, while in ANN only 95% is successfully classified. The worst classification result occurred with dataset 2, in particular, the identification of ethyl acetate. This indicates that the sensors share some similarities in the response towards the gas of interest. The overall classification accuracy, averaged over five datasets, is 88.05%. The model performance is evaluated using the cross entropy as summarised in Table. 7.13. The cross entropy is lower with the dataset of higher accuracy, and the averaged performance is 0.0478.

7.5.3 Data without Concentration Input

In real life application for detecting urine odour, it is not possible to know the gas concentration values. Therefore, to achieve a more realistic classification

Table 7.8: Confusion table obtained using the ANN algorithm (dataset 2–5 for training, dataset 1 for testing).

Predicted Outputs	**Target Outputs**			
	Acetone	**Ammonia**	**Ethyl Acetate**	**Synthetic Urine**
Acetone	21	1	1	0
Ammonia	4	22	0	0
Ethyl Acetate	2	2	24	0
Synthetic Urine	0	2	2	27
Total Number	*27*	*27*	*27*	*27*
Total Accuracy: 87.03%				

Table 7.9: Confusion table obtained using the ANN algorithm (dataset 1 & 3–5 for training, dataset 2 for testing).

Predicted Outputs	**Target Outputs**			
	Acetone	**Ammonia**	**Ethyl Acetate**	**Synthetic Urine**
Acetone	25	0	10	0
Ammonia	2	25	7	1
Ethyl Acetate	0	2	10	0
Synthetic Urine	0	0	0	26
Total Number	*27*	*27*	*27*	*27*
Total Accuracy: 79.62%				

Table 7.10: Confusion table obtained using the ANN algorithm (dataset 1–2 & 4–5 for training, dataset 3 for testing).

Predicted Outputs	**Target Outputs**			
	Acetone	**Ammonia**	**Ethyl Acetate**	**Synthetic Urine**
Acetone	23	1	1	0
Ammonia	2	25	0	2
Ethyl Acetate	1	0	26	1
Synthetic Urine	1	1	0	24
Total Number	*27*	*27*	*27*	*27*
Total Accuracy: 90.74%				

Table 7.11: Confusion table obtained using the ANN algorithm (dataset 1–3 & 5 for training, dataset 4 for testing).

Predicted Outputs	**Target Outputs**			
	Acetone	**Ammonia**	**Ethyl Acetate**	**Synthetic Urine**
Acetone	26	2	0	0
Ammonia	0	24	2	1
Ethyl Acetate	1	1	25	1
Synthetic Urine	0	0	0	25
Total Number	*27*	*27*	*27*	*27*
Total Accuracy: 92.56%				

Table 7.12: Confusion table obtained using the ANN algorithm (dataset 1–4 for training, dataset 5 for testing).

Predicted Outputs	**Target Outputs**			
	Acetone	**Ammonia**	**Ethyl Acetate**	**Synthetic Urine**
Acetone	27	0	2	0
Ammonia	0	23	1	0
Ethyl Acetate	0	1	24	1
Synthetic Urine	0	3	0	26
Total Number	*27*	*27*	*27*	*27*
Total Accuracy: 92.56%				

Table 7.13: Performance evaluation of the five datasets.

Datasets	**Cross Entropy**
Dataset 1	0.0563
Dataset 2	0.0919
Dataset 3	0.0332
Dataset 4	0.0269
Dataset 5	0.0305
Averaged	*0.0478*

outcome, the concentration level is removed as an input neuron. The humidity level, however, can be measured by a temperature humidity sensor, such as BME 280 (BOSCH). With the missing concentration information, it could be harder for

the model to classify gases. A similar topology is used with 4 input neurons instead of the previous 5 neurons, 2 hidden layers with 8 neurons each, and 4 output neurons of the target gases in binary form. Table. 7.14 to 7.18 are the confusion tables with this neural network model.

Table 7.14: Confusion table obtained using the ANN algorithm with no concentration information (dataset 2–5 for training, dataset 1 for testing).

Predicted Outputs	**Target Outputs**			
	Acetone	**Ammonia**	**Ethyl Acetate**	**Synthetic Urine**
Acetone	23	0	0	3
Ammonia	1	22	2	1
Ethyl Acetate	1	5	24	0
Synthetic Urine	2	0	1	23
Total Number	*27*	*27*	*27*	*27*
Total Accuracy: 85.19%				

Table 7.15: Confusion table obtained using the ANN algorithm with no concentration information (dataset 1 & 3–5 for training, dataset 2 for testing).

Predicted Outputs	**Target Outputs**			
	Acetone	**Ammonia**	**Ethyl Acetate**	**Synthetic Urine**
Acetone	21	0	9	1
Ammonia	2	23	5	3
Ethyl Acetate	3	3	12	0
Synthetic Urine	1	1	1	23
Total Number	*27*	*27*	*27*	*27*
Total Accuracy: 73.15%				

Table 7.16: Confusion table obtained using the ANN algorithm with no concentration information (dataset 1–2 & 4–5 for training, dataset 3 for testing).

Predicted Outputs	**Target Outputs**			
	Acetone	**Ammonia**	**Ethyl Acetate**	**Synthetic Urine**
Acetone	24	0	0	3
Ammonia	0	26	5	2
Ethyl Acetate	2	0	21	0
Synthetic Urine	1	1	1	22
Total Number	*27*	*27*	*27*	*27*
Total Accuracy: 86.11%				

Table 7.17: Confusion table obtained using the ANN algorithm with no concentration information (dataset 1–3 & 5 for training, dataset 4 for testing).

Predicted Outputs	**Target Outputs**			
	Acetone	**Ammonia**	**Ethyl Acetate**	**Synthetic Urine**
Acetone	25	2	1	0
Ammonia	0	21	0	2
Ethyl Acetate	0	2	26	1
Synthetic Urine	2	2	0	24
Total Number	*27*	*27*	*27*	*27*
Total Accuracy: 88.89%				

Table 7.18: Confusion table obtained using the ANN algorithm with no concentration information (dataset 1–4 for training, dataset 5 for testing).

Predicted Outputs	**Target Outputs**			
	Acetone	**Ammonia**	**Ethyl Acetate**	**Synthetic Urine**
Acetone	25	0	3	1
Ammonia	0	20	0	1
Ethyl Acetate	0	1	24	1
Synthetic Urine	2	6	0	24
Total Number	*27*	*27*	*27*	*27*
Total Accuracy: 86.11%				

The classification accuracy drops with the missing concentration information, and the averaged overall accuracy is 83.89%. The model error also increases as shown in Table. 7.19 to 0.0651 instead. The classification rate for detecting urine odour is now 85.92%. Different model topologies were also explored, such as 1 hidden layer of 8 neurons. The result is presented in the appendix.

Table 7.19: Performance evaluation of the five datasets.

Datasets	**Cross Entropy**
Dataset 1	0.0615
Dataset 2	0.1034
Dataset 3	0.0631
Dataset 4	0.0410
Dataset 5	0.0564
Averaged	*0.0651*

7.5.4 Data with Encoded Output

In this part, the output values are coded with the concentration information. Therefore, instead of the previous binary form with '1' for gas and '0' for no gas, the class information is evenly scaled between [-1, 1]. There are five concentration levels for each gas, hence the class information is represented by [-0.6, -0.2, 0.2, 0.6, 1] with '-0.6' as the lowest concentration and '1' as the highest concentration. '-1' is used to represent zero concentration (no gas). Same neural network topology is employed with 2 hidden layers of 8 neurons each. The Levenberg-Marquardt algorithm is used this time and the mean squared error as the performance function. It is calculated using:

$$\text{MSE} = \frac{\sum_{i=1}^{n}(x_i - \overline{x})^2}{n} \tag{7.10}$$

The classification results are presented with data plots for each target gas. Figure. 7.15 shows the classification plot of the four target gas using dataset 1 as the testing data and others as the training data.

The grey shaded areas are the regions ($\pm$ 0.2) where the corresponding colour marks target to land. Similar figures were also plotted for the other four datasets, and they are included in the appendix. The plot shows an increasing trend in the gas concentration levels, but the model was not able to determine the precise

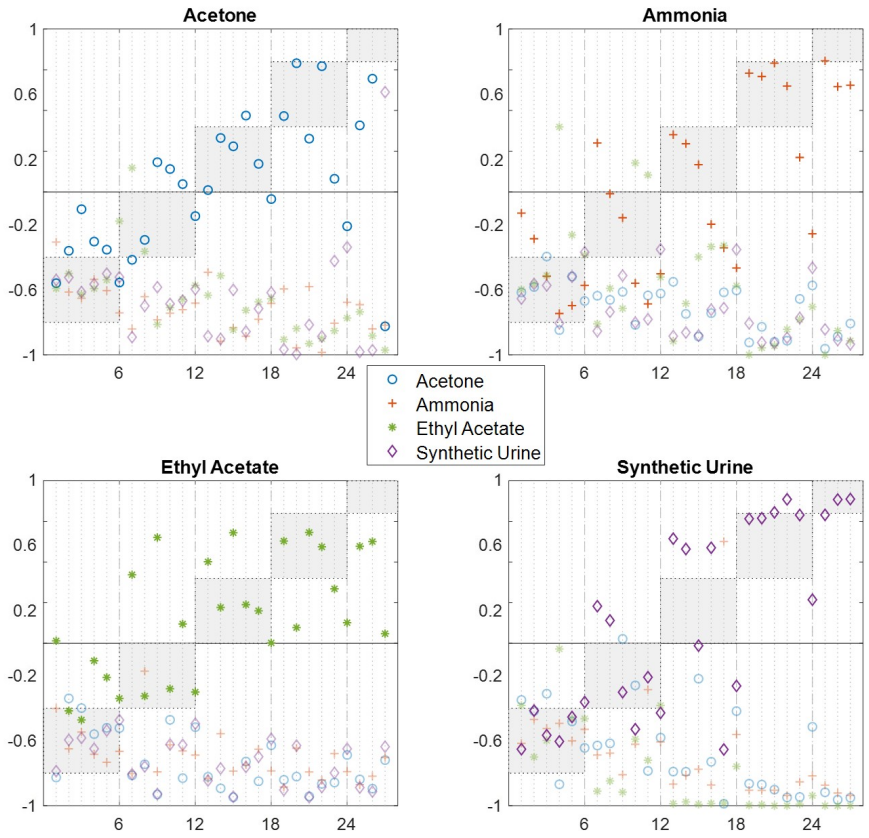

Figure 7.15: Classification results with the encoded output values using ANN with 2 hidden layers of 8 neurons each (tested with dataset 1).

concentration levels. When the output values bigger than -0.8 were considered as successful gas identifications, apart from one misclassification in acetone, all were correctly classified. Another topology was trialled with 1 hidden layer of 8 neurons. The result for the same dataset 1 is presented in Figure. 7.16. Results for the other datasets are organised in the appendix.

The second attempt was to spread the concentration encoded output between [0, 1] instead, and any value between [-1, 0] as no gas. The purpose of this is to have a more distinctive difference between gas and no gas, but the ranges for the different concentrations also become smaller. The results are not as good as the evenly spread data, so there are only included in the appendix as references. The model performances (MSE) for the five datasets under four different ANN models

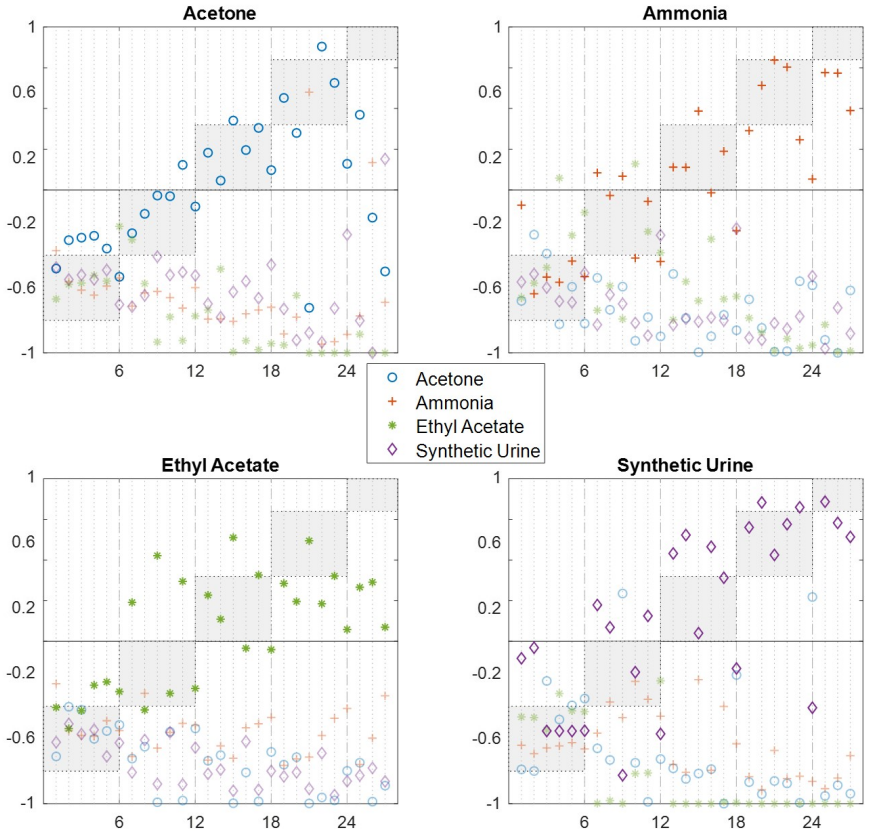

Figure 7.16: Classification results with encoded output values using ANN with 1 hidden layer of 8 neurons (tested with dataset 1).

are summarised below in Table. 7.20.

Table 7.20: Model performances (MSE) for all four ANN models.

Datasets	**Encoded Outputs ([-1, +1])**		**Encoded Outputs ([0, +1])**	
	2 Hidden Layers (8 neurons each)	**1 Hidden Layer (8 neuron)**	**2 Hidden Layers (8 neurons each)**	**1 Hidden Layer (8 neuron)**
Dataset 1	0.1502	0.1547	0.4363	0.3537
Dataset 2	0.2321	0.2646	0.3189	0.3116
Dataset 3	0.1538	0.1799	0.1802	0.1691
Dataset 4	0.1380	0.1311	0.1014	0.1094
Dataset 5	0.1399	0.1639	0.1542	0.1553
Average	0.1628	0.1788	0.2382	0.2199

7.6 Deep Neural Network

7.6.1 Algorithm Introduction and Steps

Unlike the shallow neural network, a deep neural network (DNN) model has multiple layers between the input and output nodes. It uses mathematical models to solve complex relationships, such as non-linear relationships. Each layer of the model performs a task to sort and re-organise the data for the next level processing. ANNs are inspired by the human brain functions, and DNNs are closer to human brains to solve complex classification problems using multiple approaches simultaneously. Therefore, the result of a DNN can be comparable or even better than humans. One of the most popular deep neural network models is the convolutional neural network (CNN).

CNN is a commonly used in 2D image classifications. It applies additional processing layers before a fully connected multi-layer perceptrons. Each of the additional layer processes and assembles the data into a pattern that is simplified to be used in the next layer. This algorithm mimics the human visual process system as each neuron only responds to a restricted region of the view. The regions are overlapped partially and the entire field of view is covered. With a $N \times N \times 1$ pixel image, a small region of $n \times n$ is used as the kernel that filtering through the original image and becoming a convoluted feature image. This step is known as the convolution layer. This layer extracts the image information and passes it on to the next layer, the pooling layer. A pooling layer reduces the data dimension using max or average pooling functions. Max pooling uses the maximum value of a $a \times a$ grid while average pooling uses the average data. Both the convolution layer and the pooling layer can be repeated until all features are extracted and then flattened for the fully connected layer. The fully connected layer works in the same manner as the shallow neural network, with the input (convoluted and flattened data) neurons, hidden neurons and output neurons fully connected to predict the classes. In the above example, the size variables, N, n and a follow the relationship of $a \leq n < N$.

For processing a time-series based dataset, the same approach can be applied. Instead of the $n \times n$ kernel, the kernel size is now $1 \times n$ which is a single row filtering window tiling down the entire dataset. The steps for the CNN model used here is presented in Figure. 7.17. The model is trained with four repeated data and tested with the other one.

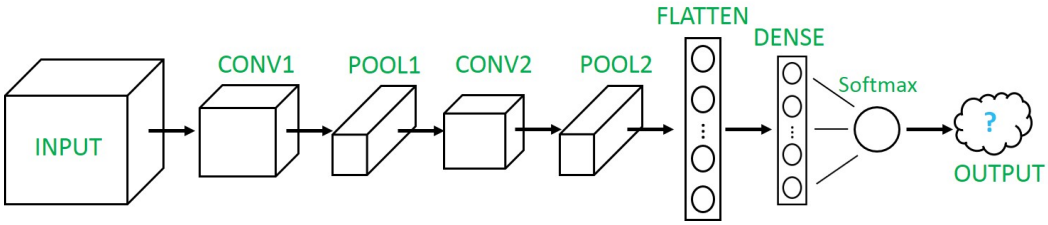

Figure 7.17: Processing steps using convolutional neural network.

7.6.2 Results

The input dataset contains the three MOX sensors response data, which are represented by three matrices of 432×3, hence the input dimension is $432 \times 3 \times 3$. Each matrix is processed through two convolution layers and two averaged pooling layers. It uses the rectified linear unit ('ReLU') as the activation function and the softmax function for the output layer. A script in Python was written to perform the task using the Keras machine learning library. A maximum of 100 epoch was set with the training process and Figure. 7.18 shows an increase in accuracy with continuance trainings. The accuracy reaches its maximum between $60 \sim 80$ epochs. Therefore any training after that is unnecessary and the model can be optimised for computation load.

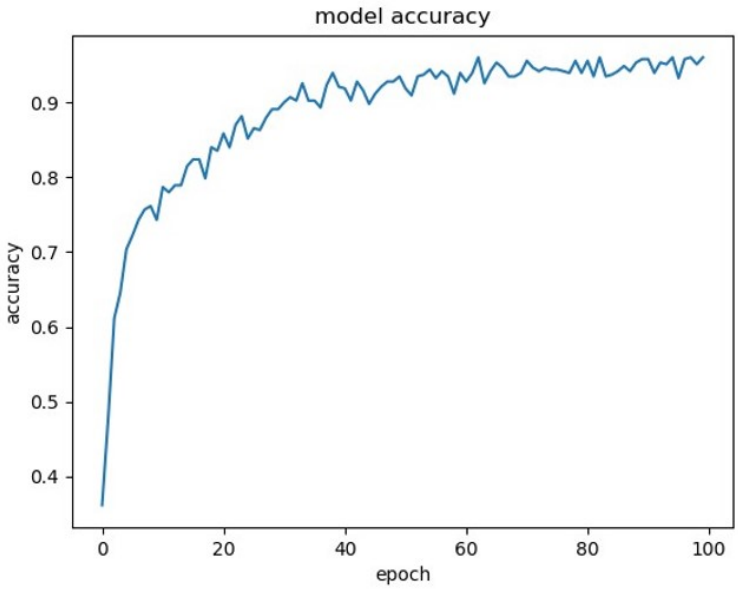

Figure 7.18: Model accuracy versus training epochs.

The trained model was then tested with the testing dataset, and results are presented in the form of confusion tables. Same as before, a classification report was generated which contained the information regarding true/false positives and true/false negatives. Table. 7.21 to 7.25 are the confusion table generated using the five datasets (dataset 1 to 5) and Table. 7.26 is the classification report using dataset 1. The overall accuracy of this CNN model is 92.59% with the highest occurs in dataset 4. The synthetic urine classification rate is 97.03%, which is not as good as some of the previous model results, but it is still a high success rate.

Table 7.21: Confusion table obtained using the CNN algorithm (dataset 2–5 for training, dataset 1 for testing).

Predicted Outputs	**Target Outputs**			
	Acetone	**Ammonia**	**Ethyl Acetate**	**Synthetic Urine**
Acetone	26	0	0	1
Ammonia	1	27	2	0
Ethyl Acetate	0	0	25	0
Synthetic Urine	0	0	0	26
Total Number	*27*	*27*	*27*	*27*
Total Accuracy: 96.30%				

Table 7.22: Confusion table obtained using the CNN algorithm (dataset 1 & 3–5 for training, dataset 2 for testing).

Predicted Outputs	**Target Outputs**			
	Acetone	**Ammonia**	**Ethyl Acetate**	**Synthetic Urine**
Acetone	23	1	10	1
Ammonia	3	26	4	0
Ethyl Acetate	0	0	12	0
Synthetic Urine	1	0	1	26
Total Number	*27*	*27*	*27*	*27*
Total Accuracy: 80.56%				

Table 7.23: Confusion table obtained using the CNN algorithm (dataset 1–2 & 4–5 for training, dataset 3 for testing).

Predicted Outputs	**Target Outputs**			
	Acetone	**Ammonia**	**Ethyl Acetate**	**Synthetic Urine**
Acetone	25	0	1	1
Ammonia	1	27	2	1
Ethyl Acetate	0	0	24	0
Synthetic Urine	1	0	0	25
Total Number	*27*	*27*	*27*	*27*
Total Accuracy: 93.52%				

Table 7.24: Confusion table obtained using the CNN algorithm (dataset 1–3 & 5 for training, dataset 4 for testing).

Predicted Outputs	**Target Outputs**			
	Acetone	**Ammonia**	**Ethyl Acetate**	**Synthetic Urine**
Acetone	27	0	0	0
Ammonia	0	25	1	0
Ethyl Acetate	0	2	26	0
Synthetic Urine	0	0	0	27
Total Number	*27*	*27*	*27*	*27*
Total Accuracy: 97.22%				

Table 7.25: Confusion table obtained using the CNN algorithm (dataset 1–4 for training, dataset 5 for testing).

Predicted Outputs	**Target Outputs**			
	Acetone	**Ammonia**	**Ethyl Acetate**	**Synthetic Urine**
Acetone	27	0	2	0
Ammonia	0	25	1	0
Ethyl Acetate	0	0	24	0
Synthetic Urine	0	2	0	27
Total Number	*27*	*27*	*27*	*27*
Total Accuracy: 95.37%				

Table 7.26: The classification report for CNN with dataset 1.

	Precision	**Recall**	**F1-score**	**Support**
Acetone	0.96	0.96	0.96	27
Ammonia	0.9	1	0.95	27
Ethyl Acetate	1	0.93	0.96	27
Synthetic Urine	1	0.96	0.98	27

7.7 Conclusions

In this chapter, different machine learning algorithms were studied with the data collected from an automatic gas sensing system. The application is to identify urine odour to aid incontinent individuals. Four gases of interest were used: acetone, ammonia, ethyl acetate and synthetic urine. Five concentrations for each gas under three humidity conditions (0%, 25% and 50%) were tested and repeated for five times. The collected data were first pre-processed with the relative difference function to obtain the sensor response data (instead of the raw voltage data) and auto-ranged between [-1, +1] for the sensor response and [0, 1] for the concentration and humidity levels. Out of the five datasets (five repeats), four were used for model training and one used for testing until all had been independently tested.

Three algorithm categories were implemented to classify urine odour from the given dataset: principal component analysis, instance based algorithms (KNN, SOM) and neural networks (ANN, CNN). The principal component analysis reduces the input data dimensions so only the principal components are used for classifications. The input data originally had five variables, which were reduced to either two or three key features. The three principal components together contained more than 98% of the data information, which were then plotted. Though clusters (classes) were observed, they did not have distinctive boundaries. Therefore, PCA is not suitable for this dataset.

The second category is the instance based algorithms, which includes the k-nearest neighbours and the self organising maps. KNN stores all the known data information and compares with the new data to assign classes. It uses distance functions to group data of the same class together in clusters and calculates the new data to its k number of neighbours. With the given dataset, the optimised k value was found to be 5. The trained model was tested with the testing data, and results were presented using confusion tables. Over the five datasets, the averaged accuracy

is 92.90% with 100% success rate for the synthetic urine odour. A classification report using the true/false positives and true/false negatives was also generated for evaluation. KNN is a high accuracy method but requires high computation power. It is a great method for off-line gas discrimination. Another instance based algorithm is the self-organising maps. It can visualise a high dimensional data in a 2D format. The 2D format is a feature map of, for instance, 10×10 neurons with each neuron has a weight assigns to it. It is a competitive learning model as neurons compete to represent the input value, and only the weight of the winning neurons and its surrounding neighbours are updated. The feature map for the given data was generated and four classes could be observed on the map. It is a great way to see the classification and weight updating processing visually, but not realistic as an on-board signal processing method.

The third method trialled was artificial intelligence, in particular, the artificial neural network and the convolutional neural network. These two methods are similar in terms of the multi-layer perceptrons topology, which means inputs neurons, hidden layers and hidden neurons, and output neurons. In ANN, two topologies were tested, 1 hidden layer 8 neurons, and 2 hidden layers with 8 neurons each. Different data combinations were experimented, including five inputs (the three sensor responses, humidity levels and concentration levels), four inputs (no concentration levels) with binary outputs, and four inputs with encoded outputs (encoded with the concentration information). Confusion tables were provided for the model with binary outputs ('gas' and 'no gas') and figure plots for models with encoded outputs. The overall classification accuracy for the data with concentration as input is 88.05% and without is 83.89%. The synthetic urine success rate is 95% with the concentration as input and 85.92% for the data without. Though ANN shows a lower classification accuracy, it is still possible to discriminate urine odour, which can be improved with a larger dataset. In CNN, one model structure was explored with the given dataset and five input variables. The convolutional neural network is a deep neural network model, which extracts the data feature prior to the fully connected multi-layer perceptrons. Data feature was obtained using convoluted layers with the kernel size of 1×3 and average pooling layers. The classification results show an overall accuracy of 92.59%, and 97.03% for synthetic urine identification.

All the work above proves the feasibility of using these sensors to detect urine odour. Different algorithms were trialled and explored, and the overall classification accuracy can be achieved at 85% or more. Therefore, this can lead to the

implementation of a real-time on-board classification algorithm that can provide an instantaneous gas indication for incontinence individuals.

References

[1] J. W. Gardner and P. N. Bartlett, *Electronic noses : principles and applications*. New York: Oxford University Press, 1999.

[2] J. E. Amoore, J. W. Johnston. Jr, and M. Rubin, "The stereochemical theory of odor," *Scientific American*, vol. 210, no. 2, pp. 42–49, 1964.

[3] World Health Organization (WHO), "World health organization calls first international consultation on incontinence," World Health Organization, Tech. Rep., 1998.

[4] D. E. Irwin, I. Milsom, Z. Kopp, P. Abrams, and L. Cardozo, "Impact of overactive bladder symptoms on employment, social interactions and emotional well-being in six European countries," *BJU International*, vol. 97, no. 1, pp. 96–100, 2006.

[5] B. A. S. Broome, "The impact of urinary incontinence on self-efficacy and quality of life," *Health and quality of life outcomes*, vol. 1, no. 35, pp. 1–3, 2003.

[6] NHS England, "Excellence in continence care: prctical guidance for commissioners, and leaders in health and social care." NHS, Tech. Rep., 2018. [Online]. Available: www.england.nhs.uk

[7] A. Ortiz Pérez, V. Kallfaß-de Frenes, A. Filbert, J. Kneer, B. Bierer, P. Held, P. Klein, J. Wöllenstein, D. Benyoucef, S. Kallfaß, U. Mescheder, and S. Palzer, "Odor-sensing system to support social participation of people suffering from incontinence," *Sensors (Basel, Switzerland)*, vol. 17, no. 1, pp. 58–73, 2016.

[8] M. Brunner, C. Droegemueller, S. Rivers, and W. E. Deuser, "Prevention of incontinence-related skin breakdown for acute and critical care patients: Comparison of two products," *Urologic Nursing*, vol. 32, no. 3, pp. 214–219, 2012.

[9] M. A. Farage, K. W. Miller, E. Berardesca, and H. I. Maibach, "Incontinence in the aged: contact dermatitis and other cutaneous consequences," *Contact Dermatitis*, vol. 57, no. 4, pp. 211–217, 2007.

[10] S. Smith, H. Burden, R. Persad, K. Whittington, B. de Lacy Costello, N. M. Ratcliffe, and C. S. Probert, "A comparative study of the analysis of human urine headspace using gas chromatography–mass spectrometry," *Journal of Breath Research*, vol. 2, no. 3, pp. 037 022–037 031, 2008.

[11] S. Esfahani, A. Wicaksono, E. Mozdiak, R. P. Arasaradnam, and J. A. Covington, "Non-invasive diagnosis of diabetes by volatile organic compounds in urine using FAIMS and Fox4000 electronic nose." *Biosensors*, vol. 8, no. 4, pp. 121–133, 2018.

[12] P. Choden, T. Seesaard, T. Eamsa-ard, C. Sriphrapradang, and T. Kerdcharoen, "Volatile urine biomarkers detection in type II diabetes towards use as smart healthcare application," in *2017 9th International Conference on Knowledge and Smart Technology (KST)*. Chonburi, Thailand: IEEE, Feb 2017, pp. 178–181.

[13] A. Roine, T. Saviauk, P. Kumpulainen, M. Karjalainen, A. Tuokko, J. Aittoniemi, R. Vuento, J. Lekkala, T. Lehtimäki, T. L. Tammela, and N. K. J. Oksala, "Rapid and accurate detection of urinary pathogens by mobile IMS-based electronic nose: a proof-of-principle study," *PloS one*, vol. 9, no. 12, pp. 114 279–114 289, 2014.

[14] A. D'Amico, M. Santonico, G. Pennazza, R. Capuano, G. Vespasiani, D. Del Fabbro, R. Paolesse, C. Di Natale, E. Martinelli, and E. F. Agrò, "A novel approach for prostate cancer diagnosis using a gas sensor array," *Procedia Engineering*, vol. 47, no. 1, pp. 1113–1116, 2012.

[15] S. Bouatra, F. Aziat, R. Mandal, A. C. Guo, M. R. Wilson, C. Knox, T. C. Bjorndahl, R. Krishnamurthy, F. Saleem, P. Liu, Z. T. Dame, J. Poelzer, J. Huynh, F. S. Yallou, N. Psychogios, E. Dong, R. Bogumil, C. Roehring, and D. S. Wishart, "The human urine metabolome," *PloS one*, vol. 8, no. 9, pp. 73 076–73 103, 2013.

[16] B. Urasinska-Wojcik, T. A. Vincent, M. F. Chowdhury, and J. W. Gardner, "Ultrasensitive WO_3 gas sensors for NO_2 detection in air and low oxygen environment," *Sensors and Actuators B: Chemical*, vol. 239, no. 1, pp. 1051–1059, 2017.

[17] B. Urasinska-Wojcik and J. W. Gardner, "H_2S sensing in dry and humid H_2 environment with p-type CuO thick-film gas sensors," *IEEE Sensors Journal*, vol. 18, no. 9, pp. 3502–3508, 2018.

[18] G. E. Searle, J. W. Gardner, M. J. Chappell, K. R. Godfrey, and M. J. Chapman, "System identification of electronic nose data from cyanobacteria experiments," *IEEE Sensors Journal*, vol. 2, no. 3, pp. 218–229, 2002.

[19] H. Hotelling, "Analysis of a complex of statistical variables into principal components," *Journal of Educational Psychology*, vol. 24, no. 6, pp. 417–441, 1933.

[20] R. E. Bellman, *Dynamic Programming*. New York: Dover Publications, Inc., 2003.

[21] T. Kohonen, "Self-organized formation of topologically correct feature maps," *Biological Cybernetics*, vol. 43, no. 1, pp. 59–69, 1982.

[22] J. A. Bullinaria, "Self organizing maps: Fundamentals," 2004. [Online]. Available: http://www.cs.bham.ac.uk/ jxb/NN/l16.pdf

[23] M. F. Møller, "A scaled conjugate gradient algorithm for fast supervised learning," *Neural Networks*, vol. 6, no. 4, pp. 525–533, 1993.

[24] Z. Zakaria, N. A. Mat Isa, and S. A. Suandi, "A study on neural network training algorithm for multiface detection in static images," *International Journal of Computer, Electrical, Automation, Control and Information Engineering*, vol. 62, pp. 170–173, 2010.

Chapter 8

Conclusion and Further Work

8.1 Overview

The main aim of this work is to develop and study low cost, high sensitive, miniature CMOS micro-hotplate based devices for gas and odour detections. There is a growing need for such devices in various applications, including air quality monitoring, industrial and laboratory conditions, military, and biomedical sectors. Among all the gas sensor technologies, two types were chosen as the main focus in this thesis, non-dispersive infra-red sensors and metal oxide semiconductors.

NDIR sensors have advantages such as good selectivities and sensitivities, long lifetime and fast response. However, conventional NDIR sensor has limitations such as bulky in size and high power consumption with a broadband infra-red emission (more than 5 μm range). To overcome these limitations, a novel plasmonic structure was employed that can tune the emission peaks to achieve higher sensitivity and selectivity. A literature review was conducted on various materials and structures. The selected design was based on a CMOS micro hotplate with three metal layers and periodic cylindrical dots to induce plasmon resonance. The COMSOL Multiphysics v5.2 was used to aid model building and simulation with various geometries tailored for different gases. The gases of interest are carbon monoxide, carbon dioxide, hydrogen sulfide, acetone and ammonia. The optimised design for each gas was then generated in a layout editor for masks, and fabricated using XI10 1.0 μm CMOS process from a commercial foundry, XFAB (Germany).

The returned devices were then measured under SEM for their geometries and tested using an automatic gas rig for their performance. Commercial detectors with optical filters were used in the sensor assembly. Gas cells of different lengths were discussed with a 10 cm aluminium tube and gold inner coating as the standard measurement system. All gases of interest were trialled at various concentration steps, and the responses for acetone and ammonia were shown in Chapter 5. The humidity influence was also investigated by testing the setup under different relative humidities. All collected data were post-processed with MATLAB to remove noise and spikes. In addition, this system was integrated into a portable, compact gas sensing unit with other sensors for a comprehensive environmental monitoring. This system has been used in applications such as EU SmokeBot and EPSRC SuperGen research project.

The second half of this thesis focuses on the data analysis side using metal oxide semiconductors. A literature review on various signal processing methods is provided in Chapter 2, including an on-board method such as thermal modulation, and off-board methods such as machine learning algorithms. The temperature modulation method uses the dynamic mode of the MOX sensors instead of their static response, therefore compensate the baseline drift and greatly increase the response speed. This method was trialled first as a post processing method, which was then adapted to an on-board algorithm compatible with a Teensy 3.6 microcontroller. By using the dynamic response of the sensors, the gas information can be obtained within a few seconds instead of tens of seconds. The results were then processed through a Fast Fourier Transform (FFT) for magnitudes analysis. The end outcome could be used directly, or processed further with prediction or regression analysis such as an artificial neural network.

The other algorithms trialled in this work are: principal component analysis, k-nearest neighbours, self-organising maps and convolutional neural network. All methods were tested with a dataset collected using three different MOX sensors and four gas types. Five concentrations and three humidity levels were explored with five repetitions. Feature extractions were performed on the dataset prior to the algorithms. The results from these algorithms were compared with a shallow neural network model, and overall an 85% or higher classification accuracy could be achieved. This work proves the feasibility to discriminate gases/odours, which can lead to the development of a real-time discrimination algorithm for portable/handheld devices.

8.2 Objectives and Achievements

Four objectives were listed in Chapter 1.4 as the main purposes of this work. In this section, these objectives are listed below against the achievements made in this thesis.

- Objective 1: Enhance the NDIR sensor performance by implementing a plasmonic nanostructure.

  Achievement: An analytical model in COMSOL was built to design and simulate the plasmonic structure of different geometries. This tunable structure allowed the maximum narrowband emissions/absorptions at the target wavelength. The simulation process investigated the frequency spectrum of the design, as well as the manufacturing tolerance of ± 5%. The optimised geometry dimensions were laid out as mask designs using Mentor Graphics L-edit for each gas of interest, and sent off for fabrication.

- Objective 2: Calibrate and assemble the device for gas measurements under the laboratory conditions.

  Achievement: The modelled structures were fabricated and diced into 2 mm × 2mm micro hotplate devices which were assembled into an NDIR system as the infra-red source. This integrated system includes a commercial detector with optical film and a gas cell of 10 cm. Various gas experiments were performed with a gas testing bench at multiple concentrations and humidity levels. Unfortunately, due to some manufacturing discrepancies, only devices designed for acetone and ammonia were able to collect visible responses. These two sensors were characterised mainly and results were presented.

- Objective 3: Develop signal processing methods and algorithms to improve sensor response and compensate issues such as drift and slow response/recovery.

  Achievement: Temperature modulation technique was applied to metal oxide semiconductors. This method reduced the sensor response time from tens of seconds to just a few seconds by using the dynamic sensor response. The micro hotplate was switching between two temperatures, and the changes were extracted followed by a fast Fourier transform and a low pass filter post-processing techniques. This technique was first implemented off-board, and later on-board in real-time with an optimised algorithm and a microcontroller. The FFT magnitudes corresponded to the gas concentrations and operating

conditions, such as humidity levels. This information was then used in an artificial neural network for both prediction and regression fitting analysis, and results were promising.

- Objective 4: Apply algorithms to the sensor data collected by a multi-sensor unit to discriminate and classify different gases.

  Achievement: A dataset was collected with three MOX sensors and four gases under three relative humidity conditions. This dataset was first pre-processed with feature extraction and auto-ranging, then used to test various algorithms for gas discrimination and classification. The algorithms trialled and tested were principle component analysis, instance based algorithms such as k-nearest neighbour and self-organising maps, shallow neural network (multi-layer perceptrons) and deep neural network such as convolutional neural network. The results were demonstrated either with plots or confusion tables. All methods could achieve an accuracy of 85% or over with the neural networks at 90% or over. This is a starting point for a real-time gas identification algorithm for a portable sensing device.

In addition to these achievements, different gas sensor applications were explored, includes EU Smokebot and EPSRC Supergen research projects to develop gas sensors for harsh environment, and a smart sensor warning device to aid incontinence individuals. Both NDIR and MOX sensors were used in the two research projects, and only MOX sensors were included in the warning device. These applications showed the sensor performance in real world scenarios that will lead to the further development of a commercial product. The results from these applications are included in this thesis. All publications are listed in the List of Publications at the beginning of this thesis.

8.3 Further work

Based on the work completed in this thesis, further improvements and researches can be made both on the plasmonic emitters and the signal processing methods. This section proposed a few directions that can be implemented in the future.

8.3.1 Plasmonic Enhanced NDIR IR Emitters

The simulation model built in COMSOL is based on the plasmonic structure with periodic arrays of cylindrical dots. There have been mentions of other structures such as pillars and beams in literature, which could have their own merits in performance and fabrication. Further modelling can include these structures for comparisons. In addition, the structure used in this work did not show distinctive peaks at wavelengths higher than 8.5 μm. This could be resolved with different plasmonic models.

The simulation in this work underestimated the manufacturing variance so that the design and actual devices had discrepancies which affected the experimental results. To avoid similar issues in the next wafer batch, the simulation model should be adjusted according to the fabricated devices to minimise the difference between simulation and measurement, such adjustments including variation sweeps and model constraints. The overall aim is to increase the simulation accuracy as close to the real result as possible for the next batch of devices.

Different fabrication processes could also be investigated to mimise or avoid such variation in the future batch. CMOS process can greatly reduce the cost but for prototyping purpose, MEMS process might be more suitable for small batch production. It also allows a more accurate control of dimensions even to nano meter resolution. Another possible way for accurate plasmonic structures could be post process based on CMOS micro heaters. By using post-processing techniques, more precise or complex structure can be fabricated.

On the experimental side, the gas cell can be improved further to reduce its size while increasing the reflectiveness. For example, instead of a straight aluminium tube, a curve shaped structure can be used and inner walls polished or spray coated with gold. This step can be achieved through a CAD modelling first with ray tracing features, and then either 3D printed or machined depending on the materials. The curved gas cell can greatly reduce the dimension of an NDIR sensor without compromising the reflective length.

Commercial detectors were used in this work with optical filters. But optical filters are bulky and expensive which is why filterless NDIR sensor is the future for miniaturisation. According to Kirchhoff's law, the same plasmonic structure of an emitter can be applied to a detector. The tuned plasmonic detector will have a

thermopile or pyroelectric instead of a micro hotplate to convert radiation back to electric signals.

The gases and odours of interest studied here include carbon monoxide, carbon dioxide, acetone, ammonia and hydrogen sulfide. More gases can be investigated in the future, such as gases below 8 μm (i.e. nitric oxide) and water influence. Water has several peaks on the spectrum, which can influence some of the sensors. Furthermore, the effect of humidity needs to be explored further, for instance, more humidity levels in the experiments and humidity compensation in the post-processing steps.

Because NDIR sensors have fast response speed, they can also be used for real-time gas indications with machine learning algorithms. However, this is a step after the improvement of sensor performance.

8.3.2 Signal Processing Methods

The first signal processing method is to compensate the sensor drift and reduce the response time of a MOX sensor. The algorithm shows promising results, but it can still be improved. For instance, the signal sample range is a few seconds, which can be faster as the switching time of the micro hotplate is millisecond. In the microcontroller operating mode, the sample range is 2s, but with the increase of sampling rate, this range can potentially be shorter. The collected data were processed through an FFT and the magnitudes were then compared. It has been found that the frequency of the magnitude could be related to the gas type, which deserves further study. The regression and prediction analysis was only conducted using one MOX sensor, therefore, repeat studies with a variety of MOX sensors will provide a more comprehensive result.

The second signal processing method studied different types of prediction algorithms including machine learning, and all models gave high accuracy predictions. To increase the accuracy further, i.e. over 95%, a larger dataset can be used for training and testing. For instance, more humidity and concentration levels, change of temperature/pressure, and more repetitions. In addition, other algorithms can be trialled, such as recurrent neural networks, support vectors machines, or black box models. The application for gas discrimination is to use it in real-time, therefore, the chosen algorithm should be easy to implement with low memory requirement. The method can then be optimised to run on a microcontroller such as a Teensy or

an Arduino.

8.3.3 Applications

From the research and project work conducted in this thesis, future work can be focused on the further development or commercialisation of the sensor unit. For instance, the sensing unit designed for harsh environment, either high temperature or low oxygen, should be tested under the designed conditions, i.e. expose to high temperature ($\sim$ 200 °C) and pure hydrogen conditions. Prior to these experiments, more laboratory measurements need to be conducted to ensure sensor performance and stability. Improvements can be made to these sensor units, such as heatproof enclosures, a gas cooling system for sensor protections, metal pipelines and sealant to prevent toxic gas leakage (i.e. hydrogen or hydrogen sulfide), feedback controls to react with environmental changes, and etc.

The warning device with the pattern recognition algorithm can be integrated and tested together with real-time classification outputs. Laboratory measurements will be performed before testing it in hospitals or care homes. The size of the device can be reduced further with an integrated microprocessor chip and fully customised circuit boards. Furthermore, the application can be extended to other areas, such as food freshness, hazardous leak detections and combustion monitoring, where real time gas/odour classifications are needed.

Appendix A

Wafer batch 0 plasmonic pattern geometries

No.	Met2/Met3	Dot Shape	(Pitch)	Radius
1	none	-	-	-
2	Met3	Circle	2.60	0.65
3	Met3	Circle	2.60	0.65
4	Met3	Circle	2.60	0.80
5	Met3	Circle	2.60	0.50
6	Met3	Circle	2.40	0.60
7	Met3	Circle	2.40	0.70
8	Met3	Circle	2.40	0.50
9	Met3	Circle	2.80	0.70
10	Met3	Circle	2.80	0.80
11	Met3	Circle	2.80	0.60
12	Met3	Circle	2.00	0.50
13	Met3	Circle	2.20	0.55
14	Met3	Circle	3.00	0.75
15	Met3	Circle	3.20	0.80
16	Met3	Circle	3.40	0.85

Continued on next page

Table A.1 – *Continued from previous page*

No.	**Met2/Met3**	**Dot Shape**	**(Pitch)**	**Radius**
17	Met3	Circle	3.60	0.90
18	Met3	Circle	3.80	0.95
19	Met3	Circle	4.00	1.00
20	Met3	Circle	4.20	1.05
21	Met3	Circle	4.40	1.10
22	Met3	Circle	4.60	1.15
23	Met3	Circle	4.80	1.20
24	Met3	Circle	5.00	1.25
25	Met3	Circle	5.20	1.30
26	Met3	Circle	5.40	1.35
27	Met3	Circle	5.60	1.40
28	Met3	Circle	5.80	1.45
29	Met3	Circle	6.00	1.50
30	Met3	Circle	6.20	1.55
31	Met3	Circle	6.40	1.60
32	Met3	Circle	6.60	1.65
33	Met3	Circle	6.80	1.70
34	Met3	Circle	7.00	1.75
35	Met3	Circle	7.20	1.80
36	Met3	Circle	7.40	1.85
37	Met3	Circle	7.60	1.90
38	Met3	Circle	7.80	1.95
39	Met3	Circle	8.00	2.00
40	Met3	Circle	Variable[1]	Pitch/4
41	Met3	Circle	Variable[2]	Pitch/4
42	Met3	Circle	Variable[3]	Pitch/4
43	Met3	Circle	Variable[2]	0.50
44	Met3	Circle	Variable[3]	1.00

Continued on next page

Table A.1 – *Continued from previous page*

No.	**Met2/Met3**	**Dot Shape**	**(Pitch)**	**Radius**
45	*Met3*	*Trapezoid*	*4.25*	⋆
46	*Met3*	*Trapezoid*	*2.60*	⋆
47	*Met3*	*Trapezoid*	*5.00*	⋆
48	*Met3*	*Trapezoid*	*8.00*	⋆
49	*Met3*	*Trapezoid*	*Variable*[1]	⋆

[1] From 2 to 8 μm.

[2] From 2 to 5 μm.

[3] From 5 to 8 μm.

⋆ Trapezoid size: 2.00 μm (H) × 2.50 μm (W1) × 1.50 μm (W2)

Appendix B

Geometries and Simulation Results with Aluminium as Metal Layer

Table B.1: Planer plasmonic geometries used in simulation with aluminium metal layer (unit: μm).

Gas of Interest	**IR Absorption Band**	**Planar**	
		Diameter	**Pitch**
CO	4.6	3.2	4.45
CO_2	4.3	2.0	4.15
H_2S	7.3	3.0	7.4
Acetone	8.2	7.0	8.2
Ammonia	10.6	7.6	10.4

Same parameter sweep was performed and the optimum geometries were chosen and simulated in COMSOL across the full spectrum of interest. Results for each design were shown below (tolerance not shown).

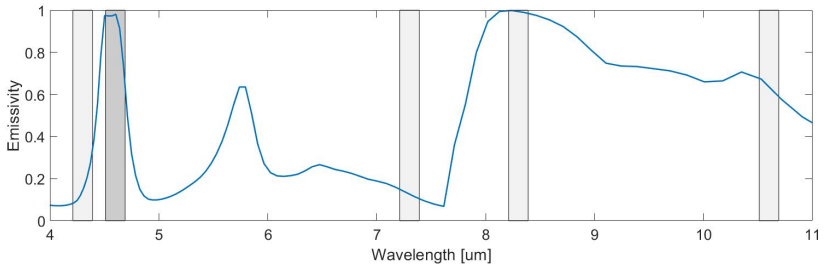

(a) Carbon Monoxide

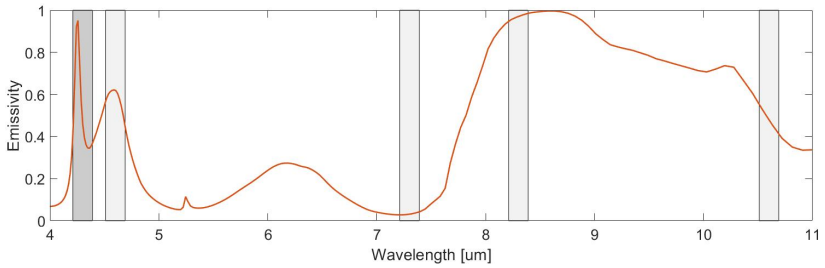

(b) Carbon Dioxide

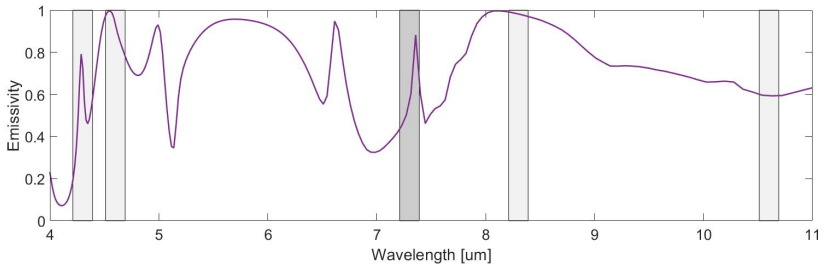

(c) Hydrogen sulfide

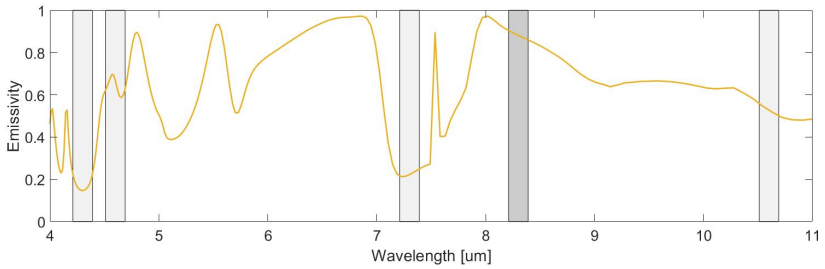

(d) Acetone

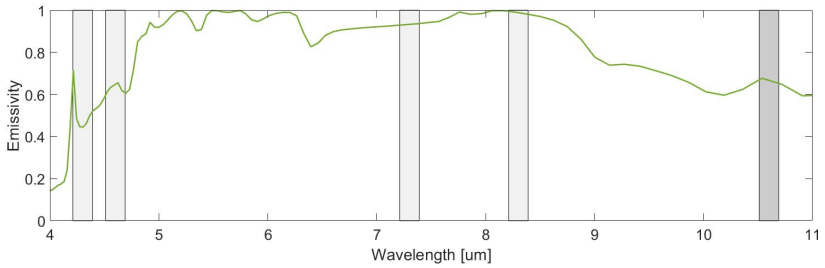

(e) Ammonia

Figure B.1: COMSOL simulation results for the plasmonic structure and tungsten metal layer.

Appendix C

Additional Machine Learning Results

C.1 KNN Results with PCA Pre-processed Data

Table C.1: Confusion table obtained using KNN algorithm and PCA pre-processed data (dataset 2–5 for training, dataset 1 for testing).

Predicted Outputs	**Target Outputs**			
	Acetone	**Ammonia**	**Ethyl Acetate**	**Synthetic Urine**
Acetone	24	0	0	0
Ammonia	2	24	3	0
Ethyl Acetate	1	0	24	0
Synthetic Urine	0	3	0	27
Total Number	*27*	*27*	*27*	*27*
Total Accuracy: 91.67%				

Table C.2: The classification report with dataset 1.

	Precision	**Recall**	**F1-score**	**Support**
Acetone	1	0.89	0.94	27
Ammonia	0.83	0.89	0.86	27
Ethyl Acetate	0.96	0.89	0.92	27
Synthetic Urine	0.9	1	0.95	27

Table C.3: Confusion table obtained using KNN algorithm and PCA pre-processed data (dataset 1 & 3–5 for training, dataset 2 for testing).

Predicted Outputs	**Target Outputs**			
	Acetone	**Ammonia**	**Ethyl Acetate**	**Synthetic Urine**
Acetone	22	0	6	1
Ammonia	3	25	4	0
Ethyl Acetate	0	2	16	0
Synthetic Urine	2	0	1	26
Total Number	*27*	*27*	*27*	*27*
Total Accuracy: 82.41%				

Table C.4: The classification report with dataset 2.

	Precision	**Recall**	**F1-score**	**Support**
Acetone	0.76	0.81	0.79	27
Ammonia	0.78	0.93	0.85	27
Ethyl Acetate	0.89	0.59	0.74	27
Synthetic Urine	0.9	0.96	0.93	27

Table C.5: Confusion table obtained using KNN algorithm and PCA pre-processed data (dataset 1–2 & 4–5 for training, dataset 3 for testing).

Predicted Outputs	**Target Outputs**			
	Acetone	**Ammonia**	**Ethyl Acetate**	**Synthetic Urine**
Acetone	24	0	0	2
Ammonia	1	25	4	0
Ethyl Acetate	0	0	23	0
Synthetic Urine	2	2	0	25
Total Number	*27*	*27*	*27*	*27*
Total Accuracy: 89.81%				

Table C.6: The classification report with dataset 3.

	Precision	**Recall**	**F1-score**	**Support**
Acetone	0.92	0.89	0.91	27
Ammonia	0.83	0.93	0.88	27
Ethyl Acetate	1.0	0.85	0.92	27
Synthetic Urine	0.86	0.93	0.89	27

Table C.7: Confusion table obtained using KNN algorithm and PCA pre-processed data (dataset 1–3 & 5 for training, dataset 4 for testing).

Predicted Outputs	**Target Outputs**			
	Acetone	**Ammonia**	**Ethyl Acetate**	**Synthetic Urine**
Acetone	25	1	0	1
Ammonia	1	22	1	0
Ethyl Acetate	1	3	26	0
Synthetic Urine	0	1	0	26
Total Number	*27*	*27*	*27*	*27*
Total Accuracy: 91.67%				

Table C.8: The classification report with dataset 4.

	Precision	**Recall**	**F1-score**	**Support**
Acetone	0.93	0.93	0.93	27
Ammonia	0.92	0.81	0.86	27
Ethyl Acetate	0.87	0.96	0.91	27
Synthetic Urine	0.96	0.96	0.96	27

Table C.9: Confusion table obtained using KNN algorithm and PCA pre-processed data (dataset 1–4 for training, dataset 5 for testing).

Predicted Outputs	**Target Outputs**			
	Acetone	**Ammonia**	**Ethyl Acetate**	**Synthetic Urine**
Acetone	25	0	0	1
Ammonia	1	20	1	0
Ethyl Acetate	0	1	26	1
Synthetic Urine	1	6	0	25
Total Number	*27*	*27*	*27*	*27*
Total Accuracy: 88.89%				

Table C.10: The classification report with dataset 5.

	Precision	**Recall**	**F1-score**	**Support**
Acetone	0.96	0.93	94	27
Ammonia	0.91	0.74	0.82	27
Ethyl Acetate	0.93	0.96	0.95	27
Synthetic Urine	0.78	0.93	0.85	27

C.2 ANN Results with One hidden Layer

Table C.11: Confusion table obtained using ANN algorithm with no concentration information and one hidden layer (dataset 2–5 for training, dataset 1 for testing).

Predicted Outputs	**Target Outputs**			
	Acetone	**Ammonia**	**Ethyl Acetate**	**Synthetic Urine**
Acetone	23	0	0	3
Ammonia	1	22	2	1
Ethyl Acetate	1	5	24	0
Synthetic Urine	2	0	1	23
Total Number	*27*	*27*	*27*	*27*
Total Accuracy: 85.19%				

Table C.12: Confusion table obtained using ANN algorithm with no concentration information and one hidden layer(dataset 1 & 3–5 for training, dataset 2 for testing).

Predicted Outputs	**Target Outputs**			
	Acetone	**Ammonia**	**Ethyl Acetate**	**Synthetic Urine**
Acetone	20	1	10	1
Ammonia	3	23	6	3
Ethyl Acetate	0	3	9	0
Synthetic Urine	4	0	2	23
Total Number	*27*	*27*	*27*	*27*
Total Accuracy: 69.45%				

Table C.13: Confusion table obtained using ANN algorithm with no concentration information and one hidden layer(dataset 1–2 & 4–5 for training, dataset 3 for testing).

Predicted Outputs	**Target Outputs**			
	Acetone	**Ammonia**	**Ethyl Acetate**	**Synthetic Urine**
Acetone	22	0	1	5
Ammonia	0	24	4	1
Ethyl Acetate	3	1	21	2
Synthetic Urine	2	2	1	19
Total Number	*27*	*27*	*27*	*27*
Total Accuracy: 79.63%				

Table C.14: Confusion table obtained using ANN algorithm with no concentration information and one hidden layer(dataset 1–3 & 5 for training, dataset 4 for testing).

Predicted Outputs	**Target Outputs**			
	Acetone	**Ammonia**	**Ethyl Acetate**	**Synthetic Urine**
Acetone	23	0	1	0
Ammonia	1	23	0	2
Ethyl Acetate	2	3	26	1
Synthetic Urine	1	1	0	24
Total Number	*27*	*27*	*27*	*27*
Total Accuracy: 88.89%				

Table C.15: Confusion table obtained using ANN algorithm with no concentration information and one hidden layer(dataset 1–4 for training, dataset 5 for testing).

Predicted Outputs	**Target Outputs**			
	Acetone	**Ammonia**	**Ethyl Acetate**	**Synthetic Urine**
Acetone	25	0	2	1
Ammonia	1	19	1	2
Ethyl Acetate	0	2	24	1
Synthetic Urine	1	6	0	23
Total Number	*27*	*27*	*27*	*27*
Total Accuracy: 84.26%				

Table C.16: Performance evaluation of the five datasets.

Datasets	**Cross Entropy**
Dataset 1	0.0615
Dataset 2	0.1215
Dataset 3	0.0878
Dataset 4	0.0428
Dataset 5	0.0500
Averaged	*0.0927*

C.3 Encoded Output in ANN with 2 Hidden Layers

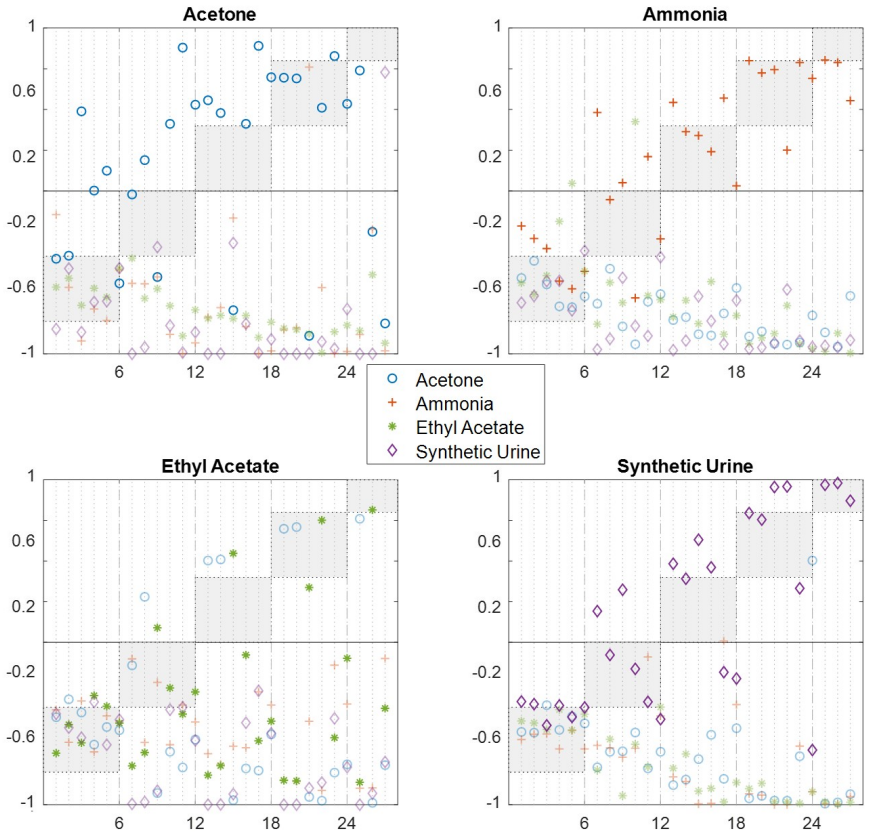

Figure C.1: Classification results with encoded output values using ANN with 2 hidden layers of 8 neurons each (tested with dataset 2).

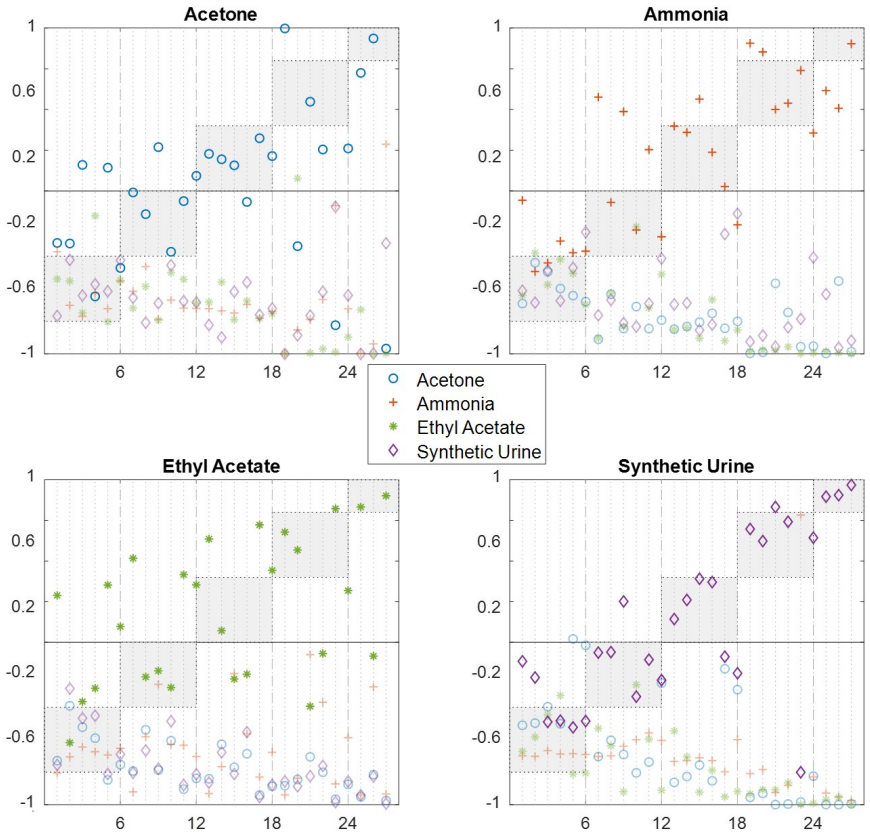

Figure C.2: Classification results with encoded output values using ANN with 2 hidden layers of 8 neurons each (tested with dataset 3).

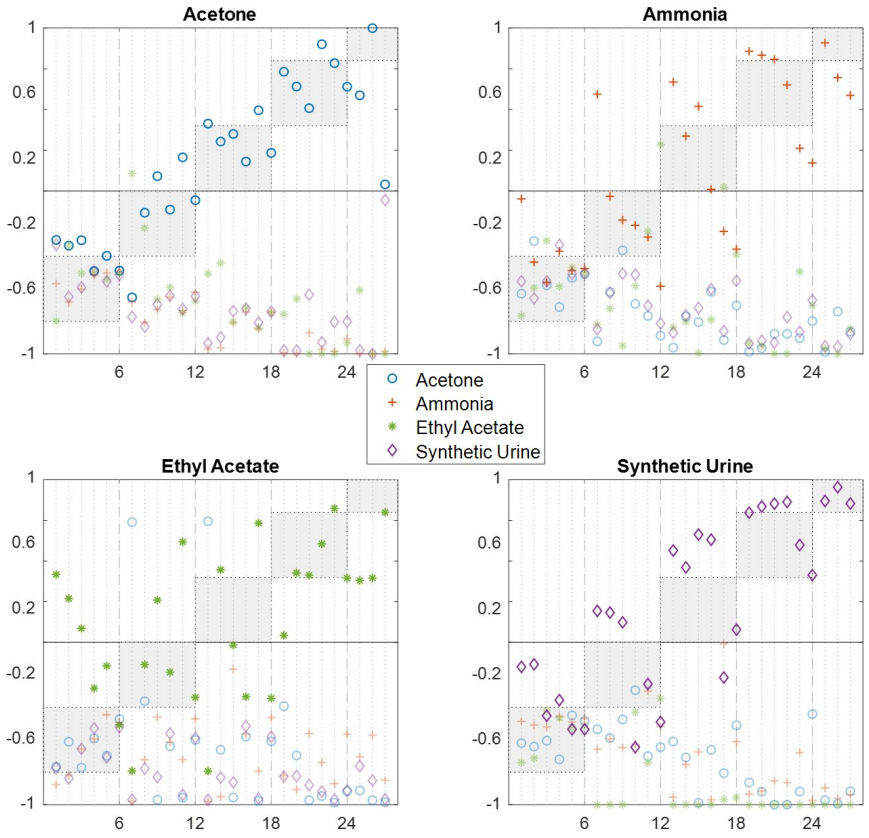

Figure C.3: Classification results with encoded output values using ANN with 2 hidden layers of 8 neurons each (tested with dataset 4).

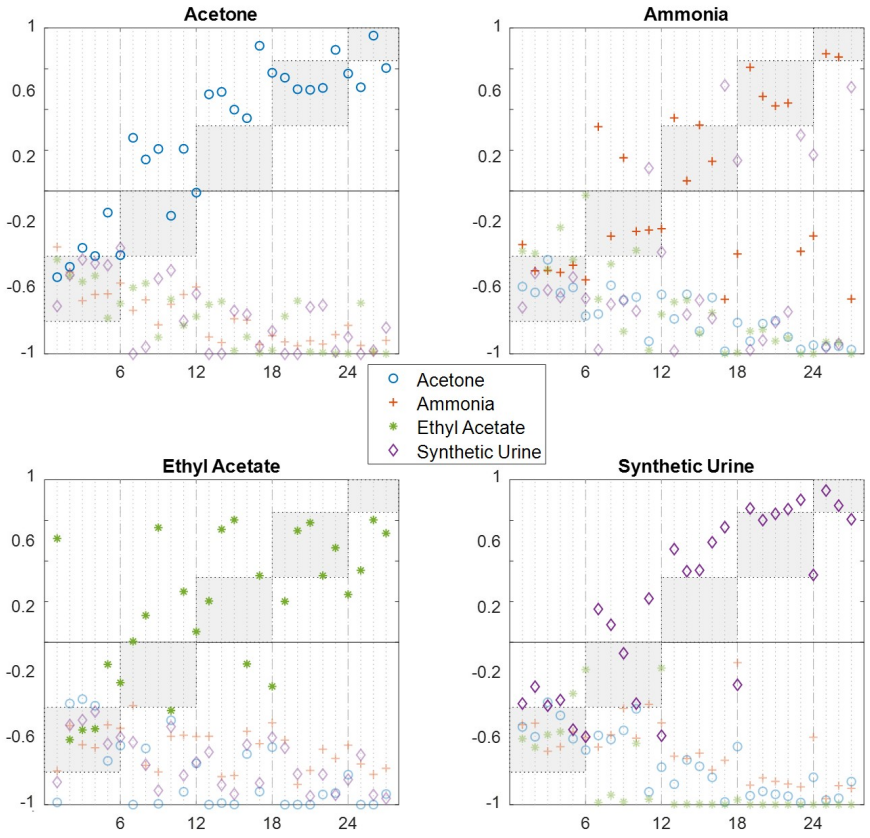

Figure C.4: Classification results with encoded output values using ANN with 2 hidden layers of 8 neurons each (tested with dataset 5).

C.4 Encoded Output in ANN with 1 Hidden Layer

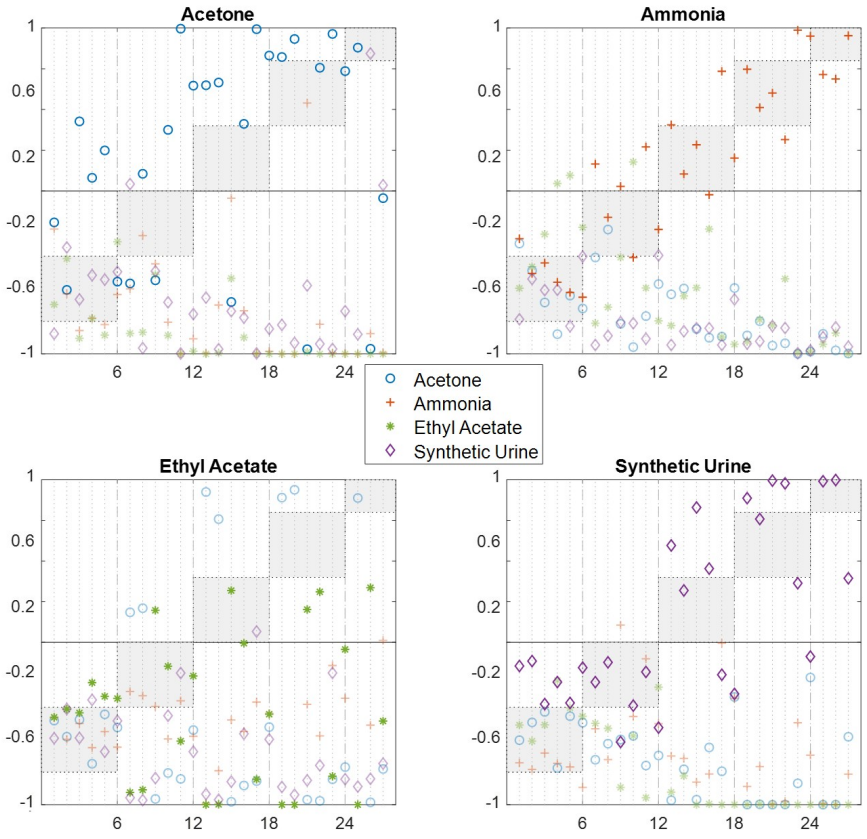

Figure C.5: Classification results with encoded output values using ANN with 1 hidden layers of 8 neurons (tested with dataset 2).

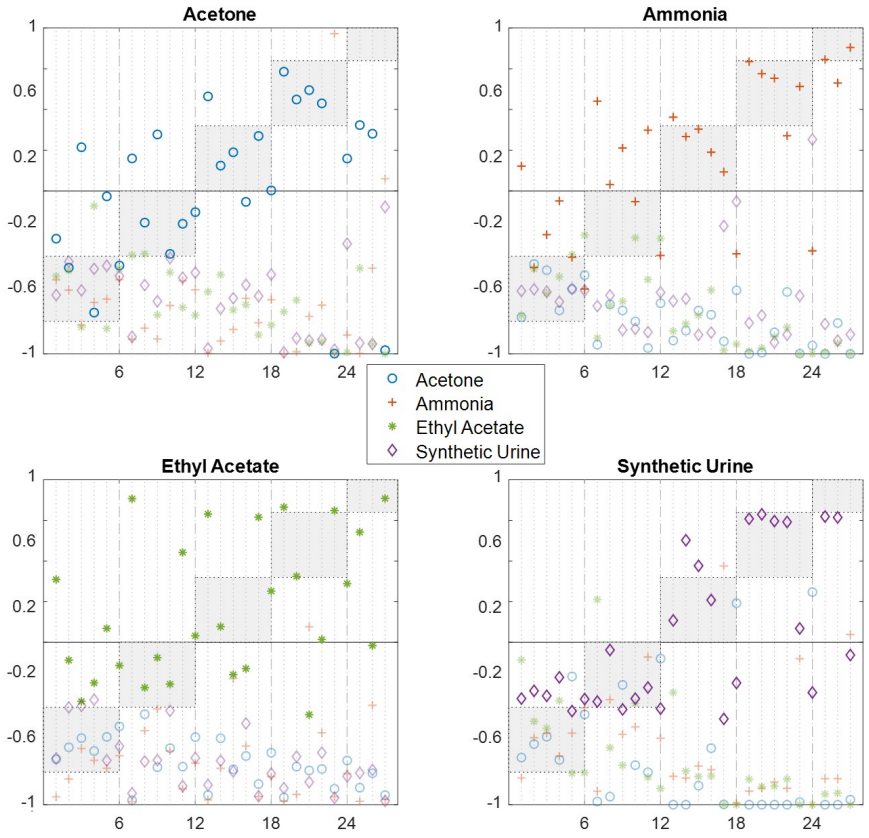

Figure C.6: Classification results with encoded output values using ANN with 1 hidden layers of 8 neurons (tested with dataset 3).

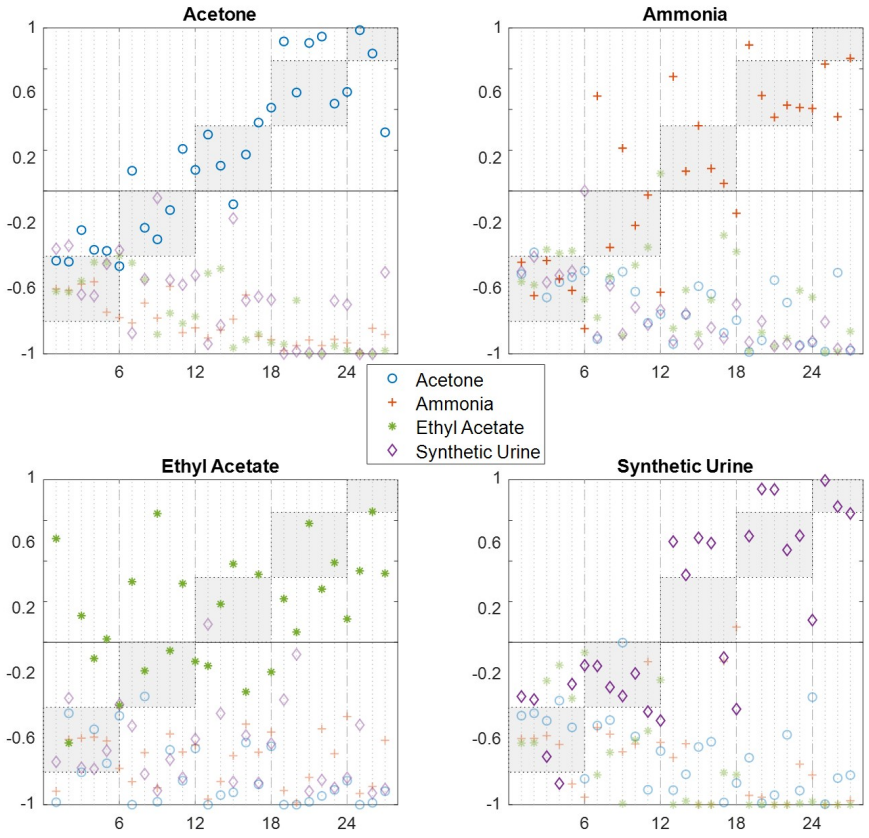

Figure C.7: Classification results with encoded output values using ANN with 1 hidden layers of 8 neurons (tested with dataset 4).

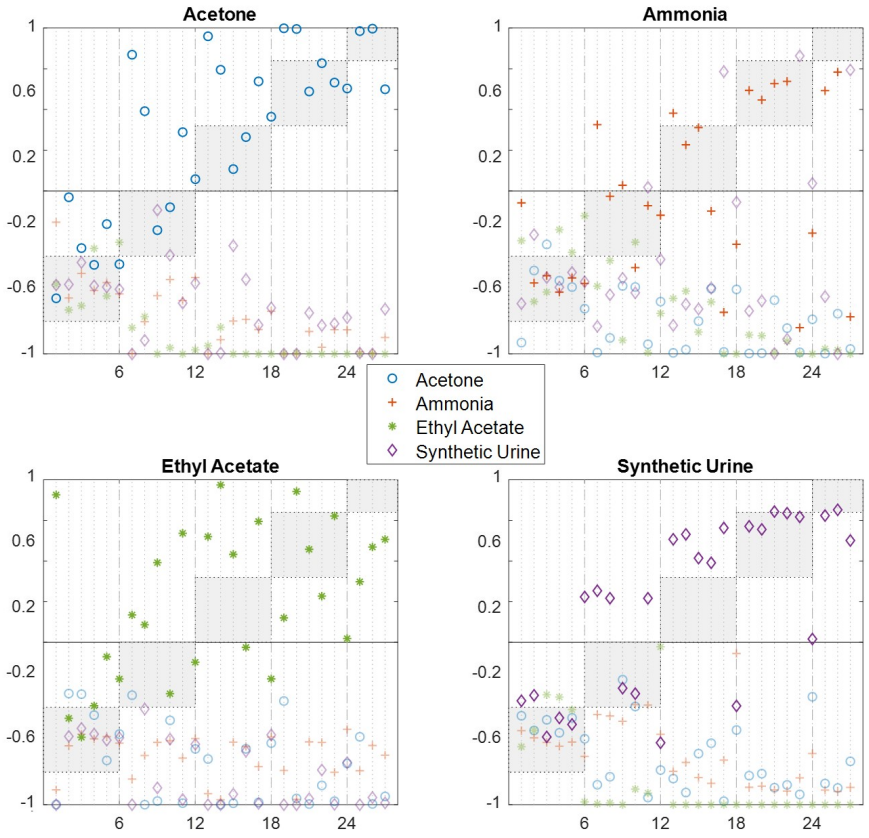

Figure C.8: Classification results with encoded output values using ANN with 1 hidden layers of 8 neurons (tested with dataset 5).

C.5 Encoded Output ([0, 1]) in ANN with 2 Hidden Layers

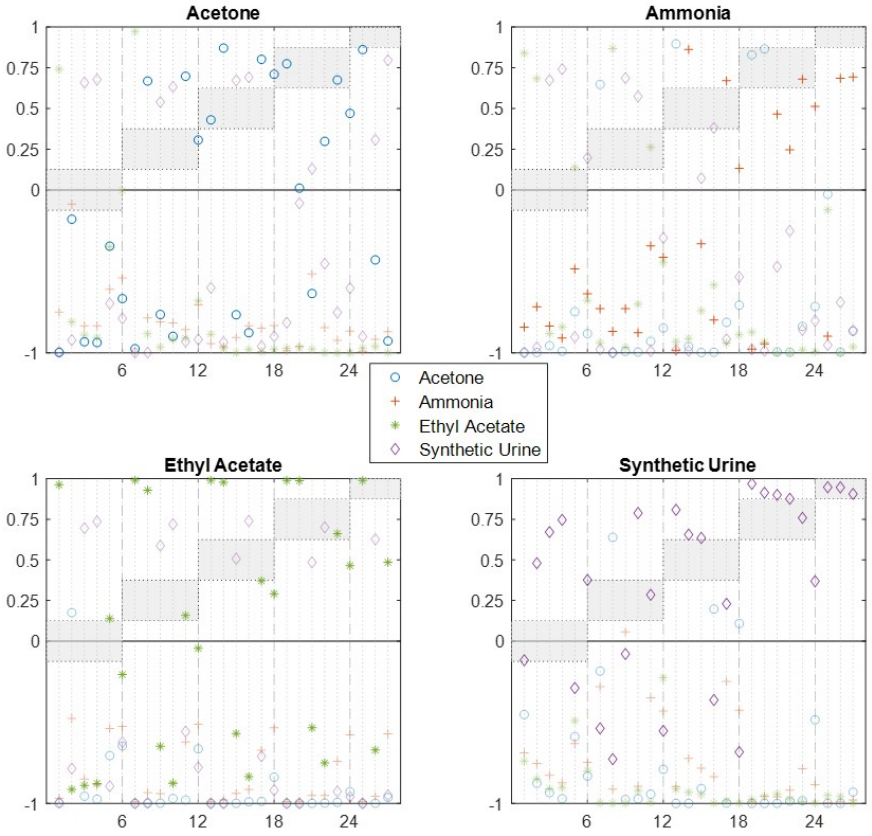

Figure C.9: Classification results with encoded output values between [0, 1] using ANN with 2 hidden layers of 8 neurons each (tested with dataset 1).

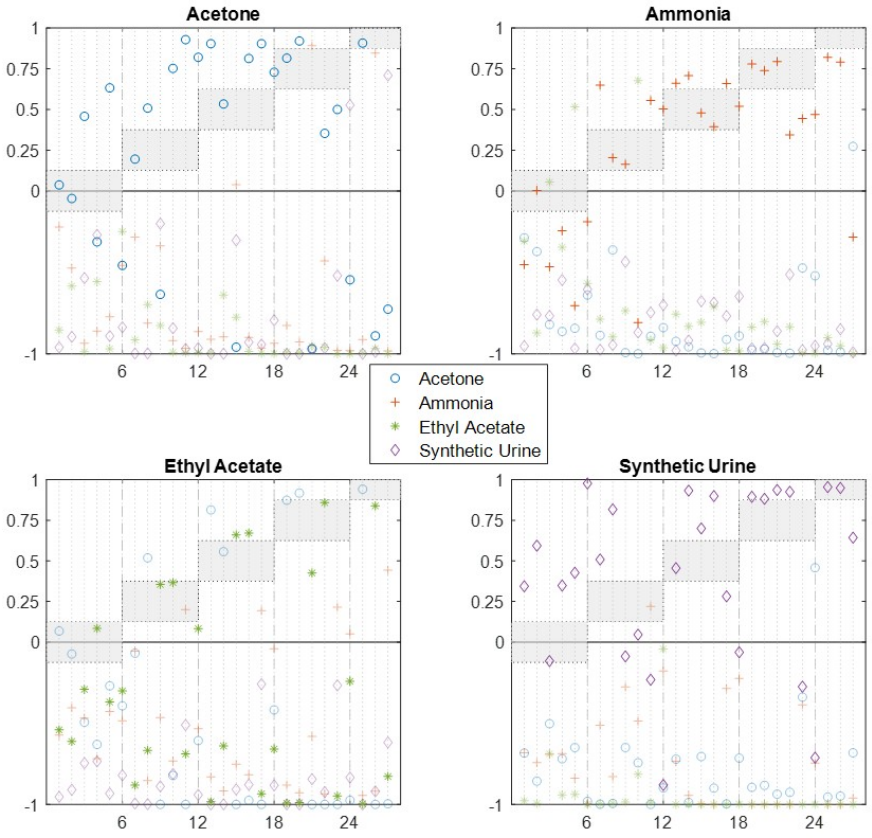

Figure C.10: Classification results with encoded output values between [0, 1] using ANN with 2 hidden layers of 8 neurons each (tested with dataset 2).

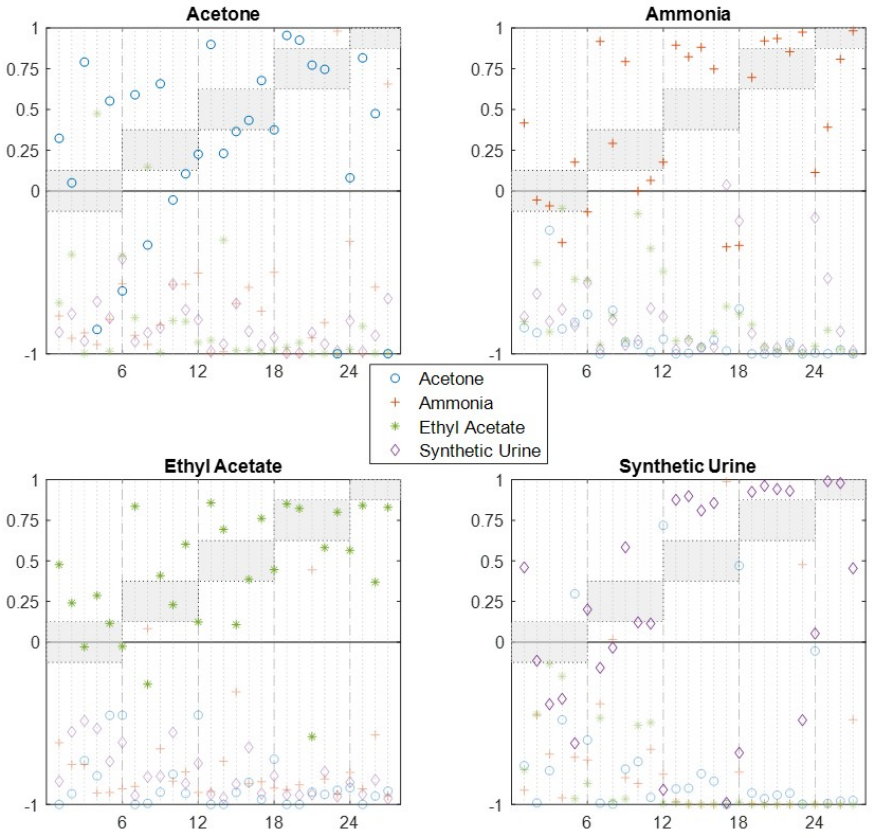

Figure C.11: Classification results with encoded output values between [0, 1] using ANN with 2 hidden layers of 8 neurons each (tested with dataset 3).

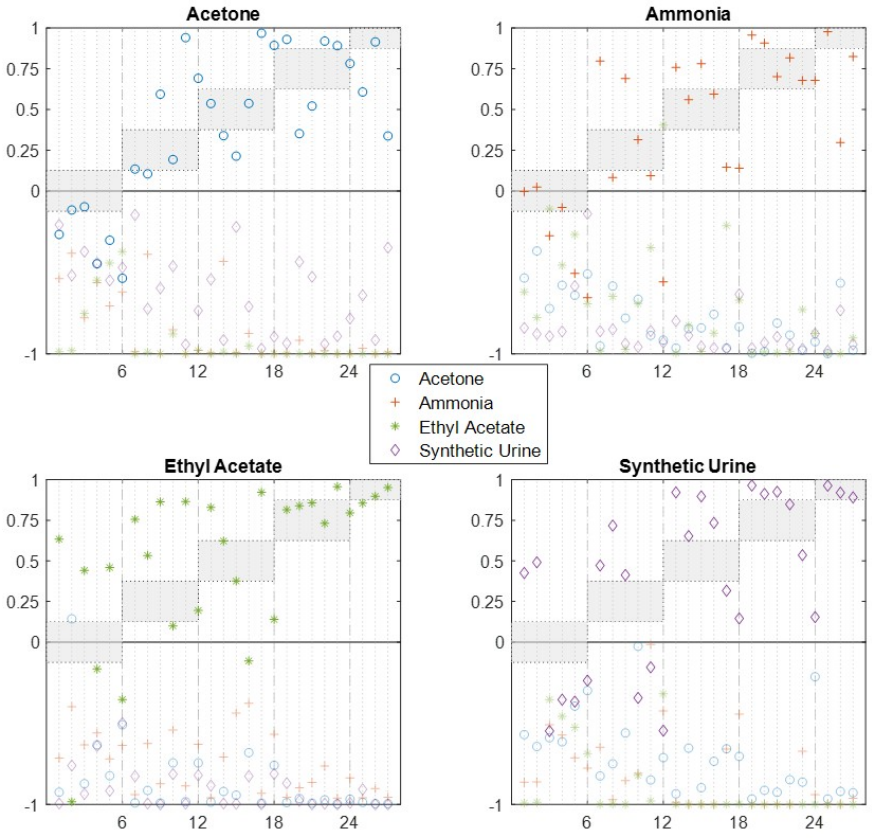

Figure C.12: Classification results with encoded output values between [0, 1] using ANN with 2 hidden layers of 8 neurons each (tested with dataset 4).

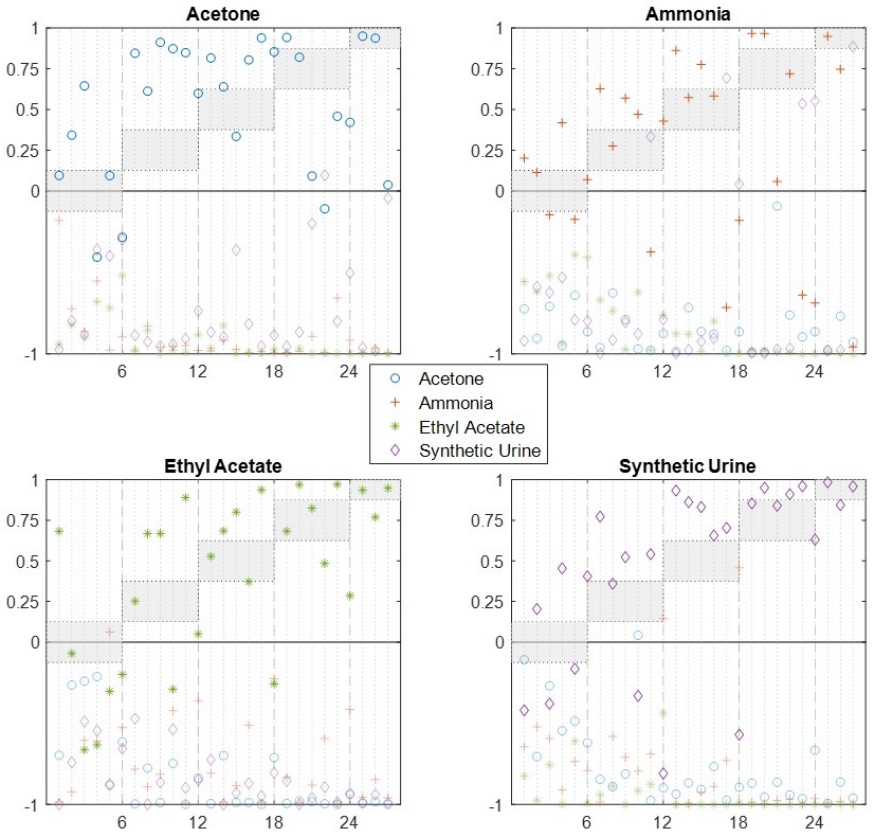

Figure C.13: Classification results with encoded output values between [0, 1] using ANN with 2 hidden layers of 8 neurons each (tested with dataset 5).

C.6 Encoded Output ([0, 1]) in ANN with 1 Hidden Layer

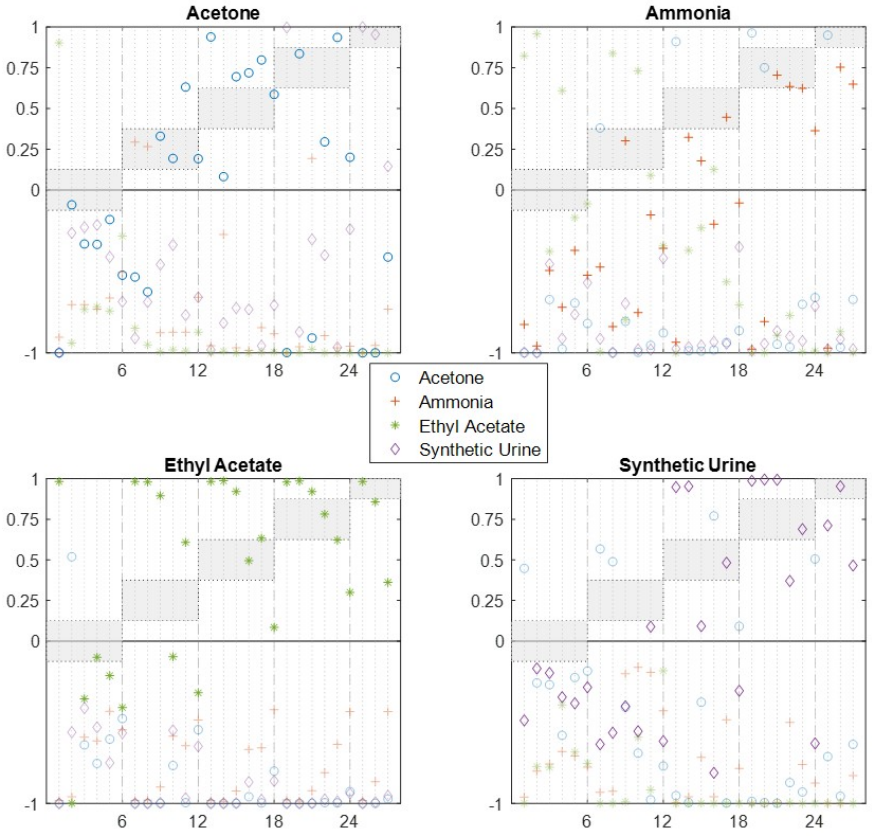

Figure C.14: Classification results with encoded output values between [0, 1] using ANN with 1 hidden layers of 8 neurons (tested with dataset 1).

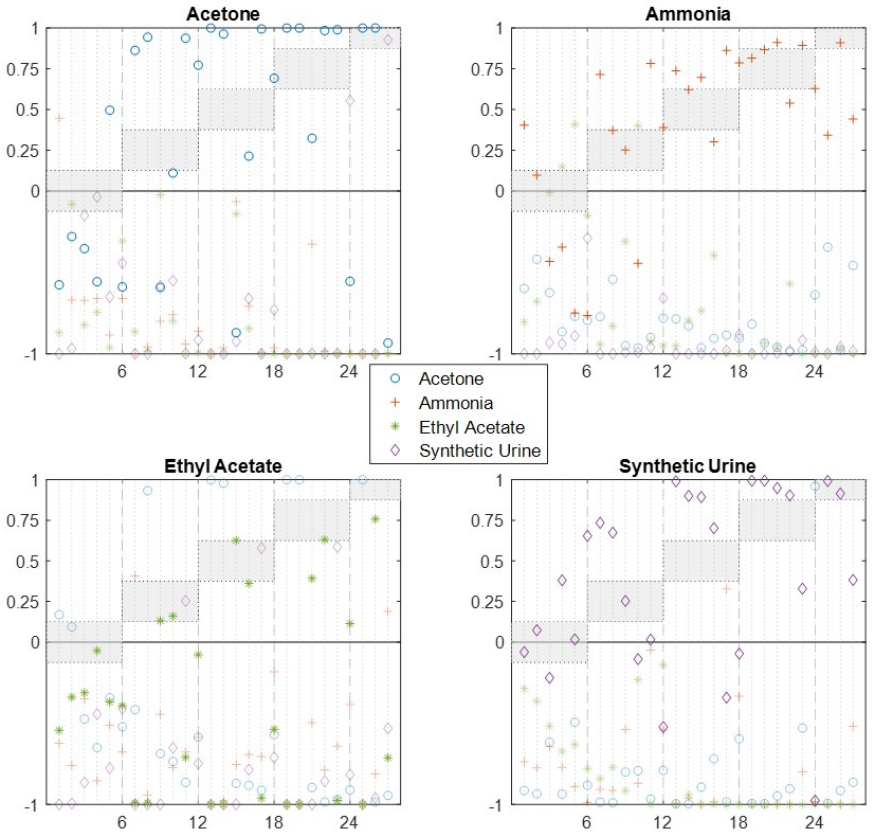

Figure C.15: Classification results with encoded output values between [0, 1] using ANN with 1 hidden layers of 8 neurons (tested with dataset 2).

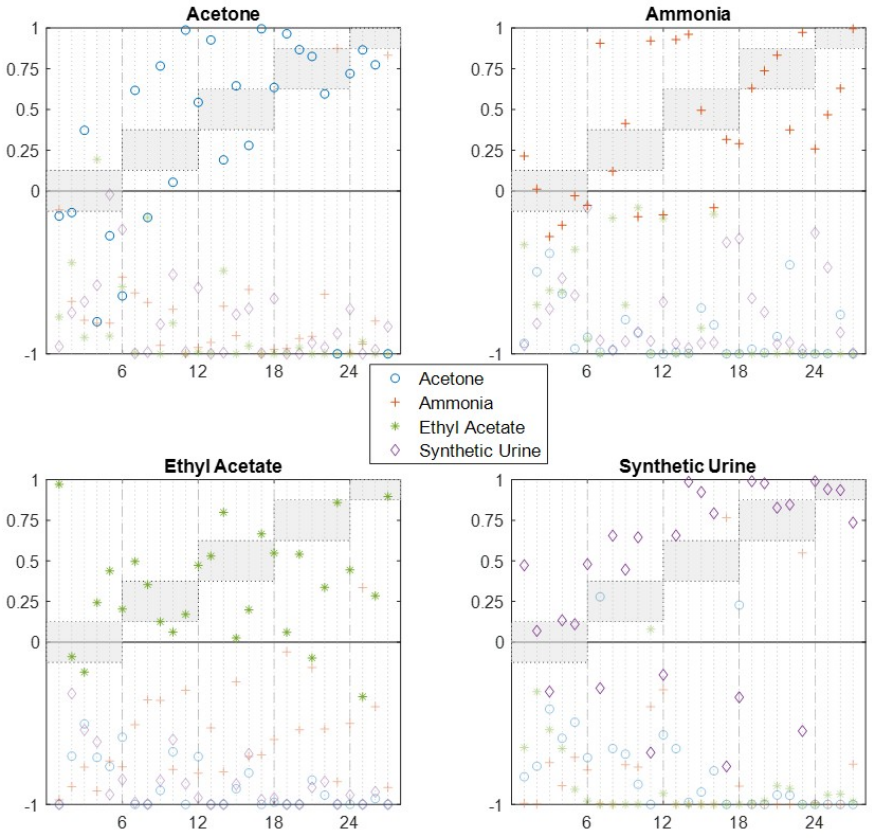

Figure C.16: Classification results with encoded output values between [0, 1] using ANN with 1 hidden layers of 8 neurons (tested with dataset 3).

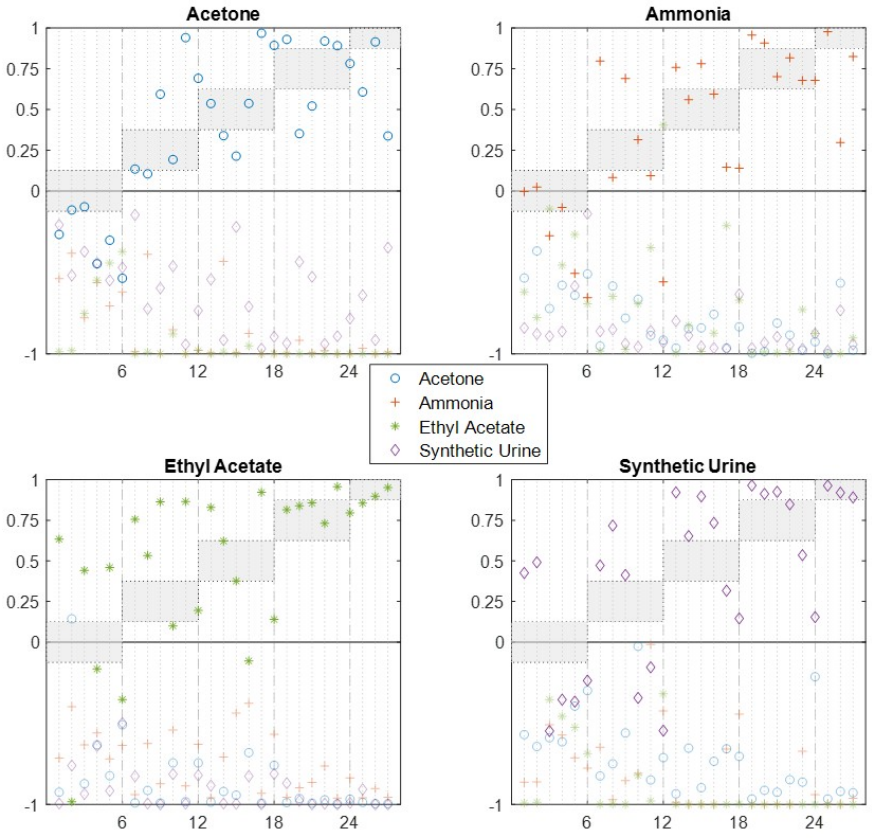

Figure C.17: Classification results with encoded output values between [0, 1] using ANN with 1 hidden layers of 8 neurons (tested with dataset 4).

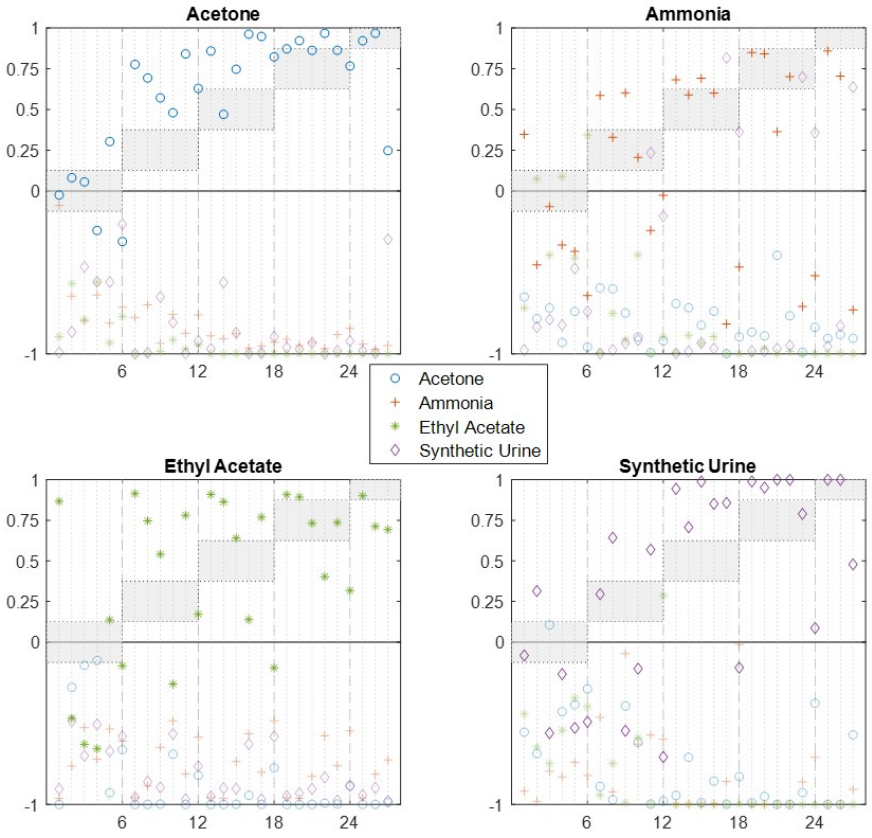

Figure C.18: Classification results with encoded output values between [0, 1] using ANN with 1 hidden layers of 8 neurons (tested with dataset 5).